University of Southampton

Free-Lagrange Simulations of Shock-Bubble Interaction in Extracorporeal Shock Wave Lithotripsy

Ahmad Riza Jamaluddin

Submitted for the degree of Doctor of Philosophy

School of Engineering Sciences

December 2005

ABSTRACT

Doctor of Philosophy

Free-Lagrange Simulations of Shock-Bubble Interaction in Extracorporeal Shock Wave Lithotripsy

by Ahmad Riza Jamaluddin

Evidence have shown that significant amounts of violent cavitation activity are present during Extracorporeal Shock Wave Lithotripsy (ESWL). This cavitation has been postulated to play a significant role in kidney stone disintegration during treatment. In this study, a swirl-free Free-Lagrange hydrocode is used to simulate the axisymmetric jetting collapse of initially stable air bubbles in water as a result of interaction with a planar lithotripter shock wave. Various cases were carried out in order to investigate the effect of bubble size, the presence of a rigid boundary at various stand-off distances as well as cases involving arrays of bubbles.

The Free-Langrange method is highly suitable for the simulation of highly deforming flows. The technique also retains sharply resolved gas/liquid interfaces regardless of the degree of geometric deformation, and reveals details of the dynamics of bubble collapse. This also helps in reducing the degree of numerical diffusion. The numerical code employs second order space and first order time accurate Godunov-type solvers. For validation purposes two different cases were carried out - simulations of the axisymmetric collapse of a bubble by a planar step shock wave of various strengths and two dimensional planar shock/water column interactions.

In addition to the above, two separate numerical acoustic codes have been developed using the Kirchhoff's method and the Ffowcs William-Hawkings formulation. When coupled to the Free-Lagrange code, each can be used to obtain the far-field pressure signatures of cavitation events. Both numerical codes have been validated against analytical results in predicting the far-field pressure signature emitted from an oscillating solid sphere. The relative merits of each method are given along with a few analyses of the far-field pressure signature predicted from the lithotripter shock wave/bubble interaction problems.

The code has been used to simulate the collapse of single cavitation bubbles in free-field and near a planar rigid boundary for various stand-off distance. Simulation of an array of bubbles are also presented. The results clearly capture the phenomena of bubble collapse that are believed to assist kidney stone fragmentation during lithotripsy treatment, i.e. high speed liquid jet impact and blast wave emission. The far-field pressure signature shows the expansion wave originating from the shock-bubble interaction and the high amplitude blast wave.

Contents

List of Figures

List of Tables

Acknowledgements

I would like to take this opportunity to thank Dr. Graham Ball for supervising my research. His assistance, encouragement and technical guidance throughout this work have been invaluable. I would also like to thank Prof. Timothy Leighton for his invaluable input in bubble dynamics and acoustics. Thanks also to my academic advisor, Dr. Graham Roberts, for some enjoyable discussions during the nine-month and transfer reviews.

I am also grateful to the financial support provided by the School of Engineering Sciences University of Southampton and the Engineering and Physical Sciences Research Council (EPSRC) for this research.

To my dearest parents, and members of family, thank you for your prayer and encouragement throughout these challenging years.

Thanks to my colleagues for technical help and discussions, and to other friends for being there when I needed some valuable support.

Nomenclature

A	cell face area
c	speed of sound
C^n_{axi}	control points along axisymmetric circumference
C^i_G	geometric control points
d	distance from centre of bubble to rigid boundary
dA	elemental area
dS	elemental line
E	specific energy, $\epsilon + (u \cdot u)/2$
$\bar{e}_y$	unit radial vector
F	force
$\bar{F}$	flux vector
$\bar{F}_k$	numerical flux on the k^{th} side
$\bar{G}$	source vectors for axisymmetric geometry
H	enthalpy of the liquid
$H(f)$	Heaviside function
$\bar{I}$	unit tensor
i, j	vector indices
K	number of polygonal boundary of *Voronoi* cell
L_c	characteristic length
m	mass
m_d	mass of daughter particle
M	Mach number
$\hat{n}$	unit normal vector
$\hat{n}_k$	unit vector normal to cell boundary
p	pressure
p_∞	pressure at infinity
p'	$p - p_0$
P_L	pressure in the liquid at the bubble surface
P_g	pressure of the gas within the bubble
P^+	maximum positive pressure amplitude
P^-	maximum negative pressure amplitude
P_{ij}	compressive stress tensor, $p'\delta_{ij}$
r	radial length
r_e	ordinate of the centroid from the symmetry axis
r_c	ordinate of cell boundary mid-point from the symmetry axis

R	bubble radius
R_{max}	bubble maximum radius
R_s	solid pulsator radius
R_0	equilibrium radius
R_{cs}	control surface radius
S	line that encloses cell area
S_c	control surface
S_k	length of polygonal cell boundary
t	time
T	temperature
T_{ij}	Lighthill's equivalent stress tensor, $P_{ij} + \rho u_i u_j - c^2(\rho - \rho_0)\delta_{ij}$
(x, t)	space-time variables of the observer
(y, τ)	space-time variables the source
$\bar{u}$	velocity vector
u_k	outward normal velocity component at the boundary
$\bar{U}$	conserved variable vector
V	volume
V_{geom}	geometric volume, $r_e A$
V_{therm}	thermodynamic volume, $(m/\rho)_{cell}$
W	weighting factor
Z	specific acoustic impedance
α	smoothing routine gain
τ	emission (retarded) time
δ_{ij}	Kronecker delta
Δt	time step
ϵ	specific internal energy
$\Box^2$	$[(1/c^2)(\partial^2/\partial t^2)] - \nabla^2$
ζ	stand-off distance
θ	angle in circumferential direction
ρ	density
ρ_∞	liquid density at infinity
ω	circular frequncy $= 2\pi f$

Acronyms

CFD	Computational Fluid Dynamics
KCHF	Kirchhoff
FWH	Ffowcs Williams-Hawking
ESWL	Extracorporeal Shock Wave Lithotripsy
EOS	Equation of State
FL	Free-Lagrange
ALE	Arbitrary Lagrangian Eulerian
BIM	Boundary Integral Method
MUSCL	Monotone Upwind-centred Scheme for Conservation Laws
CBIE	Conventional Boundary Integral Equation
HBIE	Hypersingular Boundary Integral Equation
VOF	Volume of Fluid Method
EH	Electrohydraulic
EM	Electromagnetic
PE	Piezoelectric
AMCD	Anti-Miss-Shot Device
PEAA	Piezoelectric Annular Array
AUSM	Advective Upstream Splitting Method

Chapter 1

Introduction

Owing to its destructive nature, the dynamics of cavitation bubble collapse have been studied for many years. It is understood that when single bubbles or clusters of bubbles collapse, two distinctive phenomena take place, i.e. emission of shock waves and formation of a high speed liquid microjet which pierces through the bubble interior (Fig. 1.1). The latter only occurs when asymmetry of the flow around the bubble is induced, either by the close proximity of a boundary or by a pressure pulse such as a shock wave. Several cycles of collapse and rebound may occur, resulting in several emissions of shock waves and high speed microjets.

Figure 1.1: Jet formation during the collapse of an oscillating bubble at low pressure ($0.04 - 0.05\,bar$) in a $60 - Hz$ sound field. The bubble size is *ca.* $0.2\,cm$. Photograph taken by Prof. LA Crum, University of Mississippi [28].

Extracorporeal Shock Wave Lithotripsy (ESWL) is technique for shattering stones such as kidney stones or gallstones with shock wave produced outside the body. Ever since it was first introduced in Germany in the 1980's, millions of kidney stone patients around the world have been successfully treated with lithotripsy. The popularity of the procedure has increased immensely. The perception that ESWL treatment does not cause any harm or any severe acute or lasting side effects, and as such is safe, has been the reason for its acceptance by patients and adoption by many health institution. However, it is now realised that, although ESWL appears to be an effective treatment for a wide variety of urinary tract calculi, this important technique is decidedly not problem-free.

Studies of ESWL have showed that cavitation bubbles are induced *in vivo* near the lithotripter focus by the tensile stress of lithotripter shock wave pulses [26]. The mechanical stresses generated by the shock-bubble interaction and subsequent jet impact on the kidney stone have been identified as a possible mechanism of stone fragmentation during lithotripsy. In addition, the direct impact of the incident lithotripter shock wave may also assists in the fragmentation of the kidney stone.

Although the stones can be visualised at any time during the treatment on X-ray or ultrasound, it is difficult or impossible for the operator to judge the degree of fragmentation from viewing the image. As a result, the number of shocks generated during treatment is largely empirical. It is normal practice to give a pre-set number of shocks, typically 1000 to 4000 in one treatment (spaced 1 second apart); the exact number depends on the stone and the type of lithotripter. This is generally unsatisfactory. If too few shocks are given, the patient needs repeat treatment, resulting in an increase in waiting lists, costs, management, and a decrease in health and morale. If more shocks than required to fragment the stone are given, the consequences can be worse. Firstly because each acoustic shock causes some collateral damage to soft tissues. Secondly, each shock source costs several thousand pounds and has a lifetime which is determined by the number of times it is fired. Thirdly, the longer the treatment, the fewer patients can be processed each day.

Despite these findings, current commercial lithotripters are not equipped with any means to determine whether sufficient shocks have been given to cause the necessary degree of fragmentation or even to assess qualitatively the cavitation activity in patients during clinical lithotripsy. One means of detecting the presence of cavitation bubbles is to measure their acoustic emissions [26]. In an attempt to understand the correlation between the acoustic emission and bubble dynamics, Zhong et al. [107] studied the dynamics of *in vitro* cavitation using high-speed photography and measured the associated acoustic emission in water emanating from the focus of an electrohydraulic shock wave lithotripter. Simultaneous high-speed photography and acoustic emission measurements were used to characterise the inertial cavitation and associated emission *in vitro* induced by lithotripsy shock waves. In doing this, a clear correlation between the dynamics of lithotripsy-induced cavitation bubbles and the resultant acoustic emission was identified.

Although cavitation bubbles mainly occur in clusters, most studies concentrate on the collapse of single bubbles. This is because it reduces the complexity of the problem. Furthermore, if the dynamics of a single bubble and the basic mechanisms of bubble collapse are understood, it is easier to predict and analyse the behaviour of cavitation clouds. Nevertheless, when doing so, it is imperative that a number of assumptions are addressed accordingly. In most cases, single bubbles are generated by using an electric spark discharge or intense laser beam. By employing these methods, the size and position of the bubbles can be controlled, either by inducing the cavitation near boundaries or in the free-field. In order to observe the dynamics and evolution of the bubbles, high-speed photography is employed. However, understanding of the fluid mechanics involved is incomplete owing to the limited temporal and spatial resolution of available experimental diagnostics.

Therefore, numerical simulations have become attractive since they have potential to show in detail the process of bubble collapse. The most widely used numerical approach in the simulation of bubble collapse is the Boundary Integral Method (BIM) [12, 10, 91, 105, 104]. Results obtained using this method have been shown to agree well with those acquired experimentally. The formation of a liquid jet when the collapse takes place near a solid boundary is well captured. However, the assumption that the fluid is incompressible, irrotational and that the gas scalar properties are spatially uniform makes it over-restrictive in its applications. Therefore, it is not suited to model flows which involve pressure discontinuities such as shocks.

The phenomenon of bubble collapse is a multi-phase problem which involves liquid, gas and boundaries which could either be rigid, free surface or elastic-plastic material. Furthermore, the fact that the phenomena of bubble collapse is a highly deforming fluid problem makes the study a very challenging task. It is important that the exact location of the interfaces that separate each phase or material at any time is tracked accurately. Most conventional computational fluid dynamic (CFD) codes however are limited in their ability to capture sharp material interfaces. A number of numerical interface tracking methods have been developed over the past years and these include moving-grid methods, volume-tracking methods, surface-tracking methods and gradient methods. Further discussion that covers the theoretical analysis, numerical simulations and experimental work on bubble dynamics is presented in detail in the next chapter.

The Free-Lagrange method is highly suitable for simulating the collapse of single bubbles. The method provides a distinctive advantage in multi-material flow problems. In this method, the problem is greatly simplified in that the type of fluid in each mesh cell is assigned from the start of the simulation and never changes. There are no mixed cells and hence the material interfaces always coincide with mesh cell boundaries, and are sharply resolved. The Free-Lagrange method also avoids problems of mesh distortion and entanglement because mesh connectivity is allowed to evolve naturally.

A novel Free-Lagrange computational code, *Vucalm*, has been developed by Ball [3] and used to simulate various multi-material flow problems [4, 6]. The code solves the unsteady, inviscid and compressible Euler equations on an unstructured Lagrangian reference frame using Godunov-type solvers.

1.1 Research Objectives

The current research work of the author is part of a larger research programme involving a team of researchers from the University of Southampton and the Medical Physics Department at St Thomas' Hospital, London. The aim of this research is to assist in the design of a sensor which will use the acoustic emissions generated by reflection and reverberation of the incident lithotripter pulse from the stone and tissue, as well as emissions from cavitation activity, in order to diagnose whether the lithotripter focus is still on-target, the degree to which cavitation is occurring, and the degree to which the stone has become fragmented. The interpretation of the emissions will be based on data to be obtained from *in-vitro* and *in-vivo* experiments carried out in the Medical Physics Department at St Thomas' Hospital, London, and from the numerical simulations. The instrument will be developed in view of the following facts,

- The magnitude of the primary pulse[1] reflection will confirm and monitor the accuracy of lithotripter alignment during treatment.
- Any abrupt changes in the spectral content of the primary reflection will warn of stone shattering, so that treatment is not unnecessarily prolonged.
- The cavitation signature will warn of excessive cavitation remote from the stone and associated collateral tissue damage.

The role of the author's PhD research is, in part, to provide the numerical simulation component of this project. Although comparisons of *in vivo* data could have been made with predictions of the far-field pressure made by the Gilmore theoretical model (explained in the next chapter), the assumptions inherent in this model are of doubtful validity in relation to lithotripsy. The model ignores any interactions with solids, obviously crucial for stone fragmentation. Furthermore, it also assumes that the bubbles remain spherical at all times, and the gas homogeneous, with the result that the presence of gas shocks and liquid microjets, which are extremely important for stone fragmentation, are not included. Simulations which account for these features are therefore seen as useful in understanding the dynamics of cavitation bubbles in ESWL. Thus, a Free-Lagrange computational fluid

---

[1] A pulsed pressure wave resulting from the reflection of the incident lithotripter shock wave on the kidney stone and/or from the initial collapse and rebound of cavitation bubbles.

dynamics code (*Vucalm*) is used to model the production of jets in bubbles which are subjected to lithotripter pulses near stones.

A necessary prerequisite is to simulate the interaction of an air bubble with a lithotripter shock wave using *Vucalm*. The computational code was originally developed for simulating fluid problems in the two dimensional planar co-ordinate system. In order to simulate the interaction of single cavitation bubbles with a shock wave it is necessary to extend the code into axisymmetric geometry to model a bubble which is spherical in shape. This preliminary task had been achieved [94], though further work was necessary within this PhD project to improve and further validate the code. The impetus of this study is also to gain a better understanding of the dynamics of cavitation bubbles, the collapse due to interaction with a shock, particularly the phenomena which are responsible for both cavitation erosion and stone fragmentation.

The theoretical study is also carried out to model what far field acoustic emissions might be produced from the various processes we wish to diagnose. In order to compare the acoustic signature obtained experimentally *in-vitro* and *in-vivo* with that obtained numerically, two acoustic codes were developed using the Kirchhoff's and Ffowcs Williams-Hawkings methods. The *Vucalm* code provide predictions of pressure signatures in the near-field which are then projected to the far-field using the acoustic codes. The two numerical acoustic codes are validated and comparisons are given to show the relative merit of each methods.

The objectives of the current research work can then be summarised as follows, i.e. to

- develop and validate the axisymmetric version of the Free-Lagrange code.
- simulate the interaction of a lithotripter shock wave with an air bubble in water in free-field and near a plane rigid boundary for various stand-off distance.
- investigate the dependency of the collapse on the shock strength and bubble initial radius, the formation of the high-speed liquid jet, shock wave emission, and the shape of the bubble during the collapse and rebound.
- develop a code to predict the far-field acoustic signature arising from the cavitation events using the Kirchhoff's (KCHF) and the Ffowcs Williams-Hawkings (FWH) methods.
- extend the acoustic code to problems comprising more than one bubble in order to predict the acoustic signature arising from the interaction of a lithotripter shock wave with a low density bubble cloud.

- provide information to assist in the development of a measuring instrument which can detect the various acoustic emissions arising from the interaction of lithotripsy pulses with the patient's tissues.

1.2 Thesis Outline

This thesis consists of ten chapters. The first chapter gives a general overview of the research work and the outline of the thesis. In Chapter 2, a review of the research in bubble dynamics including those in lithotripsy is presented. Here, an explanation of the dynamics of a collapsing bubble is given. This is followed by a brief description of Extracorporeal Shock Wave Lithotripsy (ESWL). This chapter also includes safety issues of the treatment, experimental and theoretical work carried out over the past years, and its relation to cavitation. Following this, a review of the relevant numerical methods for cavitation bubble simulation as well as a brief review of the KCHF and the FWH methods are given in Chapter 3.

Chapter 4 gives an overview of the *Vucalm* code and the derivation of governing equations of the axisymmetric version of the code. A more detailed derivation is given in Appendix A. A discussion on the Kirchhoff and FWH method algorithm and how the *Vucalm* near-field solution is used in each aeroacoustic codes to obtain the far-field solution is given in Chapter 5.

The following chapter presents the validation of the Free-Lagrange and the two aeroacoustic codes. Validation of the former is made by comparing the results with a published article by Ding and Gracewski [35] and also by Igra and Takayama [52]. The aeroacoustic codes, on the other hand, are validated against analytical results in predicting the far-field pressure signature emitted from an oscillating solid sphere. The case studies for the validation of the axisymmetric Free-Lagrange code involve the simulation of shock/bubble interaction for various bubble initial sizes and shock strengths. The results are compared with theoretical analysis and numerical simulations using another method. A second validation is a numerical simulation of shock wave interaction with a water column in air and comparisons are made numerically as well as experimentally using interferometer images. This allow the code to be validated against experimental work, as well as examining the code's capability to simulate two phase flow problems of air and water, including a strong planar shock wave.

In Chapter 7, a systematic methodology is established for the simulation of the interaction of a single stable cavitation bubble with a lithotripter shock wave. This includes a parametric study of mesh convergence and of the material interface smoothing routine. Based on the results, the numerical simulations of the interaction of single cavitation bubbles in free-field with lithotripter shock waves are carried out. The far-field pressure wave time history of each cases are also presented and discussed. Comparisons between the results obtained using the Kirchhoff method and FHW method are presented.

In Chapter 8, the simulations of single bubble interaction with a lithotripter shock wave for various distances from a plane rigid boundary, including attached bubbles, using the Free-Lagrange method are given. As in previous chapter, the far-field pressure wave time history of each cases are also presented and discussed.

In Chapter 9, simulations of the interaction of a shock wave with an array of bubbles of various separation distances were also conducted and the results are presented in this chapter. The analysis was carried out to determine the degree of influence and interaction of the neighbouring bubbles. This was done by methodically increasing the separation between the two bubbles, and analysing and comparing the bubble wall position time history as well as the predicted far-field pressure signature with that of a single bubble. The data collected were then used in the next study which involve extending the single bubble problem to a low density bubble cloud. Far-field pressure time histories emitted from cavitation activity from varying bubble distributions and density are presented. Finally, a conclusion and suggestions for future works are presented in the final chapter.

Chapter 2

Introduction to Bubble Dynamics

2.1 Introduction

It is believed that the cause of cavitation erosion is due to the high-speed liquid jet impact and shock wave emission as a result of the collapse and rebound of the cavitation bubbles. However, the mechanisms and impetus behind the collapse are not clearly understood. It is therefore the preliminary task of the research conducted here to review the state of current knowledge on the dynamics of bubble collapse. The review is presented in this chapter and it is divided into two parts. The first includes details of the types of bubble collapse and the physical aspects regarding the research development in bubble dynamics - experimental and theoretical works. The second part gives a brief insight into Extracorporeal Shock Wave Lithotripsy (ESWL). A few aspects of the treatment are discussed, such as the various type of lithotripters, its history, the advantages as well as disadvantages of the treatment, and its relation to cavitation bubbles.

2.2 Physical Aspects - Bubble Dynamics

2.2.1 Types of collapse

The interest in cavitation bubble dynamics can partly be attributed to its destructive action not only on solid surfaces in hydraulic machinery, but also its role in fragmentation of kidney stones in clinical lithotripsy. Much work has also been carried out on the role of cavitation collapse on the initiation of explosives [14].

Cavitation occurs when a new surface or bounded volume is created within the body of a liquid. The bounded volume, or cavity, can either be empty or contains gas or vapour [62]. This is a general definition ranging from phenomena such as underwater explosions and effervescence to the boiling of a liquid. The formation of the cavity can be stimulated by a flow, decompression, sudden deposition of electromagnetic or ionising radiation, or heat and acoustic waves. The latter is often referred to acoustic cavitation. In most practical circumstances, the cavity is not formed from the bulk of the liquid, but is seeded from a pre-existing gas pocket or nuclei in the liquid. The interaction with acoustic waves will cause the bubbles to undergo both expansion and contraction phases.

Generally, the collapse of cavitation bubbles can be classified into two categories, *symmetric* and *asymmetric collapse*. Symmetric collapse takes place in an infinite isotropic liquid, far from the presence of a boundary. In this type of collapse, the bubble wall moves in the radial direction, oscillating about its mean radius. Asymmetric collapse, on the other hand, occurs near a boundary, or when the collapse is induced by a shock wave. However, the above descriptions are only the general scenarios.

A detailed description of the mechanism of both types of collapse is given in the following subsection. In real life, the asymmetric collapse is the more common type of cavitation collapse and is also the main objective and study of the current research carried out by the author. This type of cavitation collapse is therefore given greater attention.

2.2.2 Symmetric Collapse

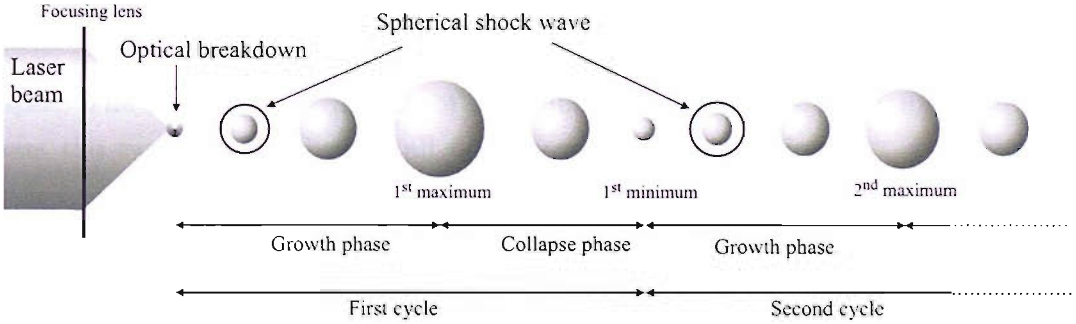

Figure 2.1: Laser-induced vapour bubble in water. Schematic diagram of symmetric collapse.

The sequence of the growth and collapse of a single bubble in an infinite liquid is shown in Fig. 2.1. Good examples of symmetric collapse are the forced oscillation of a cavitation bubble in an ultrasound field, and also spark-generated bubble in infinite fluid. Another example is laser-induced bubble where a cavitation bubble is induced optically using a high-energy laser beam focused into the water. The cycle starts with the inception of the bubble (Fig. 2.1). The initial pressure difference between the bubble and the surrounding fluid will cause it to expand. The expansion leads to the formation of a shock wave that radiates outward. This wave dissipates part of the energy contained in the bubble from inception.

When the bubble expands, the concentration of the gas decreases, and gas diffuses into the bubble from the surrounding fluid. Furthermore, the inertia of the water causes the bubble to over-expand. The bubble surface will reach its maximum size and comes to rest and a steep pressure gradient is developed across the surface of the bubble as shown in the third picture of Fig. 2.1. By this time the growth phase is completed.

As a result of the pressure gradient across the bubble interface, the collapse phase begins and the bubble surface starts to contract spherically. The velocity of the collapsing bubble interface increases gradually. Towards the end of this phase, the contraction of the bubble surface is so rapid that the gas or vapour inside the bubble becomes highly compressed. The compression ultimately arrests the inward motion and causes the cavity to rebound, resulting in the emission of a spherical shock wave into the surrounding fluid where the pressure was measured at $1\,GPa$ [62]. This clearly has damage potential if the collapse occurs in the proximity of a solid surface. But with spherical spreading, this shock wave does not retain its strength very far from the bubble. The amplitude of the radiated pressure wave diminishes with relative radial distance. The emission of the shock wave is the most distinctive phenomenon of symmetric bubble collapse and marks the end of the first cycle.

As depicted in Fig. 2.1 a similar mechanism of bubble expansion and collapse takes place in subsequent cycles. Multiple bubble cycles are common for symmetric bubble collapse. The oscillatory behaviour of the bubble arises because gas bubbles in liquids possess the two elements key to all oscillators, stiffness and inertia. The stiffness is provided by the gas where potential energy is stored in the gas as the volume of the bubble changes. This acts like a spring and causes the bubble to rebound when highly compressed. The inertia is associated with the motion of the surrounding fluid. Further rebound shocks are emitted on each cycle. Following the cyclic behaviour, the bubble may disappear as the content of the bubble diffuses into the water, or it may become a stable bubble when its pressure is in equilibrium with that of the surrounding water.

The cavitation bubble might also experience a steady increase in its equilibrium radius. This is due to a phenomena known as "*rectified diffusion*" in which gas, that is initially dissolved in the water, diffuses into the bubble. As a result of diffusion, its final stable size is larger than the initial undisturbed cavity size. Leighton [62] identified two contributory elements to a full description of the processes, an 'area effect' and a 'shell effect'. The latter is related to the difference in the concentration gradient of dissolved gas in the water enveloping the bubble during the expansion and collapse phases. The former is related to the surface area of the bubble. Since the diffusion rate of gas is proportional to the surface area of the bubble, more gas will enter during the expanded phase than will leave during the compressed phase of the bubble motion. Over a period of time, there will be a net influx of gas to the bubble interior. The growing bubble will eventually reach a stable size at which it is in equilibrium with the surrounding fluid.

2.2.3 Asymmetric Collapse

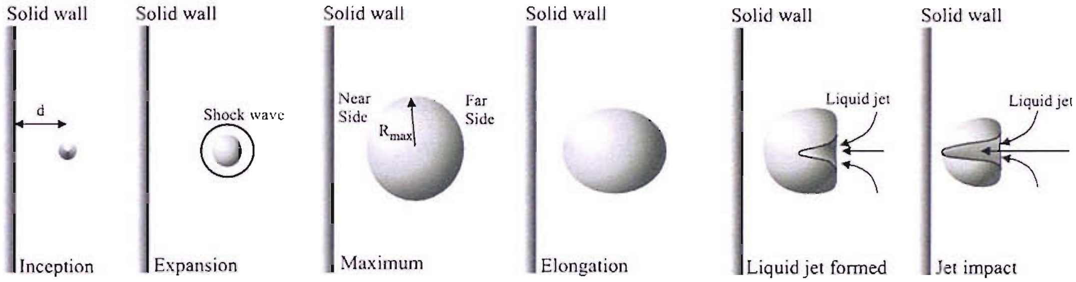

Figure 2.2: Schematic diagram of asymmetric collapse.

The asymmetric collapse of a cavitation bubble can occur not only through an induced pressure gradient across the cavity by a boundary, but also by a transient pressure pulse engendered by a shock wave. The early stages of the bubble dynamics are similar to the symmetric case. The sequence of the events that take place in this type of collapse is illustrated in Fig. 2.2.

A plane solid boundary is placed on the left hand side of the bubble at distance d. The nearest and farthest bubble interface to the wall are define in this report as 'near' and 'far' bubble surface/wall respectively as shown in the third frame of Fig. 2.2. Using this convention, sequences in the collapse process are explained as follows.

In a manner similar to the symmetric collapse, the bubble undergoes an expansion due to its having a higher initial pressure than that of the surrounding water. A spherical shock wave is emitted due to the expansion, attenuating approximately in proportion to $1/r$ through the water. This initial shock wave is reflected back into the surrounding water by the boundary.

A large pressure gradient across the bubble surface is induced as the bubble over-expands. At this moment, the pressure within the bubble is much lower than the hydrostatic pressure of the water. The bubble would have reached its maximum size, R_{max}, and the shape that it acquires depends on the initial distance, d, of the inception point from the boundary. If the inception takes place close to the wall, the shape of the expanding bubble will deviate from being spherical. On the other hand, for large distance d, the bubble is likely to retain its spherical shape as the effect of flow retardation is minimal.

When the bubble collapses, the fluid flow near the wall is retarded by the presence of the boundary and consequently causes different contraction rates at different locations on the bubble surface. The collapse of the bubble surface on the near side is prevented by the boundary and the water appears to stagnate. On the other hand, on the far side, the bubble surface has the contraction rate similar to that of the symmetric collapse because the fluid flow is not affected by the boundary. Consequently, there exists a pressure gradient across the bubble where the pressure of the liquid between the near bubble surface and the solid boundary is lower than that of the far bubble wall.

The steep pressure gradient build up also causes the bubble to elongate as its centre moves towards the solid surface. Towards the end of the collapse, the right bubble surface involutes and a high-velocity liquid jet is formed which penetrates the bubble as shown in Fig. 2.2. The liquid jet accelerates towards the solid boundary and eventually impacts on the near bubble wall. Owing to its high momentum, the impact generates an intense blast wave in the surrounding fluid. Following liquid jet impact, the bubble acquires a toroidal shape. Subsequently, the flow around the bubble turns into a ring vortex which draws the bubble closer to the boundary. The velocity of the liquid jet decreases as it is slowed down by the water layer between the solid boundary and the bubble. Besides the formation of liquid jets, shock waves are also emitted each time the bubble achieves minimum volume. In most cases, the asymmetric collapse of a bubble is violent and often leads to bubble fragmentation. This has been observed experimentally and will be reviewed later in this chapter.

The high-speed liquid jet formation, as well as the emission of the shock wave, are dependent on a dimensionless parameter known as the *stand-off parameter*, or *stand-off distance* in some texts, ζ, which is defined as the ratio of initial distance of bubble centre from the boundary, d, to the maximum bubble radius, R_{max}, i.e. $\zeta = d/R_{max}$. It has been found that the behaviour of cavitation bubbles, during expansion and collapse, is strongly dependent on the stand-off parameter and that the influence of a boundary on a cavitation bubble decreases as the stand-off parameter gets larger [61].

Investigations of asymmetry in collapsing bubbles have concentrated upon the presence of adjacent boundaries, but a second important mechanism is the acceleration of the upstream wall by a shock pulse. The name convention to describe the collapse process is depicted in Fig. 2.3. The major effect of the shock is to accelerate the upstream bubble wall so that it travels towards the downstream one. When the shock wave reaches the bubble, a relatively weak shock is transmitted into the air cavity, and a strong expansion wave is produced in the water. The resulting momentum transfer accelerates the bubble wall and starts the collapse from this side. As the shock moves on, the whole bubble is enclosed by a higher pressure and collapses from all sides, yet asymmetrically due to the

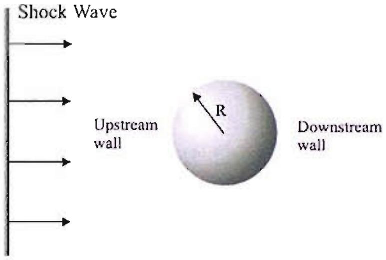

Figure 2.3: Name convention and schematic diagram of asymmetric collapse by a shock wave.

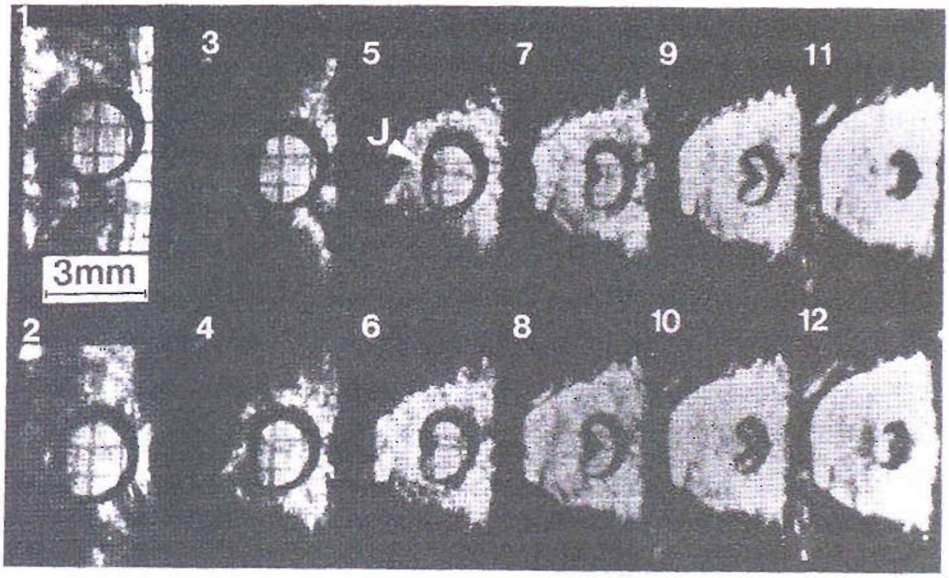

Figure 2.4: Schlieren images of a two dimensional cavity of diameter $3\,mm$, collapsed by a shock wave travelling from left to right. The upstream surface involutes to produce a jet J. Taken from reference [30].

unequal momentum transfer at different parts of the bubble wall. This leads to the formation of a liquid jet in the direction perpendicular to the shock front as shown in Fig. 2.4 which shows the collapse of a two-dimensional cavity. The details of the collapse (e.g. the jet velocity) are dependent on the shock wave amplitude and its temporal profile (Phillip *et al.* [72]). The liquid jet will impact the downstream wall, generating a blast wave into the surrounding water. After jet impact, two lobes of compressed gas are trapped in the closure and, as the jet penetrates the downstream wall, a pair of linear vortices subsequently form and travel downstream in the flow. The bubble would reach its minimum volume, and thus completes its primary collapse. On most occasions (involving strong shocks), the jet velocities produced by shock interactions are much higher than those caused by the asymmetric collapse near a boundary. Such jet impacts are likely to be a major source of damage on surfaces that are in the proximity of the collapsing bubbles. Furthermore, these events are so violent that they often lead to bubble fragmentation.

2.3 Studies of Bubble Collapse

2.3.1 Experimental Studies

Kornfeld & Suvarov [59] were the first to suggest the formation of liquid jets as early as 1944. Since then much work has been carried out which proved the existence of a jet in a cavity collapsing asymmetrically. The observation of a liquid jet in collapsing bubbles contrasts with most earlier analyses of the problem, which described the collapse as spherical. It was not until 1961 that the existence of a liquid jet in cavities was proven by Naudè & Ellis [69] using a high speed photography technique. The bubbles were generated in water by electric sparks between electrodes placed at various distances from a solid wall. This was followed by the experimental work of Benjamin & Ellis [7] who examined this phenomenon further. Their work provided an impetus for theoretical discussion of asymmetric collapse. Over the past few years, other experimental investigations have been carried out to prove the existence of a liquid jet as a result of the interaction of the bubble with an incident shock wave [14, 15, 30, 31]. The bubbles collapse by involution of the upstream wall to form a jet which crossed the bubble and impact on the downstream wall. These two mechanisms have been discussed in subsection 2.2.3. Other researchers have also provided photographic evidence of jet formation during asymmetric bubble collapse [55, 61, 72, 78].

In the earlier experiments, bubbles were produced in the laboratory by using the spark discharge method in water [69, 82, 55, 19, 80]. The problem with this method is controlling the initial size of the bubble, and the unavoidable mechanical disturbance produced by the electrodes. Nevertheless, using high-speed photography, the migration of cavitation bubbles toward a nearby solid boundary was clearly captured, as well as the formation of a high-speed liquid jet, and the damage cause by the impact of the jet on soft aluminium and indium specimens.

It was not until the 1970's that a more accurate method was developed by Lauterborn [61]. He showed that intense laser is an effective tool for investigating cavitation bubble dynamics. This breakthrough opened a new avenue for the studies of optic cavitation. Since then, the laser light focusing technique has been employed in various works [61, 87, 81, 18, 88, 78, 90, 97, 72]. The method has the advantage that the size of the bubble can be controlled and can be produced at any desired location within the fluid and at any time. In addition, the cavitation bubble can be introduced without causing any disturbance in the liquid, and the dimension, location as well as quantity of the bubbles can be conveniently controlled. Observations of the bubble behaviour are then made using high-speed photography, where the dynamics of the bubble are studied frame by frame. Using this technique, Lauterborn & Bolle [61] showed good agreement between experimental work and theory obtained by Plesset & Chapman [73] who numerically investigated the collapse of a bubble in the neighbourhood of a solid boundary. The behaviour of the bubble clearly shows the involution of the bubble wall and jet formation towards the boundary. They also measured a maximum jet velocity of $120\,ms^{-1}$ for a framing rate of 250000 frames/s and $\zeta = 3.08$. However, they implied that the jet velocity is much higher than the calculated value as the accuracy of the measured tip velocities is dependent on the framing rate used. The experimental study by Vogel and co-worker [97] was on much the same line. By using high-speed photography with up to 1 million frames per second, they observed the formation of a torus, caused by the jet flow through the bubble centre and radially along the solid boundary.

Experimental works on shock wave-induced collapse were reported by Dear *et al.* [31] who studied the properties and behaviour of 2D gas-filled cavities 'air discs' when collapsed by shock waves. The cavities were formed in a gelatine layer which was placed between two thick glass blocks. A striker was projected to impact on the gel block and high speed photography was used to record the behaviour of the cavities and jet formation under such impact. The major advantage of using this method is that the cavity size, shape, number and relative position can be controlled. Dear employed the method to look at a few simple cavity collapse configurations. In the study, a $3\,mm$ diameter cavity is collapsed by a shock wave of strength $0.26\,GPa$ that results in the formation of a microjet with an average velocity of $400\,ms^{-1}$ (Fig. 2.4). An intense blast wave is generated as this high-speed liquid jet impacts on the downstream wall. The advantage of studying bubble collapse two-dimensionally is that details of the process occurring within the cavity can be followed without the refraction problems associated with viewing through a curved wall.

A similar method of generating 2D disc cavities was also used by Bourne and Field [14, 15, 16]. Experiments on the interaction of an array of cavities with a shock wave were carried out which involved large shock strengths producing violent bubble collapse, with, in some circumstances, sonoluminescence[1]. Shock strengths in the range of 0.26 - $3.5\,GPa$

---

[1] Light emission associated with a particular form of collapse, occurring as a result of high temperatures generated within the collapsing bubble. The mechanism of this phenomena is still debatable although the few mechanisms proposed so far can be categorised into three - thermal, mechanochemical and electrical [62].

were used, generated using an impacting flyer-plate or from an explosive lens. They observed a jet in the direction of wave propagation after the shock wave-bubble interaction. It was found that if the incident shock was strong enough, the jet velocity can exceed the shock velocity in the surrounding fluid. The collapse of a $3\,mm$ cavity under a shock strength of $0.26\,GPa$ resulted in a jet velocity of $300\,ms^{-1}$ and under a shock strength of $1.9\,GPa$, the jet velocity reached a value of up to $5000\,ms^{-1}$ for a $6\,mm$ bubble. The impact of the jet isolates two lobes of highly compressed air, where considerable heating occurs. If one assumes that sonoluminescence is localised to regions of high temperatures, then from their results it can also be inferred that the highest temperature are created inside the cavity at the final moments of collapse and are associated with the impact of the jet and the later compression of an isolated pair of gas pockets.

Other workers include Tomita *et al.* [89] who examined in detail the interaction of a spark-induced shock wave with an air bubble and the induced collapse and jet formation. They found that the shock driven-collapse of an air bubble can induce a more intensive impact wall pressure than one generated by the same shock wave impinging directly onto the wall. The velocity of the jet, and consequently the impulsive pressure on the wall, are dependent on the size of the bubble, the incident shock wave strength and the stand-off distance. This observation, backed by other similar works, has led many to believe cavitation is the mechanism for stone comminution in clinical lithotripsy. A comprehensive description of the medical treatment as well as the role of cavitation are given later in this chapter.

A number of studies have been carried out to investigate the mechanism of cavitation damage. The analysis by Kling & Hammitt [55], indicated the formation of a liquid jet during collapse which, under certain conditions, impinged upon a solid boundary with sufficient force and velocity to cause damage. They found damage produced by the collapsing bubbles on aluminium alloys which appeared similar to damage produced by both the impact of a liquid jet and the impingement of a shock wave produced by the initiation of the spark-induced bubbles. The craters produced by shock wave and the jet could be differentiated because the bubble growth and collapse occurred at different locations. However, Shutler & Mesler [82], who performed an experiment on spark-induced bubbles, concluded that the cavitation damage is caused by a shock wave resulting from the collapse of the toroidal bubble, and not the jet. They indicated that the pressure pulse emitted when the bubble rebound caused the pit damage and circular patterns on the solid specimen. Possible discrepancies could be due to the experimental set up. The electrodes to initiate the spark-induced bubbles in their work could have inhibited the development of the jet as they were positioned in close proximity to the solid wall and that a lower voltage settings were used to generated the bubbles.

Tomita & Shima [87] too found a circular pattern, but gave a different explanation of the generating mechanism. They observed the collapse of bubbles with initial radii of $3.5\,mm$ and $5.1\,mm$ near an indium specimen, and by a $5\,MPa$ shock wave. Their observations using high-speed photography showed that the liquid jet penetrates the bubble, and subsequently impacts the boundary. This causes the flow around the bubble to turn into a ring vortex. A collision will occur between the radially flowing jet and the collapsing main bubble wall, resulting in the creation of micro-bubbles. Based on their analysis of the circular indentation found on the indium caused by spark-induced bubble collapse, they suggested that the damage pattern is caused not only by the collapse of the original bubble, but also the collapse of these tiny bubbles as they were exposed to high pressure from the jet impact and rebound of the original bubble. In addition, they also observed damage pits caused by the interaction of an air bubble attached to the indium specimen with a shock wave. In this case, the pit formation resulted from the impact of a liquid jet directly on the indium specimen.

The mean bubble motion (as well as the precise direction taken by the jet and its velocity history) depends on the impedance of the nearby solid wall material and its distance from the boundary [36, 72]. There have been studies of the interaction of a collapsing bubble with various surface materials [36, 91, 81, 87]. According to Shima *et al.* [81], the migration of the bubble is influenced not only by the properties of the boundary (stiffness and inertia) but also the stand-off distance, ζ. They also suggested that for a given stand-off distance, there exists a neutral bubble collapse, where the bubble centroid remains at its initial position with no migration. Studies have been carried out on the behaviour of a bubble near a boundary that behaves elastically, in order to discover a method of preventing cavitation damage to surfaces [81, 88]. An interesting observation was made by Brujan and associates [18]. They found that for some range of coating properties, no liquid jet is developed during bubble collapse, neither towards nor away from the boundary. In this case, the bubble collapses from its sides forming an hour-glass shape which eventually leads to bubble splitting.

In practical cases, where cavitation or two-phase flow occurs, cavitation bubbles seldom exist as a single bubble, and as a result they interact with each other. This is especially so in cases where clouds of bubbles exist [85, 57, 88]. The degree of influence of a bubble on its neighbours is dependent on their separation distance [57]. When several bubbles move near each other, very clear interactions are observed, which induce asymmetry and deformations on the bubble wall as well as attraction and repulsion effects [85]. It was found that the attraction is mutual and identical when the bubbles are of equivalent size. For bubble of different sizes, it is the smallest which undergo the greatest influences [88, 85]. However, in the case of very close bubbles, flattening of the

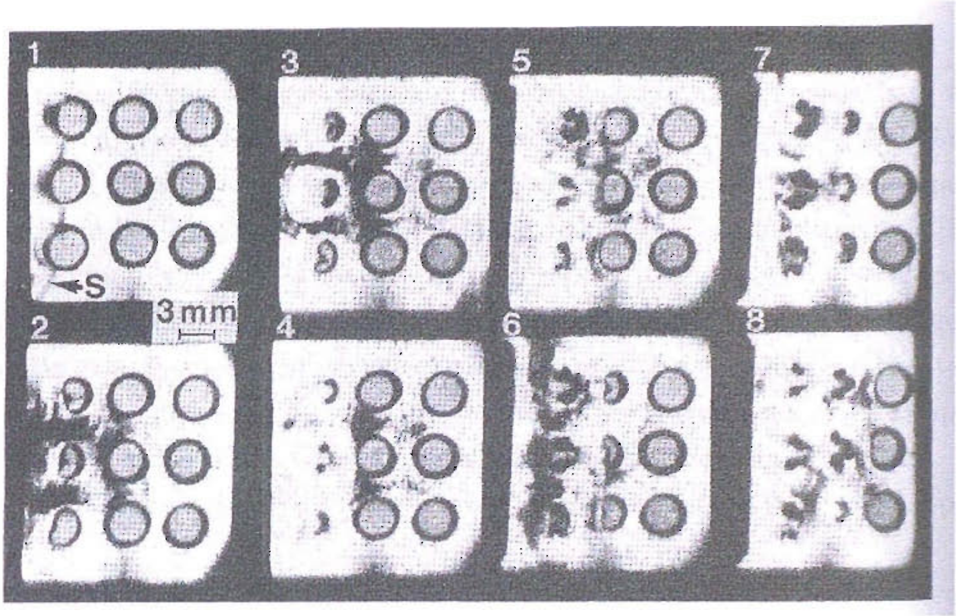

Figure 2.5: Schilieren images of a rectangular array of nine cavities of diameter $3\,mm$, collapsed by a shock wave S. Note the layer-by-layer collapse. Taken from reference [30].

bubble wall occurs which could also lead to their coalescence. However, coalescence only occurs after simultaneous implosion of the bubbles if their sizes are similar, or else after the collapse of the smallest bubble. The role of the shock waves emitted during collapse also becomes significant if the collapse and rebound of the bubbles are relatively violent. The shock waves produced by the collapse of a bubble can travel to adjacent bubbles and enhance their collapse, intensifying the bubble collapse damage capability.

Experimental studies mentioned above confirmed that the impulsive pressure generated by a multiple interaction can be much higher than that caused by a single bubble. Dear and Field [30] studied the collapse of arrays of cavities using high-speed photography, where the initial collapse is induced by an incident shock wave. The interaction of the incident shock with the cavity leads to the formation of a liquid jet, which penetrates the bubble and impacts on the downstream wall. The impact generates an intense blast wave, which is strong enough to induce the collapse of neighbouring cavities. It was shown that a chain reaction of cavity collapse can occur given the right conditions of shock strength, cavity diameter and cavity spacing. A schlieren image of this chain-reaction is shown in Fig. 2.5. However, most investigations have looked, in early work at least, at an isolated single cavity.

2.4 Theoretical and Numerical Studies

Owing to the limitations in experimental investigations, many researchers have focused their work on numerical simulations to study the dynamics of cavitation bubbles. The collapse of a bubble occurs in a very short length of time (the order of microseconds) and even with the utilisation of a high-speed camera with up to 1 million frames/s [72], the temporal resolution is low and gives only sketchy results. Consequently, the shape of the bubble and the resultant liquid microjet cannot be determined accurately. Large errors also appear in experimental works in calculating the speed of the jet that is estimated from photographs of the collapsing bubble. In addition, experimental results are incapable of showing the interaction of the surrounding liquid with the cavity at any instant. Hence, numerical simulations offer great possibilities in revealing some important aspects of bubble collapse.

The first work on cavitation bubbles resulted from observations of the rapid erosion of steam-ship propellers in the late nineteenth century [8]. A breakthrough in the theoretical analysis of bubble collapse and its relevance in engineering applications was achieved through the work of Lord Rayleigh [75]. He was the first to explain that erosion of ship propellers was due to hydraulic cavitation that occurs as a result of rapid pressure decrease caused by the high-speed movement of the propeller relative to the body of the fluid. His analysis of bubble conditions during the collapse phase laid the foundation of analytical work carried out until the present date. By considering the symmetric collapse of a spherical cavity, he succeeded in proving that the violent collapse of these bubbles could generate very high pressures. Rayleigh obtained the following result

$$\ddot{R}R + \frac{3}{2}\dot{R}^2 = \frac{1}{\rho_\infty}[P_L - p_\infty] \tag{2.1}$$

where R is the bubble radius, ρ_∞ is the liquid density at infinity, P_L is the pressure in the liquid at the bubble surface and p_∞ is the pressure at infinity. The dots denote a time rate of change. The calculation made by Rayleigh assumed incompressible fluid and that there is an absolute vacuum within the bubble. It gives the collapse time to reasonable accuracy, but predicts a collapse velocity of the bubble wall which tends to infinity as the cavity radius approaches zero. This contradicts the observed fact that the bubble rebounds when a minimum volume is reached. He recognised that a more realistic physical model is provided by allowing the cavity to contain a small quantity of insoluble gas. The compression of the gas would ultimately arrests the inward motion and cause the cavity to rebound. Furthermore, the model is limited to spherical collapse in an infinite liquid, and therefore it cannot describe the behaviour of bubbles that collapse in the vicinity of boundaries.

In reality liquids are both compressible and viscous; within the cavities there is a certain amount of vapour and gas and the change of pressure which causes the collapse of cavities takes place at some finite speed. These deviations from assumptions of the theory can only decrease the rate of collapse of cavities and, consequently, decrease the pressure. Thus Rayleigh theory only shows the possibility of great pressures arising but it fails to give their true values. In addition, any bubble producing a damaging effect in practice must, throughout its collapse, be so close to the solid boundary that very large departures from spherical symmetry are inevitable. This class of situation presents a problem significantly different and much more difficult than the Rayleigh problem.

Improved representations of the effects of gas and vapour contents and various other physical factors such as real-fluid effects of temperature, liquid compressibility, viscosity and surface tension have been included in the theory since Rayleigh's time. Plesset and Prosperetti [74] take into account the gas within the bubble, but neglect the liquid compressibility. A widely used solution, taking into account compressibility, was produced by Gilmore in 1952 [42]. Both these formulations also take into account the gas pressure, surface tension and the liquid viscosity, and are therefore more realistic than the Rayleigh formulation. The inclusion for the effect of liquid compressibility in the Gilmore model enable shock waves to form when the bubble rebounds. Nevertheless, the models were derived under assumptions such as perfect gas inside the bubble and uniform pressure field in the bubble interior.

The Gilmore equation has been extended by Akulichev to obtain the pressure field around the bubble and used to predict the far-field acoustic emission resulting from cavitation. The Gilmore-Akulichev formulation for bubbble dynamics is given by the following equations,

$$R\left(1-\frac{U}{C}\right)\frac{dU}{dt}+\frac{3}{2}\left(1-\frac{U}{3C}\right)U^2=\left(1+\frac{U}{C}\right)+\frac{U}{C}\left(1-\frac{U}{C}\right)R\frac{dH}{dR} \tag{2.2}$$

where,

$$P=B\left[(\rho/\rho_0)^m-1\right] \tag{2.3}$$

$$H=\int_{P_\infty}^{p(R)}\frac{dP}{\rho} \tag{2.4}$$

$$C=[C_l^2+(m-1)H]^{1/2} \tag{2.5}$$

$$P(R)=P_g-2\sigma/R-(4\mu/R)U \tag{2.6}$$

$$U=dR/dt \tag{2.7}$$

C is the speed of sound at the bubble wall, P and ρ are the time-varying pressure and density of the liquid respectively, H is the enthalpy of the liquid, C_l is the infinitesimal speed of sound in the liquid, $P(R)$ is the pressure at the bubble wall, P_∞ is the pressure at infinity, P_g is the pressure of the gas within the bubble, P_0 is the ambient pressure of the surrounding liquid, σ is the surface tension and μ is the coefficient of shear viscosity. Eqn. 2.3 is known as the Tait Equation, and typically for water $m = 7$ and $B = 3.31 \times 10^8\,Pa$. The inclusion of compressibility effects makes the Gilmore formulation more appropriate than earlier models for the study of high amplitude bubble behaviour, such as rectified diffusion and lithotripter shock wave pulses [22].

However, it should be noted here that the Gilmore model assumes that the bubble remains spherical at all time, the gas is homogeneous, and the presence of shock waves and liquid microjets, (which may be extremely important for stone fragmentation), are not included. Furthermore, the model also ignores any interactions with solids, which is obviously crucial for stone fragmentation. In addition, fragmentation of the bubble is also likely to occur as it approaches a minimum volume, seeding the liquid with more nuclei for subsequent driving pulses. Nevertheless, the Gilmore-Akulichev model is still employed in many acoustic cavitation analysis, because it readily predicts the far field acoustic emission resulting from cavitation that can be exploited for remote characterisation of cavitation.

Theoretical studies of bubble dynamics have mainly concentrated on spherical collapse, and therefore have limitations in the study of cavitation erosion. Such studies have evolved to include asymmetrical collapse, including those induced by nearby boundaries and shock waves. The experimental work by Benjamin and Ellis [7] was confirmed theoretically by Plesset and Chapman [73] who used a finite-difference solution of the equations of motion.

In more recent years, the Boundary Integral Method (BIM) has become a popular and useful technique to model nonspherical cavitation bubbles in liquids [10, 13, 104, 105, 91, 12]. Sato and coworkers [77] numerically investigated the behaviour of a gas bubble near a rigid boundary in an oscillatory pressure field. The BIM is employed to simulate the variation of the bubble profile with time, and image theory is applied for solving the differential equations describing the nonlinear oscillations and migrations of the spherical gas bubble. Their results showed the jet formation during collapse and also in the rebound stage, as well as the migratory behaviour of the bubble towards and away from the boundary, depending on the frequency of the oscillating pressure field in the surrounding water.

In 1986, Blake *et al.* [13] modelled, via BIM, the growth and collapse of transient cavities near a rigid boundary in the presence of buoyancy forces and an incident stagnationpoint flow. Their results showed the formation of the high-speed liquid jet when the bubble is collapsing. In another work, Zhang and associates [105] developed a three-dimensional BIM to simulate the collapse of single and multi-bubbles near a free surface. They developed a numerical code which uses a method called 'a nine-noded Lagrangian interpolation' to determine the surface characteristics and material velocity. They showed that their results agree relatively well with that from the one-dimensional Rayleigh-Plesset equation and an axisymmetric model. The temperature fields inside asymmetric bubbles in the final stage of collapse have also been numerically simulated using a combined BIM and finite volume method on unstructured adaptive grids [102]. The heat transfer of the internal gas is taken into account and the asymmetric collapse of the bubble is induced by the presence of a solid wall.

Numerical simulations using the BIM have been shown to agree well with experimental results. However, in the formulation of the BIM, the fluid dynamics is modelled by assuming the fluid to be incompressible, inviscid and irrotational and that the gas scalar properties are spatially uniform [104, 105, 10, 13]. Since surface tension forces are less important at the final stages of collapse, their effect is also neglected. Nevertheless, the effect may be important during bubble growth just after inception and also at the jet tip in the later stages of collapse [13]. Although it can be argued that compressibility effects are generally unimportant during primary expansion and collapse as the velocities are typically significantly less than the speed of sound in either the gas or the liquid, these assumptions restrict the computation to the first collapse only.

In earlier BIM, the computation had to be stopped before the rebound phase of the bubble and at the point of jet impact due to an inherent mathematical degeneracy of the conventional boundary integral equation (CBIE). The method fails when the liquid jet approaches the opposite surface of the bubble in the final stage of collapse. This is due to the use of a governing equation that only represents a singly connected surface [106]. The BIM method using the CBIE is therefore incapable of simulating the bubble dynamics beyond the first collapse [104, 11] and is also over restrictive for general application due to the assumptions made. Zhang *et al.* [104] succeeded in simulating the final stages of the collapse of a cavitation bubble near a rigid boundary including the jet impact and penetration processes, which is an advancement from earlier BIM. In their work based on the algorithm formulated by Best [9], the CBIE is modified to account for the common surface or point upon jet impact and the equation is replaced by a hypersingular boundary integral equation (HBIE) which forms a closed equation system where the old one failed. The technique introduces a 'cut surface', which allows the jet to penetrate the bubble and subsequently form a toroidal cavity. However, the incompressibility assumption made means the method is incapable of modelling blast wave emission from the jet impact and shock wave emission into the surrounding fluid when the bubble rebounds. Hence, although the BIM can resolve the formation of the high speed liquid jet and the subsequent rebound of the toroidal bubble, the method is still limited for general applications of bubble collapse due to its assumptions, especially incompressibility.

It was shown by Howle *et al.* [50] that liquid compressibility effects play an important role in the collapse of cavitation bubbles. Using the compressible Euler equations, they analysed the response of a $3\,\mu m$ bubble to a lithotripter pressure pulse where the peak compressive pressure is $100\,MPa$. They found that the collapse velocities are vastly greater than the speed of sound in liquids. In his studies on the effects of compressibility, comparison was made between the compressible Gilmore model and the incompressible Rayleigh-Plesset equation. The response of the bubble to the pressure pulse was plotted and they discovered that the compressible and incompressible theories agree well before collapse but differ greatly during and after collapse. In the compressible case, the minimum volume achieved upon collapse is larger than in the compressible case. Another apparent difference is that the oscillations following collapse are heavily damped in the former, whereas the oscillations continue indefinitely in the latter. This finding emphasizes the importance of compressibility effects in numerical simulations of cavitation events. Another method known as the *Volume of Fluid Method* (VOF) was recently employed in modelling multiple three-dimensional gas bubbles rising in a quiescent liquid [41]. The method assumes incompressible and immiscible fluids but takes into account the effects of surface tension. The motion and pulsation of a single bubble under the action of a buoyancy forces was clearly captured and they also extended the computation to five gas bubbles.

Ball *et al.* [6] used the Free-Lagrange numerical method in their simulation of a two-dimensional cylindrical air cavity in water collapsed by a $1.9\,GPa$ incident shock. The computational code '*Vucalm*', solves the two-dimensional unsteady compressible Euler equations using a second order extension of the Godunov method. The method is suited for the bubble collapse problem as it allows the air-water interface to be resolved at all times. The results show the involution of the bubble surface to form a high-speed liquid jet, with velocity of about $2600 m\,s^{-1}$, which penetrates the bubble. The impact of its tip onto the opposite side of the bubble surface produces an intense blast wave with an initial peak overpressure of more than $4.7GPa$. Although the results over-predict the temperature of the air inside the bubble due the absence of heat transfer and real gas effects, it demonstrates that severe heating of the gas does occur during the collapse. The results that were obtained also agree well with the experiments of Bourne and Field [15].

It is clear that acoustic cavitation is an enormously broad area of study of relevance in a wide variety of practical processes. The author will concentrate his study on cavitation collapse in the application of Extracorporeal Shock Wave Lithotripsy. The relation of cavitation bubbles with ESWL, and the dynamics of a bubble from the interaction with a lithotripter shock wave, are explained in the next section.

2.5 Extracorporeal Shock Wave Lithotripsy (ESWL)

Lithotripsy is a modern alternative to surgery for the treatment of kidney stones and for relief from kidney stone pain. It is a non-invasive technology which disintegrates stones into small particles. This is achieved by using intense shock waves generated outside (extracorporeal) the body so that the pulverised stone can be passed out naturally via the ureter. The device which performs the lithotripsy is called a lithotripter.

2.5.1 Types of Lithotripters

Shock waves are generated by different types of generators. Commercially available generators are

1. Electrohydraulic (EH) - Shock wave is generated using a spark gap and then focused onto the stone via an ellipsoidal reflector.
2. Electromagnetic (EM) - Planar shock wave is generated electromagnetically. The plane waves is focused by a convex acoustical lens.
3. Piezoelectric (PE) - A spherical dish made up of piezoelectric elements is used to generate shock wave pulses.

Schematics of the electrohydraulic and electromagnetic types of shock generator used in lithotripters appear in Fig. 2.6 and Fig. 2.7 respectively. In Fig. 2.6, the view is towards the top of the patient's head as the patient lays face up on a table.

The electrohydraulic-shock generated lithotripter (Fig. 2.6) uses a half-ellipsoidal reflecting chamber to focus shock waves, which are created when a powerful spark vaporises water at one focus of the ellipsoid. Part of each wave never hits the reflector, and this part (light blue) spreads out and weakens. However, the part of the wave which hits the reflector (dark blue) converges on the other focus and becomes very intense, causing the stone to crumble. The electrohydraulic will generate more than one shock from a single discharge, resulting from oscillation of the bubble generated at the first focus.

In comparison, the EM shock generator works on a similar principal to a loud speaker. The shock wave is produced electromagnetically by means of a high voltage pulsed through

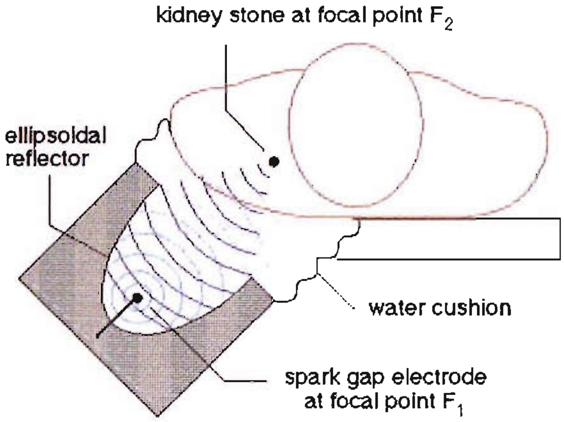

Figure 2.6: Electrohydraulic Lithotriptor (EH).

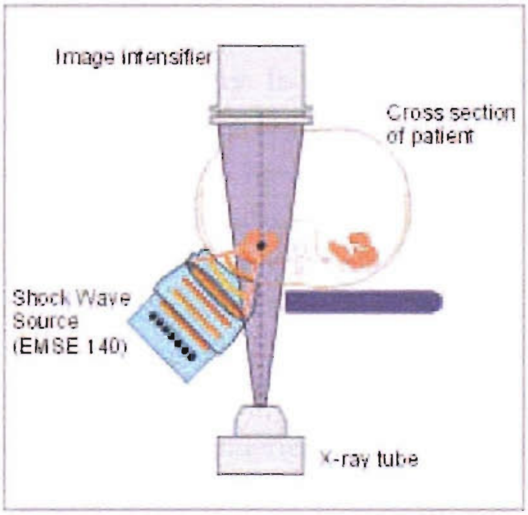

Figure 2.7: Electromagnetic Lithotriptor (EH).

a coil in the base of the shock-head. This produces a magnetic field which repels an adjacent metal membrane, thus initiating a high-pressure wave. This high pressure wave is transformed into a shock wave as it travels through de-gassed water. This plane wave is focused by a convex acoustical lens, creating a high-intensity focal zone for the effective destruction of renal stones.

Although different techniques have been used for shock wave generation and focusing, the pressure waveforms produced by most existing clinical lithotripters are similar [25]. However, Chuong *et al.* [21] found that the size and shape of the focus of the shock waves are different for all three lithotripters, resulting in varying extent of damage on a standard stone phantoms[2].

2.5.2 Advantages of Lithotripsy

ESWL has become the treatment of choice for the majority of renal calculi because of its advantages over surgery. The main advantage of lithotripsy is that it is non-invasive. In contrast, other methods of stone removal require open surgery, extraction of the stone through a puncture in the side of the patient, or the insertion of an ureteroscope via the urethra with subsequent stone fragmentation and removal by mechanical means. All these invasive procedures carry a higher risk of infection complications than non-invasive procedures such as lithotripsy. With lithotripsy, patients generally experience extreme reduction in complication and pain. The total trauma is also less than that of surgery. Furthermore, post-treatment complications are minimised and so too is the recuperation time. The lithotripsy procedure itself takes about an hour, with a recovery period of only a few days compared to weeks with surgery. In the event of disease recurrence. additional therapy can safely be administered absent of the risks encountered with repeat surgical procedures. The treatment to a patient, however, can not be repeated within a short period of time to avoid any long term injuries.

However, not all patients with kidney stones problem can be treated with lithotripsy. Surgery is reserved as an option for cases where other approaches have failed or should not be tried. The most common reasons for electing an open operation are unsuccessful endoscopic stone manipulation, presence of anatomical obstruction in the intrarenal collecting system of the ureter, obesity, underlying medical problems and large stones [2].

2.6 Acoustic Cavitation

2.6.1 ESWL-induced Cavitation Bubbles

The tensile strength of a liquid is the tension that exists in the liquid which prevent it from rupturing to form cavitation. One method to measure the tensile strength of water is through dynamic stressing by an acoustic field. At sufficiently high negative pressure amplitude, the liquid fails and cavitation will occur. The thresholds for bubble inception can be much less negative. when there are pre-existing nuclei or solid impurities in the fluid. The latter serve as nucleation sites and contain cracks and crevices in which gas pockets may stabilise against dissolution [1, 62].

The acoustic wave at the lithotripter focus in water has a form which is expected to

---

[2] A stone that is fabricated to mimic the mechanical strength and acoustic impedance of renal calculi.

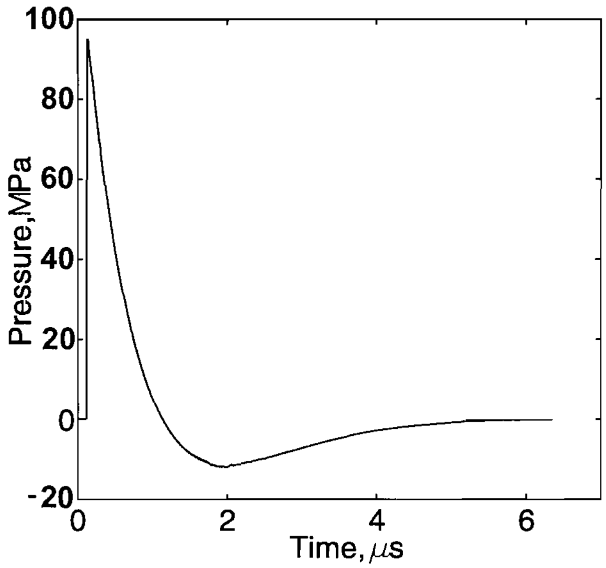

Figure 2.8: Modelled form of ESWL pressure waveform.

produce significant amounts of cavitation [26, 22, 71, 65, 86]. It consists of a leading shock front (compressive wave) with peak positive pressure up to $100\,MPa$, followed by a diffraction-induced tensile wave with a peak negative pressure down to $-10\,MPa$, and a total pulse duration of $3-7\,\mu s$ [25]. An idealised profile of the lithotripter pulse is shown in Fig 2.8. Studies of ESWL have showed that cavitation bubbles are induced *in vivo* near the lithotripter focus by the tensile stress of lithotripter shock wave pulses [22, 26]. Similar cavitation phenomena were observed by Tomita *et al.* [86] from their *in vitro* experiments. Coleman *et al.* [26] showed that cavitation bubbles could be formed after administration of a single shock.

A number of researchers have concentrated their work on providing evidence of lithotripter induced cavitation bubbles. Kuwahara *et al.* [60] showed that the presence of microbubbles correlates with evidence of injury to dog kidneys during experimental lithotripsy. Cavitation bubbles has also been found in liver parenchyma of patients undergoing gallstone lithotripsy by Zeman and associates [103]. They observed cavitation activity near the focal point of the lithotripter at every $0.83\,s$ interval, the same time interval at which shock waves were administered. Out of a total of 50 lithotripsy treatments, they found that microbubble formation within the gallbladder was identified in 31 of the 34 successful treatments. They were unable to detect any bubbles in 11 out of the 16 unsuccessful treatments. Although the presence of bubbles does not predict that stones will break, successful disintegration is far less likely in cases where intense microbubbles do not form at relatively low lithotripter power. Based on this, they suggested that the presence or absence of microbubbles in bile during lithotripsy may be used as an important marker that can be predictive of fragmentation.

2.6.2 Dynamics of Cavitation Bubbles and Acoustic Emission

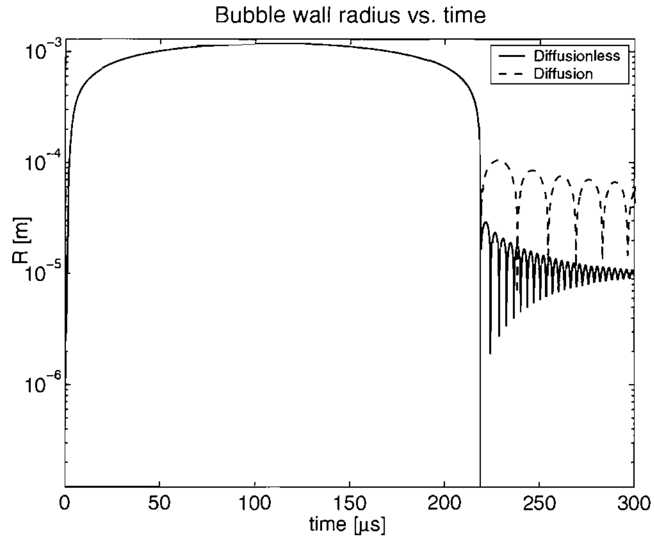

Figure 2.9: Calculated response of a bubble to a typical lithotripter shock wave. The figure shows the effect of rectified diffusion on the final bubble size.

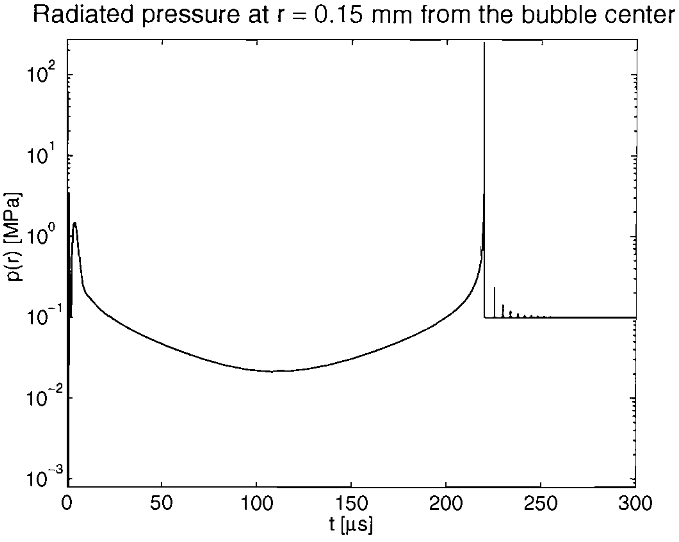

Figure 2.10: Corresponding acoustic emissions resulting from the bubble response in Fig. 2.9, recorded at 1.5 *mm* from the bubble centre.

Church [22] employed the Gilmore-Akulichev model (Section 2.4) to examine the interaction between cavitation nuclei of about $1 - 10\,mm$ in radius and a lithotripter shock wave. He showed that the nuclei will be initially compressed by the leading shock front, and then expanded by the ensuing tensile wave into a bubble of $1 - 3\,mm$ in diameter in a few hundred microseconds. The variation of the bubble wall radius with time, for the interaction of a bubble ($R_0 = 10\,\mu m$) with a lithotripter shock wave, $P^+ = 60\,MPa$ and $P^- = 10\,MPa$, is shown in Fig. 2.9. As explained earlier in Section 2.4, the Gilmore model incorporates the compressibility of the liquid, and therefore allows the prediction of the pressure pulses emitted by the bubble on rebound. It is these pulses that form the basis of non-invasive detection of cavitation *in-vivo* and *in-vitro*. The corresponding pressure emission time history at $1.5\,mm$ from the bubble centre is given in Fig. 2.10 (Section 2.2.2). The two plots were generated from a Matlab code developed by Cunningham [29], who was involved in the research project.

The lithotripter shock reaches the bubble at time $t = 0\,s$. The interaction of the shock wave with the bubble will cause it to collapse, defined here as the primary collapse of the bubble. After this, the negative tail of the driving waveform initiates an expansion phase of the bubble, as shown in Fig. 2.9. The bubble expands greatly and keeps the expanded radius long after the driving pressure has returned to atmospheric pressure. The length of this period depends on the initial bubble radius and the amplitude of the driving shock wave. Following the long expansion phase, the overgrown bubble will undergo a violent secondary collapse. Fluid momentum during this ensuing collapse phase causes the bubble to compress to much less than its initial volume. This will generate a very high temperature and pressure inside the collapsed bubble and causes the bubble to rebound. As the bubble rebound, a spherically diverging shock wave is emitted into the surrounding fluid. The bubble will then go into a collapse and rebound cycle before it eventually reaches a new equilibrium size. On each rebound, a shock wave is emitted into the surrounding fluid as shown in Fig. 2.10. Owing to rectified diffusion, the theoretical stable size of the bubble *in vivo* is estimated to be about $40\,\mu m$ [22] (Fig. 2.9). A detailed description of the dynamics of the cavitation bubble undergoing a sequence of collapse and rebound has been given in Section 2.2.2. The final stable bubble size of $40\,\mu m$ has also been estimated from experimental data by Cunningham and associates [29]. Their value was estimated not only from the theoretical analysis of the Gilmore-Akulichev model as Church had done, but also from the time of the detected acoustic emissions *in vivo* approximated using time-frequency analysis.

The ability to detect and quantify cavitation activity near the focus of lithotripter using high-speed photography and also acoustic emission measurements may help in understanding of the effectiveness and safety of the treatment. The majority of experimental works are *in vitro*, where the ultrasound is measured from within a water tank. *In vivo* acoustic field measurements on the other hand are not as straightforward. A few considerations have to be taken into account and one particular is the design of the hydrophone probe. The probe has to be small enough to be inserted inside the body without causing any changes in the structure of the surrounding tissue, and also be insulated from the internal fluids. The hydrophone also needs to be able to measure and withstand the large pressure amplitudes. It is also a major concerns that no bubbles are introduced when inserting the probe which may contribute to the measured acoustic signature. Most important of all is the fact that most hydrophones are highly directional, and it is therefore imperative that the sound field impinges the hydrophones at normal incidence.

With the right experimental set up, cavitation activity *in vivo* can be monitored and recorded using a passive, focused hydrophone, from which valuable information can be extracted [24, 107]. It is comprehensible that the response of the single bubble modeled by the Gilmore-Akulichev model is likely to differ from that of a bubble cloud in the *in vitro* experiments. This may result from the variation in bubble radii as well as the mutual interaction between bubbles. Coleman and co-workers [24] presented an assessment of the level of quantitative agreement between the Gilmore-Akulichev model and measurements of the acoustic emission from cavitation collapse in water driven by high amplitude pulsed ultrasound from an electrohydraulic lithotripter. Their results were encouraging and substantiated that useful quantitative information, such as the bubble radius, can be obtained. Certain features of the model may apply for a bubble cloud. It was found that the "quiet" period due to the long expansion phase of the bubble after primary collapse in the Gilmore-Akulichev model correlates with the measured separation of the peaks in the acoustic signal associated with the collapse of the cavitation bubbles. This finding was exploited by Cunningham and co-workers [29] to determine the radius of the cavitation bubbles.

The works of Zhong and co-workers [107] and Coleman *et al.* [26] suggest that cavitation activity during ESWL can be assessed using acoustic measurement techniques. The acoustic emission from both studies revealed two distinctive bursts. The primary and secondary acoustic emission signals were found to comprise an initial and delayed burst of pressure spikes, corresponding to the initial expansion of shock wave-induced cavitation bubbles and their secondary collapses. Intermediate bursts were also observed which correlate with the collapse of small bubbles. Additional pressure spikes of reduced amplitudes were observed in both the primary and secondary acoustic emission signals, which were likely to be generated by the rebounds of cavitation bubbles after their primary collapse [24, 107].

In another study, Delius *et al.* [33] measured shock waves *in vivo* using PVDF membrane sensors implanted in the lung wall of dogs. Ensuring that the hydrophones are correctly aligned (because of the directional nature of their sensitivity), they found that at the focus, the *in vivo* waveforms were similar in shape to what was measured *in vitro*, but the shock amplitude was reduced by about 20%. These findings were also confirmed by Cleveland *et al* who carried out similar tests on pigs. However, the peak positive pressure was about 50% of the *in vitro* waveform. Also, the shock rise time measured *in vivo* was also greater compared to *in vitro*. Both of these findings are consistent with the higher absorption in tissue compared to that in water. The similarity in shape of the waveform measured *in vitro* and *in vivo* suggested that the inhomogeneities in tissues do not alter the shock front significantly. The difference in rise time however has no effect on the dynamics of the bubble. According to Church [22], the bubble response is insensitive to the rise time of the compressive part of the lithotripter shock wave. The 30% reduction difference in recorded pressure amplitude between *in vitro* and *in vivo* measurements by Delius and Cleveland suggest the difference in attenuation between animal models. The thick layer of fat in the pig may have contributed in higher ultrasound wave absorption. The results by Cleveland *et al.* [23] indicate that *in vitro* experiments used to evaluate lithotripsy performance are directly relevant to *in vivo* conditions [23] - an important finding in the studies of ESWL.

2.6.3 Mechanisms for Stones Fragmentation and Tissue Injury

It has been recognised that the forced collapse of acoustically induced stable bubbles with subsequent shock wave pulses can significantly increase the damage to a nearby solid surface or even to the surrounding tissue [71, 87]. It is important to note the role of preceding lithotripter shocks in populating or seeding the body fluid with relatively large stable bubbles. The interaction of preceding shocks with cavitation nuclei in the fluid will cause it to undergo expansion and collapse oscillation phases until a stable condition is achieved as described earlier in the chapter.

The mechanical stresses generated by the shock-bubble interaction, and the subsequent jet impact on the kidney stone, have been identified as possible mechanisms of stone fragmentation during lithotripsy [28]. However, it should be understood that liquid jets are not proposed here to play a solitary or even dominant role in stone fragmentation. Recent studies have showed that stress waves induced by the lithotripter shock waves and by cavitation work synergistically, rather then independently, to produce effective and successful disintegration of renal calculi in ESWL [110]. It is postulated that the cavitation microjets induce discrete fissures on the order of microns, which will then propagate throughout the bulk of the stone upon repeated stresses from the shock wave itself [76].

In addition to destroying stones, it has also been found that clinical doses of shock waves induce renal injury in a majority of treated kidneys [32]. Blood stained urine is common during treatment. This finding contradicts earlier report [20] that the treatment was safe and not associated with renal damage. However, the long-term effects of ESWL on renal tissue and function are still yet to be completely determined [38]. A number of *in vivo* experimental works have been carried out in order to correlate structural and functional changes in kidney following shock wave treatment. Evan and co-workers [38] carried out a study to investigate the effect of ESWL on renal bioeffects by using minipig as animal model. Minipig is ideal as its kidney mimic that of human's in terms of size, renal anatomy and function. The changes in the tissue structure and injury to the kidneys were found to be similar with those noted on lithotripsy patients. Massive bleedings which are also called hematomas[3] was consistently noted. Evidence has shown that the severity of injury may be related to treatment variables such as the number, energy output and frequency of the shock waves. Delius and associates *et al.* [33] observed that the extremity of renal injury induced by ESWL increases with the number of shocks as well as the rate of shock administration. Similar findings were made by Willis and co-workers [99], who also showed that an increase in the frequency and energy density of the lithotripter shock waves intensify the damage, causing functional impairment of the kidneys and reduction in blood flow in humans, canines and pigs. Severity of injury also increased when the lithotripter shock waves are administered in pairs. Conversely, a recent paper by Sokolov [84] and co-workers suggested that a dual pulse lithotripter increases stone comminution at the focus by as much as 10 times in comparison to a conventional single pulse lithotripter. However, the study was carried out *in-vivo* and the implementation of the method in clinical lithotripsy was not addressed by the author.

Besides *in vivo*, *in vitro* experiments using high-speed photography have also been used to illustrate the destructive behaviour of collapsing cavitation bubbles. Phillip *et al.* [71] studied the interaction of a lithotripter shock wave with an artificially produced stable air bubble. It was shown that bubbles within a certain size collapse asymmetrically, leading to the formation of microjets along the wave propagation direction. Besides this, they found that the jet velocity is dependent on bubble size and there exists a maximum value at a certain bubble radius. For bubbles with initial radii in the range of $0.1-0.9\,mm$, maximal jet velocities of $400-800\,ms^{-1}$ were measured. Moreover, the collapse time of the bubble was about $2\,\mu s$ which means that the complete collapse phase has already ended when the tensile part of the lithotripter shock wave reaches the bubble. If the

---

[3] Blood blisters within the organ, a space completely filled with blood, and even disrupted the normal kidney architecture [32].

negative pressure were to interact with the collapsing bubble, the rate of collapse and corresponding jet velocity is expected to be reduced, and the collapse occurs less violently. This could also prevent the impact of the liquid jet on the downstream bubble wall from occurring, as the tensile part of the shock wave induces the expansion of the bubble.

In the study by Philip *et al.* [71], he used a thick and strong foil to hold the bubble in place, which caused the bubble to collapse asymmetrically and form a high-speed jet. The jet damaged the foil but did not always puncture it. The experimental results obtained by Phillip *et al.* [71] also agree well with numerical results obtained using the Gilmore model. The destructive effects of cavitation produced by shock waves generated by a Dornier HM3 lithotripter have also been demonstrated on x-ray film, thin aluminium sheets, and thick metal plates ($0.2 - 1.0\,mm$) placed at the focal point of the converging shocks [26]. Deep depressions in the metal foil were found which were believed to be caused by the impacts of high-speed liquid jet developed in the collapsing cavitation bubbles. In many cases, the jet impacts were so violent that a hole was punched completely through the foil.

Howard and Sturtevant [47] carried out experiments in "non-cavitating" fluids like castor oil. They found that stresses induced by the ESWL shock waves in uniform media (no shock scattering) did not cause any damage to thin membranes, but damage occurred when the membranes were immersed in heterogeneous media. According to them, there are two physical mechanisms, direct and indirect, which contribute to tissue injuries. The direct mechanism is attributed to scattering of the shocks from small-scale tissue inhomogeneities, whilst the indirect effect is pressurisation caused by cavitation bubble collapse. Microjets from collapsing bubbles were observed by Kodoma and Takayama [56] who made a detailed experimental investigations on the interaction of shock waves with bubbles attached to a gelatine surface, rat livers or rat abdominal aortas in order to explain the mechanism of tissue damage by cavitation bubbles during ESWL. Similar experiments were carried out by Lush *et al.* [65], who observed the formation of microjets against a gelatine surface when bubbles were collapsed by lithotripter shock pulses. The collapse of these shock-induced bubbles also resulted in the formation of many microscopic shock waves.

It is clear that despite the apparent advantages of lithotripsy, recent discoveries on tissue injuries following clinical treatment have undermined its reputation as being a safe and efficient method for kidney stone treatment. Clearly, in order to minimise collateral damage, it is desirable to limit the intensity and duration of ESWL treatment to the minimum necessary for adequate stone fragmentation, and also to minimise the volume of soft tissue exposed to the focal point of the lithotripter pulse. This can be achieved if the focal point is accurately placed on the stone. Unfortunately, erroneous targeting arises from slight movements of the patients. Furthermore, the targeting rely on approximate corrections for refraction of the lithotripter shocks by the patient's tissue. Most important of all, neither method provides a means to indicate when stone fragmentation has occurred. This would enable a timely cessation of treatment, minimising exposure to the shock waves, or would conversely warn if insufficient treatment had been given to achieve shattering. Consequently, a large number of ESWL patients currently require re-treatment because initial ESWL therapy was ineffective.

2.7 Improvement of Stone Fragmentation and Lithotripsy Safety

A key issue in the success of the treatment is the ability to focus the shock waves so that they ideally damage only the stone and not the body. Most attempts at improving lithotripsy and its safety have concentrated on increasing the accuracy of shock focusing and kidney stone tracking during clinical treatment. Others have carried out research to enhance stone fragmentation, which would reduce the duration of the treatment and thereby minimise the volume of tissue exposed to the shock waves. In order to minimise renal tissue injury, precise stone localisation with no erroneous shots to the renal parenchyma is essential.

In current lithotripters, the targeting of the focal point on the stone is carried out after the stone has been identified by an expert before treatment. Once positioned, the shock waves are always administered to the same place until repositioning is necessary due to the movement of the stone or the patient. However, the precise targeting of the kidney stone throughout the treatment is difficult, mainly because the kidney moves during breathing. Kuwahara *et al.* [60] developed an anti-miss-shot device (AMCD) to prevent erroneously focused shock waves on healthy kidney tissues during ESWL. Experiments were conducted on dogs to evaluate its effectiveness. The mechanism is similar to that of a radar system, but rather than measuring the Doppler shift as well as the time taken for ultrasound to be transmitted and echoed back, AMCD analyses the intensity of the reflected ultrasound waves. A high level of reflected waves indicates accurate targeting, while a low level will indicate that the lithotripter is incorrectly aligned. Consequently, shock waves are not generated until re-alignment is made. In the test cases that were carried out with and without AMCD, fragmentation of the stone was observed in both cases. However, microscopic examination revealed injuries to the kidneys both with and without AMCD, though the severity of the bleeding was lower in the former. Moreover, the method would reduce the number of shocks but not the treatment time.

Orkisz *et al.* [70] on the other hand, developed a software called "*Echotrack*" which performs a real-time tracking of the stone in ultrasound images and automatically adjusts the focal point of the shock waves. Their idea was to exploit the imaging system of the lithotripter and to apply an image-based target tracking algorithm to determine the current location of the stone in real time. The displacements of the stone may occur following breathing and movement of the patient. The lithotripter generator would then be aligned automatically to the position of the stone. Validation of the system could not be precisely quantified using *in vivo* tests alone. This is because the use of ultrasound imaging alone does not provide means of determining the precise moment when the stone is completely fragmented. Hence, *in vitro* tests were also necessary. Initial pointing by a physician is still required, because only a human expert is able to distinguished a stone from other patterns present in the ultrasound image. The *Echotrack* is able to track the stone as long as it is visible in the ultrasound images. Thus, the method fails when the stone is not visible in the ultrasound images. They conclude that in comparison with current generator, the integration of the system reduces the number of shocks almost by half and ensures 80% of the shocks reach their target.

The feasibility of using controlled, forced collapse of cavitation bubble for improved stone fragmentation during ESWL using tandem shock wave pulses was demonstrated by Zhong *et al.* [108]. This idea is based on the findings that cavitation bubbles play a major role in stone fragmentation. Since the bubbles are formed following the incident shock wave, but well before the arrival of the next treatment pulse, their collapsed is uncontrolled and undirected. [4] Consequently, only a small portion of their energy contributes to stone fragmentation [108], which leads to several thousand high-intensity shock waves being required to achieve successful treatment. Zhong *et al.* [108] hypothesize that stone fragmentation may be enhanced by forcing the collapse of lithotripsy-induced cavitation bubbles towards the target. This is achieved using a secondary shock wave, which is delivered to the focal point within $300 - 500\,\mu s$ delay following the primary lithotripter shock wave. Encouraging results were obtained where, for the same number of shocks, stone volume loss is greater if the secondary shocks are used. However, their validation test cases were carried out *in vitro*. *In vivo* studies are required to confirm the merits of this new ESWL method. A similar technique of stone fragmentation enhancement has been proposed by Xi and Zhong [100] as well as Zhong *et al.* [109]. In the former, the secondary shock waves are generated using a piezoelectric annular array (PEAA), while in the latter, a simple annular ring reflector is incorporated into the electrohydraulic shock wave generator. However, unlike the method discussed earlier [108], the roles of the sec-

---

[4] Although the collapse of bubbles is influenced by the proximity of the stone, the severity and instance of collapse can be greatly effected and controlled by the interaction with shock waves. If a bubble is collapsing owing to the proximity of the stone, the severity of the collapse is enhanced by the impingement of the shock wave.

ondary shock wave and the main lithotripter shock wave are reversed. The secondary shock waves precede the main lithotripter shock wave to induced inertial cavitation bubbles, while control and forced collapse of the cavitation bubbles are achieved via the main shock wave. Both studies showed improvement in stone fragmentation, but as before, validation tests were only carried out *in vitro* using stone phantoms.

Despite the encouraging results in all of the above methods, none provide a means of detecting and characterising the acoustic emissions from cavitation activity in patients during clinical lithotripsy. Moreover, the methods do not indicate when stone fragmentation is complete. An efficient and successful technique can be achieved by incorporating these techniques into a device, but at the expense of duration and complexity of the treatment.

2.8 Conclusion

The ultimate goal of ESWL is to fragment renal and ureteral calculi as efficiently as possible while minimising the potential for injury to surrounding tissues. It is hoped that comparative studies, such as those which measure shock wave, stone fragmentation, acoustic cavitation emission and bioeffects of high energy shock waves can be combined to understand further the mechanisms of stone fragmentation and tissue injury induced by shock wave lithotripsy. The understanding and findings from these studies, experimentally or numerically, can then be used to improve the safety as well as the success of clinical lithotripsy treatment.

Chapter 3

Numerical Schemes

3.1 Computational Aspects - Flow Solver

3.1.1 The Solvers - Eulerian and Lagrangian

The most common flow models that have been adopted to solve the equations of compressible and inviscid fluid dynamics are finite difference or finite volume in the Eulerian and Lagrangian reference frames. The forms of the governing equations vary for each method. However, their content is the same as they describe the same physical system whichever reference frame or flow model is adopted. However, for certain applications the use of Lagrangian grid offers significant advantages over the more common Eulerian approach. There are some basic considerations in selecting which reference frame in which the flow should be solved. In the Eulerian flow model, the reference frame is fixed and flow convects through the computational cells. A problem arises when representing the convective motion of multiple-phase flows, where it is inevitable that some numerical diffusion will occur owing to the averaging of flux between the dissimilar phases. The difficulty in capturing contact discontinuities leads to large pressure errors near the contact discontinuity, which are often refereed to in literature as 'pressure oscillations'. These pressure errors are proportional to the density ratio of the materials at the interface, and for large density jumps across an interface, the error may even degenerate into instability. Fixes for this problem are available, and one such fix is the so-called ghost-fluid method, analysed by Koren and co-workers [58]. The advantage of the Eulerian model is that it is capable of modeling flows with large deformations, where the existence of a material interface can be captured using an interface tracking or interface capturing method. The former explicitly tracks the interface and treats it like a boundary, while the latter does not require the explicit calculation of the interface.

In contrast, in the conventional Lagrangian method, the grid moves at the local flow velocity. Consequently, there is no mass transferred between grid cells. The advantage of this method is its clean capture of the material interface, which ensures an unambiguous separation of different phases during calculation. Hence, no material convects through the cells and so, at least in principle, there is no numerical diffusion[1]. Therefore, the Lagrangian scheme can sharply capture contact discontinuities and material interfaces. It is suitable for simulating multiple-phases or multiple-fluids flows where resolution of contact surfaces is important. The main problem of this method is with regards to grid management. If the flows involves significant deformation and shearing between grid cells, the grid will become increasingly distorted and will eventually leads to large numerical errors [3]. Hence, the Lagrangian scheme is limited to flows that involve small material deformations.

Arbitrary Lagrangian Eulerian (ALE) is a method which has been developed to exploit the advantages offered by both Lagrangian and Eulerian techniques as discussed above. The Free-Lagrange (FL) method is an advancement of Lagrangian method, which exploits the advantages of Lagrangian formulation. These methods are discussed in the next subsections.

3.1.2 Arbitrary Lagrangian Eulerian (ALE) Method

The disadvantages of the Lagrangian method can be alleviated by using the ALE (Arbitrary Lagrangian Eulerian) methodology - a combination of Lagrangian and Eulerian schemes. In ALE method, each time step is divided into three distinct stages: an updated Lagrangian stage, a rezoning stage and a remaping or advection stage.

In the updated Lagrangian stage, a complete Lagrangian solution of the flow problem is obtained, where the computational mesh is allowed to move with the flow. Following this stage, the second procedure is carried out in order to form a new mesh that is less distorted than the initial mesh obtained from the Lagrangian stage. The mesh velocity is calculated and from which the new mesh is constructed. The degree of rezoning depends on the amount by which the initial computational mesh has been distorted, where the Eulerian and Lagrangian forms are the limiting cases of the general ALE form. The final stage is the interpolation of flow variables where the solutions from the initial Lagrangian stage are transferred to the new mesh. The rezoning procedure undoubtedly introduces numerical diffusion in the results.

This ALE scheme has been implemented successfully by Smith [83] who modeled a $1D$ spherically symmetric underwater explosion. He utilised an ALE version of the advective

---

[1] All practical numerical schemes for solving fluid flow contain a finite amount of numerical diffusion. This is because numerical diffusion arises from truncation errors that are a consequence of representing the fluid flow equations in discrete form.

upstream splitting method (AUSM) shock-capturing scheme. Smith revealed that strong shock, contact and phase discontinuities were captured accurately using a moving grid method. Other shock capturing schemes that have been employed for solving compressible Euler equations in ALE formulations include the Godunov schemes and artificial viscosity methods [35]. All three shock-capturing schemes have been explored by Luo and co-workers [64] in modeling a one-dimensional spherically symmetric underwater explosion problem. It was found that both HLLC and Godunov methods produced identical results, but the AUSM scheme generated erroneous oscillations near the gas-water interface.

3.1.3 Free-Langrange Method (FL)

In conventional Lagrangian method the computational mesh convects in a strict Lagrangian fashion as the flow geometry evolves. As the meshes move at the local flow velocity, significant shear strain can exists between neighbouring grids and the mesh will become increasingly distorted. This leads to numerical errors which typically result in the failure of the calculation. However, in the FL method, the grid connectivity is allowed to change freely according to flow deformation and is not restricted by a fixed mesh connectivity, such that each grid point is allowed to change neighbouring nodes via a search procedure. The ability of this method to re-connect the mesh automatically results in an unstructured mesh. This fundamental principle of the FL method makes it attractive, as mesh tangling associated with highly deforming flows is avoided.

Ball has successfully implemented this method in various flow modelling applications, involving large deformations of multiple-material fluids [3, 4, 6]. Using appropriate solvers, numerical diffusion at contact discontinuities is minimised and material interfaces, that always coincide with the cell boundaries, are sharply resolved. The relative merits of ALE and FL had been compared by Ball and Barlow [95] in simulating the interaction between a cylindrical bubble of $R22$ gas, in air, with a weak shock. Both showed good agreement with experimental data. However, due to its free grid connectivity, the FL scheme is better at capturing thin material filaments. It was also found that an ALE/FL hybrid would significantly reduce computational cost compared to a full FL method. Further discussion of the FL method is presented in Chapter 4.

In the FL code that will be implemented in the author's research work, a Godunov method is incorporated. This method is a renowned shock-capturing methods for computational fluid dynamics (CFD) based on solutions to local Riemann problems. This is discussed in the next section.

3.2 Godunov's Schemes

In 1959, Godunov [43] suggested an approach for solving the numerical solution of the Euler equations. The method was originally designed to deal with gas dynamics equations, but has spread to other equations that are governed by the hyperbolic conservation laws. The main advantage of this approach, based on the solution of local Riemann problems (see section 3.3), is that it allows for the existence of discontinuous solutions.

The first-order hyperbolic equation can easily be written as follows [53],

$$\frac{\partial u}{\partial t} + c\frac{\partial u}{\partial x} = 0 \tag{3.1}$$

where the variable u is a function of time t and distance x, i.e. $u = f(x, t)$, and c is the convective speed, which must be greater than zero ($c > 0$).

Godunov's approach to solving the laws of conservation is to initially divide the domain of interest into discrete cells such that the grid points are cell centered. He postulated that the flow could then be resolved by piecing together a collection of locally exact solutions of the Euler equations of local regions. He suggested that over each computational cell, the flow variables (U) could be assumed piece-wise constant, so that at each cell boundary, a discontinuity exists. The discontinuities at each cell boundary collectively form an array of mini-shock tube problems which can then be solved by applying the Riemann problem. The updated value of each flow variables at the new time level is averaged from the solutions obtained from each cell boundary which are then assigned to the cell centred grid points as shown in Fig. 3.1(a). These smaller localised exact solutions are then pieced together to obtain the complete solution. As the Riemann problem itself is essentially discontinuous, the Godunov method can locate correctly discontinuities and deal with shocks, contact and rarefaction waves, hence getting around the limitations of classical numerical methods.

The Godunov scheme utilising the piece-wise constant cell approximation is highly diffusive. In order to overcome this problem, a piece-wise linear approximation is adopted which increases the accuracy of the solver to 2^{nd} order, but which introduces dispersion. Oscillatory behaviour in the vicinity of discontinuities, similar to that encountered with 2^{nd} order central difference schemes, reappear. This is because the formulation of the piece-wise linear cell approximation results in the creation of non-physical local maxima and minima.

The introduction of a 'Slope Limiter' algorithm can alleviate this problem. An example is *MUSCL* (Monotone Upstream-Centred Scheme for Conservation Laws), introduced by Van Leer [96] in 1979. A slope limiter examines the values at each cell boundary, as calculated by the linear fitting procedure, and compares them to the cell centre values on

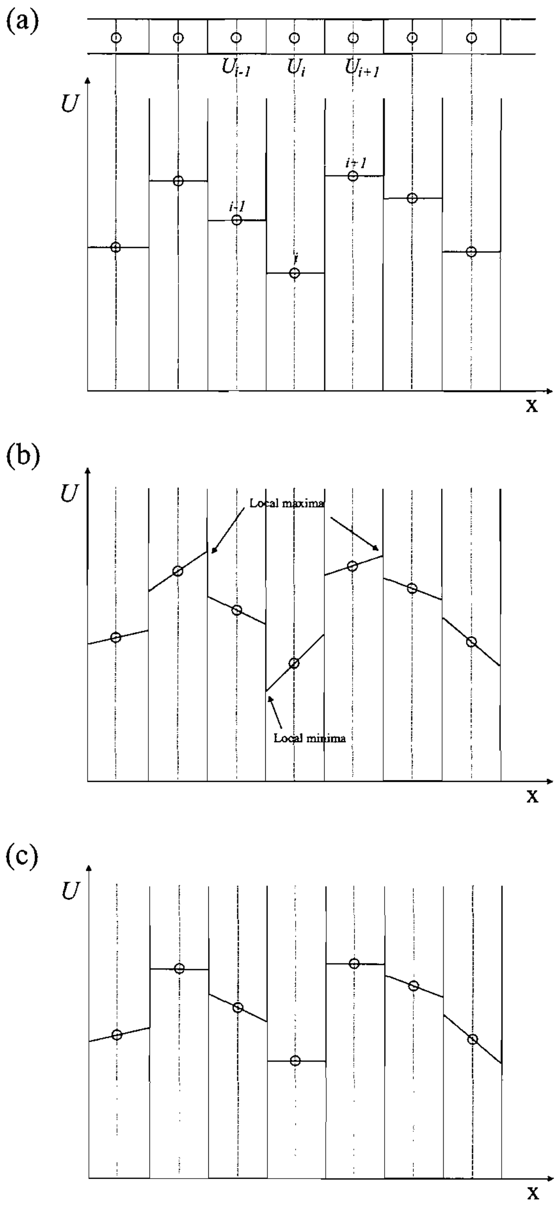

Figure 3.1: Cell average approximation of variable U. **(a)** A piecewise-constant **(b)** A piecewise-linear without slope limiting **(c)** A piecewise-linear with slope limiting.

either side of the boundary. The gradient of the slope is then limited to ensure no new maxima or minima are created. These local extrema are responsible for the oscillatory behaviour near the shock and discontinuities. Fig. 3.1 illustrate the piecewise-constant, piecewise-linear without slope limiting and piecewise-linear with slope limiting ($MUSCL$) distributions for flow variable U in one-dimensional problem. The circles represent the cell-centred value of U.

Although the scheme has been described for a one-dimensional ($1D$) uniform distribution of rectangular cells, the same principle apply to non-uniform arbitrary cell shapes. The principles of Godunov's approach easily extend to two ($2D$) or three ($3D$) dimensions by counting for the extra fluxes through the additional cell interfaces. A variant of $MUSCL$-type slope limiter was employed by Ball [3, 4, 6] to simulate $2D$ compressible flow simulations. Full algebraic details of the slope limiter are presented in [3].

3.3 Riemann Solvers

The disadvantage of Godunov's method and its higher-order extension is the difficulty of solving the non-linear Riemann problem exactly. Its solutions must be obtained using an iterative procedure at every cell interface. Clearly, this is an extremely CPU intensive process and relatively complex. Because of this, more efficient and simpler approximate Riemann solvers were developed. This was however, not at the cost of the two fundamental features of Godunov-type methods, accuracy and robustness.

Using approximate Riemann solvers, the dynamics of a flow can be solved numerically with low computational cost. An extremely effective and robust approximate Riemann solver known as HLL-Riemann solver, was suggested in 1983 by Harten, Lax & van Lerr [46]. Increased simplicity was achieved by treating the Riemann problem as two propagating pressure waves. This approach (two shock approximation method) ignores the intermediate waves, i.e. the fluid region between the shock and the rarefaction is approximated as being constant and the contact surface neglected. Einfeldt [37] exploited this method and improved it even further by proposing wave-speed estimates for the Riemann problem in order to compute the numerical flux at cell boundaries. The new approximate Riemann solver (HLLE) proposed by Einfeldt is simple and easy to implement. However, it was found that the contact discontinuities is highly diffused due to the neglected contact surface [37, 3].

Consequently an improved version of the HLL-Riemann solver, termed HLLC, was introduced by Toro and co-workers [92], where the contact surface is restored. The assumed wave structure consists of two discontinuous pressure waves and an intermediate contact wave to represent the contact surface as shown in Fig. 3.2. A significant improvement was made on the contact resolution in the Eulerian frame. The result is comparable to solutions from an exact Riemann solver, while the simplicity of the HLL method is retained. Ball [3] confirmed the superiority of the HLLC over the HLLE Riemann solver in a simulation of a blast wave problem using a FL finite volume method.

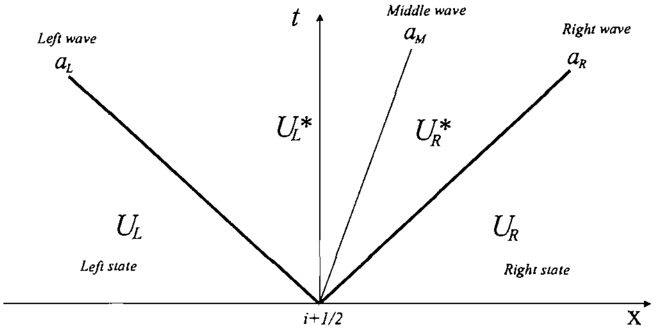

Figure 3.2: Assumed wave pattern for *HLLC* approximate Riemann solver in the $x - t$ plane. a is the associated wave speed.

3.4 Aeroacoustic Schemes

There are many applications in which it is required to predict the far-field acoustic signature produced by fluid dynamic disturbances, e.g. helicopter rotor noise, automobile exhaust noise and cavitation. Various approaches have been proposed to simulate these phenomena. The direct method solves the compressible Navier-Stokes equations and simultaneously resolves the flow and acoustic contributions. However, for practical applications this method is prohibitively expensive in terms of computer storage and CPU times. In most practical cases, it is tedious or impossible to numerically find a solution everywhere in the flow field. This is because of errors owing to increasing mesh size in the far-field to reduce memory and computing time. It is therefore, an advantage to develop ways of obtaining the far-field noise or pressure signature from near-field solutions. The ideal method seems to be the separation of the computations into two domains, one describing the non-linear generation of sound, and the other describing the linear propagation of sound. The separation of the problem into linear and nonlinear regions allows the use of most appropriate numerical techniques for each.

Hybrid methods have been developed which decouple the flow and acoustic parts, where the aerodynamic part of the flow problem is solved first to determine acoustic sources. Following this, an acoustic scheme is implemented to obtain the associated far field radiation. Examples of such methods are the acoustic analogy of Ffowcs-Williams Hawkings, and Kirchhoff's method. The Kirchhoff method and the porous Ffowcs-Williams Hawkings (FWH) are attractive because they utilize surface integrals over a source region to determine far-field acoustics, as opposed to the memory intensive volume integrals found in traditional acoustic analogy methods. Both methods have been applied to various aeroacoustic problems such as helicopter noise, jet noise and propeller noise. The application of these methods has increased substantially because of the development of reliable CFD methods that can be used for the evaluation of the near-field. These two methods and the numerical codes structure are described in the next sections.

3.4.1 Kirchhoff's Method

The Kirchhoff's method assumes that the sound transmission is governed by the simple wave equation. It includes the calculation of the nonlinear near-field on a control surface, performed by other CFD method. The solutions on the control surface are then used as inputs to Kirchhoff formulations for the evaluation of the far-field solutions. This method provides an adequate link between the aerodynamic nonlinear near-field and the acoustics linear far-field. The full nonlinear equations are solved numerically in the near-field region. The control surface is assumed to enclose all the nonlinear flow effects and noise sources. The sound pressure and its normal and time derivatives are assumed to be given over the surface enclosing the nonlinear region wherein the sound source is generated. This method has been extended for an arbitrary moving deformable surface [39].

The main advantage of this method is that it is simple and accurate. The surface integrals and the first derivatives needed for the far-field solutions can be easily evaluated from the near-field computational fluid dynamics (CFD) data. Diffusion and dispersion errors associated with wave propagation in the far-field are avoided. Also, nonlinear effects such as shock waves are accounted for in the solution of the first region [67, 68].

A disadvantage of the Kirchhoff method is that the control surface must be chosen to be in the linear flow region, such that the input acoustic pressure $p' = p - p_0$ and its derivatives $\partial p'/\partial t$ and $\partial p'/\partial n$ are compatible with the liner wave propagation. Therefore, the surface must be chosen large enough to include the region of nonlinear behaviour. However, this is a difficult task considering the linear region is not well defined and is problem dependent. Thus, it would be ideal to position the control surface well away from the source region, but in most numerical CFD calculations the solutions are not well resolved away from the body. It is important that the control surface is not positioned where the CFD mesh is coarse. A fine grid is needed in the CFD solution to ensure proper wave resolution so that the Kirchhoff control surface can be placed there [66]. Therefore, the placement or distance of the Kirchhoff control surface is critical and is usually a compromise.

Kirchhoff's method is powerful technique for calculating the far-field pressure signature utilising numerical results that simulate complex phenomena. One example of the utility of the Kirchhoff method is its successful application by Lyrintzis [68] in helicopter noise prediction. In this work, unsteady aerodynamic calculations were performed in the near field of a helicopter rotor in a reference frame fixed to the rotating blades. The results from the CFD calculation provided data on a Kirchhoff surface surrounding the blade for subsequent application of the Kirchhoff formula to predict the noise radiated by the blade.

3.4.2 Ffowcs-Williams Hawkings Method (FWH)

The Ffowcs Williams and Hawkings equation for the amplitude of aerodynamic sound radiated by a moving object in a fluid is widely accepted in modern aeroacoustics. The FWH equation is an exact rearrangement of the continuity equation and the Navier-Stokes equation into the form of an inhomogeneous wave equation with two surface source terms (monopole and dipole terms) and a volume source term (quadrupole term). The former are known as thickness and loading sources.

The monopole and dipole terms are easy to evaluate because they are surface integrals over the control surface. The nonlinear near-field flow can be evaluated using CFD calculations. The major difficulty with the FWH method is the evaluation of the quadrupole term which requires a volume integral calculation and therefore requires large computational resources. Volume integration is also difficult to implement.

However, the FWH approach has several advantages over the Kirchhoff method. First, each of the three sources in the FWH formulation as mentioned above has physical meaning which is helpful in understanding the noise generation. The loading noise is generated by the force acting on the fluid due to the presence of the body. The thickness noise on the other hand, is determined completely by the geometry and kinematics of the body. The quadrupole source term accounts for nonlinear effects, for example, the nonlinear wave propagation and steepening, variations in the local sound speed, turbulence in the flow field, vorticity as well as noise generated by shocks.

The separation of the source term is also an advantage numerically because not all terms must be computed at all times if it is known that a particular source does not contribute to the sound field. A good example of this is in low speed flow where the quadrupole term may be neglected which simplifies the problem greatly. The main advantage of the FWH method is that the formulations are well developed and have robust numerical algorithms.

In most cases, the FWH integration control surface S_c is assumed to be both coincident with the surface of a physical body and is impenetrable. However, if the surface is assumed to be porous, the general equation that is derived can be applied to a control surface S_c in a similar fashion as the Kirchhoff method explained in the previous subsection. The equation may also be compared more directly with the governing equation of the Kirchhoff formula given in the following chapter. Thus, in a similar manner to the Kirchhoff formulation, the far-field pressure signature can be evaluated based on quantities on the arbitrary control surface provided by the CFD simulations.

The mathematical manipulation in deriving the FWH for a permeable surface was shown by di Francescantonio [34]. He used a permeable and fictitious surface that does not correspond to a physical body, exactly like the Kirchhoff approach, to carry out study on far-field helicopter noise prediction. If the surface is place on the impenetrable body of the helicopter blade, the classical FWH formulation is obtained. The non-linear effects are then taken into account by the quadrupole volume terms. By moving the surface away from the body, part of the non-linearities is taken into account by the quadrupole volume terms and part by the surface integrals. If the surface is far enough from the body and that the perturbations are small, the evaluation of the volume integral can be avoided, and therefore reduces the computational cost of the acoustic calculations.

The main advantage of FWH over the Kirchhoff method is that FWH does not require that the flow obeys the linear wave equation at the control surface, so it is less vulnerable to error if there is some moderate level of non-linearity in the acoustic field at the control surface.

Chapter 4

Finite Volume Free-Lagrange method - The Vucalm code

The Vucalm flow solver used in the present work was written and developed by Ball [3] from the University of Southampton. Although the present author spent a considerable amount of time developing the code, he took no part in the original construction of the solver and initial development. As a consequence, the detailed formulation and mathematical technique of the solver does not form part of the novel contribution made by the present work. Hence, the description of the code and detailed mathematics are only briefly explained.

When the author undertook the research project, the axisymmetric version of the *Vucalm* code was newly developed and the validation work had only been carried out on a single phase conical flowfield resulted from shock interaction with a cone. Hence, further validation work against published numerical or experimental results that involves shock waves and multi-phase flow of air and water was necessary. The validation work that was carried out by the author is presented in Chapter 6. Other significant changes on the code that were made include:

- The criteria for adaptive mesh refinement and derefinement and the division of mass for particles along the axis of symmetry.

- The distribution of the material smoothing restoring forces between the target particle and its interface neighbours.

- The structure of the Voronoi mesh. The initial mesh layout of the computational domain is divided into different regions, with varying mesh densities. The mesh structure is also circular in order to create a wrinkle-free air bubble interface. A discussion on the structure of the mesh and mesh resolution study are given in

Chapter 7.

- The boundary condition had to be modified in order to generate the lithotripter shock wave profile as depicted in Fig. 2.8. This figure was generated by running a simple shock tube problem in *Vucalm*.

The changes mentioned in point number one and two above are discussed in this chapter.

4.1 The Governing Equations - Axisymmetric Euler Equations

The governing equations for fluid flow arise from three sets of physical laws which take the forms of conservation requirements - Law of Conservation of Mass, Newton's 2^{nd} Law and 1^{st} Law of Thermodynamics. These three fundamental laws represent the mathematical statements which describe the dynamics of fluid as well as solid mechanics. The principles can be applied to two different flow models, which can either be fixed in space (Eulerian), where the flow convects through the control volume, or allowed to move with the flow in a Lagrangian manner. The governing equations are expressed in integral form when applied to a finite control volume, whereas the use of an infinitesimal fluid element leads to the differential form of the governing equations.

The finite-volume method is a direct discretisation of the integral equations. The derivation of the governing equations on a finite control volume is presented here as it has two advantages. First, the method ensures that the discretisation is conservative. Second, it can be applied on an unstructured mesh that has an arbitrary number of cell boundaries, as a coordinate transformation for irregular meshes is not required. Furthermore, the method is suitable for numerical simulations that involve flow discontinuities such as shock waves as it does not assume continuous flow properties. In contrast, the finite difference method assumes that the flow is continuous, owing to the representation of the governing equations in differential form. In other words, integral equations describe what is happening to a finite amount of fluid, whereas differential equations describe what is happening at a point in the flow.

The three governing equations derived from the three physical principles are,

- Continuity equation
- Momentum equation
- Energy equation

In Appendix A, the governing equations are derived in an axisymmetric Eulerian reference frame. These conservation laws lead to three conservation equations, in integral form, as follows,

1. Physical principle: Conservation of mass (Continuity Equation)

$$\frac{\partial}{\partial t}\int_A \rho r_c dA + \oint_S \hat{n}\cdot\rho\bar{u}r_c dS = 0 \tag{4.1}$$

2. Physical principle: Conservation of momentum

$$\frac{\partial}{\partial t}\int_A \rho\bar{u}r_e dA + \oint_S \hat{n}\cdot(\rho\bar{u}\bar{u} + Ip)r_c dS = \int_A \bar{g}r_e dA \tag{4.2}$$

3. Physical principle: Conservation of energy

$$\frac{\partial}{\partial t}\int_A E\rho r_e dA + \oint_S \hat{n}\cdot(\rho\bar{u}E + \bar{u}p)r_c dS = 0 \tag{4.3}$$

where A is the area enclosed by the boundary S in a plane containing the symmetry axis, ρ is the density, $\bar{u}$ is the velocity vector, p is the pressure, I is the unit tensor, $\hat{n}$ is the outward unit vector normal to the boundary S and $E = \epsilon + (u\cdot u)/2$ is the specific energy, and ϵ is the specific internal energy. In axisymmetric flow, r_e and r_c are taken as the distance from the axis of symmetry to the elemental area dA and elemental line dS respectively.

The three equations (Eqn. 4.1, 4.2, 4.3) can be combined in a compact form using vector notation as follows:

$$\frac{\partial}{\partial t}\int_A \bar{U}r_e dA + \oint_S \hat{n}\cdot\bar{F}r_c dS = \int_A \bar{G}r_e dA \tag{4.4}$$

where the forms used for $\bar{U}$, $\bar{F}$ and $\bar{G}$ and are:

$$\overline{U} = \begin{bmatrix} \rho \\ \rho\bar{u} \\ \rho E \end{bmatrix} \quad \overline{F} = \begin{bmatrix} \rho\bar{u} & & \\ \rho\bar{u}\bar{u} & + & Ip \\ \rho\bar{u}\bar{E} & + & \bar{u}p \end{bmatrix} \quad \overline{G} = \begin{bmatrix} 0 \\ \frac{\bar{e}_y P}{r_e} \\ 0 \end{bmatrix} \tag{4.5}$$

The vector $\bar{U}$ is the Conserved Variables Vector (vector of dependent variables) as it contains the quantities conserved within the domain, i.e. mass, momentum and energy. Vector $\bar{F}$ on the other hand is the Flux Vector as it contains the flux terms across the control volume boundary. The vector $\bar{G}$ is a source vector that accounts for the axisymmetric flow geometry. P is the pressure and $\bar{e}_y$ is the unit radial vector. Equation 4.4 is therefore known as the axisymmetric, unsteady, compressible and inviscid Euler equation. The equations given above are the Euler equations with respect to the Eulerian reference frame. A complete derivation and explanation of the entire notation used in the equations above is given in Appendix A.

4.2 Transformation into the Lagrangian Reference Frame

The governing equations can be transformed from the Eulerian into the Lagrangian reference frame in which the mesh, and hence the control volume, propagates at the local flow velocity. Consequently, depending on the dynamics of the flow, the surface area A and the surface boundary S are time-dependent.

The transformation can be carried out by decomposing the flux vector into two separate terms, the convective and pressure terms. Consider the governing equation 4.5. The pressure term and convective term for the flux vector $\bar{F}$ are $(Ip, \bar{u}p)$ and $(\rho\bar{u}, \rho\bar{u}\bar{u}, \rho\bar{u}\bar{E})$ respectively. Following Trépanier et al. [93], the control volume can be assumed to convect with an arbitrary velocity $\bar{w}$. The velocity of the fluid relative to the control volumes becomes $\bar{u} - \bar{w}$. The flux vector $\bar{F}$ can therefore be written as

$$\overline{F} = \begin{bmatrix} \rho(\bar{u}-\bar{w}) & & \\ \rho(\bar{u}-\bar{w})\bar{u} & + & Ip \\ \rho(\bar{u}-\bar{w})\bar{E} & + & \bar{u}p \end{bmatrix} \tag{4.6}$$

In the Lagrangian reference frame, the control volume convects at the same local velocity as the flow, i.e. $\bar{u} = \bar{w}$. Therefore, the flux vector $\bar{F}$ is reduced to

$$\overline{F} = \begin{bmatrix} 0 \\ Ip \\ \bar{u}p \end{bmatrix} \tag{4.7}$$

It is clear from Equation 4.7 that the convective terms vanish. Consequently the continuity equation becomes

$$\frac{\partial}{\partial t}\int_A \rho r_e dA = 0 \tag{4.8}$$

This simply means that the mass inside the control volume remains constant and does not vary with time. The equation is therefore redundant. Hence, it is necessary to introduce another physical law in order to close the governing equations in the Lagrangian reference frame. An obvious choice is the conservation of volume which states

$$\begin{pmatrix}\text{Rate of change}\\ \text{of volume}\\ \text{enclosed by surface}\end{pmatrix} = \begin{pmatrix}\text{Volume Change}\\ \text{due to Movement}\\ \text{of Boundary}\end{pmatrix}$$

Equating the expression above (see Appendix A), and by conservation, we have

$$\frac{\partial}{\partial t}\int_{A(t)} r_e dA + \oint_{S(t)} \hat{n}\cdot\bar{u} r_c dS = 0 \tag{4.9}$$

Thus, the Euler equations in the Lagrangian reference frame can be written as

$$\frac{\partial}{\partial t}\int_{A(t)} \bar{U} r_e dA + \oint_{S(t)} \hat{n}\cdot\bar{F} r_c dS = \frac{\partial}{\partial t}\int_{A(t)} \bar{G} r_e dA \tag{4.10}$$

where the vector of conserved variables $\bar{U}$, the flux vector $\bar{F}$ and the source vector $\bar{G}$ become

$$\overline{U} = \begin{bmatrix} 1 \\ \rho\bar{u} \\ \rho E \end{bmatrix} \quad \overline{F} = \begin{bmatrix} -\bar{u} \\ Ip \\ \bar{u}p \end{bmatrix} \quad \overline{G} = \begin{bmatrix} 0 \\ \frac{\bar{e}_y P}{r_e} \\ 0 \end{bmatrix} \tag{4.11}$$

Equation 4.10 and Equation 4.11 describe axisymmetric, unsteady, inviscid. compressible Euler equations in a Lagrangian reference frame. Using these two equations. explicit expressions for density, temperature and velocities can be formulated for a time-marching procedure.

4.3 Time Integration

In order to advance the solution at a particle through one time step, one-dimensional Riemann problems are solved approximately at each cell boundary and the resulting numerical fluxes are summed in order to update the particle properties. Following Ball [3] and Trépanier [93], Equation 4.10 above can be approximated using the expression below.

$$\frac{\Delta[\bar{U} r_e A]}{\Delta t} + \sum_{k=1}^{K} \hat{n}_k \cdot \bar{F}_k^n r_{ck} S_k = \bar{G} r_e A \tag{4.12}$$

where

$$\bar{F}_k = A\bar{F}_k^* \tag{4.13}$$

and

$$A = \begin{bmatrix} \hat{n}_k & 0 & 0 \\ 0 & \underline{I} & 0 \\ 0 & 0 & \hat{n}_k \end{bmatrix} \quad \overline{F}_k^* = \begin{bmatrix} -u_k^* \\ p_k^* \\ u_k^* p_k^* \end{bmatrix} \quad \overline{G} = \begin{bmatrix} 0 \\ \frac{\bar{e}_y P}{r_\epsilon} \\ 0 \end{bmatrix} \tag{4.14}$$

For a K sided polygonal Voronoi cell that forms the control volume. $\bar{F}_k$ is the numerical flux on the k^{th} side, to be determined from the approximate Riemann solver, S_k is the side length, and Δt is the time step. The superscript * indicates the wave-processed state obtained from the solution of the $1D$ Riemann problem formed on the cell boundaries.

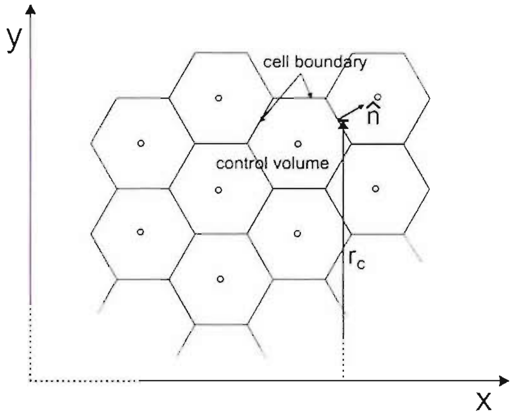

Figure 4.1: Polygonal shape computational cells of Voronoi type used to represent control volumes inside a computational domain. The Riemann problem as discussed in Chapter 3 is solved at each cell boundary.

Fig. 4.1 illustrates a typical polygonal computational mesh. For a Lagrangian mesh, the cell boundary always coincides with the contact surface of the local Riemann problem. Therefore, both u_k^* and p_k^* are evaluated at the cell boundary. The variable S is the cell side length, $\hat{n}_k$ is the unit vector normal to cell boundary, ρ is density, m is cell mass, r_c is distance of cell side mid-point form the axis of symmetry and r_ϵ is the ordinate of the cell centroid from the axis of symmetry.

Let

$$r_\epsilon^{n+1} A^{n+1} = V^{n+1} = \text{Volume at } (n+1)^{th} \text{ time level} \tag{4.15}$$

and

$$r_\epsilon^{n} A^{n} = V^{n} = \text{Volume at } (n)^{th} \text{ time level} \tag{4.16}$$

Substituting expression 4.15 and 4.16 into Equation 4.12 gives:

$$\frac{1}{\Delta t}[\bar{U}^{n+1}V^{n+1} - \bar{U}^n V^n] = -\sum_{k=1}^{K} n_k \cdot \bar{F}_k^n(r_{ck}S_k) + \bar{G}V^n \tag{4.17}$$

Rearranging for the vector of conserved variables $\bar{U}$,

$$\bar{U}^{n+1} = \frac{V^n}{V^{n+1}}\left[\bar{U}^n - \frac{\Delta t}{V^n}\sum_{k=1}^{K} n_k \cdot \bar{F}_k^n(r_{ck}S_k) + \bar{G}\Delta t\right] \tag{4.18}$$

However, it is known that the density can be written as

$$\rho(t) = m/V(t) \tag{4.19}$$

where m is the constant mass within the control volume. Hence, it is more convenient to write Equation 4.18 as

$$\bar{U}^{n+1} = \frac{\rho^{n+1}}{\rho^n}\left[\bar{U}^n - \frac{\rho^n\Delta t}{m}\sum_{k=1}^{K} n_k \cdot \bar{F}_k^n(r_{ck}S_k) + \bar{G}\Delta t\right] \tag{4.20}$$

4.3.1 Density Update

From Equation 4.11, the expressions for the three vectors are as follows

$$\overline{U} = 1 \qquad \overline{F} = -\bar{u} \qquad \overline{G} = 0 \tag{4.21}$$

Substituting these into Equation 4.20 gives an expression for updating the density,

$$\rho^{n+1} = \left[\frac{1}{\rho^n} + \frac{\Delta t}{m}\sum_{k=1}^{K} u_k^n(r_{ck}S_k)\right]^{-1} \tag{4.22}$$

where u_k is the outward normal velocity component at the boundary. This equation can then be used to update $\bar{U}$ explicitly as follows.

4.3.2 Velocity Update

Similarly as before,

$$\overline{U} = \rho\bar{u} \qquad \overline{F} = Ip \qquad \overline{G} = \frac{\bar{e}_y P}{r_e} \tag{4.23}$$

Substituting into Equation 4.20 and rearranging gives,

$$\bar{u}^{n+1} = \bar{u}^n - \frac{\Delta t}{m}\sum_{k=1}^{K} n_k \cdot p_k(r_{ck}S_k) + \frac{\bar{e}_y P}{r_e}\frac{\Delta t}{\rho^n} \tag{4.24}$$

The velocity vector can be divided into two separate components, the x-wise velocity component and the y-wise velocity component. The second term in Equation 4.24 takes into account the geometry of axisymmetric flow and only effects the velocity in the radial direction (in y-direction). Hence the two velocity components are as follows

x-component:

$$u^{n+1} = u^n - \frac{\Delta t}{m} \sum_{k=1}^{K} n_k \cdot p_k(r_{ck} S_k) \tag{4.25}$$

y-component:

$$v^{n+1} = v^n - \frac{\Delta t}{m} \sum_{k=1}^{K} n_k \cdot p_k(r_{ck} S_k) + \frac{P}{r_e} \frac{\Delta t}{\rho^n} \tag{4.26}$$

4.3.3 Temperature Update

From Equation 4.11,

$$\overline{U} = \rho E \qquad \overline{F} = \bar{u} p \qquad \overline{G} = 0 \tag{4.27}$$

Substituting into Equation 4.20 and rearranging gives an expression for the specific energy.

$$E^{n+1} = E^n - \frac{\Delta t}{m} \sum_{k=1}^{K} n_k \cdot \bar{u} p_k(r_{ck} S_k) \tag{4.28}$$

Recall that the specific energy can be written as

$$E = \epsilon + (u \cdot u)/2 \tag{4.29}$$

where the specific internal energy,

$$\epsilon = C_v T \tag{4.30}$$

Substituting these expression into Equation 4.28 gives

$$T^{n+1} = T^n - \left[\frac{(\bar{u}^{n+1})^2 - (\bar{u}^n)^2}{2C_v} \right] - \frac{\Delta t}{m c_v} \sum_{k=1}^{K} n_k \cdot \bar{u} p_k(r_{ck} S_k) \tag{4.31}$$

where

$$(\bar{u}^{n+1})^2 = (u^{n+1})^2 + (v^{n+1})^2 \tag{4.32}$$

and

$$(\bar{u}^n)^2 = (u^n)^2 + (v^n)^2 \tag{4.33}$$

The velocity vectors can be calculated from Equation 4.25 and 4.26. Thus, Equation 4.22, 4.24 and 4.31 are applied to calculate the density, velocity and temperature at a new time level.

4.4 The Vucalm Code

In the next few sections, important features of the *Vucalm* code are described. These include the adaptive mesh refinement and derefinement algorithm and the Voronoi mesh.

4.4.1 Voronoi Mesh

At the start of the calculation, the computational domain is filled with computational particles. Each particle is assigned with a fluid type, thermodynamic properties, coordinates and flow conditions. In the Lagrangian frame, the particles sit within their own Voronoi cell and the mesh moves with the flow. The Voronoi diagram is constructed based solely on the particle positions to form polygonal cells that enclose each particle and the region closest to that particle (Fig. 4.2). The discretisation algorithm of the *Voronoi* mesh is described in detail in [3, 63, 48].

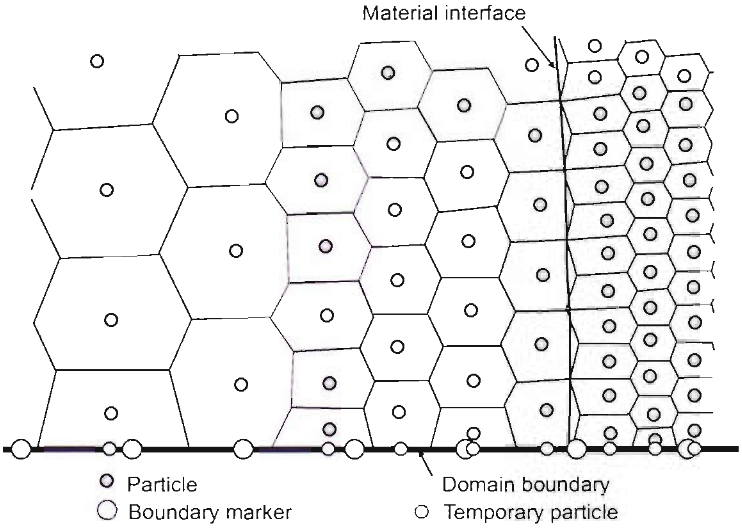

Figure 4.2: Initial Voronoi mesh used in the Free-Lagrange simulations. Bottom horizontal solid line is the axis of symmetry, the thick solid line represents a material interface and dots indicate positions of fluid particles. The bubble/water interface location is only for plotting purposes as the actual location is determined by the boundaries shared between the air and water cells.

As illustrated in Fig. 4.2, each cell is of polygonal shape and it represents the control volume for time integration. Each particle can have at least 3 neighbours. The maximum number of neighbours is unlimited and 6 is typical. Each particle adjacent to the boundary is assigned with one or more temporary particles. These temporary particles are located on the boundary and their properties are interpolated from the the adjacent particle inside the domain. The temporary particle are massless and they are used to impose boundary conditions. Boundary markers are positioned on the computational boundaries. These are used to identify the boundaries during the construction of the Voronoi mesh.

To ensure that a smooth and stable interface is achieved, a simple interface smoothing algorithm, analogous to a surface tension, is applied at the water/air interface. It prevents numerically seeded Richtmyer-Meshkov instability occurring on the interface when strongly shocked. For more details, refer to Howell and Ball [49].

4.4.2 Mesh Weighting Factor

In the current code, the Voronoi mesh can either be constructed using 'weighted' or 'unweighted' methods. For the unweighted construction, the location of each computational cell boundary is midway between a particle and its neighbour. Although the unweighted mesh is uncomplicated, stable and time efficient, error occurs in the regions where steep density gradient occurs such as in the vicinity of material interfaces. In this region, the geometric volume[1] of each computational cell deviates significantly from the thermodynamic volume of each cell[2]. This is a source of error in flux calculations because it leads to the use of incorrect cell boundary lengths at boundary segments that separate cells of different densities.

In order to minimise, a weighted mesh is implemented, where the location of each computational cell boundary is determined by taking into account a 'weighting factor'. In Vucalm, the weighting factor is taken to be a function of density and mass of the associated particle, (and the radial distance of the cell centroid from the axis of symmetry for the axisymmetric version of the code). The construction of the weighted mesh increases the accuracy of the cell boundary length and consequently gives more accurate numerical flux calculation. The weighting factor for the $2D$ version of the code is given by,

$$W_n = (m_n/\rho_n)^{1/4}, \tag{4.34}$$

where the subscript n is the particle number under consideration, m_n and ρ_n are the mass and density of the particle respectively. The axisymmetric code, the weighting factor is

---

[1] $V_{geom} = r_c A$, where r_c is the radial distance of the cell centroid from the axis of symmetry, and A is cell face area.

[2] $V_{therm} = (m/\rho)_{cell}$, where m is mass and ρ is the density.

given by,

$$W_n = (m_n/(\rho_n r_n))^{1/4}, \tag{4.35}$$

where r_n is the radial distance of the cell centroid from the axis of symmetry. Fundamentally, the weighting factor is equal to the square root of the particle length scale L_c. Hence, if the masses of neighbouring particles are equal, the cell boundary is closer to the particles of higher density.

In highly sheared flows, the mesh is completely reconstructed on every time step, so that the mesh connectivity may change freely in response to flow evolution. However, reconstruction of the mesh on every time step is very inefficient. In order to reduce CPU time, the user may opt to reconstruct the mesh less frequently, typically every $5-10$ time steps. In this case, the mesh nodes are 'coasted' where they are convected at the local flow velocity between reconstructions. However, during coasting, cells near boundaries are still restructured. The maximum number of coasting steps depends on the nature of the flow and is limited by mesh distortion and tangling.

4.4.3 Adaptive Mesh Refinement and Derefinement

The particle distribution of the Voronoi mesh reflects the local density variation. For high density regions, the grid is at its finest and so the flow structure is well resolved. Normally, for multi-material flow problems, the computational mesh near the interfaces undergoes large deformation. Consequently, a problem can arise owing to a large cell area ratio mismatch between the water and gas particles. This can lead to numerical errors in the flux calculations and for this reason, an adaptive mesh refinement and derefinement algorithm is implemented in the *Vucalm* code. It also helps in maintaining a stable and economical time step.

In regions of excessive mesh density, the 'derefinement' routine automatically identifies and merges adjacent pairs of fluid particles of the same fluid type. One example is in the simulations of shock-bubble interaction. Fig. 4.3 shows a region of high particle density in the air near the air/water interface as the air compresses as a result of the shock impacting on the upstream bubble wall. Thus, the derefinement procedure is important in keeping the computational cost to a minimum. It is important to note that the derefinement procedure is only applied to regions where unnecessary high mesh resolution have been generated to improve simulation efficiency but not at the cost of accuracy. The process is also strictly conservative.

Due to the formulation of the axisymmetric code, the mass of each individual cell is a function of the radial distance from the plane of symmetry. Consequently, the movement

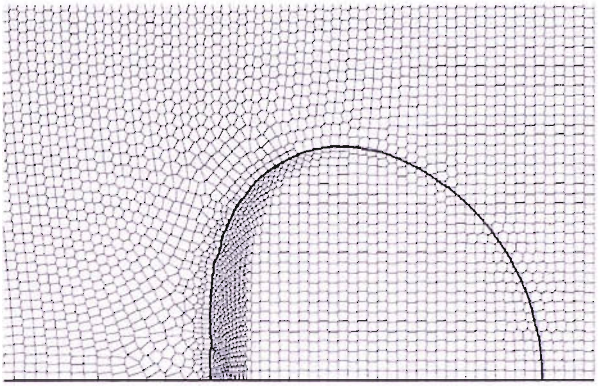

Figure 4.3: Voronoi mesh near an air/water interface. Thick solid line represents the material interface. The air/water interface location is only for plotting purposes as the actual location is determined by the boundaries shared between the air and water cells.

of particles from greater radial distance towards the symmetric line will cause grid expansion. This will coarsen the grid and degrade accuracy. The 'refinement' algorithm, which works in the opposite sense of the 'derefinement' scheme, would therefore bifurcate the coarse cell (parent particle) into two smaller cells (daughter particles). The properties of the former are then distributed conservatively to the daughter particles.

All particles inside the computational domain are eligible to be bifurcated or combined. However, it is important that these two procedures have negligible effect on the flow solutions at the time the procedure is carried out. It is also essential that the resulting grid structure permits a healthy and stable calculation. In the current work, the cells are bifurcated based on two criteria:

- a non-dimensional parameter, the '*characteristic length*', L_c
- the number of times the cell has previously been bifurcated.

The L_c of a target particle is the characteristic dimension of its *Voronoi* cell, which is based on the density of the cell, ρ, the mass associated with the cell, m, and the ordinate of the centroid in y-axis, r_e. This is approximately the length scale or distance between two particles. L_c is given by the following equation,

$$L_c = \sqrt{\left(\frac{m}{\rho \times r_e}\right)} \tag{4.36}$$

Cells are bifurcated when L_c of a target particle is twice that of its neighbouring cells. The second criteria is created in order to prevent particles from being over-bifurcated. A number is assigned to each particles in the computational domain to indicate the number of times each particle has been bifurcated. This number is incremented each time the particle is bifurcated but is limited to a certain value, specified at the beginning of the simulation. A typical value of 50 is used in the simulations of cavitation bubble collapse presented in Chapter 7 and 8.

In the $2D$ version of $Vucalm$, following the refinement procedure, each of the daughter particle has a mass that is half of that of the parent particle, i.e.,

$$m_{di} = m_p/2 \tag{4.37}$$

where m_d is the mass of daughter particle $i = 1, 2$, m_p is the mass of the parent particle. This is satisfactory for mesh construction using the weighted mesh method (see Section 4.4.2) because the common cell boundary shared between the daughter particles lies midway between them. However, this is not true in the axisymmetric version of the code. If the same approach is applied to the mesh in axisymmetric geometry, the common cell boundary of the two daughter particles will be formed closer to the particle that has a larger distance from the axis of symmetry. This is because the volume of each computational cell is a function of radial distance from the symmetry axis. This is a common problem especially near the axis of symmetry where the ratio of radii between the two daughter particles are large.

In order to generate a common boundary that is equal distance to the two daughter particles, the mass division of the parent particle is determined by taking into account the distance of the daughter particle from the symmetry axis, i.e.

$$m_{di} = m_p \times \frac{y_{di}}{y_{d1} + y_{d2}} \tag{4.38}$$

where y_{d1} and y_{d2} are the distance of the two daughter particles from the axis of symmetry. The refinement procedure is also essential as fine grid along the bubble boundary is crucial to maintain a smooth interface. Thus, efficient grid structure can be achieved by the use of localised grid refinement.

4.4.4 Material Interface Smoothing Algorithm

As explained in Section 4.1.3, material interfaces are resolve accurately in Free-Lagrange method. This is because the interfaces always coincide with mesh cell boundaries. However, the interfaces tend to wrinkle on a scale comparable to the mesh resolution and this wrinkle may grow when subjected to mesh-induced high wave-number instabilities. A simple smoothing algorithm is implemented in the $Vucalm$ code to counter this effect [49]. A modified version of the algorithm is used to control the interface wrinkling.

The interface smoothing algorithm is incorporated into the code formulation by adding a source term to the governing equations that acts as an artificial surface tension. This source term is only applied to particles which are in direct contact with a material interface. The force acting on these particles reduces both the amplitude and growth rate of small-scale perturbations.

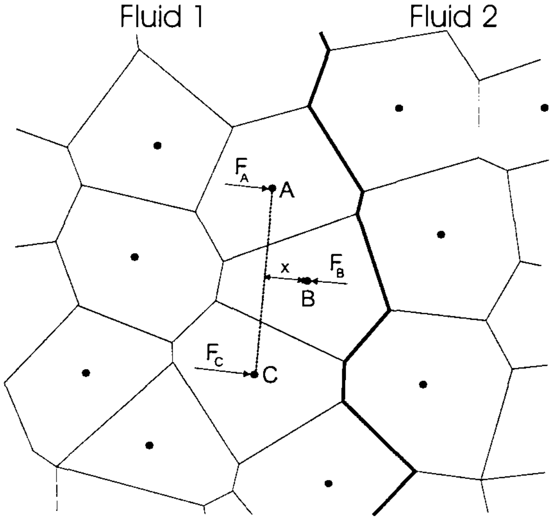

Figure 4.4: Close-up of the Voronoi mesh near an interface of two different fluid types showing irregularities on the interface. Dots represent fluid particles. Illustration of the interface smoothing algorithm construction.

The smoothing technique is illustrated in Fig. 4.4. The figure shows a close-up of the Voronoi cells of two dissimilar fluids in the proximity of the material interface. The dots represent the coordinates of the fluid particles while the material interface is represented by the thick solid line.

On each time step, all the particles on the interface are identified. For each particle, termed a 'target particle' (B), two neighbouring particles (A and C) on the interface and of the same fluid are identified. The normal displacement, x of the target particle from an imaginary line joining the interface neighbours $A \rightarrow C$ is determined. Restoring forces (F_a, F_b, F_c) that are normal to $A \rightarrow C$ are then applied to three particles so as to drive the displacement x towards zero.

The effect of the restoring forces is to shift the particles to form a straight line. These forces are applied to all eligible target particles and consequently help to reduce the amplitude of wrinkles in particle alignments adjacent to interfaces. The thick solid line in Fig. 4.4 shows that the material interface is defined by the boundary of the Voronoi cell between the particles of dissimilar fluids. Therefore, the effect of the applied restoring force to the target particles is indirect. However, it is apparent that when the interface particles of both fluids are arranged in a smooth fashion, then the interface itself will also be smooth.

The method implemented here is a simplified version of the technique described by Howell & Ball [49]. First consider a force of magnitude F_0 obtained from

$$F_0 = S_c \alpha x \tag{4.39}$$

where α is a gain specified by the user and S_c is a non-dimensional scaling factor given by

$$S_c = \frac{m\hat{L}_c}{\hat{m}L_c} \tag{4.40}$$

where m is the mass of the target particle, and L_c is the characteristic length defined earlier in section 4.4.3. The parameter $\hat{m}$ and $\hat{L}$ are similarly defined for a typical particle at the start of the simulation. In the original formulation [49], the restoring force was applied to only the target particle, i.e. $F_a = F_c = 0$ and $F_b = F_0$. This approach was effective but has an undesired side-effect of slightly increasing the pressure within bubbles. Hence, a new approach is taken where the restoring forces is distributed between the target particle and its interface neighbours such that $F_B = F_0/2$ and $F_A = F_B = F_0/4$. Using this formulation, the net restoring force on each particle at the interface is zero for a smooth circular bubble. The choice of smoothing gain α is based on user experience, and suitable values are found by running inexpensive trial simulations.

For the current work, test cases were carried out to find the optimum value of α for the shock/bubble interaction problem. The analysis and findings are described in Chapter 6.

4.4.5 Conclusion

The Lagrangian methodology, in which the mesh moves with the local flow velocity and offers minimum numerical diffusion, makes it and ideal and attractive method for simulating multi-phase and multi-material dynamics problems. The two-dimensional planar version of the code has been successfully used in the past to investigate a confined cylindrical blast wave [3], shock and blast attenuation by aqueous foam barriers [4], damping of mesh-induced errors in Free-Lagrange simulations of Richtmyer-Meshkov instability [49], high velocity impact of elastic-plastic materials [48] and the collapse of a cylindrical air cavity in water when impacted by a $1.9GPa$ shock wave [6]. These works have demonstrated the utility of Free-Lagrange method for unsteady multi-material flow.

Validation of the axisymmetric Free-Lagrange code, *Vucalm*, has been carried out and is presented in Chapter 6. Initial validation work has also been carried out on conical shock flows by Turangan [94].

Chapter 5

The Aeroacoustic Codes

5.1 Introduction

An important task of the research work is to investigate and evaluate the acoustic signature generated in the far-field during the shock-bubble interaction, which will then enable comparisons to be made with experimental data. Two aeroacoustic codes using the Kirchhoff's method and Ffowcs-Williams Hawkings formulation (see Chapter 3, were developed by the author.

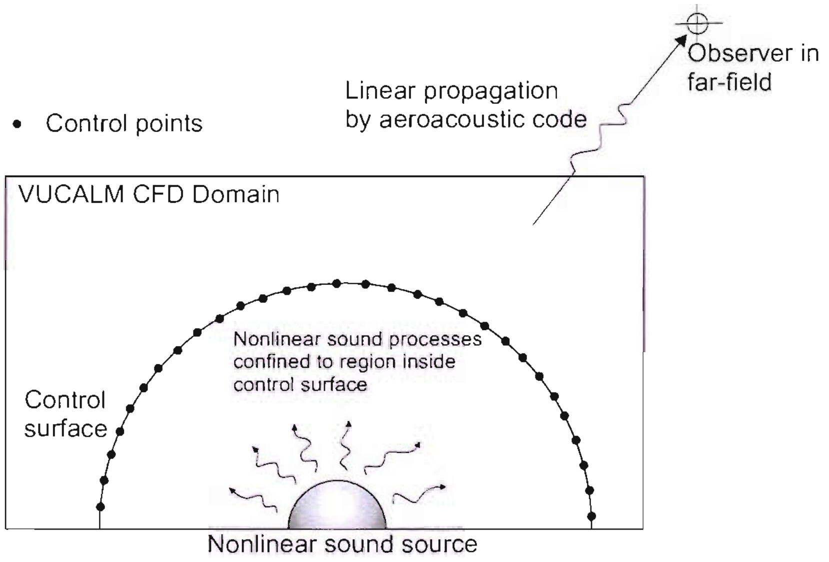

Figure 5.1: Schematic of *Vucalm* and aeroacoustic codes integration.

The integral formulations if the acoustic methods, allow the radiating sound to be evaluated based on quantities on an arbitrary near-field control surface that encloses all the near-field sources. The two aeroacoustic codes allow the observer[1] location to be anywhere outside the source region. Whereas, if the CFD *Vucalm* code is used for this task alone, a mesh must be constructed from the source to the observer. The cost involved and the errors incurred in long range propagation through the finite volume mesh make the technique an inappropriate choice for the far-field pressure computation. Therefore, calculation of the far-field acoustic signature is carried out by taking a surface integral. The numerical simulation using the main code *Vucalm* is used to evaluate the flow-field solution in the near field and thus on the control surface. This will then give enough information for the analytical calculation in the far-field (Fig. 5.1).

5.1.1 Kirchhoff's Method Formulation

The Kirchhoff formulation derived by Farassat & Myers [39] gives the far-field signature owing to sources contained within the Kirchhoff control surface.

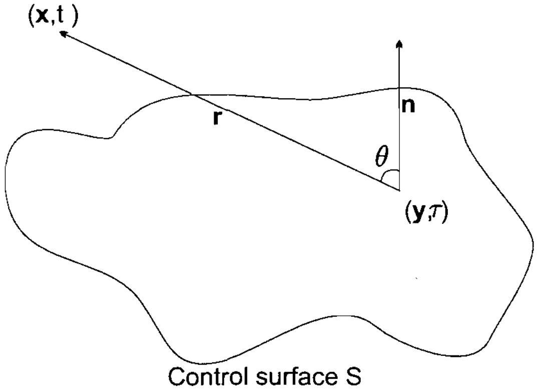

Figure 5.2: Kirchhoff's surface S and notation.

The classical Kirchhoff formulation for a stationary control surface S (Fig. 5.2) can be written as [66]

$$\Phi(\mathbf{x},t) = \frac{1}{4\pi}\int_S \left[\frac{\Phi}{r^2}\frac{\partial \mathbf{r}}{\partial \mathbf{n}} - \frac{1}{r}\frac{\partial \Phi}{\partial \mathbf{n}} + \frac{1}{cr}\frac{\partial \mathbf{r}}{\partial \mathbf{n}}\frac{\partial \Phi}{\partial \tau}\right]_\tau dS \tag{5.1}$$

where Φ is a quantity satisfying the wave equation (i.e. pressure disturbance, velocity potential) in the exterior of the surface S:

$$\frac{1}{c^2}\frac{\partial^2 \Phi}{\partial t^2} - \nabla^2 \Phi = 0 \tag{5.2}$$

---

[1] Point in the far-field at which the wave propagation from near-field sources are resolved.

Φ and its normal and time derivatives $\frac{\partial p}{\partial n}$, $\frac{\partial p}{\partial t}$ must be continuous outside surface S. c is the speed of sound at ambient conditions. In the formulation, it is assumed that the surface is not deformable (rigid) and that it encloses all the nonlinear effects and sound sources.

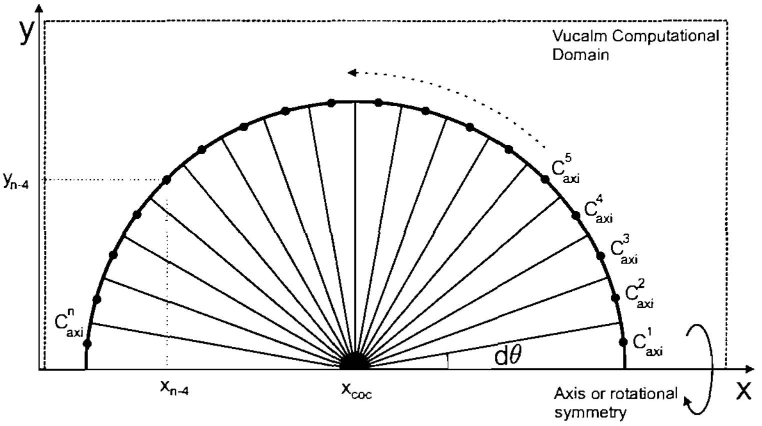

Figure 5.3: Kirchhoff's control points and the axisymmetric form of the problem.

The subscript τ indicates the evaluation of the integrands at the emission (retarded) time. This is given by,

$$\tau = t - \tau' = t - \frac{\mathbf{r}}{c} \tag{5.3}$$

where (x, t) and (y, τ) are the space-time variables of the observer and the source respectively, τ' is the wave propagation time to observer, $\mathbf{r} = \mathbf{x} - \mathbf{y}$ is the radiation vector, $r = |\mathbf{x} - \mathbf{y}|$ is the distance between the observer and the source, and θ is the angle between the normal vector on the surface $\mathbf{n}$ and the radiation vector $\mathbf{r}$. Equation (5.1) is an integral representation of Φ at points exterior to S in terms of information prescribed on the control surface S and can be used for the computation of acoustic pressure at an arbitrary point, if the solution is known on surface S.

The Kirchhoff scheme requires stored data for pressure and its derivatives on the control surface. Since Kirchhoff's method assumes that the linear wave equation is valid outside the closed control surface S, S must be chosen large enough to include the region of all non-linear behaviour. However, the accuracy of the numerical solution is limited to the region near the surrounding of the source because of the increase of mesh spacing further away from the source in CFD codes. Thus, a judicious choice of S is required for the effectiveness of the Kirchhoff method.

In the current work, the control surface that has been chosen is a sphere. The idea here is to incorporate the control surface in the *Vucalm* CFD solution in axisymmetric form. In axisymmetric form, the half-circumference as depicted in Fig. 5.3 is rotated about the axis of rotational symmetry, chosen here to be the x-axis, to give a spherical control surface and volume as depicted in Fig. 5.4.

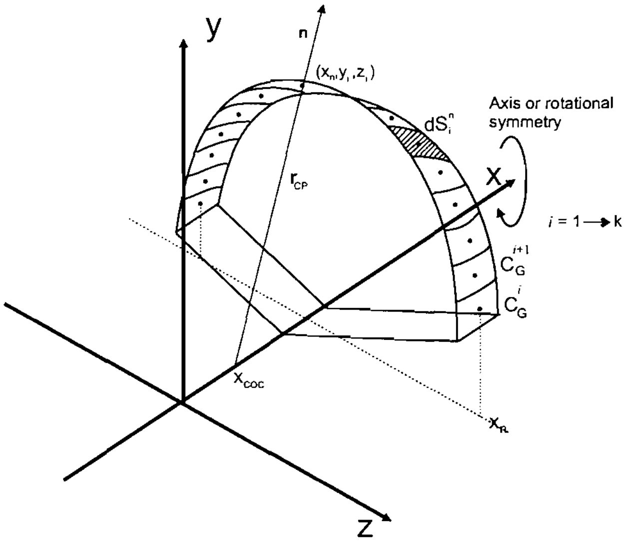

Figure 5.4: Kirchhoff's geometric control points.

Control points are distributed uniformly along the circumference of the circle, separated by a constant angle $d\theta$. During the *Vucalm* run, the pressure and its normal and time derivatives are evaluated at these control points (C^n_{axi}) by interpolation from neighbouring cell centres. This data is stored for subsequent post-processing by the Kirchhoff code. These stored data are then interpolated onto the geometric control points (C^i_G) (Eqn. 5.4), each with an elemental area dS^n_i and coordinates (x_n, y_i, z_i), where i is the number of control points in one symmetrical rotation (Fig. 5.3).

$$C^n_{axi}(x_n, y_n) = C_G^{i=1,k}(x_n, y_i, z_i) \tag{5.4}$$

The interpolation from the *Vucalm* particles to the control points is shown in Fig. 5.5. Three closest *Vucalm* particles of the same material, A, B and C to a control point P are determined by carrying out spatial search. Initially, the nearest particle is predetermined and two other particles are then selected to construct a triangle enclosing the control point. Following this, a linear interpolation is used between the three *Vucalm* particles and the flow properties at the control point is then calculated based on the flow gradient within the constructed triangle.

The Kirchhoff integral is then evaluated by summing the contribution of each geometric control points to obtain the pressure at an arbitrary point outside of the surface S.

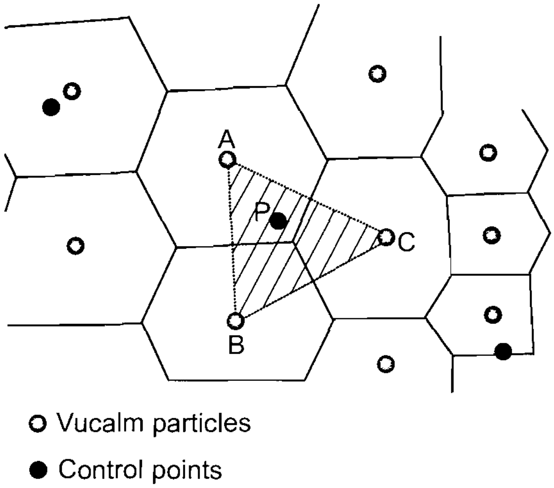

Figure 5.5: Interpolation from *Vucalm* mesh to the aeroacoustic control volume.

The normal unit vector at each control point is calculated using the following expression,

$$\mathbf{n}_{CP} = \left(\frac{x_n - x_{coc}}{R_{cs}}\right)\hat{i} + \left(\frac{y_i}{R_{cs}}\right)\hat{j} + \left(\frac{z_i}{R_{cs}}\right)\hat{k} = \frac{\mathbf{r}_{CP}}{R_{cs}} \tag{5.5}$$

where R_{cs} is the control surface radius and $\mathbf{r}_{CP}$ is the radial vector of each geometric control points (C^i_G).

5.1.2 Porous FWH Method Formulation

The FWH equation can be written as the following inhomogeneous wave equation in differential form [17],

$$\begin{aligned} \Box^2 p'(\mathbf{x},t) \; = \; & \frac{\partial^2}{\partial x_i x_j} T_{ij} H(f) \\ & - \frac{\partial}{\partial x_i}[P_{ij}\hat{n}_j + \rho u_i(u_n - v_n)]\delta(f) \\ & + \frac{\partial}{\partial t}[\rho_0 v_n + \rho(u_n - v_n)]\delta(f) \end{aligned} \tag{5.6}$$

where u_n is the fluid velocity in the direction normal to the control surface described by the equation $f(\mathbf{x},t) = 0$ and v_n is the surface velocity in the direction normal to the control surface. p' is the acoustic pressure, $p - p_0$ outside the source region. P_{ij} is the compressive stress tensor, which includes the surface pressure and the viscous stress. For an inviscid fluid, $P_{ij} = p'\delta_{ij}$, and δ_{ij} is the Kronecker delta. $T_{ij} = P_{ij} + \rho u_i u_j - c^2(\rho - \rho_0)\delta_{ij}$ is Lighthill's equivalent stress tensor. If the perturbations is small, the term $c^2(\rho - \rho_0)$ can be replaced by p'. Ambient quantities are indicated by the subscript 0, while the vector and tensor have indices i and j. A dot symbol indicates source-time differentiation. $H(f)$ is the Heaviside function which is unity for $f > 0$ and zero for $f < 0$.

It is important to note that because the control surface is taken to be permeable and fictitious, the fluid flow across the surface S has to be considered. The flow can be due to fluid perturbation velocity ($u_n \neq 0$), and to the motion of the surface ($v_n \neq 0$), with the net flow being $u_n - v_n$. In the classical formulation, this term disappears because of the non-penetration condition across the control surface. The $\Box^2$ is the wave operator, $[(1/c^2)(\partial^2/\partial t^2)] - \nabla^2$.

Equation 5.6 above is the appropriate form of the FWH equation from which to develop an integral representation that is easier to implement. A full derivation is given in References [17, 34, 40]. The mathematical manipulation can be greatly simplified by defining the variables U_i and L_i as used by di Francescantonio [34], given by,

$$U_i = [1 - (\rho/\rho_0)]v_i + (\rho u_i/\rho_0) \tag{5.7}$$

and

$$L_i = P_{ij}\hat{n}_j + \rho u_i(u_n - v_n) \tag{5.8}$$

Hence, using these definitions, the FWH equation as given by Equation 5.6 may be written as,

$$\Box^2 p'(\mathbf{x},t) = \frac{\partial^2}{\partial x_i \partial x_j}[T_{ij}H(f)] - \frac{\partial}{\partial x_i}[L_i\delta(f)] + \frac{\partial}{\partial t}[(\rho_0 U_n)\delta(f)] \tag{5.9}$$

The contribution of the Lighthill stress tensor, T_{ij} is the strength density of acoustic quadrupoles distributed throughout the region exterior to the control surface S.

The dipole term, L_i involves an unsteady force, and U_i gives rise to a monopole-type contribution that can be thought of as unsteady mass addition. di Francescantonio [34] interpreted the terms L_i and U_i as a modified velocity and a modified stress tensor respectively. Equation 5.9 is particularly useful because it can be utilised directly to write an integral representation of the solution as follows,

$$p'(\mathbf{x},t) = p'_T(\mathbf{x},t) + p'_L(\mathbf{x},t) + p'_Q(\mathbf{x},t) \tag{5.10}$$

where the subscript T, L and Q represent the thickness, loading and quadrupole sources respectively and can be written as Equation 5.11 and 5.12 below.

$$\begin{aligned} 4\pi p'_T(\mathbf{x},t) &= \int_{f=0} \left[\frac{\rho_0(\dot{U}_n + U_{\dot{n}})}{r(1-M_r)^2}\right]_\tau dS \\ &+ \int_{f=0} \left[\frac{\rho_0 U_n (r\dot{M}_r + c(M_r - M^2))}{r^2(1-M_r)^3}\right]_\tau dS \end{aligned} \tag{5.11}$$

$$\begin{aligned} 4\pi p'_L(\mathbf{x},t) &= \frac{1}{c}\int_{f=0} \left[\frac{\dot{L}_r}{r(1-M_r)^2}\right]_\tau dS \\ &+ \int_{f=0} \left[\frac{L_r - L_M}{r^2(1-M_r)^2}\right]_\tau dS \\ &+ \frac{1}{c}\int_{f=0} \left[\frac{L_r(r\dot{M}_r + c(M_r - M^2))}{r^2(1-M_r)^3}\right]_\tau dS \end{aligned} \tag{5.12}$$

$p'_Q(\mathbf{x},t)$ can be determined by any method that is currently available. The derivation of Equation 5.11 and 5.12 is given in [40]. $L_M = LiM_i$ and a subscript r or n indicates a dot product of the vector with the unit vector in the radiation direction $\hat{\mathbf{r}}$ or the unit vector in the surface normal direction $\hat{\mathbf{n}}$ respectively.

Equation 5.9-5.12 above was derived directly from the equations of conservation of mass and momentum. Therefore, it could be applied to an arbitrary surface whether or not the propagation is linear outside the control surface. If the surface S is to be placed on the body of a source that is impenetrable, the classical FWH formulation is obtained where the non-linear wave propagation is taken into account by the quadrupole volume terms. As the surface is moved further away from the source, part of the nonlinearity is taken into account by the quadrupole terms and part by the surface integrals. If the surface is far enough away, the Lighthill stress tensor outside S can be neglected as given in Equation 5.11 and 5.12 above, so that $p'_Q = 0$.

A stationary control surface is used in the current work and therefore $U_{\dot{n}} = M = M_r = \dot{M}_r = L_M = 0$. Therefore, Equation 5.11 and 5.12 can be simplified further as shown in Equation 5.13-5.15 respectively.

$$4\pi p'_T(\mathbf{x},t) = \int_{f=0} \left[\frac{\rho_0 \dot{U}_n}{r}\right]_\tau dS \tag{5.13}$$

$$4\pi p'_L(\mathbf{x},t) = \frac{1}{c}\int_{f=0} \left[\frac{\dot{L}_r}{r}\right]_\tau dS + \int_{f=0} \left[\frac{L_r}{r^2}\right]_\tau dS \tag{5.14}$$

Therefore,

$$p'(\mathbf{x},t) = \frac{1}{4\pi}\Big\{ \int \Big[\frac{\rho_0 \dot{U}_n}{r}\Big] dS + \frac{1}{c}\int \Big[\frac{\dot{L}_r}{r}\Big] dS + \int \Big[\frac{L_r}{r^2}\Big] dS\Big\} \tag{5.15}$$

where

$$U_i = \rho u_i / \rho_0 \tag{5.16}$$

and

$$L_i = P_{ij}\hat{n}_j + \rho u_i u_n \tag{5.17}$$

The porous FWH method is applied on the Kirchhoff-type surface and therefore, the same discretisation technique and control surface geometry as discussed in section 5.1.1 is implemented here.

5.1.3 Retarded-time Algorithms

The interpretation of Equation 5.1 and 5.15 above is that the integration occurs over the physical surface with the integrand evaluated at the emission, or retarded time as that recorded in the *Vucalm* calculation. The formulation requires that the observer time t and location $\mathbf{x}$ are fixed during the evaluation of the integral. Because retarded time formulation is utilised, temporal interpolation of the input data is required. A time history of the variables, p' and its derivatives for the Kirchhoff method and p', ρ and $\mathbf{u}$ for the FWH, are developed by choosing both the observer position and the observer time, evaluating the surface integrals and then step to the next observer time in the time history.

Hence, in the CFD numerical simulation, the input data is expediently evaluated at the control points by spatial interpolation at the source time. At the end of the CFD simulation, a time history of the required data are stored and utilised in the aeroacoustic codes. A time increment of the observer time is specified by the user and the upper and lower integral limit are calculated based on the duration of the recorded CFD data. Following this, a temporal interpolation of the data to the retarded time τ at each location in the input data are performed. The retarded time for each control point is simply the difference between the observer time t and the wave radiation time from the corresponding control point to the observer. Interpolation in time is necessary so that the contributions from all control points can be added together at the same observer time. A simple linear interpolation is used to determine the value of the near-field data at the retarded time.

5.1.4 Conclusion

Both the above formulations provide a Kirchhoff like formulation if the quadrupoles outside the control surface ($p'_Q(\mathbf{x}, t)$) are ignored. The two methods work well, and therefore deciding which method to use for a particular application can be difficult. The FWH requires the storage of (ρ, p' and ρu_i) for each control point, while ($p, \partial p/\partial n$ and $\partial p/\partial t$) are required by Kirchhoff. The Kirchhoff method is simpler, and easier to implement. Also, the porous FWH method allows for nonlinearities on the control surface, whereas the Kirchhoff method assumes a solution of the linear wave equation on the surface S. Thus if the CFD solution does not satisfy the linear wave equation on the control surface the results from the Kirchhoff method change dramatically. This leads to a higher sensitivity for the choice of the control surface for the Kirchhoff method. The solution of the FWH equation requires a surface and a volume integral, but the solution is often well approximated by the surface integral alone. Furthermore, according to Brentner [17], the solution is less sensitive to placement of the control surface even if the quadrupole volume term is neglected. In summary, the Kirchhoff method puts more stringent requirements on the CFD method to reach to the linear acoustic field. Validations for both formulations are given in the next chapter and, along with the *Vucalm* CFD calculation, both methods are used in the current work to predict the far-field pressure signature from the shock/bubble interaction.

Chapter 6

Code Validations

In this chapter, validation of the Free-Lagrange code, *Vucalm*, is presented in order to show the ability of the code to solve flow problems in axisymmetric form as well as multi-phase flows. The validation was performed by carrying out two numerical simulations involving multi-phase flows. The two problems are

- axisymmetric shock-induced collapse of a spherical air bubble by a planar step shock (Ding and Graceswki [35])
- $2D$ planar shock interaction with a water column (Igra and Takayama [52])

These studies are attractive because the simulations using *Vucalm* can be compared with published axisymmetric numerical simulations and experimental findings. The two-dimensional form of the *Vucalm* code has been validated and implemented to perform various numerical flow problems in the past. However, the code was recently converted to an axisymmetric form by Turangan [94], and although validation was carried out in his work, comparisons were only made with that of single phase flows involving conical shock waves. Thus, further validation of the axisymmetric version of the *Vucalm* code is necessary. Both published works mentioned above are ideal as they involve multi-phase flows problems of air and water, as well as shock waves, and therefore relate directly to the work carried out here. Although the second validation work mentioned above is a 2-dimensional problem, the results are nevertheless useful as direct comparison can be made with experimental results.

Validation work for the Kirchhoff and Ffowcs Williams-Hawkings aeroacoustic codes are also presented in this chapter. The problem that has been chosen for the validation of the aeroacoustic codes involves predicting the acoustic pressure in the far-field, radiated by a rigid pulsator.

6.1 Introduction - The numerical work of Ding and Gracewski

Ding and Gracewski [35] performed an Arbitrary Lagrangian Eulerian (ALE) simulation of axisymmetric, inviscid, compressible flow for air bubble/shock interactions with both weak shocks ($P < 30\,MPa$) and strong shocks ($500 < P < 2000\,MPa$). The use of ALE combines the advantages of both the Lagrangian and Eulerian methods (refer to section 3.1.2 in Chapter 3). The numerical work solves the Euler equations in axisymmetric cylindrical coordinates using a finite volume method to investigate the response of an air bubble to a step shock wave. To capture the shock, an artificial viscosity technique is implemented. The bubble is initially spherical and is statically in equilibrium with the surrounding liquid. Compressibility of the fluid is taken into account and the model also assumes an adiabatic process except within the shock front. It neglects any diffusion between the air bubble and the surrounding fluid. The artificial viscosity method introduces a dissipative term in the shock front. Body forces, surface tension and shear viscosity are also neglected.

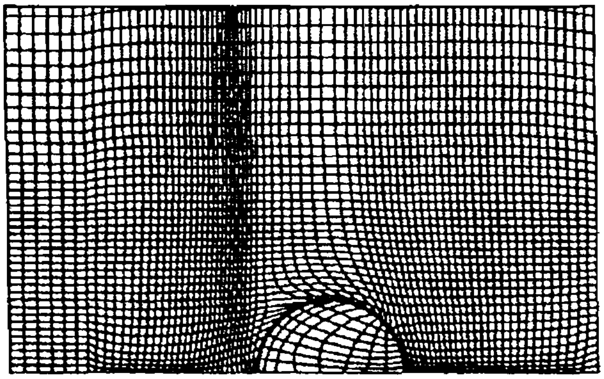

Figure 6.1: Computational mesh (ALE). The initial bubble radius is $1.0\,mm$. The highly compressed mesh indicates the position of the planar incident shock. (Ding and Gracewski 1996).

A non-uniform rectangular mesh (Fig. 6.1) is used. The mesh motion involves a weighting method, where the mesh size is adapted using the pressure gradient in order to generate finer meshes near the shock front and around the air bubble. This was desirable owing to the large deformation involved in the proximity of the bubble, and also to define the shock front by a thin layer in the computational mesh. Also, starting approximately 24 meshes from the bubble centre, the mesh size increases with a ratio of 1.05 farther away from the bubble. In the computational domain a total of 80 x 160 cells are used. The mesh design uses less computational time than uniform cells and maintains a good resolution near the air bubble. In the numerical work of Ding and Graceswki, the computation had to be stopped at the moment of jet impact as the cells within the air bubble were too small, and the time step became unacceptably small. Thus, comparisons could not be made for numerical results beyond the point of jet impact. Ding and Gracewski set the initial thermodynamic properties to ISA sea level conditions.

6.1.1 Problem Specification

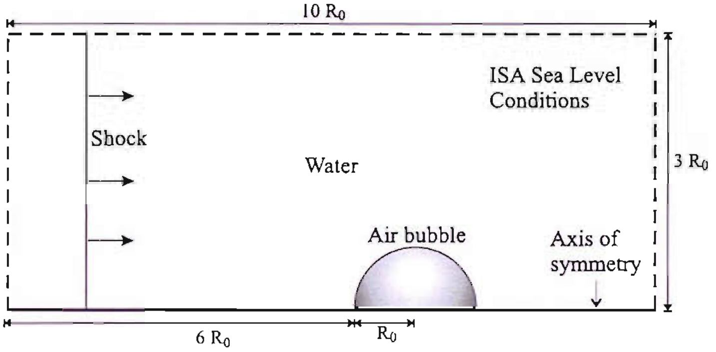

Figure 6.2: The Geometry of the Ding and Graceswki problem. R_0 is the initial bubble radius. Not to scale.

The problem studied in the present code validation work is illustrated in Fig. 6.2. As stated earlier, this problem has been selected to match, as far as is practicable, the numerical simulations carried out by Ding and Gracewski [35]. Nine strong shock wave cases are studied, with initial bubble radius of $0.1\,mm$, $1.0\,mm$ and $10\,mm$, imploded by a shock of strength $0.528\,GPa$, $1.011\,GPa$ and $2.06\,GPa$. The tenth case is the weak shock problem where the shock strength is $0.0205\,GPa$ and the initial bubble radius is $0.1\,mm$. The various cases are summarized in Table 6.1. Attention will be focused on the simulation where the air bubble initial radius is $0.1\,mm$ and shock strength of $0.528\,GPa$. Fig. 6.2 above shows the geometry of the computational domain used for the simulation. A spherical air bubble, having one of the various sizes mentioned earlier, is immersed in water at ISA sea level conditions. The initial density and pressure of the air are $1.2246\,kgm^{-3}$ and $10^5\,Pa$ respectively. The shock wave propagates through the water from left to right as shown; all elapsed times are measured from the first shock/bubble contact unless stated otherwise. The bottom domain boundary represents the axis of symmetry.

Boundary conditions on the left boundary are initially fixed at post-shock values in order to generate the incoming shock wave. However, from time $t = 1.5\,\mu s$ onwards, non-

Case	Initial Radius, R_0 (mm)	Shock Strength, P (GPa)	Post-shock density, ρ (kgm^{-3})	Post-shock velocity, u (ms^{-1})
1	0.1	0.528	1146	259
2	0.1	1.011	1221	428
3	0.1	2.060	1326	712
4	1.0	0.528	1146	259
5	1.0	1.011	1221	428
6	1.0	2.060	1326	712
7	10.0	0.528	1146	259
8	10.0	1.011	1221	428
9	10.0	2.060	1326	712
10	0.1	0.0205	1009	13

Table 6.1: Various cases of shock bubble interaction problems

reflecting boundary conditions are applied in order to allow the escape of left-running waves which are generated by the shock/bubble interaction. In this simulation, the size of the domain was large enough such that the numerical simulation was stopped before the left-coming wave reaches the left boundary. Because the mesh is moving at the same local velocity as the flow (as defined by the Lagrangian principle), particles on the left domain will tend to move away from the boundary, leaving a gap that will cause volumetric errors and mesh problems. To resolve this, uniform columns of particles with post shock conditions are introduced along the left boundary when needed. The upper and right boundaries are non-reflecting at all times. For a shock with $P = 0.528\,GPa$, the inflow velocity is $259.26\,ms^{-1}$. For a shock strength $P = 1.011\,GPa$, it is $428.26\,ms^{-1}$ and for $P = 2.06\,GPa$, the speed is $711.94\,ms^{-1}$. A mesh of approximately 19×10^3 cells has been used; in the initial (unperturbed) mesh the individual cells are annuli of square cross-section for convenience.

6.1.2 Strong Shock Problems

Fig. 6.3(a) and (b) show Mach contours for the numerical results of Case 4 using ALE and Free-Lagrange methods respectively. Time $t = 0$ shows the point at which the shock had just impacted the gas cavity, and the top cavity wall experienced a high-momentum impact with a speed of about $500\,ms^{-1}$. The maximum Mach contour has been set at 0.21 in accordance with the contouring plot of Ding and Gracewski, i.e. contours of Mach greater than 0.21 are not plotted. At the initial conditions, the acoustic impedance of water is approximately 3600 times that of air. As a consequent, as the incident water shock (A) strikes the upstream bubble wall, a relatively weak shock is transmitted into the

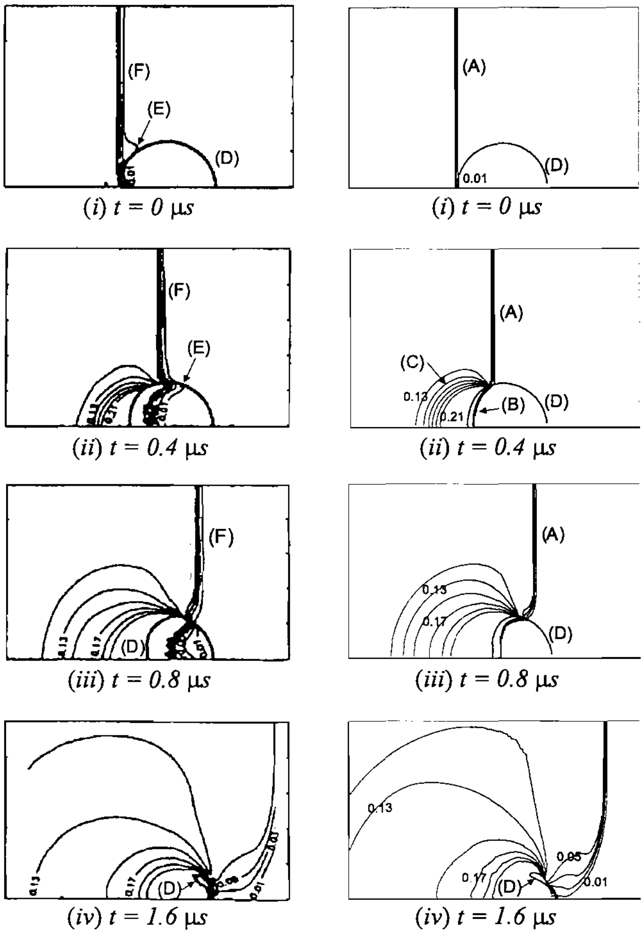

(a) Ding and Graceswki (*ALE*) (b) *Vucalm* (*Free-Lagrange*)

Figure 6.3: Mach contours of a bubble, $R_0 = 1\,mm$, collapsed by a shock $P = 0.528\,GPa$. Comparison between: **(a)** *Ding & Graceswki*, **(b)** *Vucalm*. Labels (A)-(F) are described in the text.

air cavity (B), and a strong expansion wave is produced in the water, running upwards and leftwards (C). The particle velocity behind the expansion wave is large, causing the upstream bubble wall to deform (D).

Although the two simulations are generally in good agreement, there are minor discrepancies. If the results of Ding and Gracewski are examined carefully, it can be seen that there is unphysical behaviour in the simulation attributable to the mesh structure. Owing to the difference in acoustic impedance, and the sound speed in air and water, the weak air shock propagates more slowly and should decouple from the incident shock (Fig. 6.3(ii)). However, the ALE simulation shows localised unphysical behaviour in that the air shock develops a numerical precursor (E) at the bubble boundary which advances ahead of the incident shock (F). The poor local mesh resolution inside the bubble in the Ding and Graceswki's problem contributed to unphysical behaviour. A reasonable good mesh resolution in the bubble is important to capture the shock and the flow of the air inside the bubble as it plays a part in dictating the collapse rate and direction of the bubble wall. Shock resolution is generally better in the Free-Lagrange result, particularly within the bubble, where compression of the Lagrangian mesh leads to "natural" refinement (see Chapter 4, section 4.4.3).

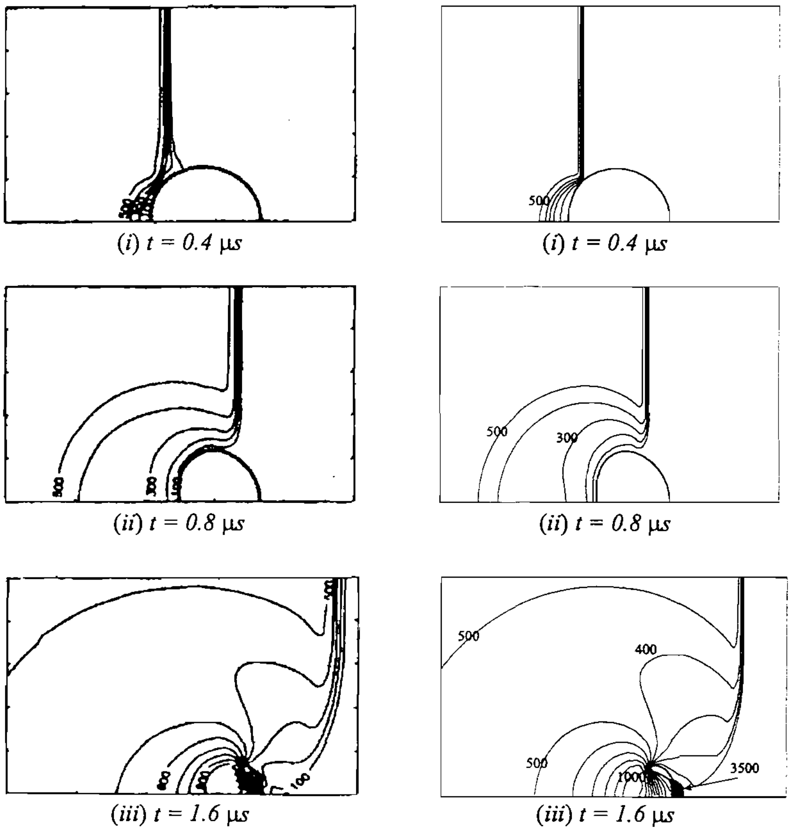

(*i*) t = 0.4 μs (*i*) t = 0.4 μs

(*ii*) t = 0.8 μs (*ii*) t = 0.8 μs

(*iii*) t = 1.6 μs (*iii*) t = 1.6 μs

(a) Ding and Graceswki (ALE) (b) *Vucalm* (Free-Lagrange)

Figure 6.4: Pressure contours of a bubble, $R_0 = 1\,mm$, collapsed by a shock $P = 0.528\,GPa$. Comparison between: **(a)** *Ding & Graceswki*, **(b)** *Vucalm*.

Fig. 6.4 shows the pressure contours for Case 4. At $t = 0$, the shock front reaches the upstream of the air bubble. Fig. 6.4(i) onwards show the expansion wave as the shock is reflected at the air/water interface. The spatially non-uniform deformation of the bubble wall yields a higher water velocity on the bubble centreline. At $t = 0.8\,\mu s$, (Fig. 6.4(ii)) the incident water shock has traversed almost the full bubble width. At this moment, the upstream interface is being forced into the bubble. The interaction between the shock and the expansion waves originating at the bubble surface has resulted in significant weakening and curvature of the shock. The pressure gradient in the water near the upstream of the bubble increases as time progresses.

It can be seen that as the rarefaction wave spreads away from the air bubble, the pressure gradients drive the water particles to flow toward the bubble. The shock front or flow velocity meets the upstream of the bubble wall frontally, and therefore the momentum transfer is maximum. However, owing to the interaction of the rarefaction wave and the incident shock, the resultant momentum transfer is weaker near the right and downstream part of the bubble. Furthermore, the shock front now meets the rest of the bubble boundary at an angle, and therefore the impact is weaker than that experienced at the upstream of the bubble wall. These effects result in the asymmetric movement of the bubble wall where the upstream part of the bubble interface moves rapidly, while the downstream bubble wall remains static.

A distinct liquid jet is formed which runs rightwards along the symmetry axis. At $t = 1.6\,\mu s$, the liquid jet has penetrated through the bubble, isolating a lobe of trapped and highly compressed gas which form a toroid in three dimensions (Fig. 6.4(*iii*)). The jet velocity reaches its highest value near the point of impact (Fig. 6.7(i)), where it acquires a velocity of about $2250\,ms^{-1}$, which is in good agreement with the value of $2200\,ms^{-1}$ measured by Ding and Gracewski. The liquid-liquid impact produces an intense blast wave in the surrounding water with an initial peak overpressure exceeding $3.5\,GPa$. It is clear from these frames that the downstream bubble wall remains stationary throughout the collapse until hit by the jet. The results of Ding and Graceswki agree well with the *Vucalm* simulation in terms of the general pattern of rarefaction and shock waves,

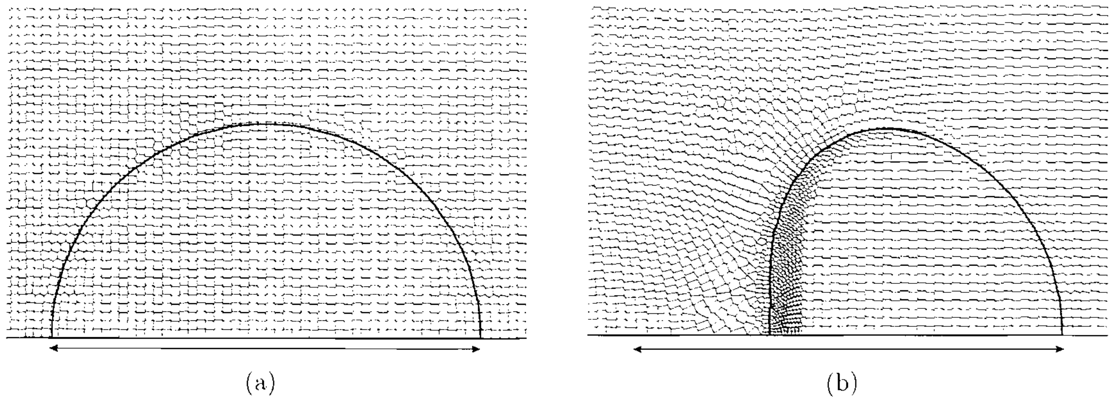
(a) (b)

Figure 6.5: Shock/cavity interaction, $R_0 = 1\,mm$, (a) $t = 0.0\,ms$ (b) $t = 1.0\,ms$. Close-up of Free-Lagrange Voronoi mesh. Heavy line is cavity boundary; dots indicate positions of 'particles' at which flow properties are stored. Horizontal arrow indicates initial position and size of bubble.

although evaluation is difficult to make due to the low resolution of the frames taken from reference [35]. A slight disparity can be seen in the last frame of Fig. 6.4. In the results obtained using *Vucalm*, the jet has penetrated through the downstream cavity wall, producing a blast wave due to liquid-liquid impact. In Fig. 6.4$a(iii)$, no blast wave from the liquid-liquid impact is present, assuming that the jet is at the point of impact, though this disparity is still questionable due the low picture quality. Overall, the dynamics of the bubble and surrounding fluid from both numerical methods are in good agreement.

The structure of the computational mesh in the vicinity of the bubble at $t = 0\,\mu s$ and $t = 1\,\mu s$ is shown in Fig. 6.5(a) and Fig. 6.5(b) respectively. The particle distribution of the Voronoi grid reflects the local density variation[1]. For high density regions, the grid is at its finest and so the flow structure is well resolved. Fig. 6.5(b) shows the increase in mesh density within the cavity behind the air shock, mirroring the increase in air density. However to maintain a stable and economical time step, the adaptive mesh 'refinement' and 'derefinement' algorithm are implemented. Fig. 6.5 also shows the alignment of mesh cells along the bubble boundary as a result of the action of the interface smoothing routine, which acts as an artificial surface tension. A more detailed description of this routine is given in Ref. [49].

In this validation work, the cells are bifurcated based on the non-dimensional '*characteristic length*', L_c. In the present work, the following criteria must be satisfied for refinement to take place,

- Criterion 1: Only cells along the air/water interface are bifurcated if the L_c of a particle is at least twice the size of any of its *Voronoi* neighbours.

Ding and Graceswki's employed an adaptive mesh generation technique, where the mesh automatically adapted to the pressure gradient. Therefore, the meshes at the shock front and the region around the bubble are finer because the pressure gradients are higher. However, they reported that their ALE calculation was halted at jet impact due to deteriorating mesh structure in the bubble, leading to an unacceptably small timestep. In our work, a 'derefinement' procedure has allowed the simulation to run beyond jet impact, while maintaining an acceptable timestep (Fig. 6.6).

The liquid jet impact on the downstream bubble wall produces an intense blast wave in the surrounding water with an initial peak overpressure exceeding $3.5\,GPa$. The shape of the blast wave is highly asymmetric (Fig. 6.6(a)) as the wave advances relatively slowly to the left because of the high water velocity of the liquid jet. At $t = 4.65\,\mu s$ (Fig. 6.6(b)), the cavity is drawn into a vortex flow, created from the interaction of the high velocity liquid jet and the relatively static surrounding fluid.

---

[1] This is only true is there is no refinement or derefinement.

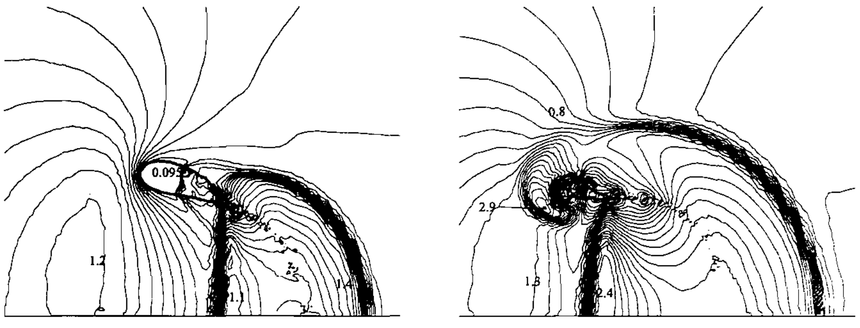

(a) $t = 4.58\,\mu s$

(b) $t = 4.65\,\mu s$

Figure 6.6: Dynamics of the flow beyond jet impact at $t = 1.6\,\mu s$. $\Delta P_{water} = 0.1\,GPa$, $\Delta P_{air} = 0.050\,GPa$. The thick line represents the bubble interface.

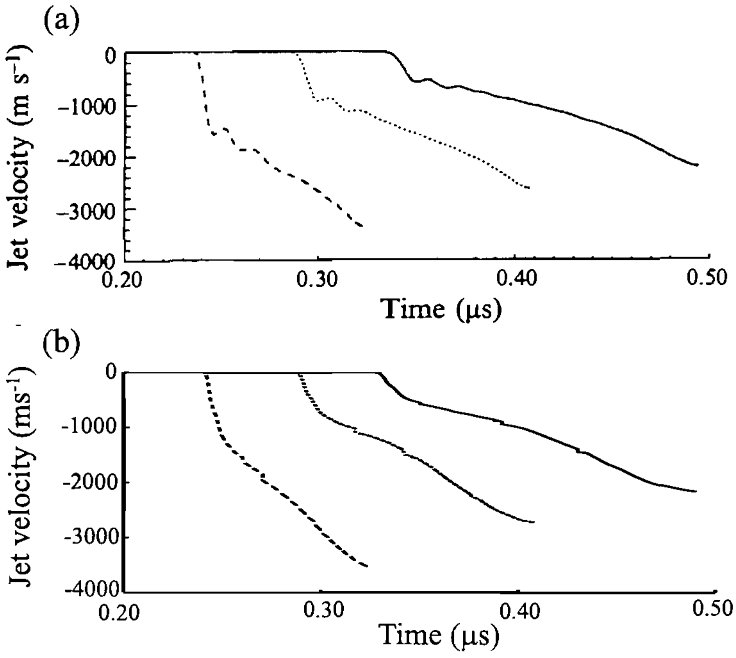

Figure 6.7: The velocities of the jet tip for $R_0 = 0.1\,mm$. The solid line represent velocities with $P = 0.528\,GPa$. The doted curve represent velocities with $P = 1.011\,GPa$. The dashed curves represent velocities with $P = 2.06\,GPa$. (a) Ding and Gracewski (b) *Vucalm*.

Numerical simulations were also carried out for the various other cases listed in Table 6.1. The results obtained by Ding and Gracewski and those using *Vucalm* are given below (Fig. 6.7 - Fig. 6.9(a) and (b) respectively), which show the variation of the jet tip velocity with time. The jet tip velocity using the *Vucalm* code was measured by taking the average of the absolute velocity of particles at the tip of the jet. The kinks on the curve are due to the derefinement and refinement algorithm. When particles are combined

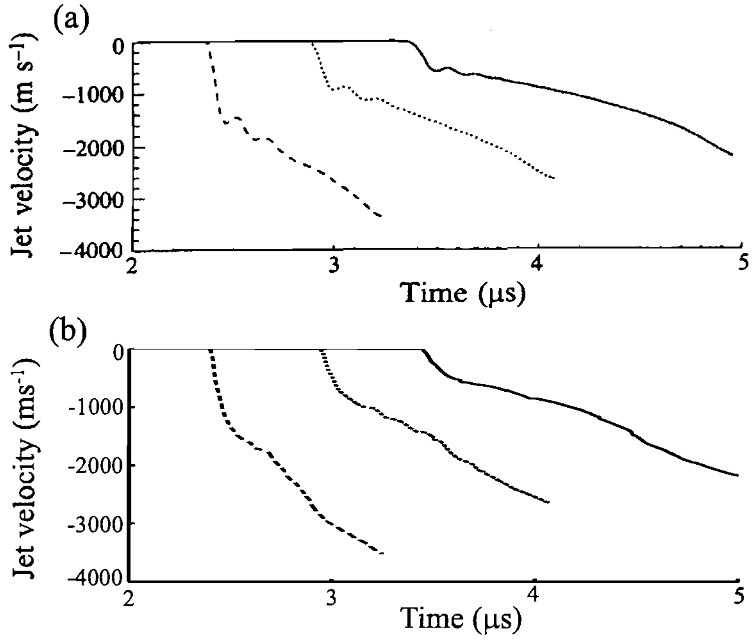

Figure 6.8: The velocities of the jet tip for $R_0 = 1.0\,mm$. The solid line represent velocities with $P = 0.528\,GPa$. The doted curve represent velocities with $P = 1.011\,GPa$. The dashed curves represent velocities with $P = 2.06\,GPa$. (a) Ding and Gracewski (b) *Vucalm*.

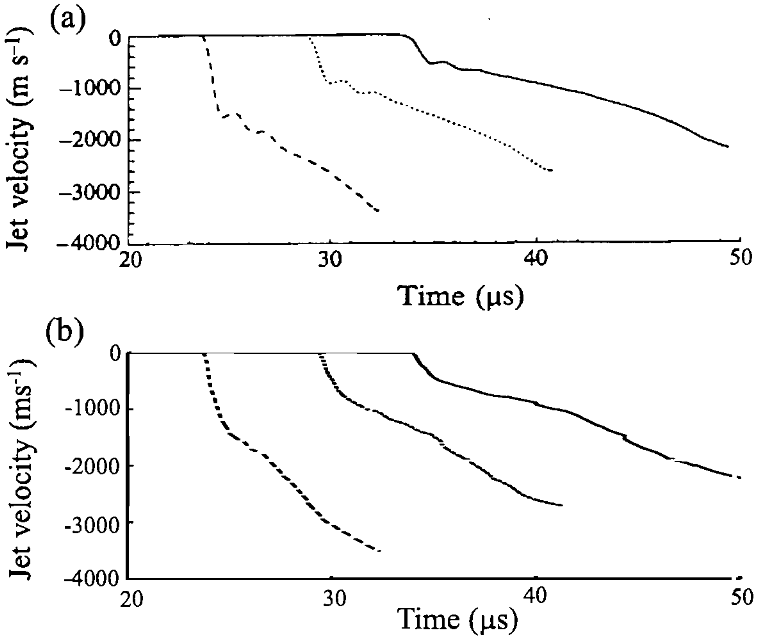

Figure 6.9: The velocities of the jet tip for $R_0 = 10.0\,mm$. The solid lines represent velocities with $P = 0.528\,GPa$. The doted curve represent velocities with $P = 1.011\,GPa$. The dashed curves represent velocities with $P = 2.06\,GPa$. (a) Ding and Gracewski (b) *Vucalm*.

or divided, a new set of particles near the jet tip are chosen for the calculation of the absolute velocity. The averaging of the absolute velocity of the new set of particles give rise to the kinks on the curves in Fig. 6.7(b), Fig. 6.9(b) and Fig. 6.8(b). However, Ding and Gracewski did not give any explanation on the way the jet velocities are measured in their numerical simulation. It is impossible to tell the point or region at which the jet velocities are taken - whether it is directly at the tip or somewhere in the proximity of the tip of the high-velocity liquid jet. Nevertheless, the results show good agreement as shown in Fig. 6.7 (Cases 1 – 3), Fig. 6.8 (Cases 4 – 6) and Fig. 6.9 (Cases 7 – 9).

Slight disparity can be seen during the first few microseconds after the point of shock impact. In the results obtained by Ding and Gracewski, the variation of the jet velocity with time show an oscillating feature which is not present in the results obtained from *Vucalm*. The numerical results by Ding and Graceswki and *Vucalm* (Fig. 6.7-Fig. 6.9) suggest that for a given shock strength, the liquid jet velocity time history is almost identical, independent of the initial bubble size. This is expected as the shock wave has a step profile and has no physical length scale. Therefore, although the results are not shown here, regardless of the size of the bubble, the general pattern of the pressure and velocity field are similar to that shown for Case 4 (of Table 6.1) as given in Figure 6.3 and Figure 6.4. The argument also holds for the jet velocity time histories which are identical for all three bubble sizes. The only difference is in the time scale, which increases proportionally to the increase in the bubble size. The figures also show that the jet speed is dependent on the applied shock strength. In addition, the maximum jet velocity achieved upon liquid-liquid impact of the liquid jet with the downstream bubble wall increases with increasing shock strength. The stronger the applied shock, the greater the jet speed, and the sooner the air bubble collapses.

In the experimental work conducted by Bourne and Field [15], they showed that the liquid jet velocity increases as cavity diameters are reduced (given that a particular incident shock pressure is held constant). However, it should be noted that the experiments conducted were in two-dimensional geometries (refer to Section 2.3.1). The spherical geometry of the air bubble in both numerical works, *Vucalm* and that of Ding and Graceswki, transmits a focussing air shock into the bubble and an expansion fan which decreases in strength as it propagates spherically away from the bubble. Although focusing of the shock waves still occur in $2D$, the focussing effects are stronger in three-dimensional geometry.

According to Hammitt [45], the 'real-fluid' effects, in probable order of importance from the viewpoint of bubble collapse, are thermal effects, liquid compressibility, viscosity, and surface tension. Heat transfer has been neglected in both methods. Consequently, the numerical code does not consider effectively the restraints upon bubble collapse imposed by changes in internal pressure due to heat-transfer. However, the collapse occurs in the order of microseconds and hence the effect of heat transfer can be considered negligible. The results using *Vucalm* do show that the rate of increase of the jet velocity decreases with time as the bubble becomes highly compressed, resulting in increases in internal pressure and temperature. Liquid compressibility is considered in both the ALE and the Free-Lagrange codes. The compressibility effect is important in this study, as it involves the interaction of the air bubble with very strong shock waves and the generation of very intense blast wave from the liquid jet impact on the downstream wall. Furthermore, a fraction of the energy of the bubble motion is radiated away as pressure waves. The effect of viscosity becomes important for relatively small bubbles and it is clear that it must, at least to some extent, reduce the rates of growth or collapse compared to those attained in an inviscid liquid. Viscosity has a damping effect and provides a mechanism for the conversion of mechanical energy to thermal energy. Viscous effects do alter the pressure at the bubble wall and thus reduce the effective pressure differential in such a way as to reduce rates of either growth or collapse. In view of the dominant influence of water inertia on the flow dynamics, it seems unlikely that viscosity and surface tension will play a major role. In addition, the short time scale of the whole collapse process suggest that inter-phase mass transfer will be unimportant.

6.1.3 Weak Shock Problem

The results of Ding and Graceswki, and from *Vucalm*, for the interaction of a spherical bubble with a weak shock are presented in Fig. 6.10(a) and (b) respectively. The initial density is $1000\,kgm^{-3}$ in water and $1.2\,kgm^{-3}$ in air. Both the initial pressure and temperature are at ISA sea level conditions. The initial radius of the bubble is $0.1\,mm$.

Fig. 6.10 shows the Mach contour when a shock of strength $20.5\,MPa$ impinges on the bubble. The results using *Vucalm* and the ALE method are almost identical. The time interval between each successive plot is $0.1\,\mu s$. As a result of the impedance mismatch, a rarefaction waves can be seen clearly in the water and a very weak shock is transmitted in the gas after the shock interacts with the air-water interface. Fig. 6.10(a) shows the moment the shock first interacts with the bubble.

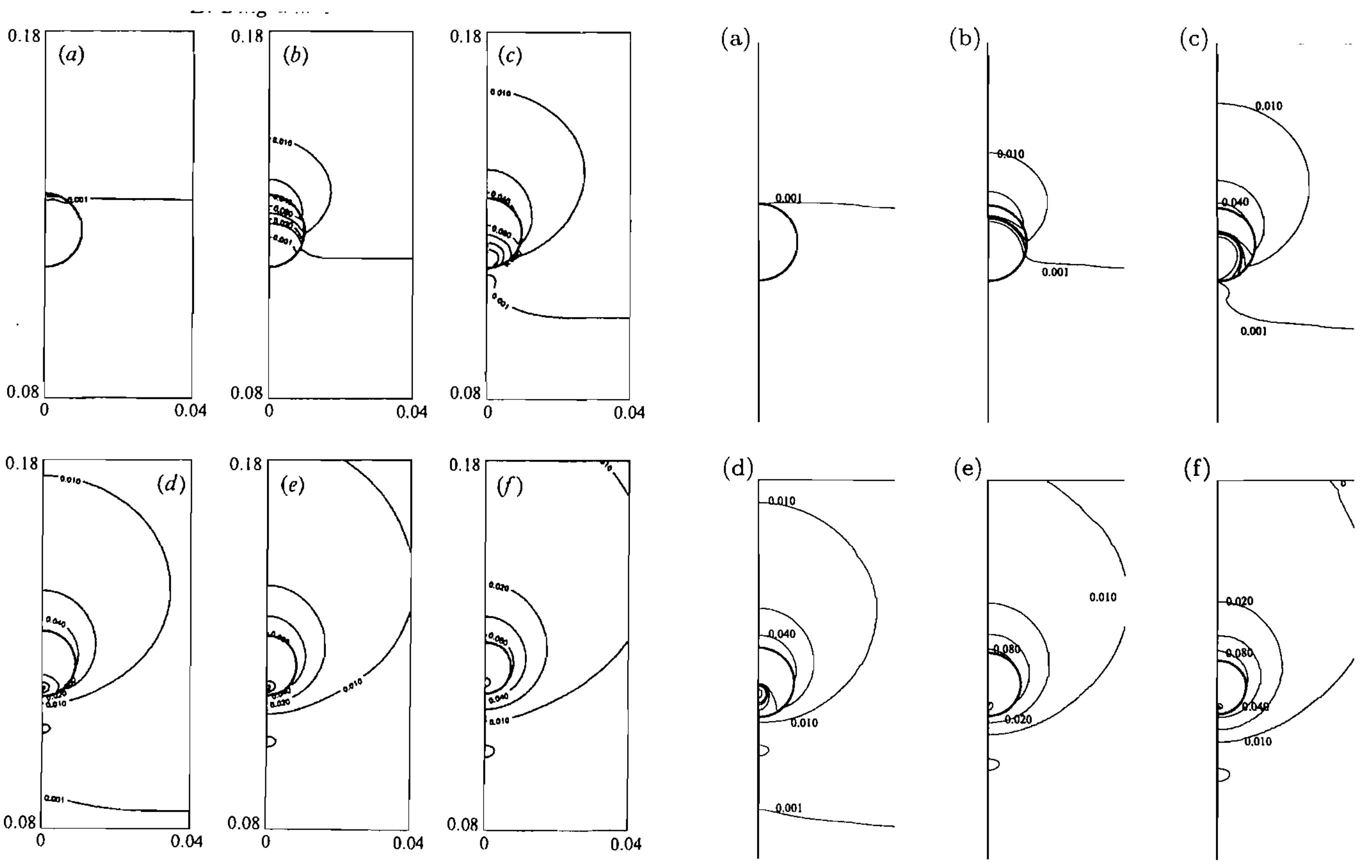

(a) Ding and Graceswki (1996)

(b) *Vucalm*

Figure 6.10: Comparison between *Ding and Graceswki's* and *Vucalm* for weak shock problem. Mach contour of a gas cavity ($R_0 = 0.01\,cm$) impacted by a weak shock ($P/P_0 = 205$). The time interval between each plot is $0.1\,\mu s$.

In Fig. 6.10(b), the shock has propagated past half of the bubble diameter. As a result of the difference in acoustic wave speed in air and water, the incident shock has decoupled and propagated ahead of the weak air shock. There is no significant deformation of the bubble wall during this time because the incident shock is weak in comparison with the strong shock problems presented earlier. As can be seen in Fig. 6.10(c)-(f), owing to the axisymmetric nature of the problem, the shock within the gas converges near the downstream wall of the bubble. Although the transmitted shock in the gas is weak, it will result in an increase in pressure in that region and will affect the direction of the flow within the gas bubble. This observation highlights the importance of having a reasonable mesh resolution within the gas bubble to represent the structure of the flow and hence the dynamics and motion of the bubble wall. The low mesh resolution in the bubble in Ding and Gracewski's numerical simulation also leads to poor shock capturing - the air shock is highly diffused and conforms to the mesh structure, whereas the air shock is captured relatively well in the problem using the *Vucalm* code. The flow around the bubble on the other hand is dictated by the inertia of the surrounding water. A pressure gradient is created around the bubble which drives the fluid towards the bubble, causing the bubble wall to collapse. As expected, the collapse of the bubble is much slower compared to the strong shock case. The nonsymmetric movement of the bubble interface is small, so that no distinct liquid jet is formed, and the collapse proceeds almost spherically.

A successful comparison with a different numerical scheme has been made. The results generated using *Vucalm* agreed well with that using the ALE method of Ding and Graceswki [35].

6.2 Introduction - The numerical work of Igra and Takayama

In this section, validation of the code is carried out by comparing the results with the numerical scheme of Igra and Takayama [52] and also with appropriate interferograms from experimental work.

The motivation of Igra and Takayama's [52] work is to develop a scheme which could properly describe a gas-liquid interface without smearing the density jump across the interface on an Eulerian reference frame. They achieved this by using a density function interface tracking method which is similar in fashion to the interface tracking CIP scheme. In the CIP scheme, a density function serves as a marker corresponding to each fluid type, where a different value is allocated to each fluid. The movement of the density function and hence the interface can then be described using the advection equation [52].

An improved method was presented by Xiao and Yabe [101], where a tangent transformation of the density function was employed which yields a sharper interface, but minute oscillations on the interface still exist. The oscillations can be neglected for two-phase flows of small density ratio, but generate negative density near the interface for problems which involve large density ratio such as air and water. To overcome this problem, the regular CIP scheme is modified [52] and a limiter is imposed to give a higher degree of accuracy. This modification is then employed into a scheme known as C-CUP (CIP Combined Unified Procedure) which can treat both compressible and incompressible flows. Improvement was also made by Igra and Takayama to this scheme, by solving the density of each phase separately. As a result, density diffusion that occurred at the interface in compressible flows problem can be minimised. The interface tracking problem in Eulerian methods, and in particular the CIP scheme as discussed here, highlights the advantage of Lagrangian scheme over other numerical methods. In the Free-Lagrange method, the interface of the different phases present are always sharply resolved and no mass transfer exists between cells of differing material.

Using the modified scheme, Igra and Takayama [52] simulated the deformation and breakup of a cylindrical water column on shock wave loading. Comparisons were then made with experimental findings [51]. A cylindrical water column with an initial diameter of 4.8 mm in air is exposed to a planar shock wave of Mach number $M = 1.47$. In the present validation work, the numerical results using the CIP scheme, as well as interferogram images, are compared with the numerical results using the *Vucalm* code.

6.2.1 Problem specification

The problem studied in this second code validation exercise is illustrated in Fig. 6.11.

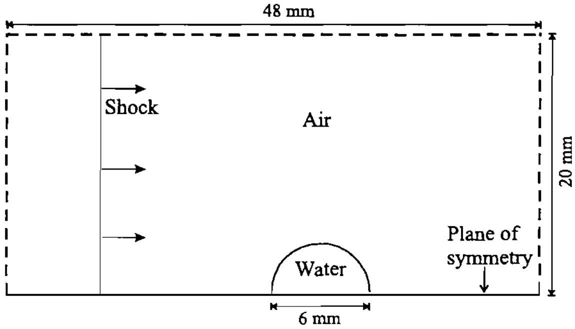

Figure 6.11: The Geometry of the 2D Igra & Takayama validation problem (not to scale).

The problem has been selected to match, as far as is practicable, the numerical simulations carried out by Igra and Takayama [52]. There are uncertainties in the diameter of the cylindrical water column and size of the computational domain. Fig. 6.11 above shows the geometry of the computational domain used for the simulation. The initial pressure for both air and water is $10^5\,Pa$, while the densities are $1.2246\,kgm^{-3}$ and $1000\,kgm^{-3}$ respectively. The shock wave propagates through the air from left to right and all elapsed times are measured from the first shock-water column contact. The lower domain boundary represents the plane of symmetry.

Boundary conditions on the left boundary are initially fixed at post-shock values in order to generate the incoming shock wave, but, from $t = 50\,\mu s$ onwards, non-reflecting boundary conditions are applied in order to allow the escape of left-running waves which are generated by the shock-water column interaction. The upper and right boundaries are non-reflecting at all times. A mesh of approximately 31000 cells has been used: in the initial (unperturbed) mesh, the individual cells in the main domain are square for convenience, while the structure of the mesh in the water column is circular in order to generate a smooth air-water interface.

6.2.2 Flow evolution

The interaction of a planar shock wave, with mach number $M_s = 1.47$ in atmospheric air, with a water column is shown in Fig. 6.12. Fig. 6.12(a) and (b) are the numerical results obtained using the CIP scheme and Free-Lagrange method respectively. The figure shows the isopycnics in air $23\,\mu s$ after the impact of the incident shock wave on the water column surface. The contouring interval for the isopycnics is not given in the published paper. Hence, a value was chosen that provide not only good comparison with the results plotted by Igra and Takayama, but also shows the characteristics of the shock wave-water column interaction. Although estimates to the flow geometry (water column and domain size) and isopycnic contouring interval were made, the results of the two numerical scheme agrees relatively well. Both results show the Mach stems[2] and triple point[3] well. As the shock impacts on the water column wall, a strong reflected shock is propagated upstream. Intersection of the Mach stems occurs downstream of the water column. According to Igra and Takayama, this intersection initiates the creation of a secondary reflected shock wave system.

Fig. 6.13(a) and (b) show an interferogram corresponding to Fig. 6.12(a) and (b) respectively. The double exposure holographic interferogram of Fig. 6.13(a) was taken from an experiment while Fig. 6.13(b) was generated numerically using an interferogram

---

[2] The shock front formed by the merging of the incident and reflected shock fronts. The term is generally used with reference to a shock wave, reflected off a surface. The Mach stem is nearly perpendicular to the reflecting surface and presents a slightly convex (forward) front. The Mach stem is also called the Mach front.

[3] The intersection of the incident, reflected, and fused (or Mach) shock fronts.

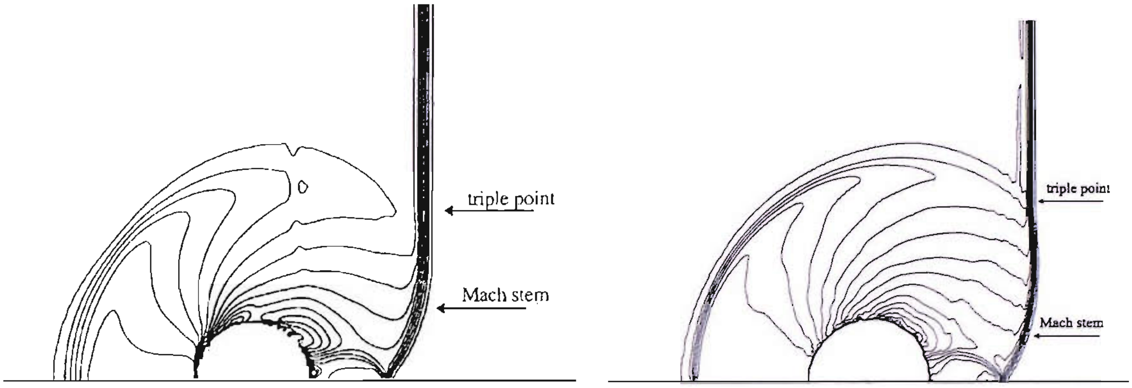

(a) Igra and Takayama (b) *Vucalm*

Figure 6.12: Comparison between *Igra and Takayama* and *Vucalm* for the interaction of a shock wave with a water column. The density contour interval, $\Delta\rho$ for (b) is $0.1\,kgm^{-3}$. The time is $23\,\mu s$.

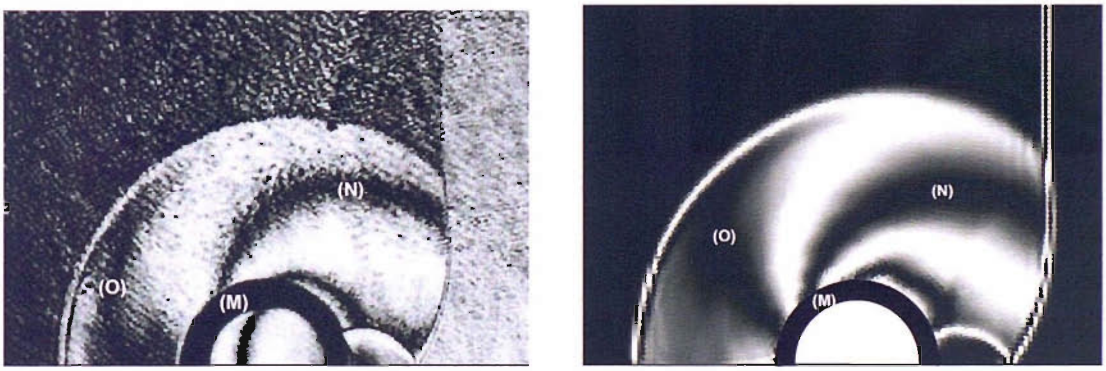

(a) Igra and Takayama (experimental) (b) *Vucalm* (numerical simulation)

Figure 6.13: Interferogram images. Comparison between *Igra and Takayama* and *Vucalm* for the interaction of a shock wave with a water column. The time is $23\,\mu s$.

simulation algorithm written in *Vucalm* based on an equation given in Ball *et al.* [5]. The dark ring (M) seen on the interferogram of Fig. 6.13(a) indicates the wet area where the water column contacted with a glass surface. Both images shows shock fronts similar to the gas phase isopycenics shown in Fig. 6.12. The comparison between the two interferogram images show that the general fringe pattern in air agrees well. In particular the form and position of the fringe that extends from the water column to the incident shock just below the triple point (N), as well as the fringe on the downstream of the column (O) are well-predicted. The major difference is in the thickness of the fringes where the interferogram image generated via *Vucalm* are much thicker.

The relationship between fringe order and path averaged gas density is given by the following equation [5],

$$N = \left(1 - \frac{\rho}{\rho_0}\right)/G \tag{6.1}$$

where N is the fringe order, G is an arbitrary value and is defined here as the gain and ρ_0 is the path mean fluid density at the fringe of order zero, i.e. the reference density. The difficulty is in determining the fringe order spacing or gain and the value of the reference density. A 'trial and error' approach was adopted to match the interferogram fringes of the numerical simulation to that of the experimental work by varying the value of G and ρ_0. The fringe number is controlled by the gain, G, while the fringe spacing and position can be controlled by altering the value of the reference density, ρ_0.

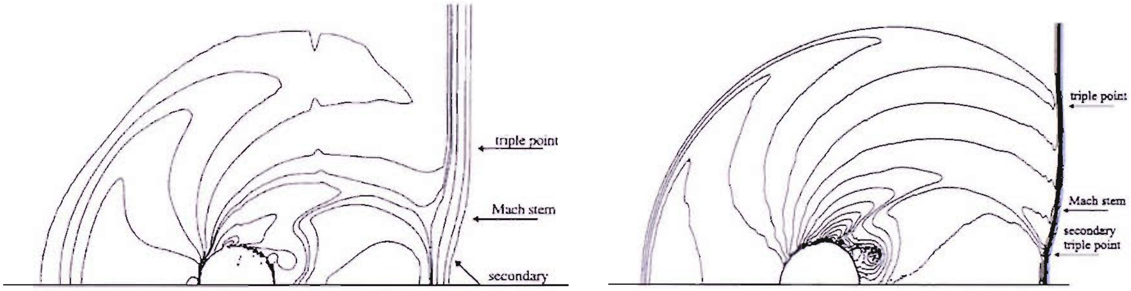

(a) Igra and Takayama (b) *Vucalm*

Figure 6.14: Comparison between *Igra and Takayama* and *Vucalm* for the interaction of a shock wave with a water column. The density contour interval, $\Delta\rho$ for (b) is $0.1\,kgm^{-3}$. The time is $43\,\mu s$.

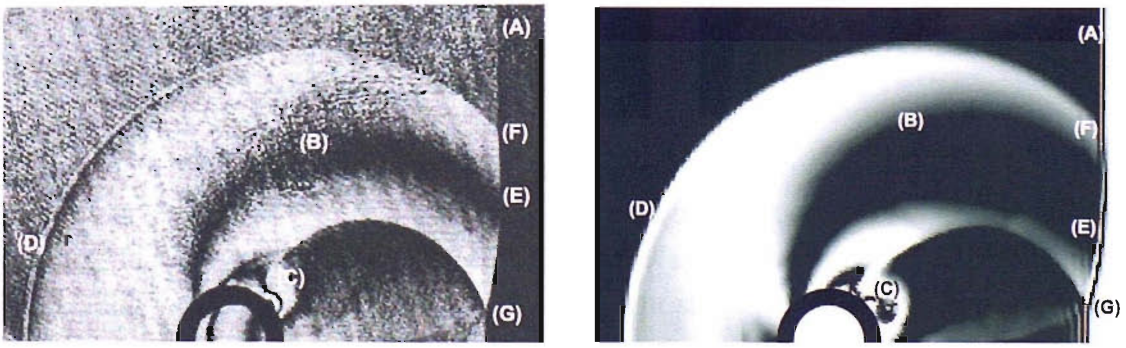

(a) Igra and Takayama (experimental) (b) *Vucalm* (numerical simulation)

Figure 6.15: Interferogram images. Comparison between Igra and Takayama (1999) and *Vucalm* for the interaction of a shock wave with a water column, $53\,\mu s$ after shock impact. Labels (A)-(F) are described in the text.

Fig. 6.14(a) and (b) shows the isopycnics in air at 43 μs for Igra and Takayama and *Vucalm* respectively. Here again, the contouring interval chosen by Igra and Takayama could not be determined. The figures show that both the incident shock wave and the reflected shock wave have propagated further away from the water column. On the downstream side of the water column, a complex secondary wave system is formed, consisting of a reflected shock wave which is created by reflection of the curved Mach stems. The latter initiates a secondary triple point [52]. These flow characteristics can be seen in both figures. The shock front of the results by Igra and Takayama appears to be diffused compared to the results from *Vucalm*. According to Igra and Takayama, this is due to the shock capturing performance of the CIP scheme. Furthermore, the grid spacing in their solution increases as a function of distance away from the water column, which is also condusive to a highly diffused shock front. A high pressure region is generated near the downstream side of the water column which causes a deformation of the water-air interface. Both results show a small vortex near the rear of the water column. The general structure of the isopycnics curves for both sets of results agree relatively well.

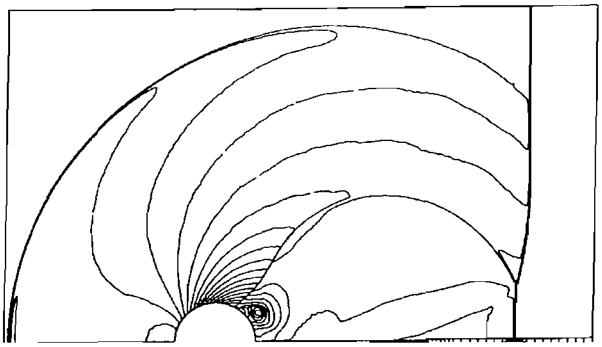

Figure 6.16: Numerical isopycnics at $t = 43\,\mu s$ for shock wave interaction with a solid cylinder. Taken from Igra and Takayama [52].

Fig. 6.15(a) shows a double exposure holographic interferogram taken from the experiment, while fig. 6.15(b) is a numerical interferogram generated from *Vucalm* data. The dark ring seen on the interferogram of fig. 6.15(a) indicates the wet area where the water column contacted a glass surface. The incident shock wave has traversed the water column (A). The comparison between the two interferogram images show that the general fringe pattern in air agrees well. In particular, it correctly predicts both the vortex structure (C) on the downstream side of the column, and the form and position of the fringe that extends from the upstream of the water column to the Mach stem (B). Furthermore, the predicted location of the reflected wave (D), Mach stem (E), triple point (F) and secondary triple point (G) are in excellent agreement with experiment.

For comparison purposes, Igra and Takayama also ran a problem of an interaction of a shock wave with a solid cylinder. The isopycnics obtained for the flow field are shown in Fig. 6.16. A vortex exists near the rear of the solid cylinder and the reflected secondary shock wave reaches the solid wall. These features are less apparent in the numerical results obtained for the water column by Igra and Takayama (Fig. 6.14). They argued that the differences are attributed to the deformation of the water column surface, though the size of the vortex in Fig. 6.16 seems to agree well with that obtained using the *Vucalm* code as shown in Fig. 6.14(b).

6.2.3 Conclusion

The validation of the axisymmetric and $2D$ version of the *Vucalm* code has been carried out using two different cases. The simulations are compared with the results from an alternative numerical simulations using ALE in the work of Ding and Graceswski [35] and by Igra and Takayama [52] where comparisons were also made with experimental findings.

In the validation work, the dynamics of the bubble using *Vucalm* match that of Ding and Graceswki. This includes the liquid jet velocity, impact or collapse time as well as the flow around the bubble, shown by the mach, pressure, and the jet velocity time history plots. Despite the different methods used, the results agree well. The differences are mainly attributed to the mesh structure used by Ding and Graceswki where a coarser computational grid was used within the bubble.

The interaction of a planar shock wave with a water column was presented in the second part of this chapter. Isopycnics curve and interferogram images at two different stages of the flow were obtained from reference [52] and were compared with that using the *Vucalm* code. The results obtained agreed well with the numerical and experimental findings of Igra and Takayama. Both results show the Mach stems and triple point as well as secondary triple point at later stages of the flow. The interferogram at $t = 43\,\mu s$ not only revealed a high pressure region downstream of the water column but also a vortex flow. The fringe number and spacing in air agree well with the experimental interferogram images.

Therefore it can be concluded, based on the works carried out in this chapter, the *Vucalm* code has been successfully validated for typical axisymmetric shock-bubble flow field as well as against experimental findings of flows consisting of air, water and shock waves.

6.3 Aeroacoustic Codes Validation Test Cases

The problem that has been chosen for the validation of the Kirchhoff and FWH aeroacoustic codes involves predicting the acoustic pressure in the far-field, radiated by a rigid pulsator. The sound pressure resulting from the pulsating rigid sphere was compared by means of values obtained with the Kirchhoff and FWH approach and with the exact solution. Fig. 6.17 shows the geometry of the problem where a single solid sphere is immersed in water. The initial density for water is $1000\,kgm^{-3}$ while the initial pressure and temperature are $0.1\,MPa$ and $288.15\,K$. The mean radius of the solid sphere is $R_s = 0.02\,mm$. The lower domain boundary represents the axis of symmetry.

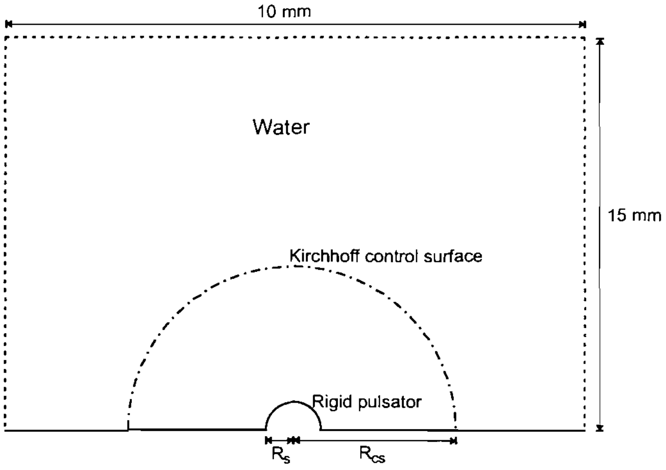

Figure 6.17: The Geometry of the problem (Not to scale).

6.3.1 Kirchhoff Test Cases

The problem studied here is different to that involving a pulsating air bubble in water. Here, the pressure within the pulsating body does not vary as its volume changes during the oscillation, i.e. its internal pressure is invariant. Thus, the pressure in the fluid is governed by the interface motion alone. The pulsation of the solid sphere radiates a spherical sinusoidal wave into the surrounding water.

The following analysis for the Kirchhoff validation test cases is based upon Leighton [62]. When the rigid sphere pulsates, the variation of the bubble radius with time is given by the following expression,

$$R(t) = R_0 + R_\varepsilon(t) = R_0 - R_{\varepsilon 0} e^{i\omega t} \tag{6.2}$$

where R_0 is the equilibrium radius of rigid sphere, R_ε is the displacement of sphere from equilibrium, such that $R(t) = R_0 + R_\varepsilon(t)$ and $R_{\varepsilon 0}$ is the radial displacement amplitude of the pulsator.

Differentiating (6.2) with time gives,

$$\dot{R}(t) = \dot{R}_\varepsilon(t) = -i\omega R_{\varepsilon 0} e^{i\omega t} = U_0 e^{i\omega t} \tag{6.3}$$

$$\ddot{R}(t) = \ddot{R}_\varepsilon(t) = \omega^2 R_{\varepsilon 0} e^{i\omega t} = i\omega U_0 e^{i\omega t} \tag{6.4}$$

where $U_0 = -i\omega R_{\varepsilon 0}$ and must equal the radial fluid particle velocity $\dot{\varepsilon}$ at the sphere wall at all times. Therefore the acoustic pressure at the wall can be found from the product of the specific acoustic impedance for spherical diverging waves and the wall velocity [62].

It is known that the specific acoustic impedance for spherical waves, Z, is given by the following expression,

$$Z = \frac{P(r,t)}{\dot{\varepsilon}(r,t)} \tag{6.5}$$

It is shown in [62] that the diverging spherical waves that any point source radiates have the form,

$$P = \frac{\psi}{r} e^{i(\omega t - kr)} \tag{6.6}$$

where Ψ has the units of $[Pa.m]$, is numerically equal to the acoustic pressure radiated by the source at unit distance from that source. Eqn. 6.6 can be explicitly modified to incorporate inconstant source strength and attenuation. For example [62], if the source is damped with time constant β^{-1}, and if the attenuation coefficient is b, the pressure of spherical diverging waves is given by,

$$P = \frac{\psi}{r} e^{-\beta(t - r/c)} e^{-br} e^{i(\omega t - kr)} \tag{6.7}$$

where the use of $(t - r/c)$ allows for the propagation time, and ψe^{-b} is the acoustic pressure amplitude 1 metre from the centre of the source at time $t = r/c$.

Thus differentiation of 6.7 with respect to r, and integration with respect to t, gives the oscillatory liquid particle velocity

$$\dot{\varepsilon}(r,t) = \left(1 - \frac{i}{kr}\right) \frac{P}{\rho_0 c} \tag{6.8}$$

Hence, the acoustic impedance can be written as

$$Z = \rho_0 c \frac{kr}{kr - i} = \frac{\rho_0 c kr}{1 + (kr)^2}(kr + i) \tag{6.9}$$

of magnitude

$$|Z| = \frac{\rho_0 ckr}{\sqrt{1+(kr)^2}} \tag{6.10}$$

and of phase

$$tanX = 1/kr \tag{6.11}$$

At some fixed radius r, the acoustic pressure is given by

$$P = P_A e^{i\omega t} \tag{6.12}$$

where $P_A = \Psi e^{-ikr}/r$.

From (6.5) and (6.10) , the pressure amplitude P_A, the specific acoustic impedance Z and the speed amplitude U_0 can be written such that

$$P_A = U_0|Z| = U_0\rho_0 c\cos X \tag{6.13}$$

and

$$\cos X = \frac{kr}{\sqrt{1+(kr)^2}} \tag{6.14}$$

Substituting (6.10), (6.14) and (6.3) into (6.5) and since

$$Z = |Z|e^{i\alpha} = \frac{\rho_0 ckr}{\sqrt{1+(kr)^2}} e^{iX_0} \tag{6.15}$$

the acoustic pressure at the wall can be written as

$$P(R_0,t) = \rho_0 cU_0 \cos Xe^{i(\omega t+X_0)} \tag{6.16}$$

where evaluation of equations (6.11) and (6.14) at the sphere wall ($r = R_0$) gives

$$\cot X_0 = kR_0 \tag{6.17}$$

and

$$\cos X_0 = \frac{kR_0}{\sqrt{1+(kR_0)^2}} \tag{6.18}$$

From above, the acoustic pressure at the wall can also be expressed as

$$P(R_0,t) = \frac{\Psi}{R_0} e^{i(\omega t-kR_0)} \tag{6.19}$$

Equating (6.19) and (6.16) gives

$$\Psi = \rho_0 c U_0 R_0 \cos X_0 e^{i(kR_0+X_0)} \tag{6.20}$$

Therefore, the expression for the acoustic pressure at any radius $r \geq R_0$ is given by

$$P(r,t) = \rho_0 c U_0 \frac{R_0}{r} \cos X_0 e^{i(\omega t - k(r-R_0)+X_0)} \tag{6.21}$$

the magnitude of which is

$$|P(r,t)| = \frac{\rho_0 c |U_0| R_0^2 k}{r\sqrt{1+(kR_0)^2}} \tag{6.22}$$

The results of the acoustic radiation of the pulsator were obtained using direct calculation. Instead of using the *Vucalm* code to simulate the near-field problem, the near-field pressure time history at every control point on the control surface were calculated from Equation 6.22. This is carried out in order to separate the influence of mesh resolution on the Kirchhoff integral evaluation. For sufficient accuracy in the far-field calculations, the surface quantities (p, $\frac{\partial p}{\partial t}$, $\frac{\partial p}{\partial n}$) should be very accurate. This can be achieved through the use of a very fine mesh in the CFD calculations. However, memory and time constraints make this impractical. Test cases using *Vucalm* to produce the Kirchhoff control surface data were also carried out and is presented at the end of Section 6.3.1.

The pressure and its normal and time derivatives are therefore calculated using Equation (6.21) and (6.22) directly into Equation (5.1). Taking the real part of Equation (6.21) gives,

$$\Re\{P(r,t)\} = A\frac{\cos(\omega t + X_0 - k(r-R_0))}{r} \tag{6.23}$$

where

$$A = \frac{\rho_0 c U_0 R_0^2 k}{\sqrt{1+(kR_0)^2}} \tag{6.24}$$

Hence it follows that,

$$\frac{\partial p}{\partial t} = -\frac{A}{r}\omega \sin(\omega t + X_0 - k(r-R_0)) \tag{6.25}$$

$$\frac{\partial p}{\partial x} = \frac{A}{r^2}\Big[kx\sin(\omega t + X_0 - k(r-R_0)) - \frac{x}{r}\cos(\omega t + X_0 - k(r-R_0))\Big] \tag{6.26}$$

$$\frac{\partial p}{\partial y} = \frac{A}{r^2}\Big[ky\sin(\omega t + X_0 - k(r-R_0)) - \frac{y}{r}\cos(\omega t + X_0 - k(r-R_0))\Big] \tag{6.27}$$

where x and y are the control points CP^n_{axi} coordinates and $r = \sqrt{x^2+y^2}$. The normal derivative can then be calculated using the dot product with the normal vector $\mathbf{n}$ at each control point. The analytical solution is then calculated directly using the equations above for a solution at a single point (observer) in the far-field. In all the analysis, the observer is positioned $500\,mm$ from the centre of the oscillating rigid sphere, i.e. $\mathbf{x} = (0, 500\,mm, 0)$.

The following test cases were carried out in order to validate the Kirchhoff code and also to examine the sensitivity of the formulation to the following conditions:

- Placement/Size of the integration surface
- Frequency of the radiated pressure wave
- Number of control points
- Data storage time increment (time interval or resolution at which data are recorded)
- Asymmetry between the centre of pulsator and the centre of the Kirchhoff control surface
- Driving pressure profile (complexity of the radiated pressure)

Frequency and Control surface Placement/Size Analysis

The parameters of the driving pressure for the test cases are given in Table 6.2. In order to analyse the effect of wave frequency, two different frequencies are used, one being 10 times greater than the other.

Case	ω (s^{-1})	U_0 (ms^{-1})	f (Hz)	Period (μs)	Wave length (mm)
High-frequency	4.7837×10^6	20	7.6×10^5	1.313	2.0
Low-frequency	4.7837×10^5	20	7.6×10^4	13.1	20.0

Table 6.2: Driving pressure parameters

Tests are also carried out for large $(10\,mm \leq R_{cs} \leq 20\,mm)$ and small $(1\,mm \leq R_{cs} \leq 2\,mm)$ control surface radii (R_{CS}), to examine any dependencies between R_{cs} and the driving pressure phase and wavelength. The results (Fig. 6.18 and 6.19) show that the formulation gives the same far-field pressure signature regardless of the driving pressure frequency and is independent of the control surface placement. Fig. 6.18 and 6.19 also show that the start time of each plot is different for the two control surface radius sizes. This is because calculation of the far-field pressure wave only starts when the radiating pressure waves emitted by the pulsator reaches the control surface. This also explains the different time bases.

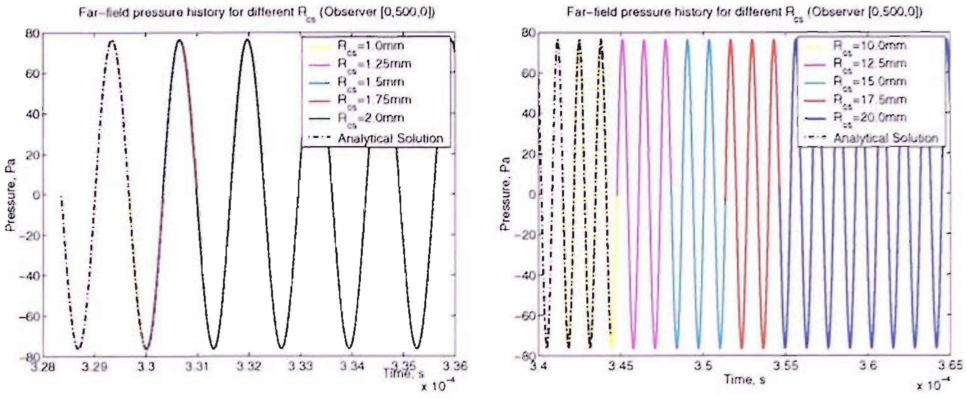

(a) Small Control Surface Radius (b) Large Control Surface Radius

Figure 6.18: Control surface radius, R_{CS} study for high-frequency wave.

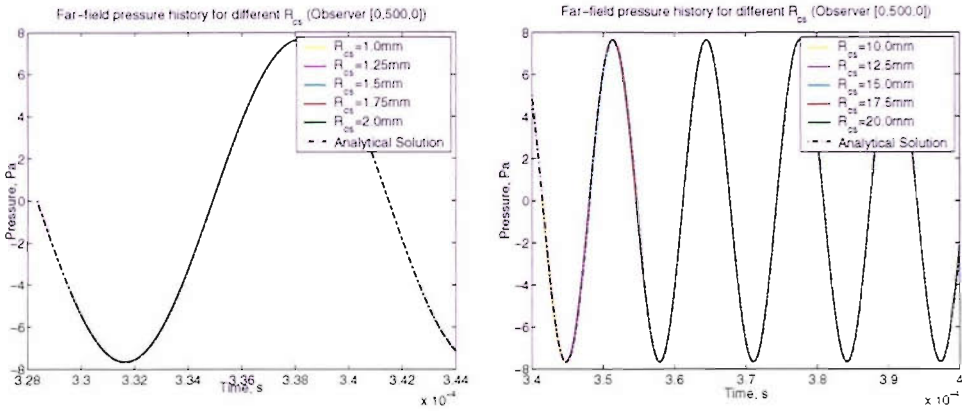

(a) Small Control Surface Radius (b) Large Control Surface Radius

Figure 6.19: Control surface radius, R_{CS} study for low-frequency wave.

Control point resolution study

The number of control points (NCP) C^n_{axi} is adjusted by altering the value of $\Delta\theta$ which automatically alters the number of geometric control point (C^i_G) in one rotation of the half circle along the x-axis (symmetry axis). Fig. 6.20(a) shows that the difference in the far-field pressure signature is small for $NCP \geq 292$. The calculated far-field noise approaches the analytical solution as the number of control points increases. This is clearly depicted in Fig. 6.20(b).In all subsequent work, $NCP = 1152$ is used.

Timestep study

Good time resolution is needed to resolve details such as high-frequency content of the solution on the Kirchhoff's surface S. Fig. 6.21 shows the effect of the number of points

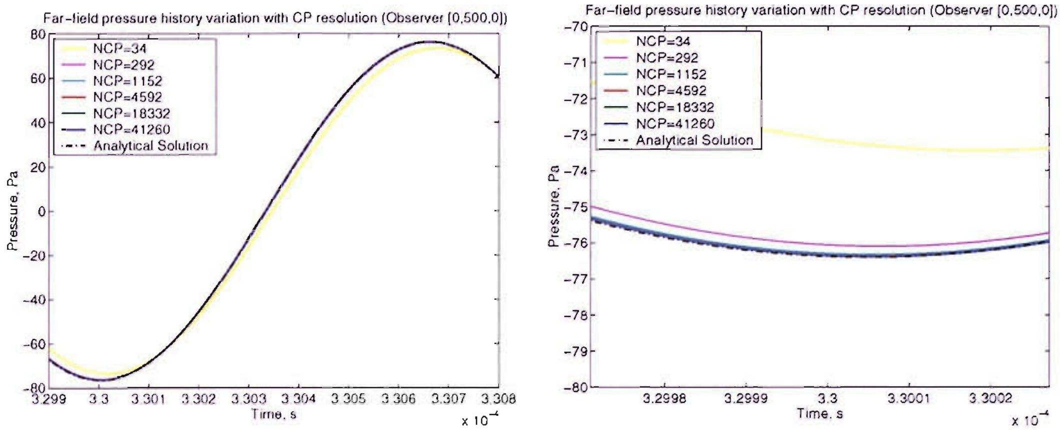

(a)

(b)

Figure 6.20: Far-field pressure history for test cases with differing number of control points. Figure (b) is a close-up of the curve near the trough of the signal wave.

per period and per wavelength in the retarded time. In this study, $\omega = 4.7837 \times 10^6$. Fig. 6.21(b) is a closer look of the curve near the trough at around $330\,\mu s$. It clearly shows that the error increases as dt increases especially for the case where $dt = 0.064\,\mu s$, i.e about 20 times smaller than the period of the signal. The severity of the error would increase as the frequency of the source wave increases. The smaller the time step in the retarded time, the more accurate the prediction of the noise in the far-field. Therefore, it is important that the retarded time-step chosen for the calculation of the far-field is small enough to accurately capture the high-frequency events and discontinuities in a signal. Determination of the optimum retarded time step is via trial error and first approximation is made based on the *Vucalm* simulation run time step.

Driving pressure profile analysis

This analysis is carried out in order to determine the code capability in evaluating the far-field acoustic signature of a complex driving pressure wave. Two cases are studied here, in which the driving pressure is constructed by combing two sinusoidal pressure cycle of differing amplitude and frequency. The amplitude of the test signal is such that the test problems are essentially linear. The parameters are given in the table below (Table 6.3). Tests are carried out for different control surface radius, R_{CS}. The results are presented in Fig. 6.22 and 6.23 and clearly show that the wave profile in the far-field matches the profile of the driving pressure. The agreement holds for various Kirchhoff control surface placements and sizes. Therefore, it can be concluded that the code is capable of capturing the details of complex pressure waves and predict its acoustic signature in the far-field.

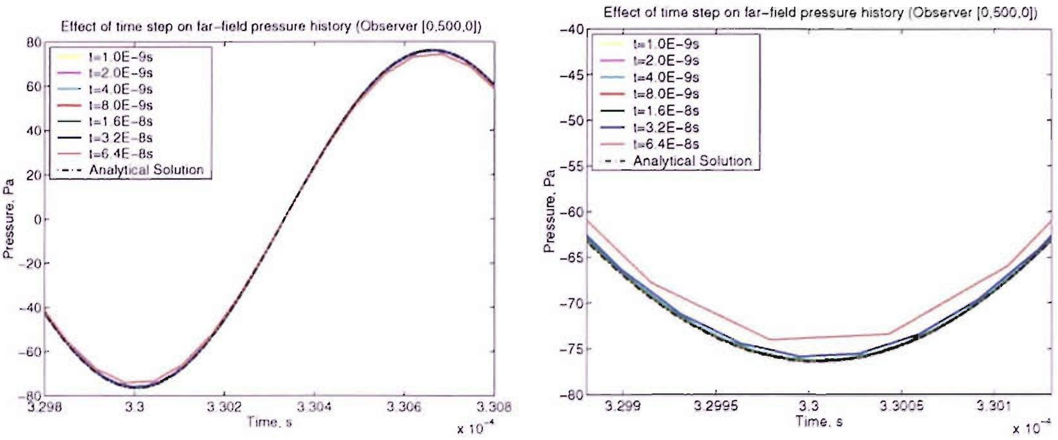

(a)

(b)

Figure 6.21: Results for timestep study for different R_{CS}. Figure (b) is a close-up of curve (a).

providing that the time-step chosen for the analysis is small enough.

Case	ω_1 (s^{-1})	Pressure amplitude P_1 (MPa)	ω_2 (s^{-1})	Pressure amplitude P_2 (MPa)
1	4.8×10^6	4.0	2.4×10^6	2.0
2	4.8×10^6	4.0	1.9×10^7	2.0

Table 6.3: Driving pressure parameters made up of two separate contributors of differing pressure amplitude, P and frequency.

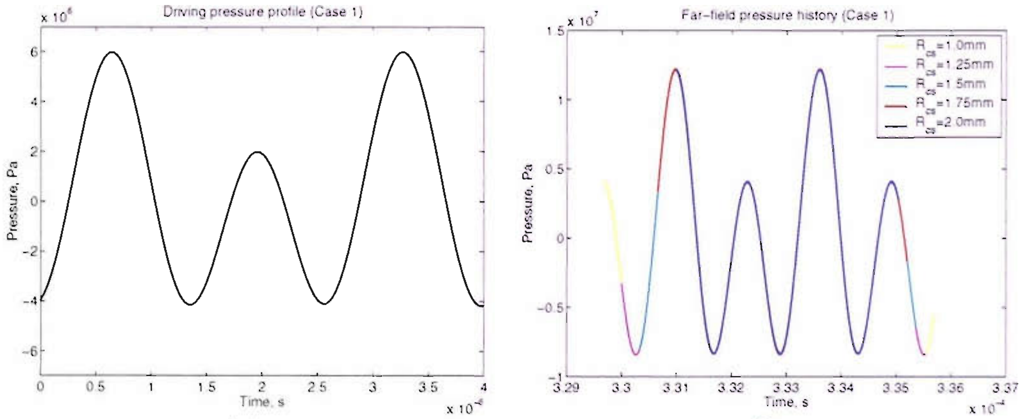

(a)

(b)

Figure 6.22: Case 1. (a) Driving pressure profile (b) Far-field pressure history at observer with coordinates $[0\,mm, 500\,mm, 0\,mm]$ for different R_{CS}.

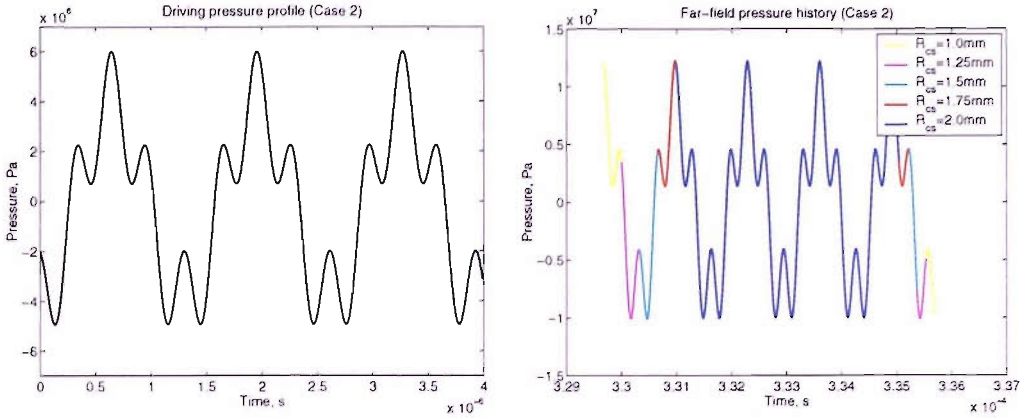

(a) (b)

Figure 6.23: Case 2. (a) Driving pressure profile (b) Far-field pressure history at observer with coordinates $[0\,mm, 500\,mm, 0\,mm]$ for different R_{CS}.

Asymmetry study

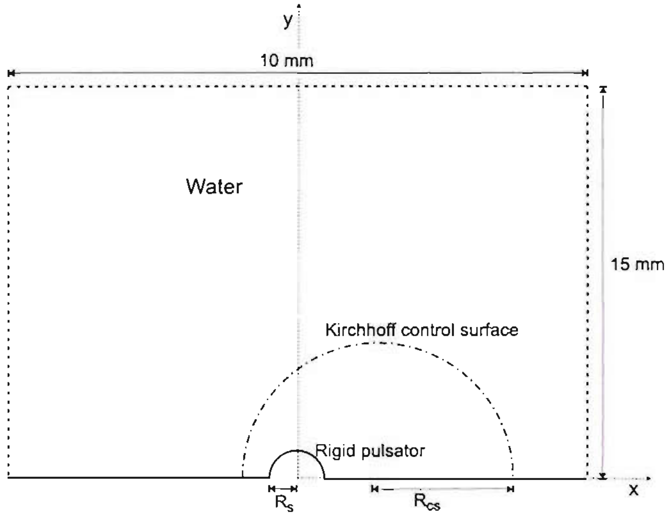

Figure 6.24: The geometry of the problem for asymmetry study.

In the asymmetry study, the centre of the rigid oscillating sphere and the Kirchhoff control surface do not lie at the same coordinates. This is illustrated in Fig. 6.24. Therefore, the radiated spherical pressure wave arrives at each control points at differing time, amplitude and phase. The observer coordinates is the same as in previous cases $[0\,mm, 500\,mm, 0\,mm]$, i.e. $500\,mm$ away from the centre of the oscillating sphere. The Kirchhoff control surface radius, R_{cs} and the rigid sphere radius, R_s is $2.0\,mm$ and $0.02\,mm$ respectively. The results clearly shows exact agreement between the predicted far-field acoustic pressure wave and the analytical solution, despite the asymmetry between the position of the pulsator and the Kirchhoff control surface.

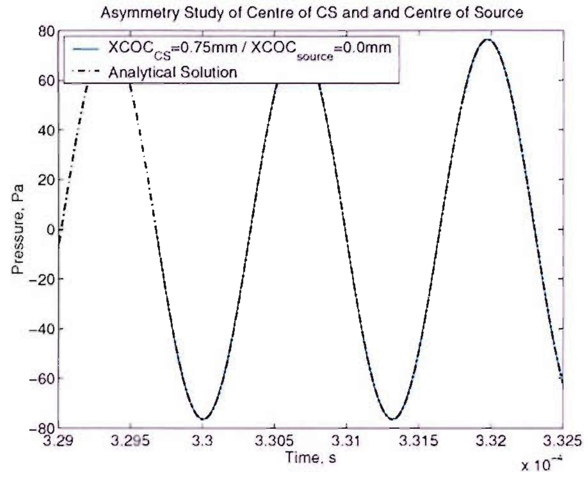

Figure 6.25: Asymmetry study. Comparison of far-field pressure history between numerical and analytical solution.

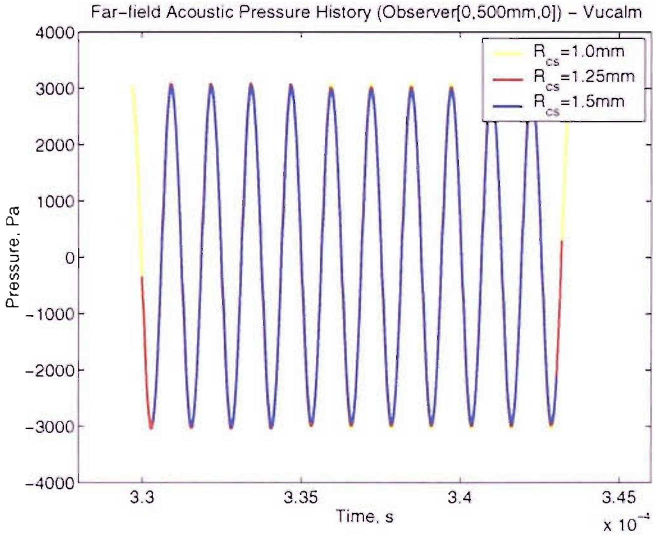

Figure 6.26: Estimated far-field pressure time history at three different R_{cs}. The *Vucalm* code was used to produce the Kirchhoff near field data.

Vucalm-Kirchhoff Hybrid Calculation

Test cases were also carried out to investigate the accuracy of the Kirchhoff control surface data calculated using the *Vucalm* code. The layout of the computational domain is as shown in Fig. 6.17. The far-field results from three different control surface radii were calculated, i.e. at $R_{cs} = 1.0\,mm$, $R_{cs} = 1.25\,mm$ and $R_{cs} = 1.5\,mm$. The resolution of the Voronoi mesh in the region of the control surface were kept constant for all cases to eliminate any possible ambiguity in the results owing to the influence of mesh resolution on the Kirchhoff integral evaluation. The observer is positioned $500\,mm$ from the centre of the rigid pulsator. The result is shown in Fig. 6.26.

The result show that the near field data calculated using *Vucalm* produces accurate estimation of the far-field pressure-time history and is independent of the control surface placement within the *Vucalm* computational domain. However, it is understood that for the latter, the accuracy of the solution is highly influenced by the density of the CFD computational mesh in the proximity of the control points.

6.3.2 FWH Test Cases

Different set of equations for the pressure and velocity terms are used in order to take into account the phase difference between the two terms from near-field to the far-field. This is because unlike the Kirchhoff formulation, an accurate calculation of the particle velocity is necessary in the surface and volume integral of the FWH method as described in section 4.5.2. The amplitude of the test signals for the FWH test problems satisfies the linear wave equation. In addition, since there is a large similarity in the hydrocode structure of the two aeroacoustic codes and in the way the two are integrated into *Vucalm*, the validation analysis is not carried out as detailed as that of the Kirchhoff method. It is comprehensible to believe that the analyses shown above and its results are applicable here. Therefore, a simple test case is carried out to validate the formulation of the FWH code and its ability to predict noise in the far-field. The test cases carried out here is to examined whether the FWH formulation has been implemented correctly. The analysis is a for a spherical spreading wave originating from a point source.

First, consider that the acoustic particle velocity in the r direction, U, is in phase with the acoustic pressure, p, everywhere in the far-field of a simple acoustic source radiating spherical waves. In the far-field, the quantities p and U are related by the characteristic impedance as

$$p(r,t)/U(r,t) = \rho c \tag{6.28}$$

In general p and U are related by the r component of Euler's equation [54]

$$\rho\frac{\partial U}{\partial t} + \frac{\partial p}{\partial r} = 0 \tag{6.29}$$

Suppose that in the near-field of a time harmonic source, the pressure is given by

$$p = -iQ_s \frac{e^{ik(r-ct)}}{r} \tag{6.30}$$

Then the corresponding particle velocity component in the r direction is

$$U = \frac{1}{\rho c}\left(1 + \frac{i}{kr}\right)p \tag{6.31}$$

It is clear from Equation 6.31 above that as kr becomes very large in the far-field, the simple plane wave relation (Eqn. 6.28) results. The real parts of Equation 6.30 and 6.31 are

$$p(r,t) = (Q_s/r)sin(\omega(r/c - t) \tag{6.32}$$

and

$$U(r,t) = (Q_s/\rho cr)sin(\omega(r/c - t)) + (Q_s/k\rho cr^2)cos(\omega(r/c - t)) \tag{6.33}$$

respectively.

Equation 6.32 and 6.33 are used to generate the data at the control points for input to the FWH integral for the far-field calculation.

Frequency and Control surface Placement/Size Analysis

The parameters of the driving pressure for the test cases are given in Table 6.4.

Case	ω (s^{-1})	Q_s (Pa)	f (Hz)	Period (μs)	Wave length (mm)
High-frequency	4.7837×10^6	2.0×10^3	7.6×10^5	1.313	2.0
Low-frequency	4.7837×10^5	2.0×10^3	7.6×10^4	13.1	20.0

Table 6.4: Driving pressure parameters

Tests are carried out for large ($5\,mm \leq R_{cs} \leq 7.5\,mm$) and small ($0.2\,mm \leq R_{cs} \leq 2\,mm$) control surface radii (R_{CS}), to examine any dependencies between R_{cs} and the driving pressure phase and wavelength. Both the low-frequency and high-frequency driving pressure wave are used for this analysis. The results are similar to the analysis obtained using the Kirchhoff method. Fig. 6.27 and 6.28 show that the predicted far-field signature are independent of control surface placement and in excellent agreement with the analytical result regardless of the driving pressure frequency. The wave patterns, phase, amplitude and frequency of the predicted far-field noise are essentially identical to the analytical result.

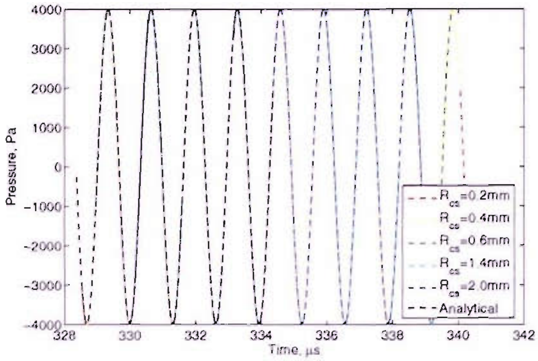

(a) Small Control Surface Radius

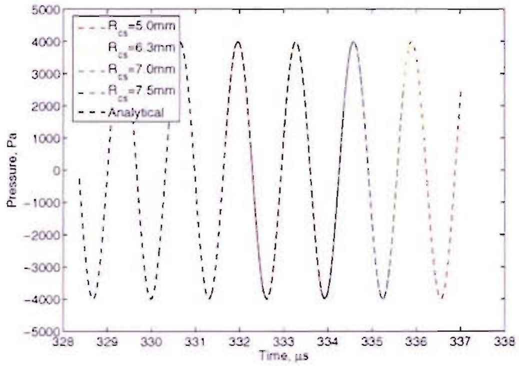

(b) Large Control Surface Radius

Figure 6.27: Control surface radius, R_{CS} study for high-frequency wave (a) $0.2mm \leq R_{CS} \leq 2.0mm$ (b) $5.0mm \leq R_{CS} \leq 7.5mm$.

6.3.3 Conclusion

The validation of both aeroacoustic codes, Kirchhoff and FWH, has been carried out to analyse the sensitivity of the methods to various parameters - frequency of the radiated pressure wave, size and placement of the control surface, number of control points, time increment, asymmetry and complex driving pressure. The results obtained using the aeroacoustic codes are in excellent agreement with respective analytical results. Therefore, the tests presented in this chapter shows that the developed codes have been implemented correctly.

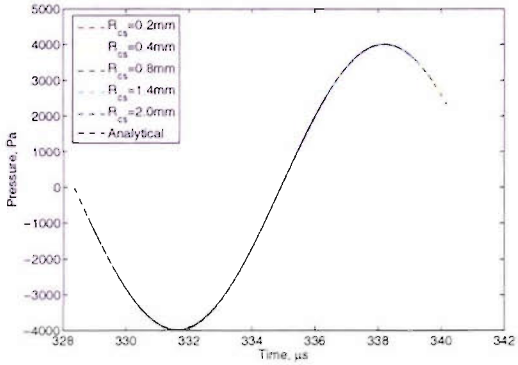

(a) Small Control Surface Radius

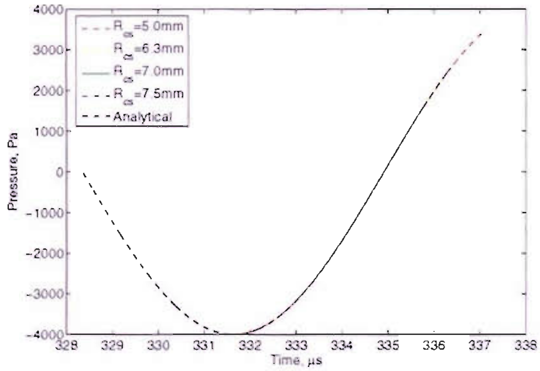

(b) Large Control Surface Radius

Figure 6.28: Control surface radius, R_{CS} study for low-frequency wave (a) $0.2mm \leq R_{CS} \leq 2.0mm$ (b) $5.0mm \leq R_{CS} \leq 7.5mm$.

Chapter 7

Simulations of Lithotripter Shock Wave-Bubble Interaction in Free-field

In the next few chapters, simulations of the response of an air bubble to a lithotripter shock wave using the *Vucalm* Free-Lagrange method are presented. In this chapter, shock-induced collapse are investigated for the case when the bubble is in free-field (infinite fluid).

The objectives of the current simulations are to model the interaction of a lithotripter shock wave with a stable spherical bubble, and to observe:

- the reflection, transmission and refraction of the shock waves as well as the velocity fields near the bubble.
- the collapse of a spherical bubble in free-field
- the formation of the high-speed liquid jet and its velocity-time history
- the bubble volume-time history
- the effect of mesh resolution on the accuracy of the results

Besides the numerical simulations of the shock-bubble interaction using *Vucalm*, pressure time history in the far-field are also calculated using both the Kirchhoff and FWH aeroacoustic codes. Comparisons between the results are also given.

The first part of this chapter was presented at the 2^{nd} *International Conference of Computational Fluid Dynamics in July 2002, Sydney, Australia.*

Prior to running the numerical simulations, a consistent methodology regarding some numerical aspects was first established. This includes material interface smoothing (artificial surface tension) and mesh resolution (grid convergence).

7.1 Interface Smoothing Algorithm Study

The effects of different values of the non-dimensional smoothing gain, α, is demonstrated here. The interface smoothing algorithm was discussed in Section 4.4.1. Four different values of α were used for the simulations of shock/bubble interaction. The sole purpose of this study is to determine an optimum value of α that allows the bubble to evolve naturally while effectively maintain a smooth material interface.

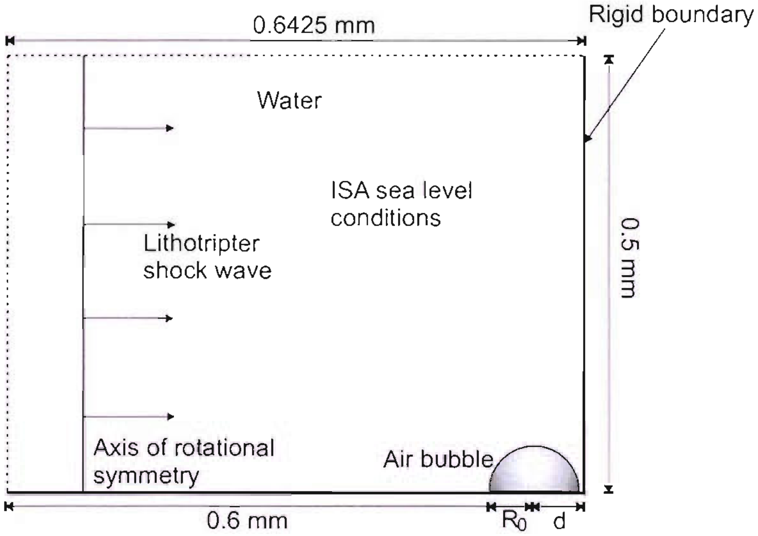

Figure 7.1: The geometry of the computational domain for near plane rigid boundary problem.

For this preliminary study, simulations of single cavitation bubbles near a plane rigid boundary are carried out. The computational domain is shown in Fig. 7.1. The distance of the initial bubble centre from the boundary, d, is $0.0425\,mm$ (giving a stand-off parameter, ζ of 1.0625). The bubble initial radius is $0.04\,mm$ [29]. A planar lithotripter pulse, with $P^+ = 60\,MPa$ and $P^- = -10\,MPa$, propagates through the water from left to right (see Fig. 7.2). The water is represented by the Tait Equation of State (EOS) and is initially at ISA sea level conditions, i.e. the pressure, temperature and density are $101.325\,kPa$, $288.15\,K$ and $1000\,kgm^{-3}$ respectively. The bubble is assumed to contain air and is represented by the ideal gas EOS. With ratio of specific heat, $\gamma = 1.4$. The initial temperature, density and pressure for the air are $288.15\,K$, $1.2246\,kgm^{-3}$ and

Case	1	2	3	4
α	0	4×10^3	8×10^3	16×10^3

Table 7.1: Cases for smoothing gain study

101.325 kPa respectively. The lower domain boundary represents the axis of symmetry while the top and right boundaries are non-reflecting at all times. All elapsed times are measured from the first shock/bubble impact. The lithotripter pulse is introduced by imposing a time-dependent pressure boundary condition on the left boundary.

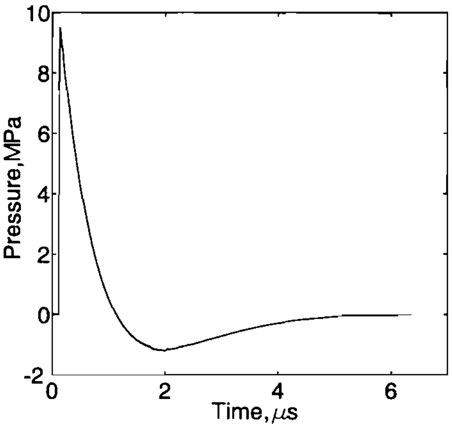

Figure 7.2: Modelled form of ESWL pressure waveform.

The analytical expression for the lithotripter pulse shock wave shape can be written as follows [22],

$$P_s(t) = 2P_a e^{-\alpha_d t} \cos(\omega t + \pi/3) \tag{7.1}$$

Here, P_a is the amplitude of the shock wave, equal to the postive peak pressure P^+ when the rise time is zero, α_d is the decay constant, $9.1 \times 10^5 s^{-1}$, and $\omega = 2\pi f$ is the radial frequency with $f = 83.3\,kHz$.

A simulation where no interface smoothing is included was conducted as a reference simulation. Three different smoothing gains, α, were used as given in Table 7.1. The values for α were obtain via a trial and error method and from the values used in the validation work. The value for α is problem dependent and therefore further studies on the effect of the interface smoothing gain was necessary as the amplitude of the lithotripter shock wave is much less than that used in the validation work. In all the simulations carried out, the restoring force distribution of $F_B = F_0/2$ and $F_A = F_C = F_0/4$ were used (refer to Fig. 4.4). The reason for implementing this modified smoothing technique was given in Section 4.4.4. During the early stages of the bubble collapse, the deformation of

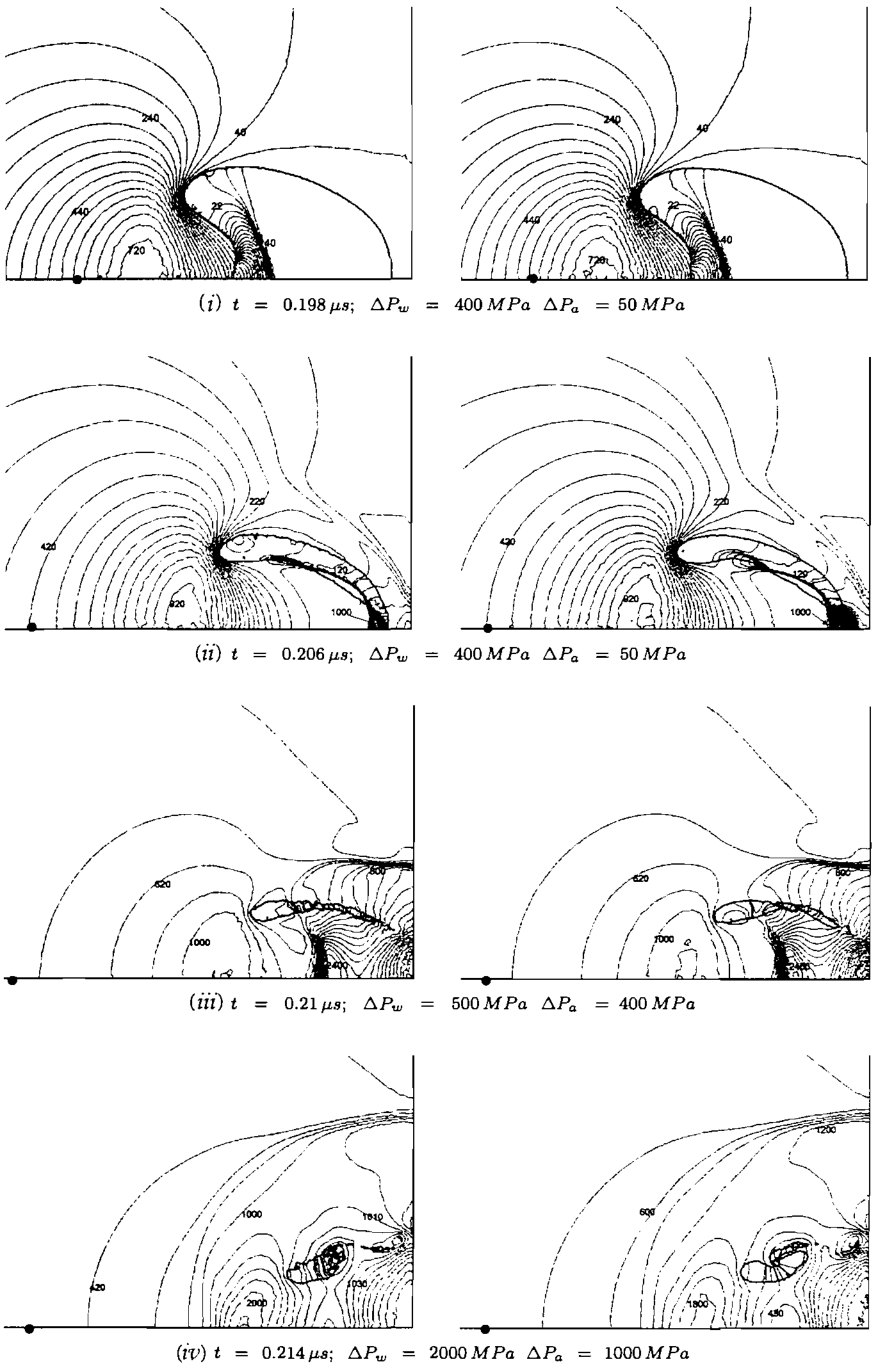

(i) $t = 0.198\,\mu s$; $\Delta P_w = 400\,MPa$ $\Delta P_a = 50\,MPa$

(ii) $t = 0.206\,\mu s$; $\Delta P_w = 400\,MPa$ $\Delta P_a = 50\,MPa$

(iii) $t = 0.21\,\mu s$; $\Delta P_w = 500\,MPa$ $\Delta P_a = 400\,MPa$

(iv) $t = 0.214\,\mu s$; $\Delta P_w = 2000\,MPa$ $\Delta P_a = 1000\,MPa$

(a) (b)

Figure 7.3: Variations in the dynamics of the bubble and material interface for different smoothing gains α. Comparison between **(a)** $\alpha = 0$ and **(b)** $\alpha = 4 \times 10^3$. ΔP_w and ΔP_a indicate the increments between contours in the water and air respectively. Solid 'dot' indicates initial centre of the bubble.

the bubble surface is minimal. Therefore, the results are identical and the figures of the bubble collapse during early collapse stages are not plotted and introduced here.

However, towards the final stages of the collapse, the bubble undergoes a rapid deformation. The upstream bubble wall starts to involute to form a high-speed liquid jet. The selection of a suitable value of α is therefore made based on the comparison of the bubble evolution towards the end of the collapse stage. The comparison of the bubble collapse between $t = 0.198\,\mu s$ and $t = 0.214\,\mu s$ are shown in Fig. 7.3 and Fig.7.4. The results from all three cases show consistency with the undamped case.

At approximately $t = 0.206\,\mu s$, the jet has impacted onto the downstream bubble wall, producing a toroidal bubble and generating a spherical blast wave into the surrounding water. It is clear from Fig. 7.3$(a)(ii - iv)$ that for the case when $\alpha = 0$, the highly shearing flow caused wrinkles on the bubble interface. Increasing the smoothing gain α to 4000 improved the appearance of the material interface although signs of wrinkles on the interface still exist as depicted in Fig. 7.3$(b)(iii)$. Following jet impact, the collapsed bubble is drawn into a vortex flow and moves closer to the rigid boundary. The thickness of the bubble at $t = 0.21\,\mu s$ varies for different values of α. The size of the bubble for the case when $\alpha = 16 \times 10^3$ are bigger than the other three cases at $t = 0.24\,\mu s$. The restoring force associated with the smoothing gain excessively damps the interface and causes an increase in pressure inside the bubble. This dampened the collapse of the bubble beyond jet impact and initiated an early expansion of the bubble.

Fig. 7.5 shows the bubble volume time history for all four cases. Fig. 7.5(b) is a closeup of (a) and it is clear from the results that the excessive force applied to the interface particles when the smoothing gain α is too high induces a higher collapse rate. Given that the simulation with $\alpha = 0$ is the bench mark for correct physical features of bubble collapse, comparison of bubble shape for various values of α shows that the use of $\alpha = 8 \times 10^3$ appears to be optimum in keeping the interface wrinkles to a minimum while preserving the physical evolution of the bubble.

Thus, based on the analysis, the restoring force is applied to the target particle and its interface neighbours with $\alpha = 8 \times 10^3$. This value of α is used for all simulation presented later in the report.

7.2 Mesh Resolution Study

The initial mesh layout of the computational domain is divided into three regions. The first region covers the area within the gas bubble. The second regions covers a few cells thick around the circumference of the air-water interface, while the third region surrounds both the first and second region and is defined here as the main domain area. The Voronoi

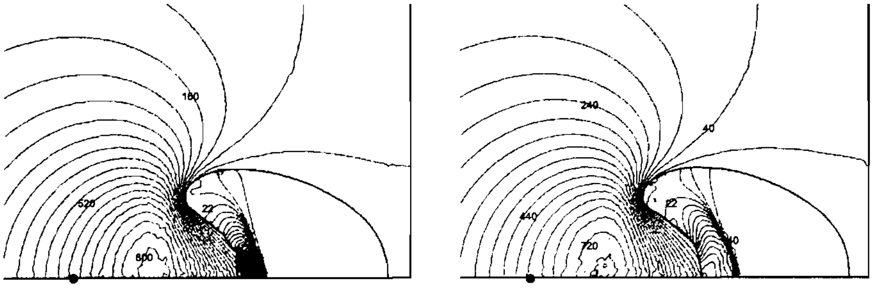

(*i*) $t = 0.198\,\mu s$; $\Delta P_w = 400\,MPa$ $\Delta P_a = 50\,MPa$

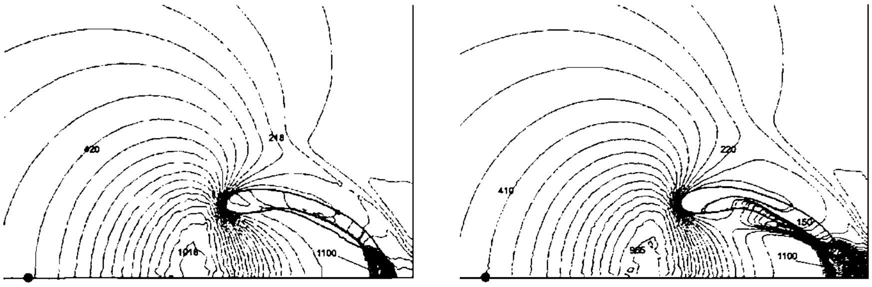

(*ii*) $t = 0.206\,\mu s$; $\Delta P_w = 400\,MPa$ $\Delta P_a = 50\,MPa$

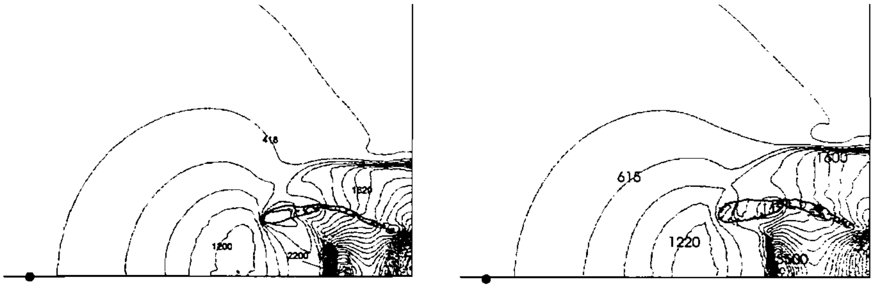

(*iii*) $t = 0.21\,\mu s$; $\Delta P_w = 500\,MPa$ $\Delta P_a = 400\,MPa$

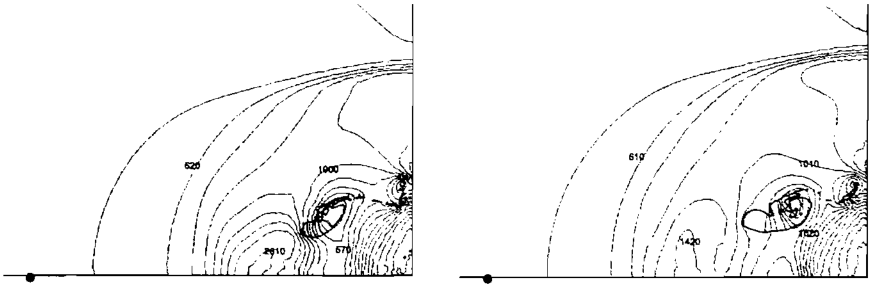

(*iv*) $t = 0.214\,\mu s$; $\Delta P_w = 2000\,MPa$ $\Delta P_a = 1000\,MPa$

Figure 7.4: Variations in the dynamics of the bubble and material interface for different smoothing gains α. Comparison between **(a)** $\alpha = 8\times10^3$ and **(b)** $\alpha = 16\times10^3$. ΔP_w and ΔP_a indicate the increments between contours in the water and air respectively. Solid 'dot' indicates initial centre of the bubble.

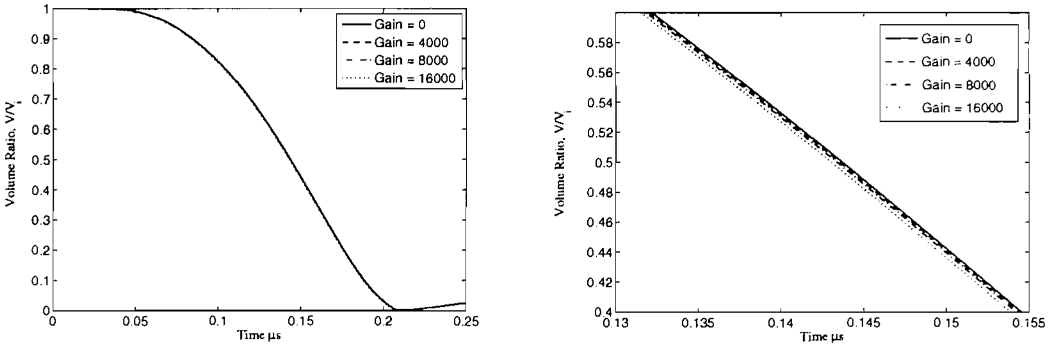

(a) (b)

Figure 7.5: Bubble volume ratio time history for different value of α (**b**) is a close-up of (**a**).

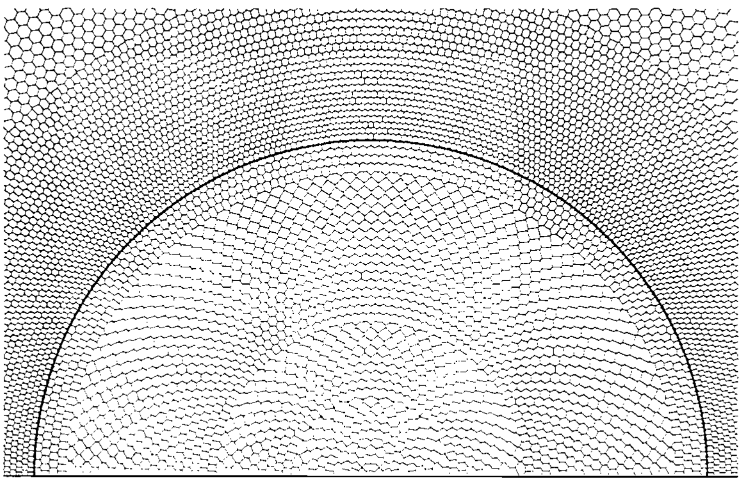

Figure 7.6: Initial Voronoi mesh used in the Free-Lagrange simulations. Bottom solid line is the axis of symmetry, the semi-circular solid line represents material interface and dots indicate positions of fluid particles. This figure is a close-up of Fig. 7.6 to show the Voronoi cells in the bubble and near the material interface.

mesh of the problem near the bubble is shown in Fig. 7.6. The first and second regions are made out of hexagonal Voronoi meshes that are generated in a circular manner to give a smooth bubble surface. The second region however, is made finer than the first. This is because, during the collapse of the bubble, the movement of particles due to the formation of the high-speed liquid jet will result in coarser mesh, especially around the circumference of the bubble surface and near the liquid jet area. Hence, a high initial mesh resolution is needed to capture the dynamics of the flow accurately, and also to maintain a smooth air-water interface. Moreover, the size of the computational cells increases gradually further away from the bubble. In the main domain area on the other hand, the computational cells size are made much coarser in order to save on computational cost. However care is taken to avoid any sudden change in the cell size at the transition boundary between the second region and the main domain area. The cell size of the main domain is approximated from the area of the computational cell in the second region that lies near the transition boundary (Fig. 7.7). This is to prevent any abrupt changes in the mesh cell size between the second region and the main domain.

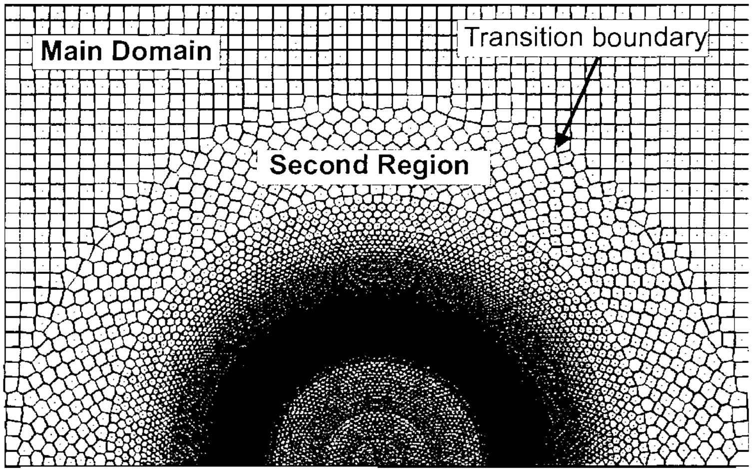

Figure 7.7: Initial Voronoi mesh used in the Free-Lagrange simulations, depicting the mesh transition between the main domain and the second region.

It is necessary to conduct a grid convergence study to determine the optimum degree of mesh resolution or number of grid points required to resolve the bubble evolution and to capture the dynamics of bubble collapse at minimal computational cost. The initial conditions are the same as in Section 7.1. The smoothing gain α that is used in this study is kept constant at 4.0×10^3 for all cases. Three cases were simulated, with the number of initial grid points set at 6135 for the course mesh, 32085 for the intermediate mesh and 77406 for the fine mesh. Fig. 7.8 shows the initial structure of the *Voronoi* mesh for all three cases.

Throughout the duration of the simulation, the number of grid points quoted above would change as a result of the refinement and derefinement procedure that prevents a cell area ratio mismatch. The way in which both 'derefinement' and 'refinement' procedure works was explained earlier in the report, in Section 4.4.3. As the bubble starts to collapse as a result of the interaction with the lithotripter shock wave, the size of the computational cells on the air-water interface, and near the region of the liquid jet, increases due to radius variation. During the collapse stage where the jet liquid starts to form, the refinement

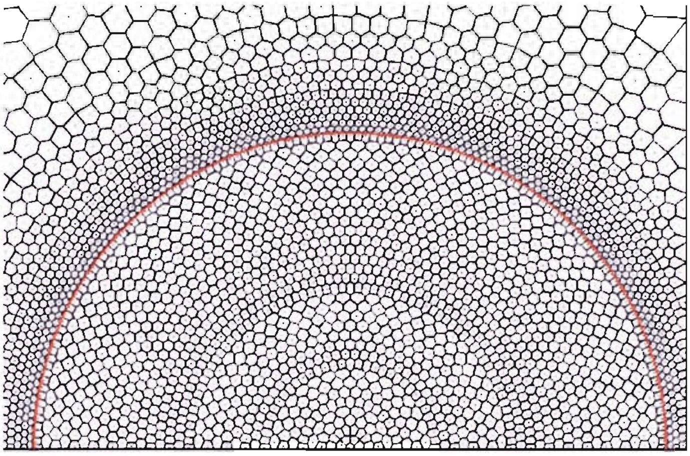

(a) Coarse Mesh

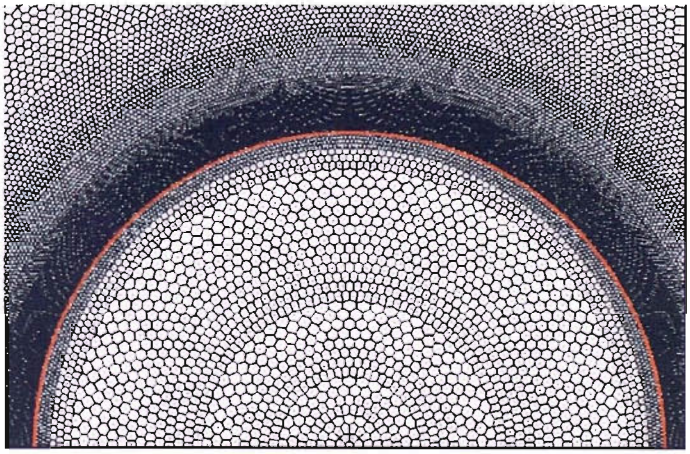

(b) Intermediate Mesh

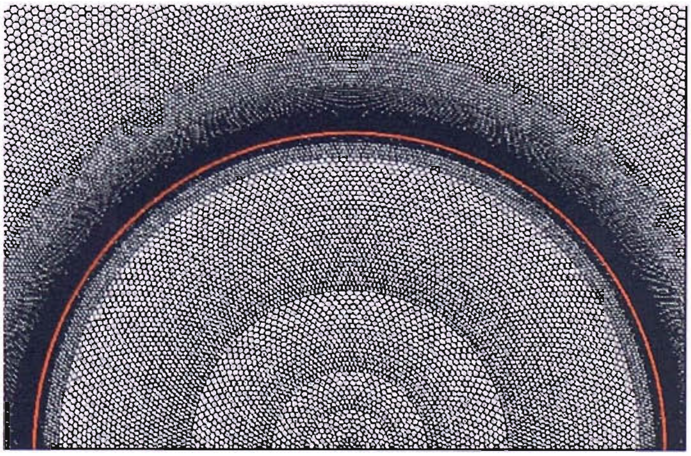

(c) Fine Mesh

Figure 7.8: *Voronoi* mesh of three different initial mesh resolutions.

Case	Initial Grid Points	Derefinement t_d, s
1	6135	3.0×10^{-12}
2	32085	3.0×10^{-12}
3	77406	8.0×10^{-13}

Table 7.2: Cases for grid convergence study

procedure is automatically executed to bifurcate the computational cells of the water in the upstream region near the interface. In contrast, the derefinement procedure is called in order to reduce the high particle number density in air near the vicinity of the bubble surface as the bubble collapses. The refinement and derefinement procedure that occurs in air and water are reversed when the bubble is expanding following the primary collapse. Hence, the two procedures control and dictate the grid resolution especially near the air-water interface.

The derefinement procedure is executed when the time-step of the simulation falls below a value predefined by the user at the start of the simulation. In the three cases considered here, three different time-steps that trigger the derefinement were used. This is given in Table 7.2. It is clear that the accuracy of the solution increases as the time-step decreases, but at the expense of an increase in computational cost.

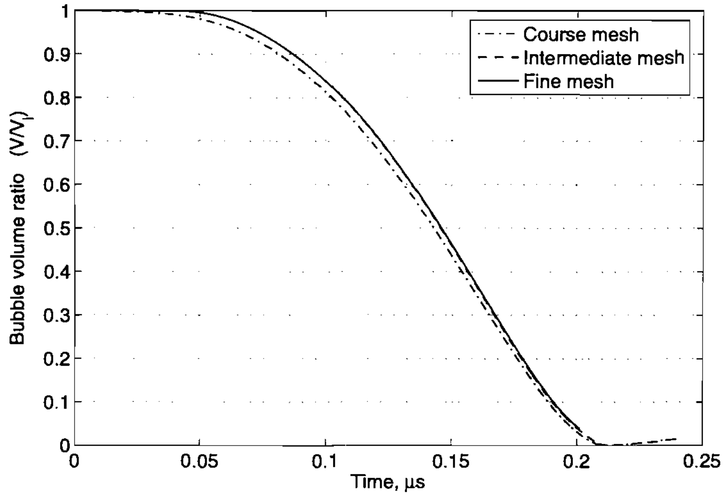

Figure 7.9: Bubble volume time history for various mesh resolution. V_i is the initial bubble volume. The intermediate and fine mesh curves are in very good agreement.

Fig. 7.9 shows the bubble volume-time history of the three cases. Time is measured from the moment the shock front reaches the upstream bubble wall. It can be seen clearly that the bubble volume history of the intermediate and fine mesh are in very good agreement, from the start of the collapse until the point where the simulation was stopped at $t \approx 0.24\,\mu s$. The bubble collapse rate in the coarse grid case is greater than the other two cases. This is apparent from $t = 0$ to $t \approx 0.21\,\mu s$, where the bubble starts to rebound. The difference is apparent in the early stages, i.e. $t = 0$ to $t \approx 0.15\,\mu s$ where the collapse for the bubble with the course mesh seems to occur earlier in time. Since the percentage difference is almost constant during the collapse, the absolute difference in volume naturally decrease as the bubble collapses. Furthermore, the effect of the smoothing interface forces on the fluid interfaces are less for the fine mesh compared to the course mesh. This is because, the distance x which dictate the magnitude of the restoring forces (Fig. 4.4) is smaller in the fine mesh case compared to the coarse mesh problem. Therefore, it is postulated that the interface restoring forces increases the bubble collapse rate in the latter. Following bubble rebound, the discrepancy in the bubble volume amongst these three mesh resolution is minute. The reason for this could be attributed to the fact that the refinement and derefinement procedure that took place after the rebound leave the size of the meshes for all three cases approximately the same in the region of the bubble on rebound. Based on the plotted result for the three different grid resolutions, the intermediate mesh resolution is optimum in capturing the dynamics of the bubble collapse. It is therefore used for the simulations that are presented in this report unless stated otherwise.

7.3 Lithotripter shock wave-bubble interaction in Free-field

The simulation of single cavitation bubbles in free-field is presented here.

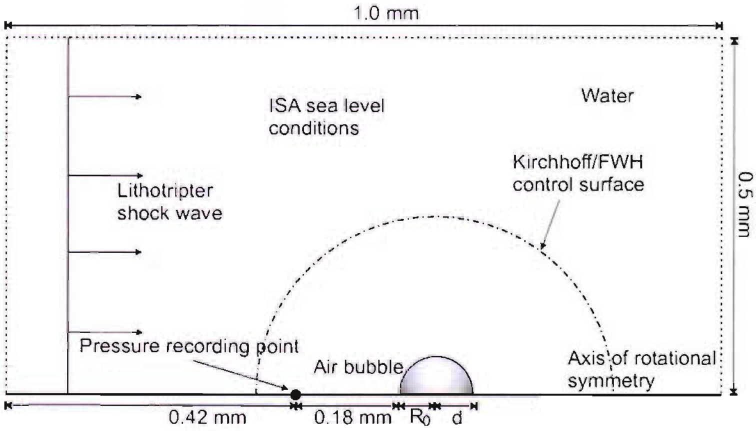

Figure 7.10: The geometry of the problem.

The problem studied in the present work comprises a single spherical air bubble immersed in water (Fig. 7.10). The boundary and initial conditions are similar to that discussed in Section 7.1. A pressure recording point is positioned on the axis of rotation, $0.18\,mm$ from the initial bubble centre in order to register pressure pulses produced by cavitation event.

The initial air bubble radius $R_0 = 0.06\,mm$, which according to Coleman *et al.* [24] was a typical radius of a secondary stable bubble[1]. Recent findings by Cunningham *et al.* [29] suggested that the radius of a stable air bubble near the focal point of the lithotripter shock wave may be as little as $40\,\mu m$. The work presented in this section was carried out before such findings were made, and therefore an initial bubble radius of $60\,\mu m$ was used.

However, it should be noted that the calculations of the predicted far-field pressure signature presented later in this chapter was made on a collapse of an air bubble with initial radius of $40\,\mu m$. This correction was made in view that the results were to be compared with those obtained from experimental work. When comparisons were made between the $40\,\mu m$ and $60\,\mu m$ bubble radius cases, the results showed that the dynamics of the collapsing bubble are similar. Both results showed the formation of the high-speed liquid jet and blast wave from the liquid-liquid impact. The only major difference is in the duration of the collapse and a slight reduction in the magnitude of the blast wave in the $60\,\mu m$ radius case.

7.3.1 Results and discussion

The results for the lithotripter shock wave-bubble interaction problem in free-field are given in Fig. 7.11 and Fig. 7.12. As a result of the profound acoustic impedance mismatch, a relatively weak shock is transmitted into the air bubble when the lithotripter shock (IS) (refer to Fig. 7.12) hits the left bubble wall, whilst a strong expansion fan is produced in the water, running leftwards and upwards (EX in Fig. 7.12(a)). The high particle velocity behind the incident shock causes the bubble wall to deform to the right. At $t = 0.07\,\mu s$, the incident shock has traversed almost the full bubble width (Fig. 7.11(a)). The interaction between the shock and expansion waves originating at the bubble surface results in weakening and curvature of the shock. The air shock propagates more slowly and decouples from the incident shock. The deformation of the upstream bubble wall continues after the incident shock has passed, because of the inertia of the water.

Interaction of the lithotripter pulse with the bubble causes it to collapse rapidly. The

---

[1] A secondary stable bubble is a bubble which has been formed as a result of the interaction of a preceding lithotripter pulse with a cavitation nucleus, and which has reached a state of mechanical equilibrium with the surrounding fluid.

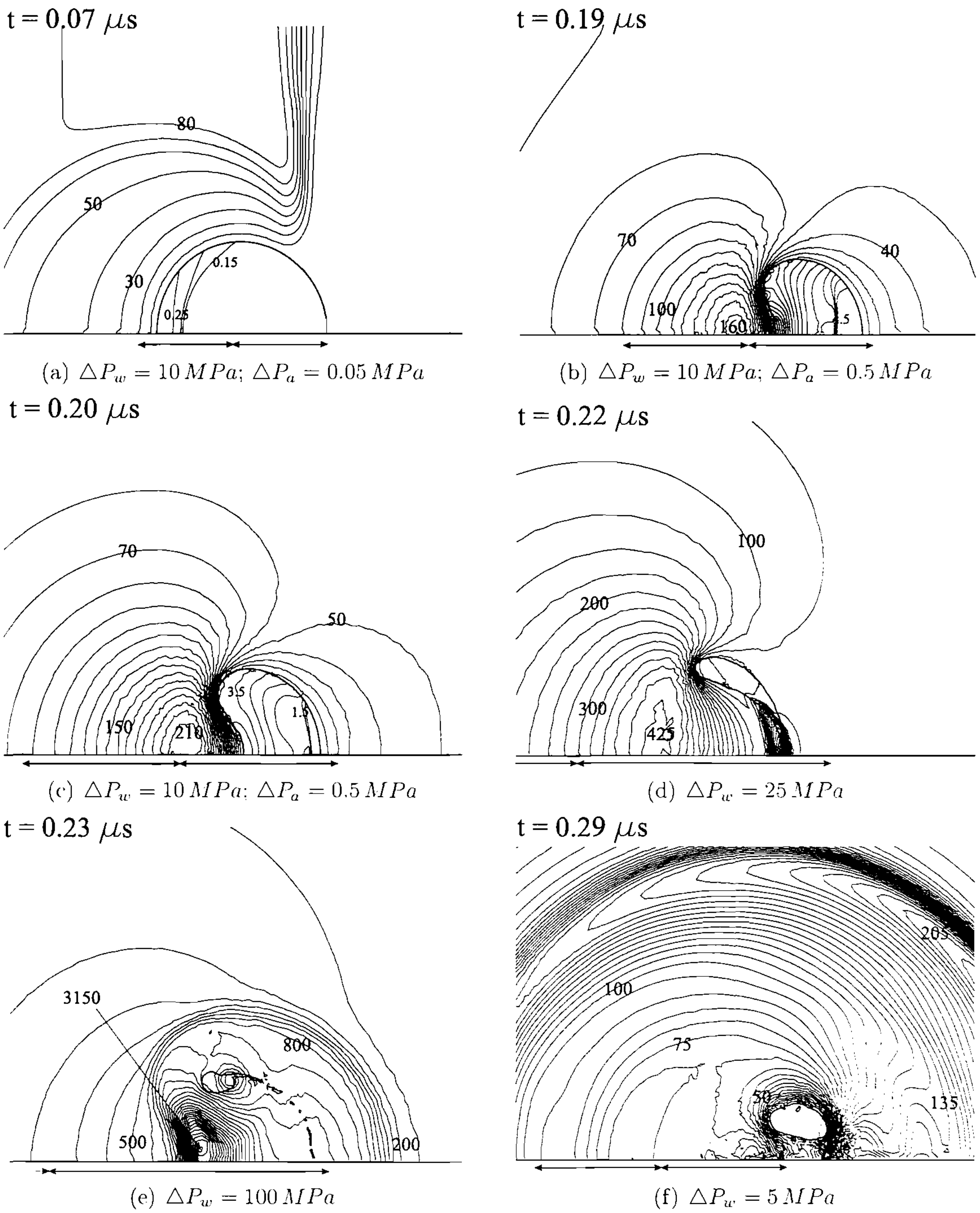

t = 0.07 μs

(a) $\triangle P_w = 10\,MPa$; $\triangle P_a = 0.05\,MPa$

t = 0.19 μs

(b) $\triangle P_w = 10\,MPa$; $\triangle P_a = 0.5\,MPa$

t = 0.20 μs

(c) $\triangle P_w = 10\,MPa$; $\triangle P_a = 0.5\,MPa$

t = 0.22 μs

(d) $\triangle P_w = 25\,MPa$

t = 0.23 μs

(e) $\triangle P_w = 100\,MPa$

t = 0.29 μs

(f) $\triangle P_w = 5\,MPa$

Figure 7.11: Pressure contours for an air bubble impacted by a lithotripter shock with $P^+ = 90\,MPa$ and $P^- = 10\,MPa$. Horizontal arrows indicate initial position and size of bubble. The symbols $\triangle P_w$ and $\triangle P_a$ indicate the increments between contours in the water and air respectively.

pressure gradient in the water near the upstream bubble increases as time progresses.

It is clear from Fig. 7.11 that the collapse is asymmetric as the downstream bubble wall remains stationary up to about $t = 0.11\,\mu s$ (Fig. 7.11(b)). At about $t = 0.20\,\mu s$ (Fig. 7.11(c)), the upstream bubble wall starts to involute to form a distinct jet of liquid running to the right along the symmetry axis. The motion of the bubble during this phase is controlled almost exclusively by the inertia of the water. The liquid jet continues to accelerate and hits the downstream wall at about $t = 0.22\,\mu s$, isolating a lobe of trapped and highly compressed gas which form a toroid in three dimensions (Fig. 7.11(d)). The variation of jet velocity with time is shown in Fig. 7.12(b). The jet continues to accelerate as it pierces the bubble, reaching a maximum of over $1200\,ms^{-1}$ immediately prior to jet impact. It is believed that high-speed jets of this type play a primary role in cavitation erosion [7] as well as formation of circular pits and indentation on metal foils [26] as discussed in Chapter 2. It is clear that the initial collapse and all the bubble motion shown in Fig. 7.11 are driven solely by the compressive component of the lithotripter pulse as the bubble does not encounter the tensile portion of the pulse before the primary collapse is complete.

The impact of the jet on the downstream bubble wall produces an intense blast wave in the surrounding water. It also leads to the creation of bubble fragments (Fig. 7.11(e)). These fragments may coalesce with the main cavity or act as nuclei for further cavitation events. The peak overpressure exceeds $1.0\,GPa$. As a result of the high velocity of the jet fluid, the blast wave advances relatively slowly to the left below the bubble. Consequently, the blast front is asymmetric. The interaction between the high-momentum liquid jet and the downstream low-momentum water produces a strong vortex flow.

In Fig. 7.11(e), the air cavity is drawn into the vortex core while the blast wave continues to propagate outwards radially from the bubble. The blast wave produces a sharp peak (BW) on the pressure-time history curve recorded at the pressure point (Fig. 7.12(a)). The strength of the blast wave decreases as it propagates into the surrounding water. The radiated blast wave could explain the large pressure spikes recorded by Zhong *et al.* [107] near primary collapse in their experimental studies.

The time history of the cavity volume is shown in Fig. 7.12(a). The volume reduces almost linearly with time from shock-bubble impact, until the first minimum at $t \approx 0.22\,\mu s$. The end of the linear phase correlates with the liquid jet impact. At this time the internal pressure greatly exceeds that of the surrounding water, and therefore the bubble begins to expand, entering an oscillatory state with two further cycles of expansion and collapse. The simulation was halted after the third collapse, however the Gilmore-Akulichev model predicts that when the bubble encounters the tensile portion of the lithotripter pulse it will enter a phase of prolonged expansion, followed by a series of lower-frequency oscillations [22] (Refer to Section 2.6.1 in Chapter 2).

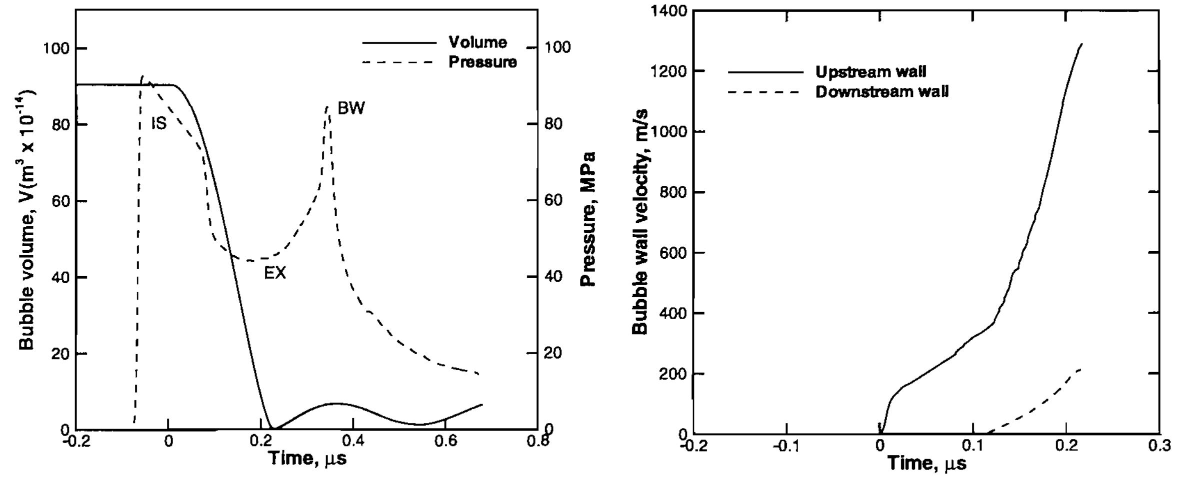

(a)

(b)

Figure 7.12: **(a)** Pressure and bubble volume time history. Pressure is measured at point 'x' on Fig. 7.10. IS - Lithotripter shock, EX - Expansion waves, BW - Blast wave **(b)** Liquid jet velocity history.

7.3.2 Far-field Pressure Signature

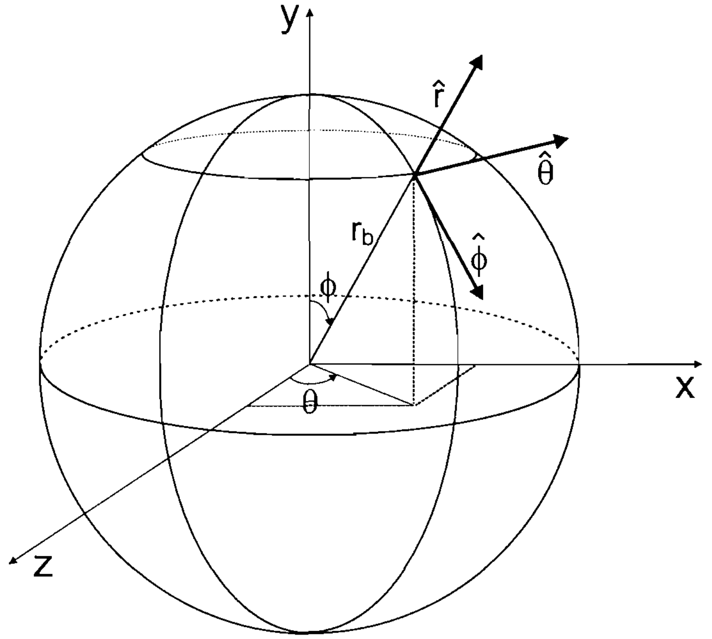

Figure 7.13: Nomenclature and the aero-acoustic problem geometry.

A spherical control surface for the evaluation of the Kirchhoff and FWH integrals is positioned in the *Vucalm* CFD computational domain as shown in Fig. 7.10. The radius of the control surface is $R_{cs} = 0.2\,mm$ and the number of control points along the half circumference of the surface is 90. In the calculation, the observer is placed at a distance of $150\,mm$ from the initial bubble centre, i.e. $r_b = 150\,mm$. This value is chosen because it is typical of the radiation distance wave from the lithotripter focal point to the hydrophone placed on the patient's skin during clinical *in-vivo* treatment.

The nomenclature, geometry and reference frame for the aero-acoustic problems are illustrated in Fig. 7.13. The nomenclature used here in describing the observer position is identical to the one used for structuring and discretisation of the spherical control surface as described in Chapter 5 in Section 4.5.1. The reference frame (x, y, z) in Fig. 7.13 is analogous to the one used in the $Vucalm$ formulation, i.e. the lithotripter shock wave propagates in positive-x direction. However, in the latter, the x-axis represent the axis of symmetry.

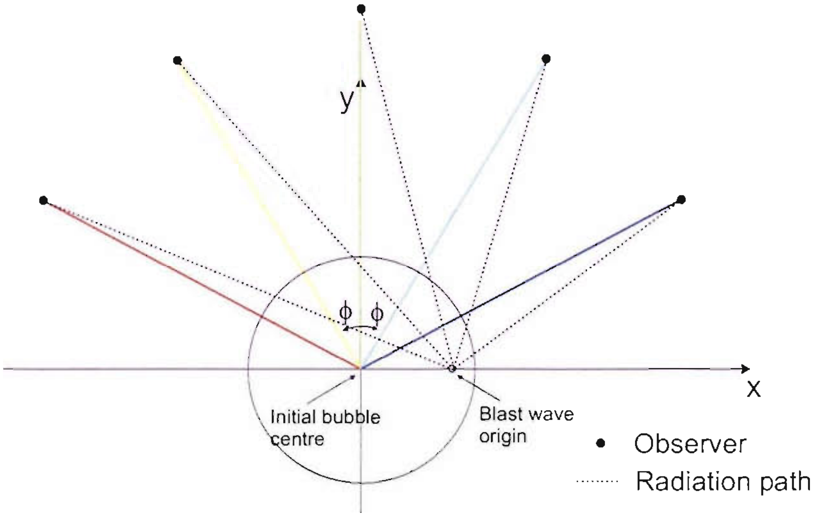

Figure 7.14: Blast wave radiation path to observer for different θ and ϕ on the XY-plane.

The variables θ and ϕ are used to described the position of the observer, while r_b is the observer distance measured from the initial bubble centre. Based on the geometry shown in Fig. 7.13, the polar coordinates for any point on the control surface and the observer are easily given by,

$$\begin{aligned} x &= r_b \sin\theta \sin\phi \\ y &= r_b \cos\phi \\ z &= r_b \cos\theta \sin\phi \end{aligned} \tag{7.2}$$

and

$$r_b = \sqrt{x^2 + y^2 + z^2} \tag{7.3}$$

Kirchhoff Results

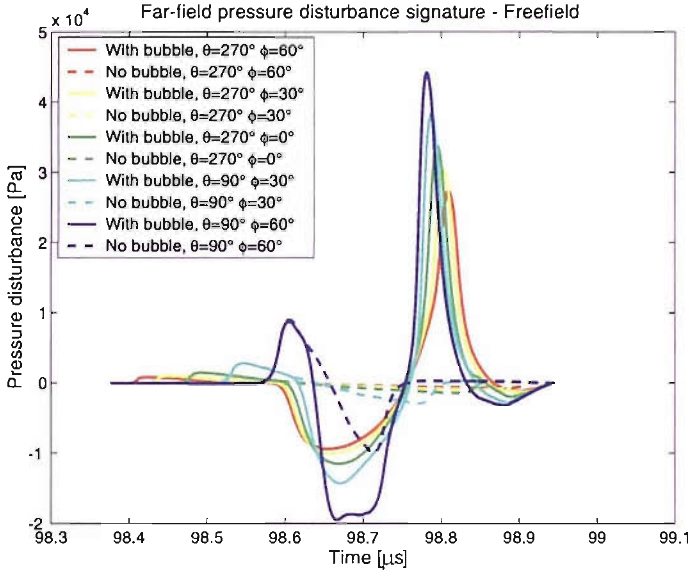

Figure 7.15: The free-field pressure signature predicted using the Kirchhoff method at an observer positioned 150 mm from the initial bubble centre. The results for various θ and ϕ are plotted for comparison.

Fig. 7.15 shows the pressure-time history calculated in the far-field using the Kirchhoff formulation given in Eqn. 4.41. Results for various θ and ϕ are plotted for comparison in order to determine the variation in the far-field pressure profile at different observer position and the dependency on the directionality of the lithotripter shock wave. The same set of integration surface and CFD input data were used for all calculations. Calculations were also carried out for bubble-free problems where no lithotripter shock wave-bubble interaction occurs (plotted as dashed lines in Fig. 7.15). In these cases, an 'empty' computational domain is created and the shock wave is allowed to propagate across the Kirchhoff control surface. This calculation is necessary because the Kirchhoff formulation assumes that the entire source region is enclosed within the surface. Therefore, the contribution of the shock wave to the near-field input data could be a source of error in the prediction of the far-field noise. However, the results in Fig. 7.15 (dotted curves) show that the 'sweeping' of the propagating shock waves across the control surface has minimal effect on the amplitude and profile of the far-field waveforms resulting from the shock-bubble interaction.

Comparison can be also made between the near-field pressure-time history (Fig. 7.12(a)) and the predicted far-field aeroacoustic waveforms (Fig. 7.15). The plotted results from the Kirchhoff calculations (Fig. 7.15) show that the predicted far-field pressure profile has similar characteristics to that calculated directly from CFD calculation (Fig. 7.12(a)). The trough of the expansion wave and the sharp peak of the spherical blast wave generated by the liquid jet impact on the downstream bubble wall are clearly captured. Owing to the asymmetry of the bubble collapse, the peak positive pressure of the blast wave is greater when $\theta = 90^\circ$, i.e. the observer is positioned closer to the origin of the blast wave compared to when $\theta = 270^\circ$. As the observer position is rotated on the XY-plane from $\theta = 90^\circ, \phi = 60^\circ$ (blue line) to $\theta = 270^\circ, \phi = 60^\circ$ (red line), the waves travel longer distance to arrive at the observer location and therefore, the amplitude of the pressure seen by the observer decreases. However, since $R_{cs} = 0.2\,mm$ and observer position $r_d = 150\,mm$, the maximum variation in path length for the blast wave with θ is only of the order $0.05\,\%$. Therefore, it is believed that the directional nature of the blast wave is more likely to explain the observations.

FWH Results

Although discussion on the advantages and disadvantages of the FWH formulation and the Kirchhoff formulation were given in Chapter 4, the deciding factor is how well these methods compare in practice. According to di Francescantonio [34] the main advantage to applying the FWH equation on a Kirchhoff-type integration surface is that interaction with CFD codes is easier because the normal derivative of pressure is no longer required. Although this is true in most CFD numerical simulation, the calculation of the normal derivatives in the *Vucalm* code is easily and readily obtained. Furthermore, the calculations carried out in this work and in previous test cases do not include the quadrupole source term, which greatly simplified the aeroacoustic problem.

It is important to note here that the numerical accuracy of both the Kirchhoff and FWH codes are very similar because the quadrature is based on the CFD grid, i.e. all retarded time computations and quadrature points are identical for these two codes. Furthermore, the characteristics of the control surface are identical where a spherical control surface is used. In addition in both methods, similar discretisation of the surface and spatial interpolation technique of the input data are implemented. As in the Kirchhoff problem discussed above, the integration surface is located $150\,mm$ from the initial bubble centre. The calculation is performed on 90 control points placed along the half circumference of the axisymmetric control surface.

The results of the predicted far-field noise using the FWH method for control surface radii of $0.2\,mm$ and $0.35\,mm$ are shown in Fig. 7.16 and Fig. 7.17 respectively. The results

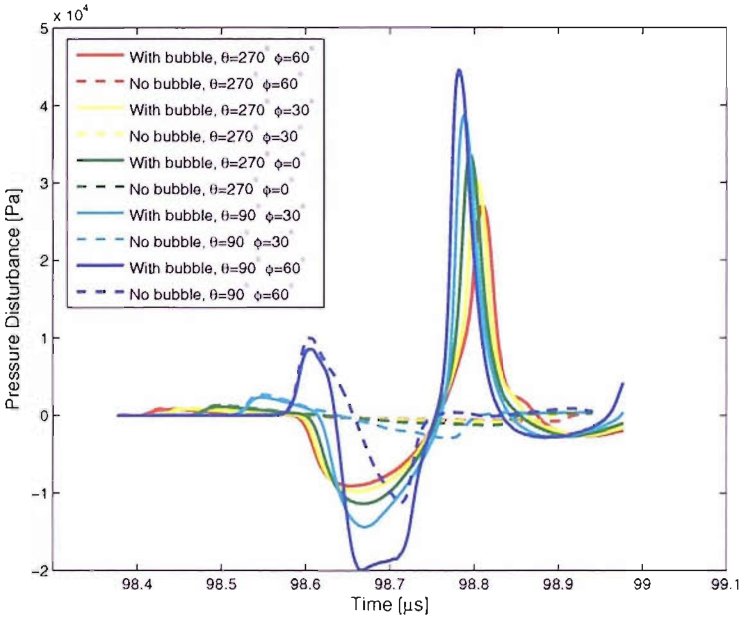

Figure 7.16: The free-field pressure signature predicted using the FWH method at an observer positioned 150 mm from the initial bubble centre. The results for various θ and ϕ are plotted for comparison. Control surface radius, $R_{cs} = 0.2\,mm$.

for $R_{cs} = 0.2\,mm$ are in agreement with that of the Kirchhoff results (Fig. 7.15). The variation of the pressure waveform for different observer position agrees well. However, as the control surface radius is increased to $0.35\,mm$ the amplitude of the far-field pressure is smaller for all 5 observer positions. This could be attributed to the attenuation and spreading of the near-field pressure in *Vucalm* calculation as it propagates across a coarser mesh. Another explanation for the difference could be attributed directly to the formulation of the FWH code itself. According to Brentner & Farassat [17] and di Francescantonio [34], as the integration surface is moved farther away, more and more of the quadrupole source contribution is accounted for by the surface integrals. Hence, the reduction in the amplitude of the far-field blast wave pressure might be because of the inclusion of higher degree of non-linearity in the FWH calculation. The nonlinearity causes steepening and shock dissipation. However, if this was the case, one would expect the difference between the two methods to be greater when $R_{cs} = 0.2\,mm$. This is because the degree of nonlinearity is greater when $R_{cs} = 0.2\,mm$ than when $R_{cs} = 0.35\,mm$. The Kirchhoff method is expected to be prone to error if the control surface is in non-linear region, while FWH is not. However, the results presented here show that the Kirchhoff and FWH methods agree well for $R_{cs} = 0.2\,mm$. Therefore, it is unlikely that the discrepancy

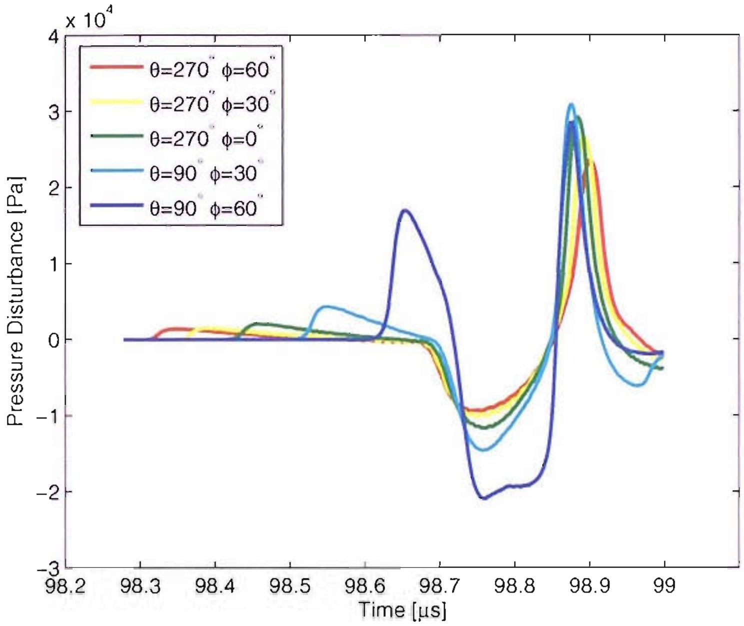

Figure 7.17: The free-field pressure signature predicted using the FWH method at an observer positioned 150 mm from the initial bubble centre. The results for various θ and ϕ are plotted for comparison. Control surface radius, $R_{cs} = 0.35\,mm$.

is due to the greater non-linearity in region $R_{cs} = 0.2\,mm$. One possible explanation is the dissipation and dispersion errors due to coarsening of the Voronoi mesh in the *Vucalm* calculation.

7.3.3 Non-linear Wave Propagation

The usually assumed linearity of acoustic pressure with density is only an approximation valid at infinitesimal amplitudes. A more accurate pressure density relationship is given by the series expansion,

$$p = c_0^2 \rho + \frac{1}{2}\frac{c_0^2}{\rho_0}\frac{B}{A}\rho^2 + \ldots \tag{7.4}$$

where c_0 is sound speed and B/A is the second order parameter of nonlinearity. Excluding the second term in Eqn. 7.4 leads to linear acoustics. Keeping the first two terms enables one to deal with problems in nonlinear acoustics.

Nonlinear absorption is a process associated with nonlinear propagation that leads to a change in the amplitude and shape of the propagating wave. A method for transforming plane-wave solutions to account for spreading of spherical waves is given in Hamilton and Blackstock [44]. The solution for the pressure of a spherical wave with source condition

$p = f(t)$ at $r = r_0$ is given by Eqn. 7.5.

$$p(r,\tau) = \frac{r_0}{r} f\big(\tau \pm \frac{\beta p r}{\rho_0 c_o^3} \ln \frac{r}{r_0}\big) \tag{7.5}$$

where r is the radial coordinate (defined positive outward), ρ is the density, c is the sound speed, τ is the coordinate for the retarded time frame (i.e. $\tau = t \mp (r - r_0)/c_0$) and β is the traditional coefficient of nonlinearity for the fluid in which the wave propagates, given by $1 + \frac{B}{2A}$.

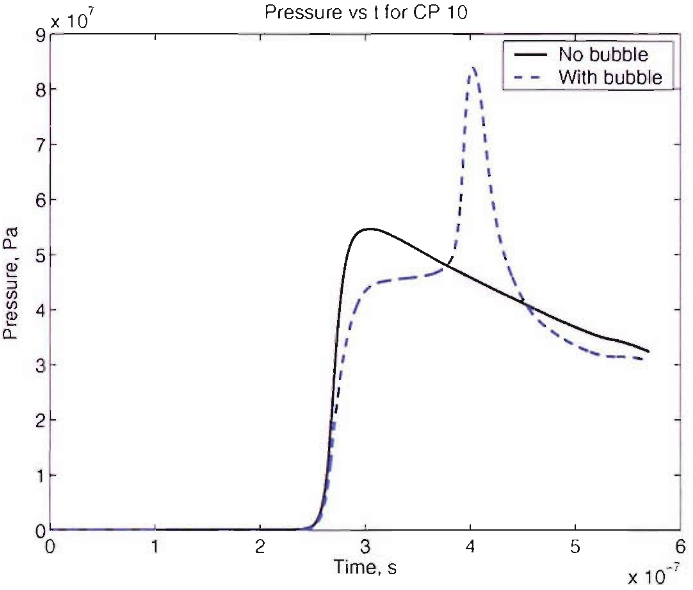

Figure 7.18: The pressure-time history at a control point.

The pressure-time history recorded at one of the control points on the control surface is depicted in Fig. 7.18. The pressure-time history for a bubble-free problem is also plotted. For simplicity, we will ignore pressure contribution from other control points. Notice that in Eqn. 7.5 for any distance r, the higher pressure values will travel faster than the lower pressure values. As a result, at some propagation distance, the high amplitude compressional pressure will overtake the lower pressure portion of the waveform. The nonlinearity effect on the pressure plotted in Fig. 7.18 is given in Fig. 7.19. The solution is no longer valid because it predicts a multivalued waveform, which is not physical.

The acoustic propagation to the far-field using the Kirchhoff and FWH methods discussed above were performed using linear wave propagation. Given the amplitudes and distances involved, some additional non-linear propagation may have occurred which will have changed the shape of the waveforms observed. The extent of this effect can be estimated by analysing the nonlinear spherical wave propagation as shown in Fig. 7.19.

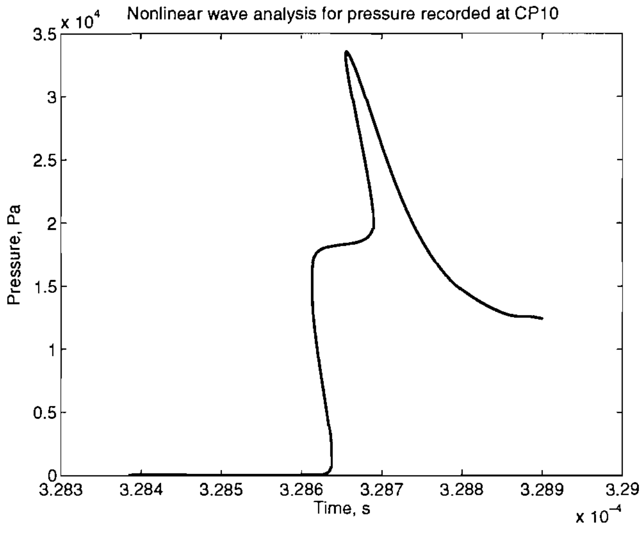

Figure 7.19: The effect of non-linearity on the pressure amplitude and shape of the waveform shown in Fig. 7.18

It is clear that the solution predicts multi-valued waveform. Technically the wave should be propagated in small steps. Each time the wave starts to become multi-valued the multi-valued region should be replaced with a shock front using the equal area rule (see reference [44], page 102). The shock is then propagated at the mean of the two velocities appropriate to the pressures either side of the shock front. This is a weak shock model. However, this approach was not taken, but it would remove the multi-valued regions.

7.3.4 Conclusion

The simulation of the near field interaction of a single air bubble with a lithotripter pulse, in axisymmetric form, has been performed using the Free-Lagrange code *Vucalm*. The results showed that the method allows sharp capture of the bubble boundary at all times and successfully predicts many details of the shock/bubble interaction. The impact of the shock on the upstream bubble wall causes it to involute and form a jet of liquid. The jet penetrates the interior of the bubble and strikes the downstream wall, generating a strong near-spherical blast wave into the surrounding fluid. Successive cycles of rebound and collapse occur prior to the long expansion phase, each collapse of the bubble emitting weak pressure waves into the surrounding water. This is predicted by the Gilmore-Akulichev model but has been overlooked by other workers. It is postulated that the liquid jet and strong spherical blast wave may assist in the fragmentation of kidney stones during clinical lithotripsy.

Comparison of the two aeroacoustic tools: the FWH equation and the Kirchhoff formulation for a stationary surface has been discussed. The FWH approach can include nonlinear flow effects in the surface integration if the usual assumption of impenetrable surface is relaxed. Both the expansion wave and the intense blast wave were sharply captured in the far-field using both methods. The results also showed good agreement on integration surface located at $R_{cs} = 0.2\,mm$ from the initial bubble centre, but FWH showed a reduction in the amplitude of the blast wave when the FWH control surface is positioned at $R_{cs} = 0.35\,mm$. However, with the current information gathered and due to limited time, it is not possible to determine the exact explanation for the differences.

Chapter 8

Simulations of Lithotripter Shock Wave-Bubble Interaction Near a Solid Wall

Numerical simulations of single bubble collapse near, or in contact with, a plane rigid boundary are presented in this chapter. Simulation runs are carried out at various stand-off distances.

The objectives of the current chapter are to investigate:

- the reflection, transmission and refraction of the shock waves as well as the velocity fields near the bubble.
- the collapse of a spherical bubble near a solid boundary and that of an attached bubble
- the effect of the dimensionless stand-off distance parameter, ζ
- the formation of the high-speed liquid jet and the velocity-time history
- the pressure-time history measured on the rigid wall
- the bubble volume-time history

The pressure time histories in the far-field are presented and comparisons between the FWH and Kirchhoff results are discussed.

8.1 Computational Domain and Initial Conditions

The problem chosen to study the interaction of a single spherical air bubble immersed in water near a solid boundary with a lithotripter shock wave is shown in Fig. 8.1. The

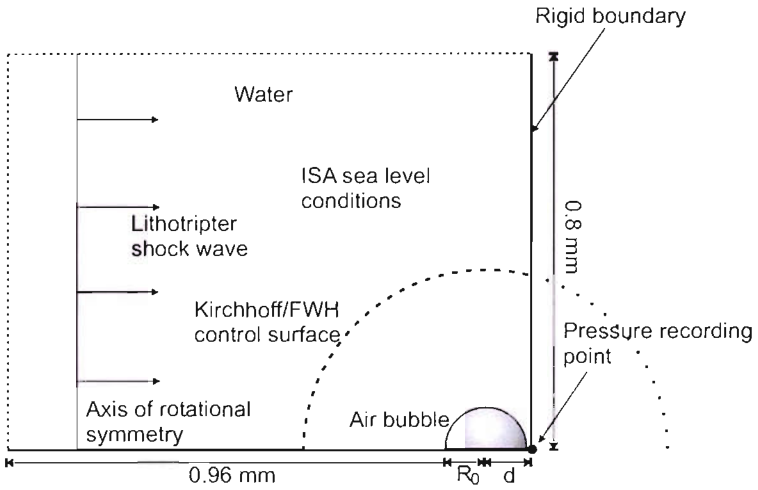

Figure 8.1: The geometry of the problem. Not to scale.

initial density for air and water are $1.2246\,kgm^{-3}$ and $1000\,kgm^{-3}$ respectively while the initial temperature and pressure for both fluids are $0.1\,MPa$ and $288.15\,K$. The initial air bubble radius $R_0 = 0.04\,mm$ [24], while d is the distance of the initial bubble centre to the boundary.

At the initiation of the calculation, in a manner similar to the problem in 'free-field' (see Section 7.3), the lithotripter pulse is introduced by imposing a time-dependent pressure boundary condition on the left boundary. A planar lithotripter pulse, with $P^+ = 60\,MPa$ and $P^- = -10\,MPa$, propagates through the water from left to right. The top boundary is non-reflecting at all times. A pressure recording point is positioned at the solid boundary on the axis of symmetry, in order to register pressure pulses produced by the cavitation event. A mesh of approximately 35×10^3 cells has been used. The lower domain boundary represents the axis of symmetry. All elapsed times are measured from the first shock/bubble impact.

The Kirchhoff and the FWH control surface is shown in Fig. 8.1. The radius of the control surface is $R_{cs} = 0.2\,mm$ and the number of control points along the half circumference of the surface is 90. In the calculation, the observer is placed at a distance of $150\,mm$ from the initial bubble centre, at 5 different location on the $XY-plane$ with $r_b = 150\,mm$. Beyond the rigid boundary, the control points lie outside the CFD computational domain (dotted line) and the data recorded at each of these points are for ambient conditions with zero pressure disturbance, $p' = 0$. Therefore, the only contributors to the far-field pressure signature are the control points that lie within the computational domain (shown as dashed line).

The parameters of the simulations are given in Table 8.1. The initial bubble radius

Case	Initial Radius, R_0 (μm)	Shock Strength, P^+ (MPa)	Distance, d (μm)	Stand-off distance, ζ
1	40	60	42.5	1.0625
2	40	60	45.0	1.125
3	40	60	55.0	1.375
4	40	60	65.0	1.625
5	40	60	75.0	1.875
6	40	60	85.0	2.125

Table 8.1: Various cases for '*stand-off distance* study

and lithotripter shock strength are kept constant in the study, while varying the distance of the bubble centre from the solid wall. In the calculation of the parameter 'stand-off distance', the value for R_{max} is taken as the bubble initial radius. This assumes that the initial radius is the maximum radius the bubble before it is collapsed by the lithotripter shock wave. The water is represented by the Tait EOS and is initially at ISA sea level conditions. The bubble is assumed to contain air and is represented by the ideal gas EOS. Thus the ratio of specific heat, γ, is 1.4.

8.2 Results and Discussion

8.2.1 Detailed analysis of $\zeta = 1.0625$ (Case 1)

In this problem, the asymmetric collapse of the bubble is induced not only by the relatively strong incident lithotripter shock wave but also by the presence of the rigid boundary in the vicinity of the bubble. These two factors are contributory elements to a full description of the bubble collapse processes. The results of shock/bubble interaction for Case 1 is given in Fig. 8.2-8.4 in which pressure contours are plotted to illustrate the changes in bubble dynamics and in the surrounding fluid. The stand-off distance for this problem is 1.0625.

Fig. 8.2(a) is 0.02 μs after shock impact. As a result of the large difference in acoustic impedance between the air and water, a weak shock is transmitted into the air and a relatively strong expansion wave is generated in the surrounding water when the lithotripter shock wave strikes the upstream bubble wall. The particle velocity behind the shock is high and therefore a large momentum will impact the gas-water interface. This causes the bubble wall to deform to the right. Fig. 8.2(b) onwards show the reflection of the shock on the air/water interface, where it is reflected as an expansion wave. The expansion waves propagates leftwards and upwards while the main incident shock traverses downstream

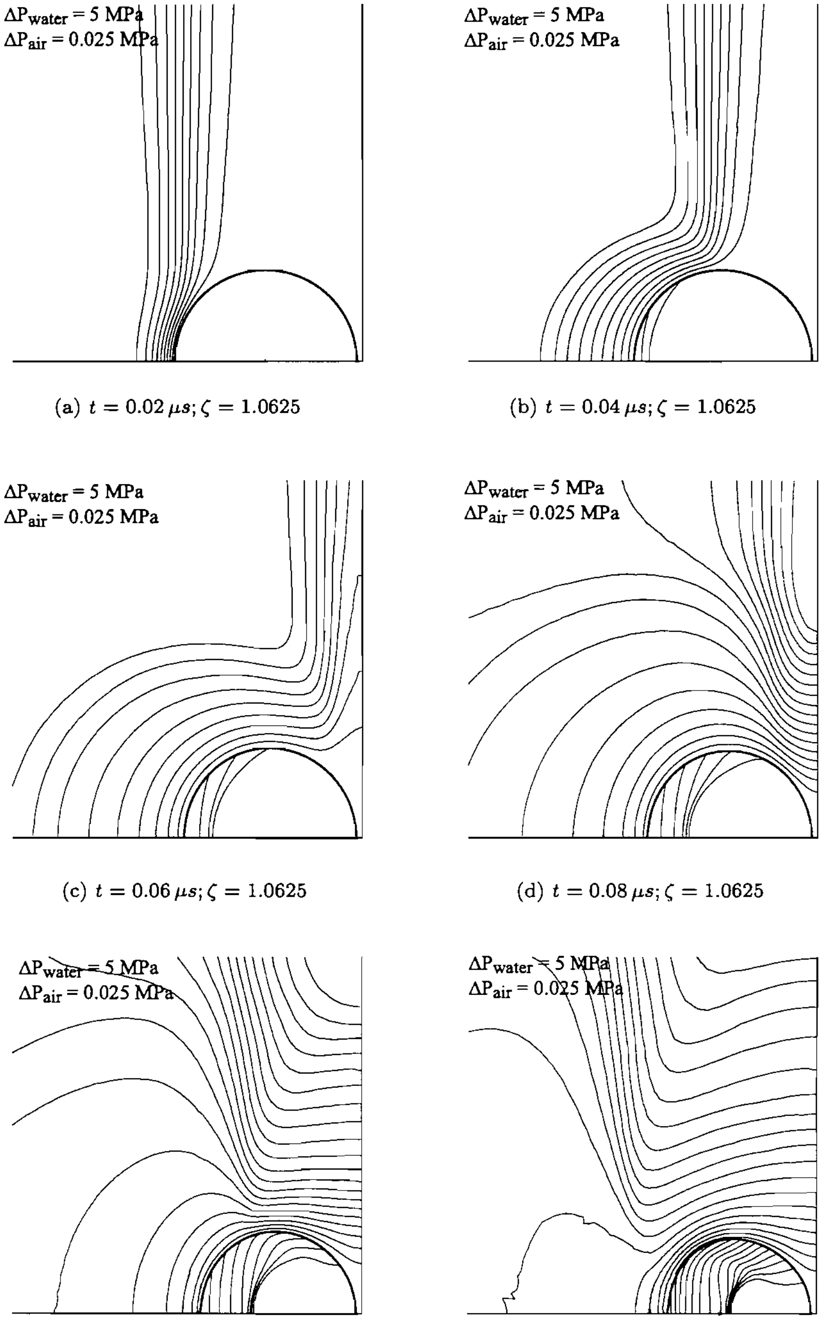

(a) $t = 0.02\,\mu s; \zeta = 1.0625$

(b) $t = 0.04\,\mu s; \zeta = 1.0625$

(c) $t = 0.06\,\mu s; \zeta = 1.0625$

(d) $t = 0.08\,\mu s; \zeta = 1.0625$

(e) $t = 0.10\,\mu s; \zeta = 1.0625$

(f) $t = 0.12\,\mu s; \zeta = 1.0625$

Figure 8.2: Pressure contours of a bubble with initial radius $R_0 = 40\,\mu m$ collapsed by a lithotripter shock wave with strength of $P^+ = 60\,MPa$. The *stand-off parameter*,ζ is 1.0625.

and impact on the right solid wall. Although the transmitted shock inside the bubble is very weak compared to the compressive wave of the lithotripter shock, it will induce substantial heating of the bubble gas.

The interaction between the incident lithotripter shock and the expansion waves originating at the bubble surface has resulted in significant weakening of the shock. At $t = 0.06\,\mu s$ (Fig. 8.2(c)), the incident shock has traversed the full bubble width and impacts on the nearby solid boundary. The reflected shock further interacts with the expansion wave and is weakened further. At this moment, the top of the interface starts to collapse. The shock which has been transmitted into the air bubble will propagate more slowly and will decouple from the incident shock, while the bubble wall continues to deform. However, the downstream bubble wall nearest to the solid boundary is not aware of the presence of the shock and is not affected by the shock impact. This results in the asymmetric movement of the bubble wall where the upstream part of the bubble interface moves rapidly to the right, while the downstream wall of the bubble remains static. The reflected shock impacts on the downstream side of the bubble and strengthens the air shock. The impact also increases the incidence angle of the air shock at the point of shock contact on the bubble interface. The smooth curvature of the air shock which conforms to the upstream bubble interface shape is disrupted by a weak transmitted air shock from the top right of the bubble surface.

The pressure gradient in the water near the top of the bubble increases as time progresses (Fig. 8.3(a)-(f)). The pressure gradients drive the particles to flow toward the bubble. Further interaction with the reflected incident shock leads to a build up of non-uniform pressure distribution around the bubble surface with the pressure on the upstream higher than that on the downstream side near the solid boundary. As the reflected shock moves on, the whole bubble is enclosed by a higher pressure and collapses from all sides, yet asymmetrically due to the unequal momentum transfer and pressure distribution at different parts of the bubble wall. At $t = 0.014\,\mu s$ after shock impact, the bubble has lost its spherical symmetry. It is clear that the flow converges towards the rigid boundary and in the direction perpendicular to the incident shock [14, 15].

The initially weak air shock propagating within the bubble has strengthened due to the focusing effect arising from the spherical geometry of the problem and curvature of the bubble interface (Fig. 8.3(a)). By $t = 0.14\,\mu s$, the left moving reflected shock has traversed the full bubble width, severely weakened as it traverses through the expansion wave originating from the bubble surface. As depicted in Fig. 8.3(b), the shock within the gas converges near the downstream wall of the bubble and will result in an increase in pressure in that region. The intricate shape of the air shock is a consequence of both the geometry of the bubble wall which confines the shock and the variation of the geometry with time. Moreover, the spatially non-uniform deformation of the bubble wall yields a higher water velocity on the bubble centreline. This in turn generates additional compression waves in the air near the upstream bubble wall, which strengthen the air shock. This is as shown in Fig. 8.3(e)-(f) and Fig. 8.4 onwards.

When $t = 0.18\,\mu s$ (Fig. 8.4(a)), it is clear that the bubble has elongated and the downstream bubble wall has flattened due to the presence of the solid boundary. The water on the upstream wall accelerates towards the rigid wall, but the water layer trapped between the downstream bubble wall and the rigid boundary appears to stagnate. The slight elongation of bubble in the axial direction is due to the interaction with the reflected incident shock which induces the contraction of the top bubble surface. This bubble behaviour or deformation is not seen in the problem for shock-bubble interaction in free-field. At this stage, the bubble undergoes a rapid deformation with a formation of a distinct liquid jet running to the right along the symmetry axis (Fig. 8.4(a)). Another feature which is not seen in the free-field problem is in the shape of the liquid jet head. There appears to be an indentation in the jet tip on the symmetry axis. This is clearly depicted in the magnification of Fig. 8.4(a). It is postulated that this resulted from a recirculating flow at the tip of the jet, induced near the upstream of the bubble wall from the interaction of the reflected incident shock with the strong expansion wave originating from the bubble surface. Furthermore, as the jet deforms the upstream bubble wall, compression waves are produced in the air. The build up in pressure near the proximity of the liquid jet induces a secondary air shock, which propagates to the right within the bubble.

After $0.184\,\mu s$ after shock impact, the jet tip is more pronounced and has reached half way through the collapsing bubble (Fig 8.4(b)). As the jet accelerates towards the rigid boundary, the pressure inside the bubble increases rapidly. The strength of the secondary air shock increases and impacts on the opposite bubble surface. This shock has formed an oblique reflection at the top bubble wall. The incidence angle at the point of reflection increases with time due to the wall curvature but will undergo a near-normal reflection on the downstream wall which has flattened due to the presence of the solid boundary. The liquid jet hits the downstream wall between frames Fig. 8.4(b) and (c). On impact, the jet produces an intense blast wave in the surrounding water. The maximum effect of the blast wave is localised at the point of liquid-liquid impact and the peak over-pressure decays rapidly with distance from the jet impact point.

At $t = 0.192\,\mu s$, the jet has penetrated through the bubble, isolating a lobe of trapped air and highly compressed gas that resembles a tear-drop (Fig. 8.4(d)). It also leads to the creation of bubble fragments, originating from the air layer trapped between the jet tip and the downstream interface prior to impact. This is probably a numerical artefact

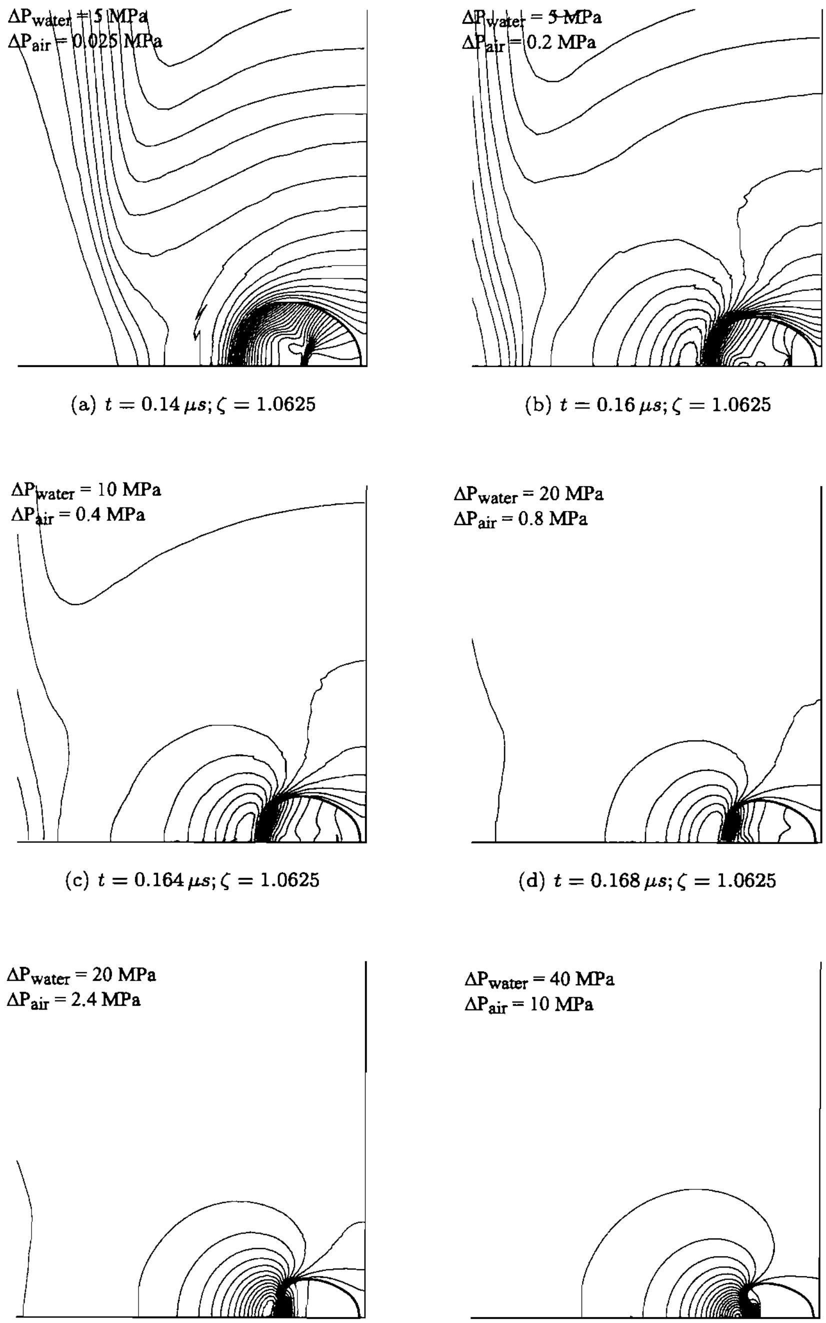

(a) $t = 0.14\,\mu s; \zeta = 1.0625$

(b) $t = 0.16\,\mu s; \zeta = 1.0625$

(c) $t = 0.164\,\mu s; \zeta = 1.0625$

(d) $t = 0.168\,\mu s; \zeta = 1.0625$

(e) $t = 0.172\,\mu s; \zeta = 1.0625$

(f) $t = 0.176\,\mu s; \zeta = 1.0625$

Figure 8.3: Pressure contours of a bubble with initial radius $R_0 = 40\,\mu m$ collapsed by a lithotripter shock wave with strength of $P^+ = 60\,MPa$. The *stand-off parameter*,ζ is 1.0625.

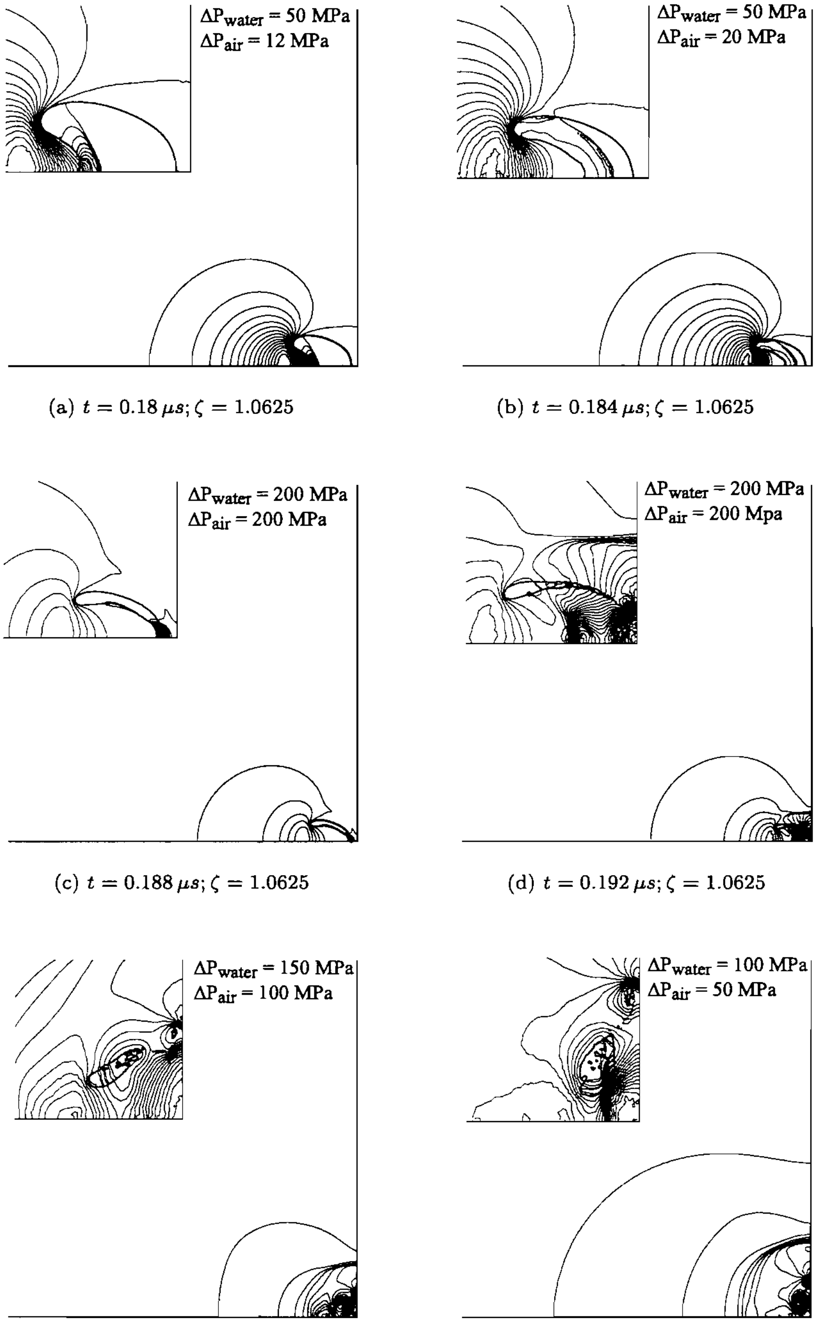

(a) $t = 0.18\,\mu s; \zeta = 1.0625$

(b) $t = 0.184\,\mu s; \zeta = 1.0625$

(c) $t = 0.188\,\mu s; \zeta = 1.0625$

(d) $t = 0.192\,\mu s; \zeta = 1.0625$

(e) $t = 0.196\,\mu s; \zeta = 1.0625$

(f) $t = 0.200\,\mu s; \zeta = 1.0625$

Figure 8.4: Pressure contours of a bubble with initial radius $R_0 = 40\,\mu m$ collapsed by a lithotripter shock wave with strength of $P^+ = 60\,MPa$. The *stand-off parameter*,ζ is 1.0625. The insert frame is a magnification of the flow and bubble interface.

, although it is possible that such a mechanism could occur in reality. However, it is very difficult to quantify experimentally due to the physical size and time scale of the problem. If such tiny isolated islands of gas do exist, they may coalesce with the main cavity as the flow evolves or act as nuclei for further cavitation events. The interaction of these nuclei with the tensile part of the lithotripter shock wave will cause them to expand and collapse, either spherically or asymmetrically, depending on the nature of the flow around the bubble and the degree of influence of the nearby solid boundary. These bubble fragments could also be collapsed by shock waves emitted from the collapse of neighbouring bubbles.

The interaction between the high-momentum liquid jet and the downstream low-momentum water produces a strong toroidal vortex flow. In addition, the flow is also redirected radially along the rigid boundary. As a result of the high-velocity in the jet fluid, the blast wave advances relatively slowly to the left below the bubble (Fig. 8.4(d)). The strong spherical blast wave propagating to the right will impact on the rigid boundary and will be reflected back into the surrounding fluid. Part of this wave will interact with the remaining cavity (Fig. 8.4(f)).

In Fig. 8.4(e) and (f), the air cavity as well as the bubble fragments are drawn into the vortex core that brings the bubble even closer to the solid boundary. The rebound and collapse of this air cavity is expected to cause further damage to the nearby solid boundary. This has been postulated by Shima [79], who identified four damage mechanisms from bubble collapse positioned either very close or attached to a solid boundary:

1. primary bubble collapse
2. the impact of the high-speed liquid jet on the downstream bubble wall
3. the collapses of many minute bubbles (bubble fragments) from the interaction between the outward radial flow following the liquid jet impact and the collapsing bubble surface
4. the rebound of the torus-like bubble.

The damage pattern arising from these impulsive pressure and jet formation of the main cavity and bubble fragments has been observed on 0.02 mm thick aluminum foil and indium specimen by Coleman *et al.* [26] and Tomita and Shima [87] respectively. The rebound of the cavity occurs soon after the jet impact when the air inside the bubble becomes highly compressed. Similarly to the free-field problem, a second collapse is expected to take place when the bubble pressure drops below the surrounding water pressure.

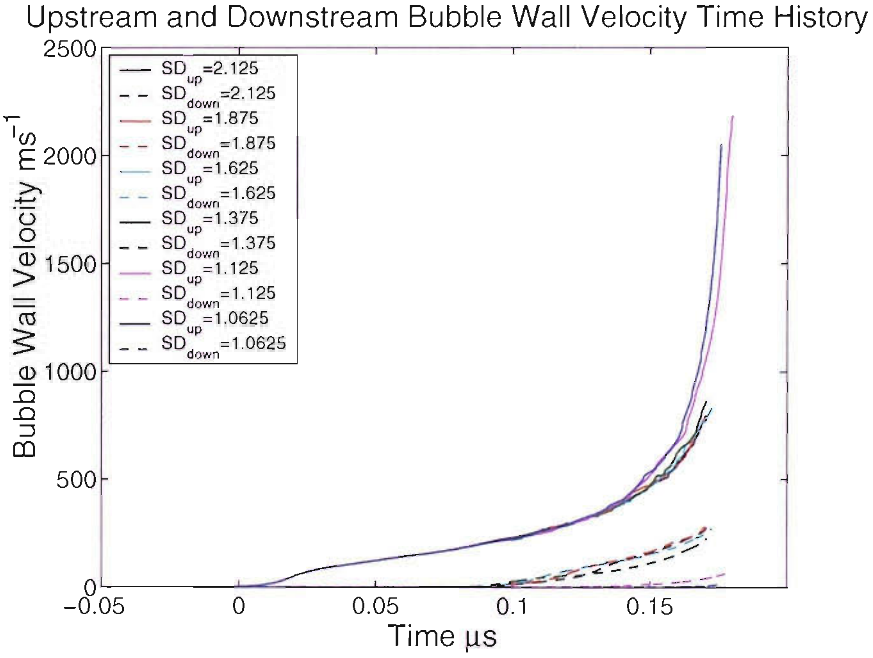

Figure 8.5: Upstream and downstream bubble wall velocity time history. Comparison for different stand-off distance (SD), ζ, as given in Table 8.1.

8.2.2 The effect of *Stand-off Distance*, ζ, on the bubble behaviour

In this section, studies are made to observe the behaviour of the air bubble at six different stand-off distances from the solid boundary. The initial conditions of the various problems are similar to Case 1 and have been given earlier in this chapter. The various parameters are summarised in Table 8.1.

The variation of the bubble wall velocity for different stand-off distance is depicted in Fig. 8.5. Upstream bubble wall velocity (UV) refers to the wall velocity of the upstream wall near the symmetry axis, which will later deform into a high-speed liquid jet. The jet tip velocity of the collapsing bubble is measured by taking the average of the absolute velocity of particles at the tip of the jet (identified as particles on the interface and the symmetry axis). It should be recalled here that the jet has a $3D$ axisymmetrical structure in that it is a body of revolution. The reason why it is important here is because the liquid jet has an off-axis component which is slightly divergent. The jet has a concave tip such that the leading annular front of the jet will actually impact on the downstream wall earlier than the jet centreline. However, the average motion of the liquid jet is along the axis of symmetry and therefore, the value calculated here gives a good approximation of the jet velocity. The downstream bubble wall velocity (DV) on the other hand is the wall velocity of the bubble in contact with the axis of symmetry and nearest to the solid boundary.

The solid curves and the dashed line represents UV and DV respectively. All six cases a show similar trend in that the velocity of the wall increases towards the end of the collapse phase. As discussed in Chapter 2, the asymmetry in the collapse of the bubble can be induced by two different mechanisms, the close proximity of a rigid solid boundary and from the interaction with a shock wave. Based on the plotted wall velocity curves, the degree of influence or contributory effects from both elements can be identified. Both curves representing the upstream wall and downstream wall can be categorised into two groups. It is clear that there exist a transition point (a value for ζ) at which the influence of the solid boundary on the collapse of the bubble is significant. UV and DV for both cases where $\zeta = 1.0625$ and $\zeta = 1.125$ can be distinguished from the other sets of curves which represent cases where the distance of the bubble from the rigid wall is relatively large. In the two former cases, the bubble is positioned very close to the solid wall.

The curves which represent the upstream wall velocity for $\zeta = 1.0625$ and $\zeta = 1.125$ shows that after $t = 0.15\,\mu s$ the jet velocity increases dramatically as it approaches the opposite wall. These differ from the other four cases, $3 - 6$, where the variation shows a more gradual rise. Both the upstream wall velocity for Cases 1 and 2 approaches over $2000\,ms^{-1}$ compared to Cases 3 to 6 where the maximum jet velocity is less than $1000\,ms^{-1}$. The rate at which the velocity of the upstream wall increases for $\zeta = 1.0625$ is higher than that for $\zeta = 1.125$ though the maximum wall velocity achieved in Case 2 is approximately $100\,ms^{-1}$ higher. However, the higher acceleration in Case 1 means that the jet impact occurs earlier than that in Case 2.

The variation of the downstream bubble wall velocity for Cases 1 and 2 can also be easily differentiated from the other cases. However, the trend is reversed such that the wall velocity is smaller for Cases 1 and 2 in comparison to Cases 3 to 6 where the DV increases gradually to about $250\,ms^{-1}$. This correlates with earlier explanation that the collapse is highly asymmetric. The water on the upstream wall accelerates towards the rigid wall, but the water layer trapped between the downstream bubble wall and the rigid boundary appears to stagnate. The downstream wall for Case 1 stays almost stationary but the wall velocity increases with increasing ζ. When the bubble is very close to the rigid boundary, the downstream wall is shielded from the oncoming lithotripter shock wave as well as from its reflection off the rigid boundary. As ζ increases, the incident shock will induce the collapse of the downstream wall and this is further enhanced by the impact of the reflected shock wave onto the bubble surface.

The time history of the bubble volume at different stand-off distance is shown in Fig. 8.6, normalised by the initial volume, V_i. The volume reduces almost linearly with

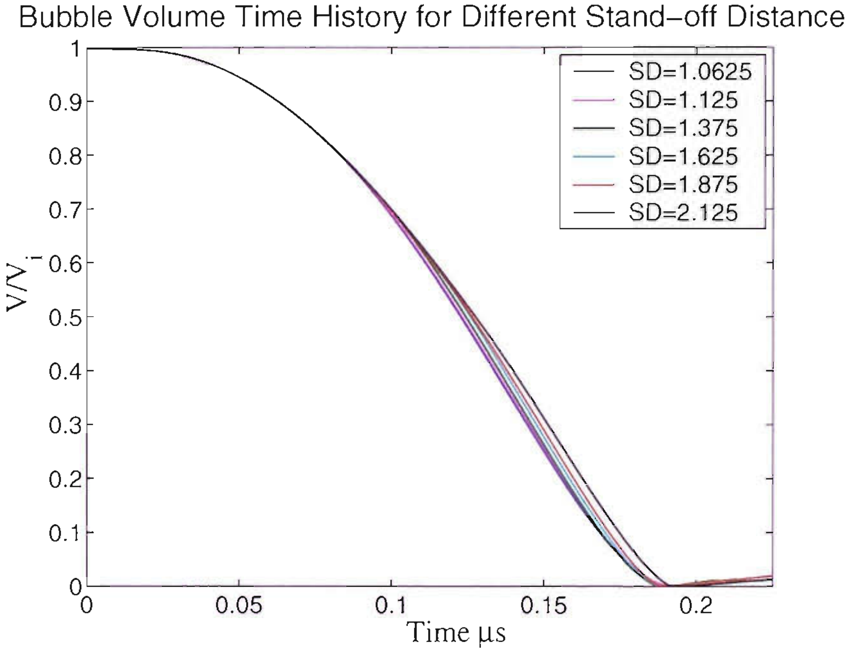

Figure 8.6: Bubble volume time history. Comparison for different stand-off distance, ζ, as given in Table 8.1.

time from $t \simeq 0.1\,\mu s$ to $t \simeq 0.17\,\mu s$, during which interval the volume ratio, V/V_i falls from $\simeq 0.7$ to $\simeq 0.15$. This linear phase ends as the liquid jet approaches the downstream bubble wall. Following the jet impact, the results shows that the volume continues to decline, but at a reduced rate, reaching a minimum at about $t = 0.18\,\mu s$. As discussed earlier, the jet tip lies away from the symmetry axis and impacts on the opposite bubble wall a distance away from the bubble centre line. Therefore, the minimum volume is actually achieved after liquid jet impact. At around minimum volume ($1.26E - 15\,m^3$), the cavity enters the vortex core and begins to expand under the influence of the increased in local static pressure in the air.

The curves also show an apparent trend in the rate at which the bubble collapses where the rate increases with decreasing ζ. This agrees with the bubble wall velocities plot (Fig. 8.5) discussed earlier. One might expect that the collapse rate for Cases 3 to 6 should be higher than Cases 1 and 2 because of the fact that the contraction of the bubble wall occurs in all directions, including from downstream, which remains almost static in the latter. However, the high liquid jet velocity and the deformation of the upstream wall in Cases 1 and 2 compensate for the small contraction rate of the downstream bubble wall and therefore the rate of collapse is greater as ζ decreases. The figure also shows that the time for the bubble to reach minimum volume increases with increasing ζ. In

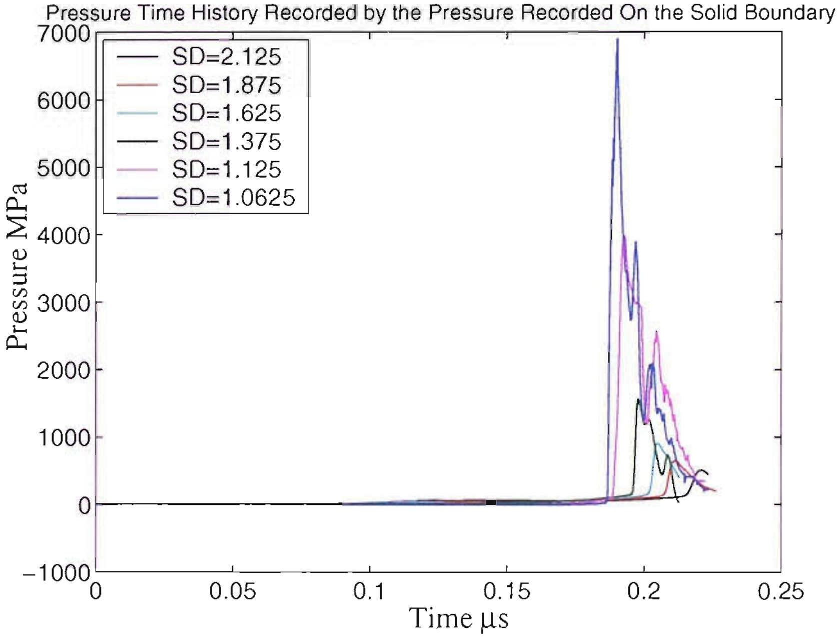

Figure 8.7: Pressure loading time history recorded on the symmetry axis at the solid boundary for different stand-off distance as given in Table 8.1.

comparison, for $\zeta = \infty$ (free-field), the bubble does not experienced lateral compression. In the near rigid boundary cases, the interaction with the reflected incident shock wave leads to lateral compression of the collapsing bubble. The collapse near a rigid boundary is also more violent that that in the free-field case. For $\zeta = 1.0625$, the liquid jet velocity exceeds $2000\,ms^{-1}$ (Fig. 8.5), while for $\zeta = \infty$, the maximum velocity of the upstream wall is approximately $1300\,ms^{-1}$ (Fig. 7.12).

The general profile of the pressure loading time history recorded at a particular point near the bubble is presented in Fig. 8.7. In this case, a pressure recording point is placed at the corner of the domain between the rigid boundary and the axis of symmetry as shown in Fig. 8.1.

The results are quite similar to the pressure-time history measured for the free-field problem as presented in Chapter 7. The pressure peak registered on the rigid boundary corresponds to the blast wave that is produced from the liquid-liquid impact of the high-speed liquid jet. The pressure due to the primary incident shock is not apparent on the curves as the transducer on the boundary is shielded by the bubble. As the strength of the blast wave decreases with increasing distance from the impact point, the peak pressure recorded on the rigid boundary decreases with increasing ζ. This is because the blast wave, which propagates approximately spherically, attenuates approximately in proportion to $1/r^2$ through the liquid. Following the sharp pressure peak of the blast

Case	Figure	Left Column	Right Column
1 and 2	Fig. 8.8 - 8.11	$\zeta = 1.0625$	$\zeta = 1.125$
3 and 4	Fig. 8.12 - 8.15	$\zeta = 1.375$	$\zeta = 1.625$
5 and 6	Fig. 8.16 - 8.19	$\zeta = 1.875$	$\zeta = 2.125$

Table 8.2: Listing of figures for ζ parameter study

wave, two other peaks can be observed for $\zeta = 1.0625$, $\zeta = 1.125$ and $\zeta = 1.375$. The first registers the large dynamic pressure of the high-speed liquid jet as it hits the rigid boundary. It is postulated that the second peak registers the pressure wave emitted from the rebound of the collapsed bubble. The amplitude is much lower than the other two peaks and as ζ increases, the amplitude of these two pressure peaks decreases. The maximum pressure loading recorded varies from nearly 7000 MPa for $\zeta = 1.0625$ to a mere 500 MPa for Case 6 where $\zeta = 2.125$. It is likely that it contributes to the cavitation erosion on the nearby surface and stone fragmentation in ESWL.

Evolution of the bubble with different stand-off distance is depicted in Fig. 8.8-Fig. 8.19. Pressure contours are plotted in air and water; while the heavy line represents the bubble interface. The contouring interval for both air and water is given in each frame and the value chosen is different in some sequences. Listing of the all the figures is given in Table 8.2.

The first figure for each stand-off distance sequence is at 0.16 μs after shock impact and the sequence follows the same time interval in all cases. By this time the incident lithotripter shock wave has reflected off the rigid boundary and traversed the full bubble width for the second time. The weak air shock that was transmitted into the air as a result of the shock impact has strengthened and propagates towards the rigid boundary. This air shock front can be seen clearly in frames (a)-(d) in Fig. 8.8, Fig. 8.12 and Fig. 8.16.

The relatively large momentum impact of the incident lithotripter shock on the gas-water interface causes the bubble wall to deform to the right. The results for Cases 2 – 6 presented here show that the bubble evolution and the pressure field are similar as in Case 1. The interaction of the incident shock and the bubble causes it to deform and leads to the formation of a liquid jet. One obvious difference between the sequences at $t = 0.16\,\mu s$ - $t = 0.168\,\mu s$ (Fig. 8.8, 8.12, 8.16) for all six cases is the size and shape of the air bubble. It is clear that for $\zeta = 1.0625$ and 1.125 (Fig. 8.8), the bubble is much larger and has elongated due to the influence of the rigid boundary. The bubble for Cases 3 – 6 (Fig. 8.12, 8.16) on the other hand, are much smaller and are more similar to the collapse of a bubble in free-field. This agrees with earlier discussion that the behaviour of the bubble with different ζ studied here shows two different trends, and

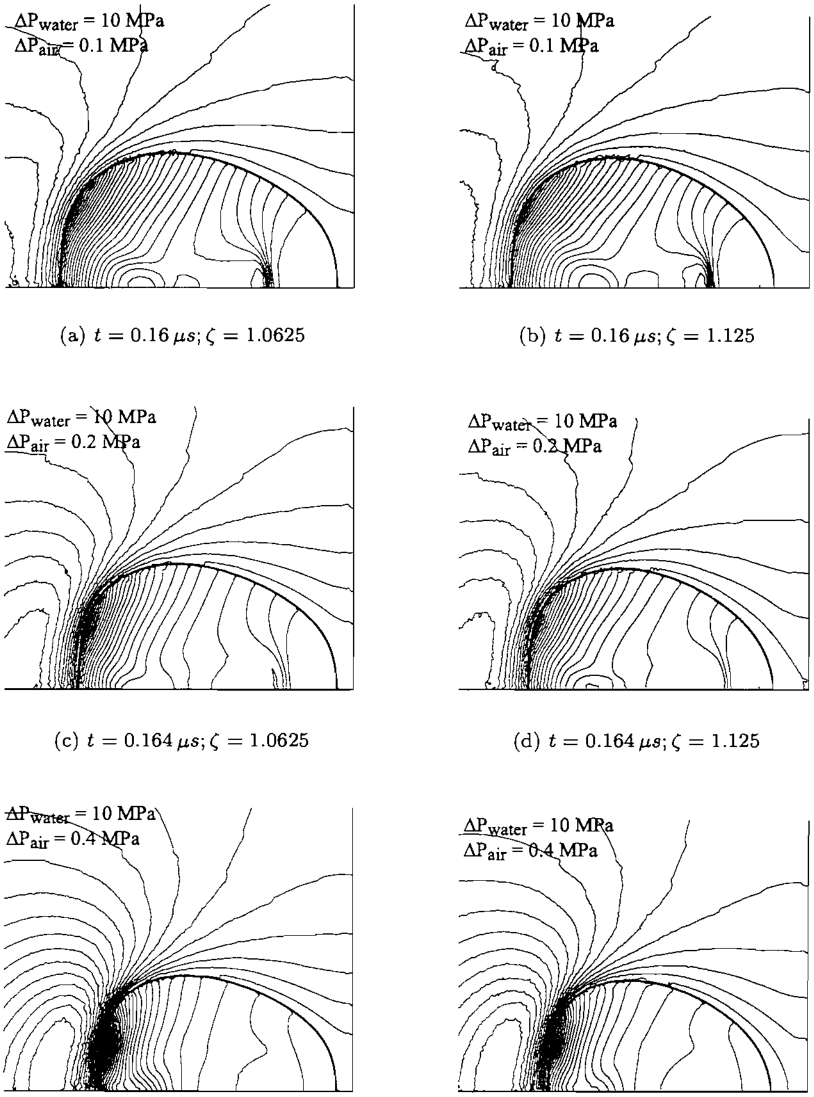

(a) $t = 0.16\,\mu s; \zeta = 1.0625$

(b) $t = 0.16\,\mu s; \zeta = 1.125$

(c) $t = 0.164\,\mu s; \zeta = 1.0625$

(d) $t = 0.164\,\mu s; \zeta = 1.125$

(e) $t = 0.168\,\mu s; \zeta = 1.0625$

(f) $t = 0.168\,\mu s; \zeta = 1.125$

Figure 8.8: *Stand-off parameter* study, ζ. Pressure contours of a bubble with initial radius $R_0 = 40\,\mu m$ collapsed by a lithotripter shock wave with strength of $P^+ = 60\,MPa$. Left column $\zeta = 1.0625$; Right column $\zeta = 1.125$.

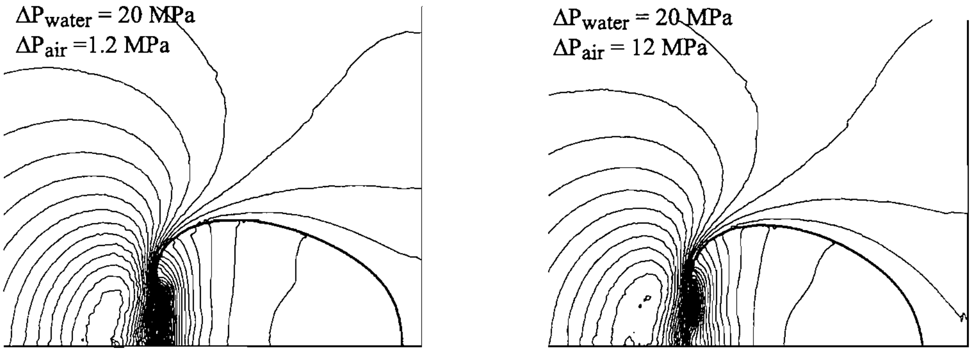

(a) $t = 0.172\,\mu s; \zeta = 1.0625$

(b) $t = 0.172\,\mu s; \zeta = 1.125$

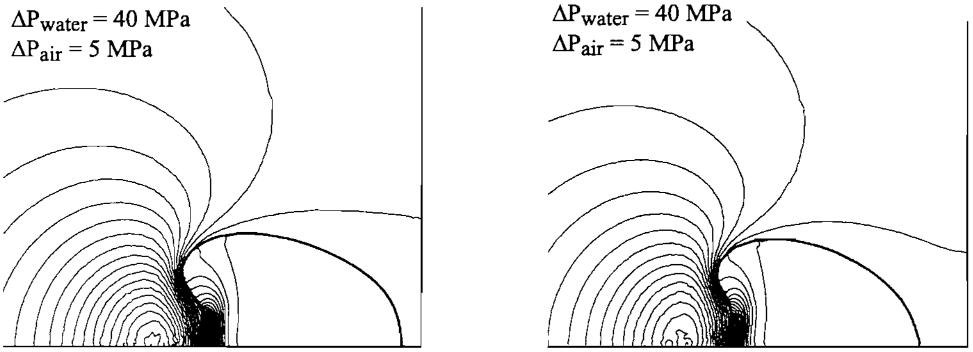

(c) $t = 0.176\,\mu s; \zeta = 1.0625$

(d) $t = 0.176\,\mu s; \zeta = 1.125$

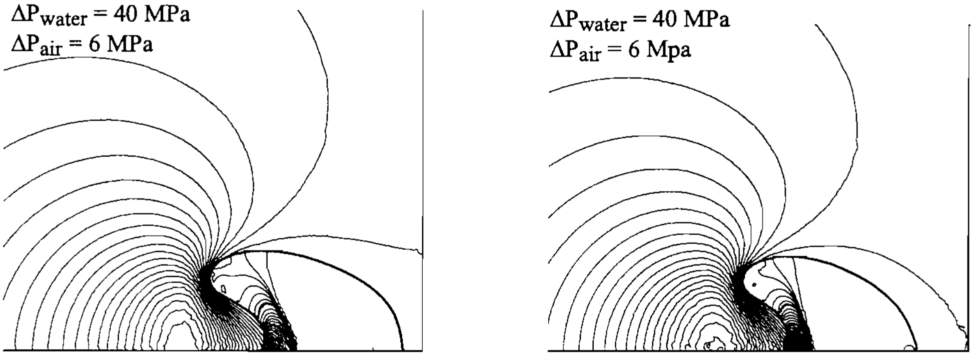

(e) $t = 0.18\,\mu s; \zeta = 1.0625$

(f) $t = 0.18\,\mu s; \zeta = 1.125$

Figure 8.9: *Stand-off parameter* study, ζ. Pressure contours of a bubble with initial radius $R_0 = 40\,\mu m$ collapsed by a lithotripter shock wave with strength of $P^+ = 60\,MPa$. Left column $\zeta = 1.0625$; Right column $\zeta = 1.125$.

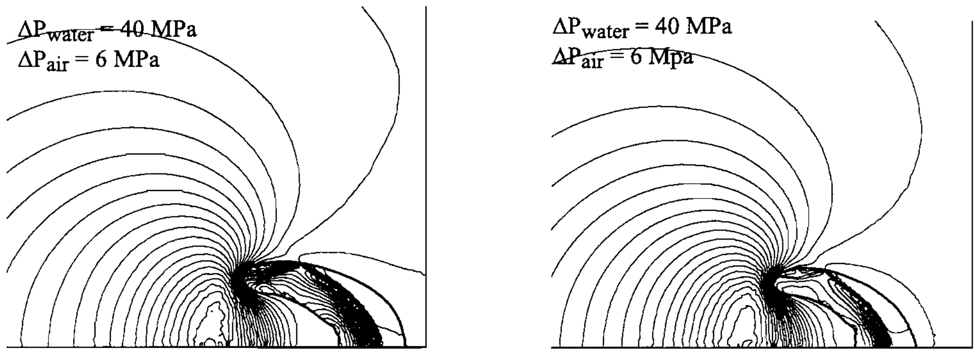

(a) $t = 0.184\,\mu s; \zeta = 1.0625$

(b) $t = 0.184\,\mu s; \zeta = 1.125$

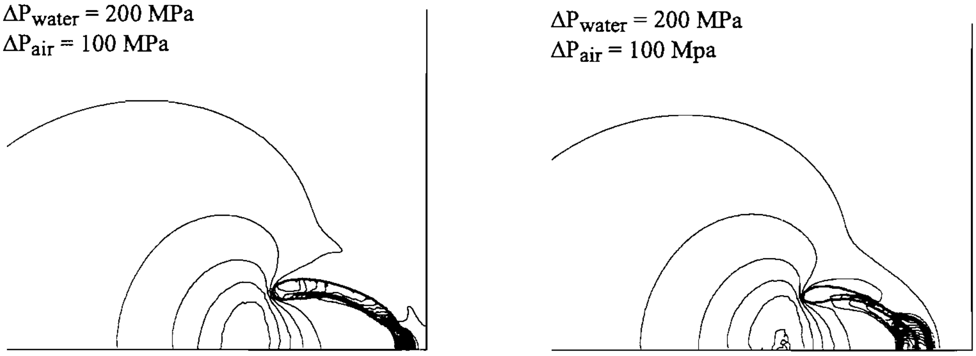

(c) $t = 0.188\,\mu s; \zeta = 1.0625$

(d) $t = 0.188\,\mu s; \zeta = 1.125$

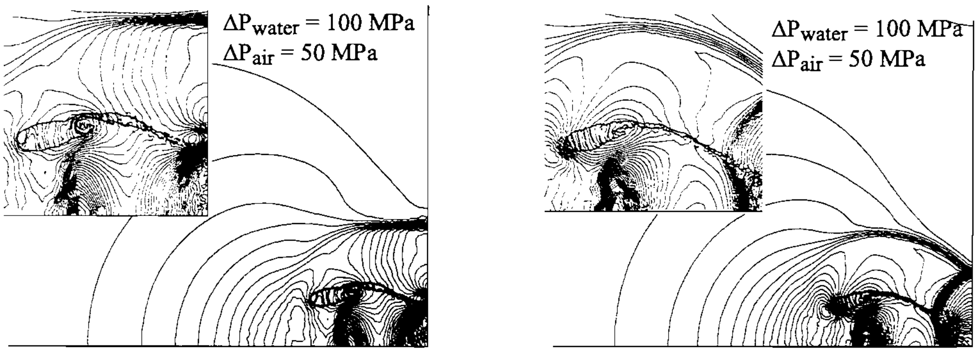

(e) $t = 0.192\,\mu s; \zeta = 1.0625$

(f) $t = 0.192\,\mu s; \zeta = 1.125$

Figure 8.10: *Stand-off parameter* study, ζ. Pressure contours of a bubble with initial radius $R_0 = 40\,\mu m$ collapsed by a lithotripter shock wave with strength of $P^+ = 60\,MPa$. Left column $\zeta = 1.0625$; Right column $\zeta = 1.125$. The insert frame is a magnification of the flow and bubble interface.

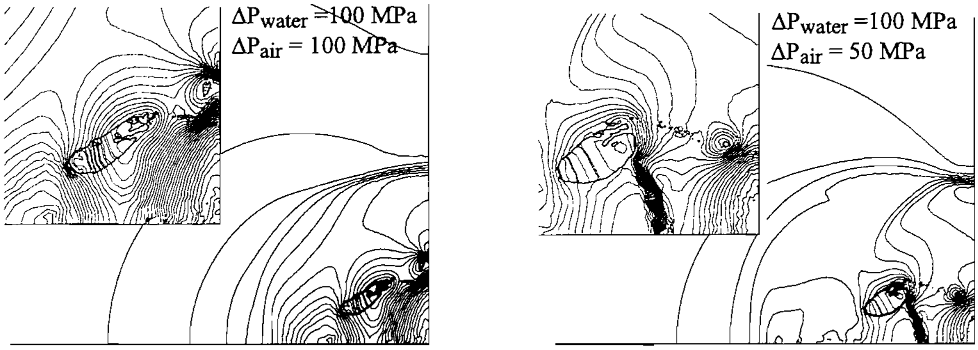

(a) $t = 0.196\,\mu s; \zeta = 1.0625$

(b) $t = 0.196\,\mu s; \zeta = 1.125$

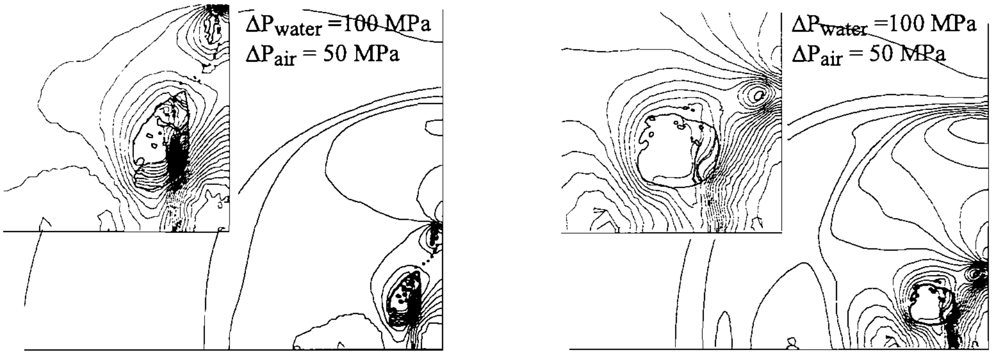

(c) $t = 0.200\,\mu s; \zeta = 1.0625$

(d) $t = 0.200\,\mu s; \zeta = 1.125$

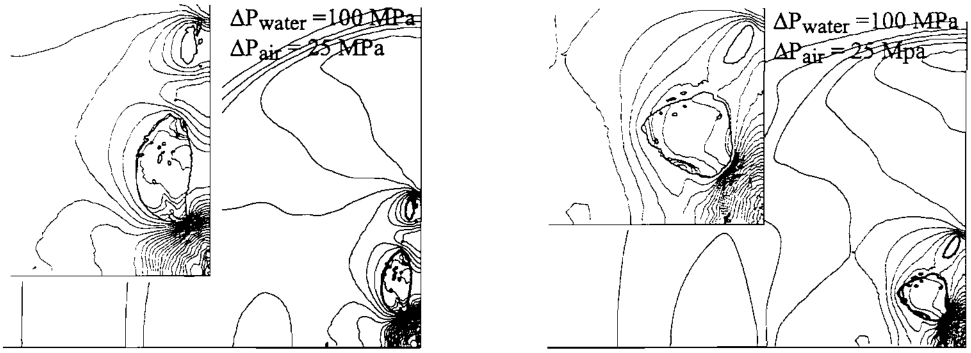

(e) $t = 0.204\,\mu s; \zeta = 1.0625$

(f) $t = 0.204\,\mu s; \zeta = 1.125$

Figure 8.11: *Stand-off parameter* study, ζ. Pressure contours of a bubble with initial radius $R_0 = 40\,\mu m$ collapsed by a lithotripter shock wave with strength of $P^+ = 60\,MPa$. Left column $\zeta = 1.0625$; Right column $\zeta = 1.125$. The insert frame is a magnification of the flow and bubble interface.

that a transition point for ζ that reflects the asymmetry effect of the solid boundary lies somewhere between 1.125 and 1.375. Below a certain value of ζ, the contributory effect from the rigid boundary is significant.

For ζ = 1.0625 and 1.125, flow is retarded by the presence of the rigid boundary and causes the downstream bubble wall to become flattened. The downstream surface essentially stagnates as the bubble collapses. This results in the asymmetric movement of the bubble wall where the upstream part of the bubble interface moves rapidly to the right, while the downstream wall of the bubble remains static. However, in Cases 3 to 6, the interaction of the downstream bubble surface with the incident lithotripter shock and its reflection has induced the collapse of the surface from this side of the bubble. The pressure gradients drive the particles to flow toward the bubble. This correlates well the upstream and downstream bubble wall velocity profile plotted in Fig. 8.5. Since the collapse occurs in all direction, the size of the bubble is much smaller in comparison to the bubble in Cases 1 and 2. If comparison is made of the size of the bubble at a certain time in the bubble evolution in Fig. 8.8, Fig. 8.12 and Fig. 8.16, it is apparent that the size of the bubble decreases with increasing ζ. However, it should be noted here that a different scale was used for Cases 3 – 4 plots. The size of the bubble increases with increasing ζ, though the rate of change of bubble volume decreases with increasing ζ. This is shown clearly in the bubble volume-time history curves in Fig. 8.6.

Moreover, because the the downstream surface in Cases 3 to 6 collapses and moves away from the rigid boundary, an impact of the air shock on the downstream wall occurs at about $t = 0.68\,\mu s$ (frame (e) and (f) in Fig. 8.12 and Fig. 8.16). The air shock in Cases 1 and 2 on the other hand, converges to the bottom right of the bubble and no impact on the downstream bubble wall takes place. Because of the larger impedance of water relative to air, the air shock is reflected back as a shock wave and travels to the left in the direction away from the rigid boundary. The sequences are shown in Fig. 8.12(a) and (c) for $\zeta = 1.375$; Fig. 8.12(b) and (d) for $\zeta = 1.625$ and Fig. 8.17(a) to (e) for $\zeta = 1.875$; Fig. 8.17(b) to (e) for $\zeta = 2.125$.

After $t = 0.16\,\mu s$, in all six cases, the contraction of the bubble surface is more pronounced especially from the right side, where the high pressure region builds up. In all six cases, an increase in pressure gradient occurs at a small distance away from the axis of symmetry on the upstream bubble wall. It is postulated that this resulted from a circulating flow near the upstream bubble surface, induced from the interaction of the reflected incident shock with the strong expansion wave originating from the bubble surface. The time at which it occurs is smaller with decreasing ζ, which relates with the propagation of the reflected incident lithotripter shock wave from the rigid boundary. The build-up of this pressure gradient and circulating flow near the upstream bubble

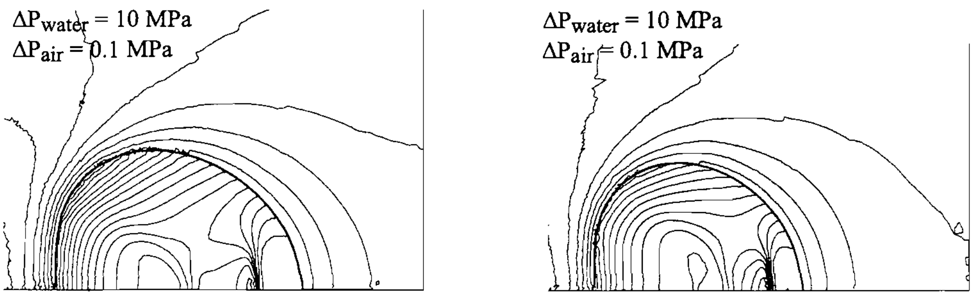

(a) $t = 0.16\,\mu s; \zeta = 1.375$ (b) $t = 0.16\,\mu s; \zeta = 1.625$

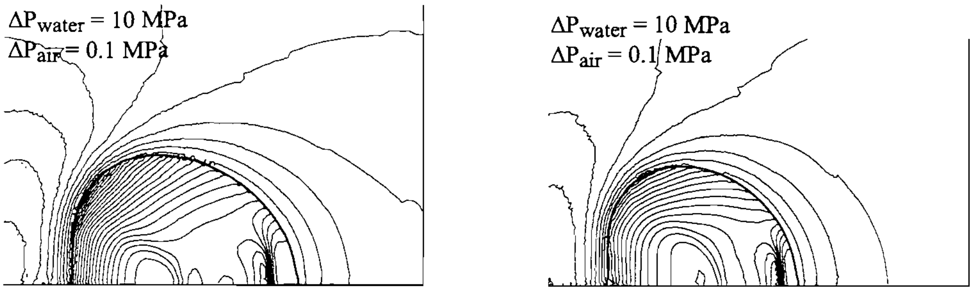

(c) $t = 0.164\,\mu s; \zeta = 1.375$ (d) $t = 0.164\,\mu s; \zeta = 1.625$

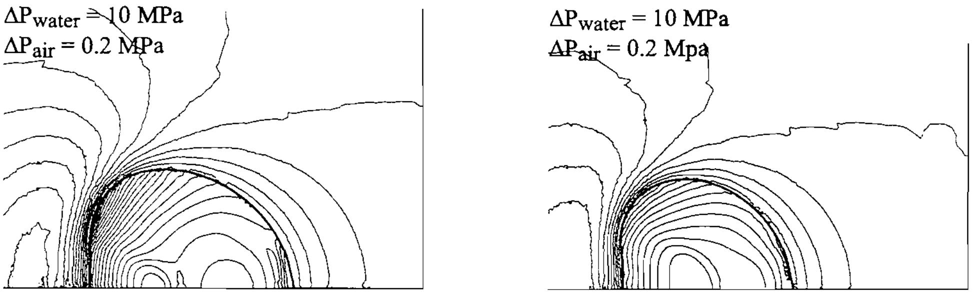

(e) $t = 0.168\,\mu s; \zeta = 1.375$ (f) $t = 0.168\,\mu s; \zeta = 1.625$

Figure 8.12: *Stand-off parameter* study, ζ. Pressure contours of a bubble with initial radius $R_0 = 40\,\mu m$ collapsed by a lithotripter shock wave with strength of $P^+ = 60\,MPa$. Left column $\zeta = 1.375$; Right column $\zeta = 1.625$.

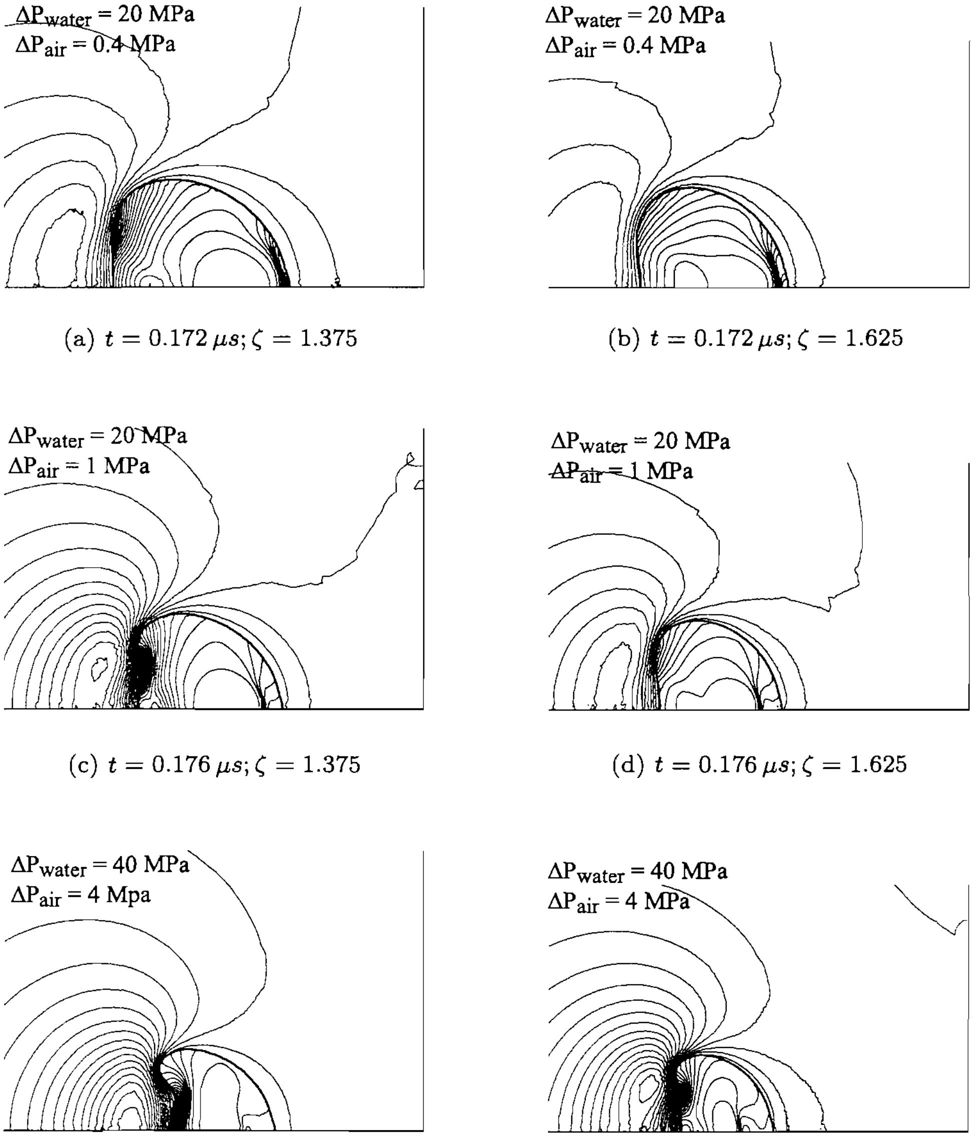

(a) $t = 0.172\,\mu s; \zeta = 1.375$

(b) $t = 0.172\,\mu s; \zeta = 1.625$

(c) $t = 0.176\,\mu s; \zeta = 1.375$

(d) $t = 0.176\,\mu s; \zeta = 1.625$

(e) $t = 0.18\,\mu s; \zeta = 1.375$

(f) $t = 0.18\,\mu s; \zeta = 1.625$

Figure 8.13: *Stand-off parameter* study, ζ. Pressure contours of a bubble with initial radius $R_0 = 40\,\mu m$ collapsed by a lithotripter shock wave with strength of $P^+ = 60\,MPa$. Left column $\zeta = 1.375$; Right column $\zeta = 1.625$.

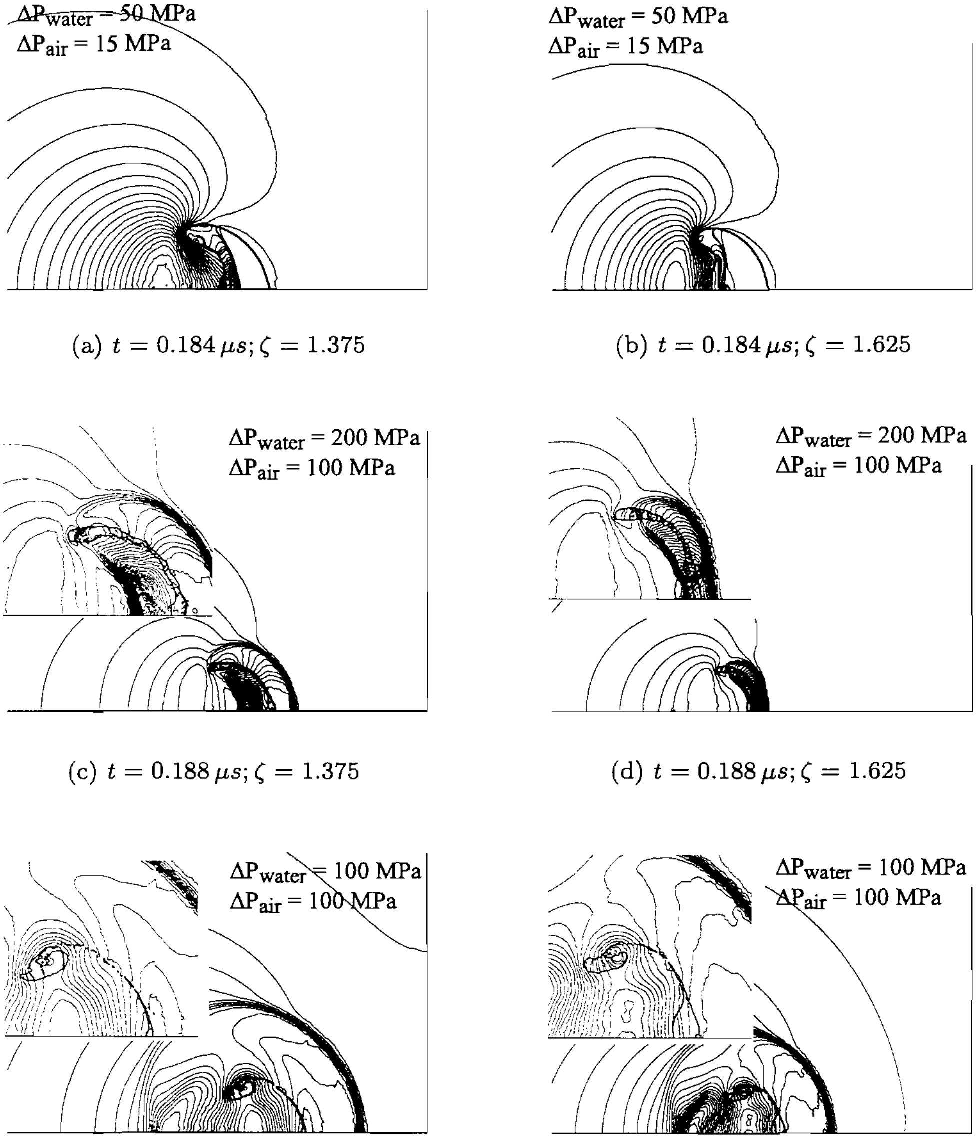

(a) $t = 0.184\,\mu s; \zeta = 1.375$

(b) $t = 0.184\,\mu s; \zeta = 1.625$

(c) $t = 0.188\,\mu s; \zeta = 1.375$

(d) $t = 0.188\,\mu s; \zeta = 1.625$

(e) $t = 0.192\,\mu s; \zeta = 1.375$

(f) $t = 0.192\,\mu s; \zeta = 1.625$

Figure 8.14: *Stand-off parameter* study, ζ. Pressure contours of a bubble with initial radius $R_0 = 40\,\mu m$ collapsed by a lithotripter shock wave with strength of $P^+ = 60\,MPa$. Left column $\zeta = 1.375$; Right column $\zeta = 1.625$. The insert frame is a magnification of the flow and bubble interface.

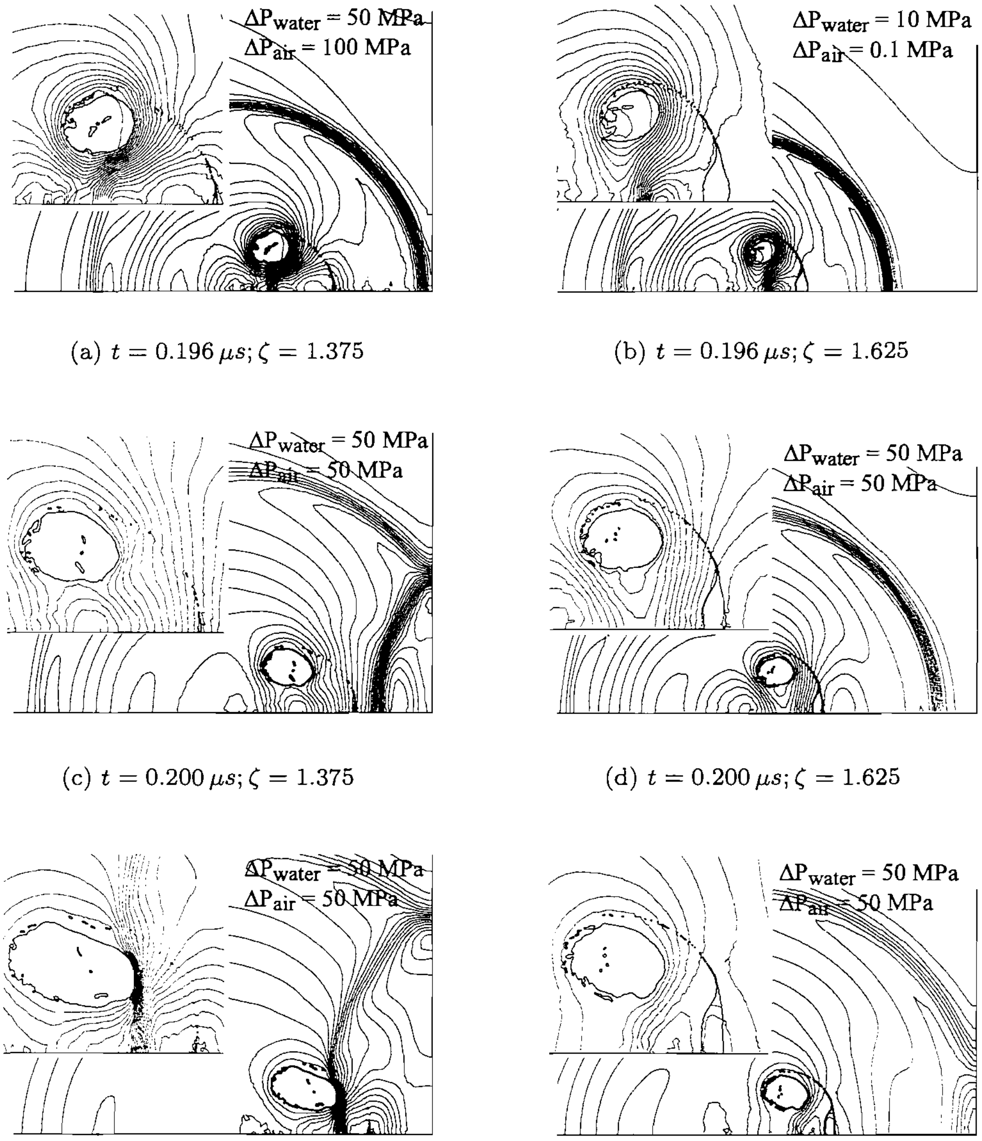

(a) $t = 0.196\,\mu s; \zeta = 1.375$

(b) $t = 0.196\,\mu s; \zeta = 1.625$

(c) $t = 0.200\,\mu s; \zeta = 1.375$

(d) $t = 0.200\,\mu s; \zeta = 1.625$

(e) $t = 0.204\,\mu s; \zeta = 1.375$

(f) $t = 0.204\,\mu s; \zeta = 1.625$

Figure 8.15: *Stand-off parameter* study, ζ. Pressure contours of a bubble with initial radius $R_0 = 40\,\mu m$ collapsed by a lithotripter shock wave with strength of $P^+ = 60\,MPa$. Left column $\zeta = 1.375$; Right column $\zeta = 1.625$. The insert frame is a magnification of the flow and bubble interface.

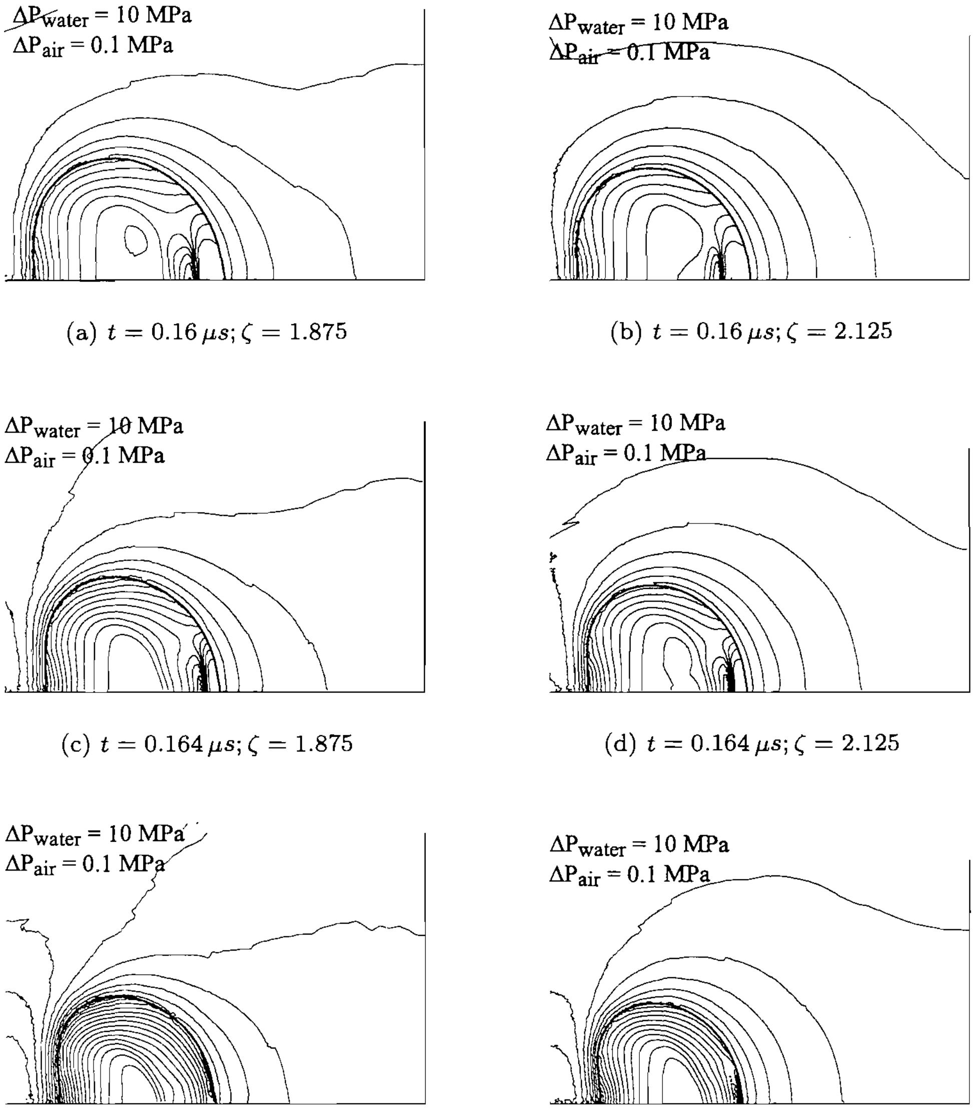

(a) $t = 0.16\,\mu s; \zeta = 1.875$

(b) $t = 0.16\,\mu s; \zeta = 2.125$

(c) $t = 0.164\,\mu s; \zeta = 1.875$

(d) $t = 0.164\,\mu s; \zeta = 2.125$

(e) $t = 0.168\,\mu s; \zeta = 1.875$

(f) $t = 0.168\,\mu s; \zeta = 2.125$

Figure 8.16: *Stand-off parameter* study, ζ. Pressure contours of a bubble with initial radius $R_0 = 40\,\mu m$ collapsed by a lithotripter shock wave with strength of $P^+ = 60\,MPa$. Left column $\zeta = 1.875$; Right column $\zeta = 2.125$.

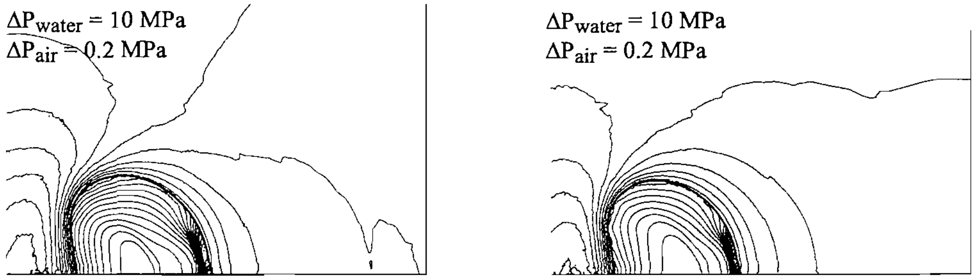

(a) $t = 0.172\,\mu s; \zeta = 1.875$ (b) $t = 0.172\,\mu s; \zeta = 2.125$

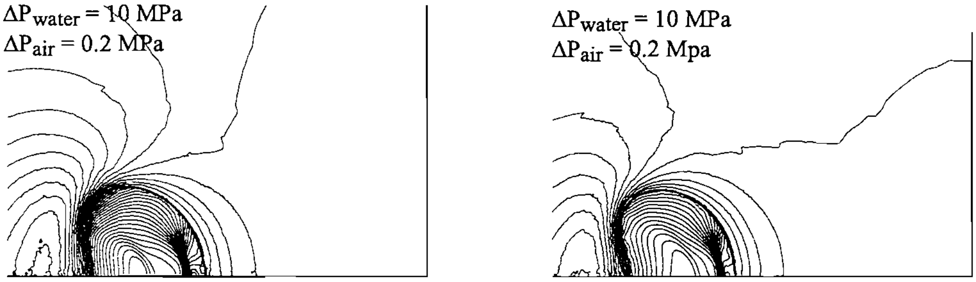

(c) $t = 0.176\,\mu s; \zeta = 1.875$ (d) $t = 0.176\,\mu s; \zeta = 2.125$

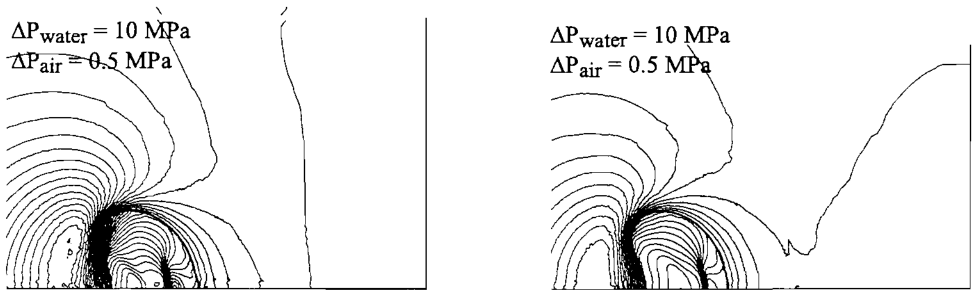

(e) $t = 0.18\,\mu s; \zeta = 1.875$ (f) $t = 0.18\,\mu s; \zeta = 2.125$

Figure 8.17: *Stand-off parameter* study, ζ. Pressure contours of a bubble with initial radius $R_0 = 40\,\mu m$ collapsed by a lithotripter shock wave with strength of $P^+ = 60\,MPa$. Left column $\zeta = 1.875$; Right column $\zeta = 2.125$.

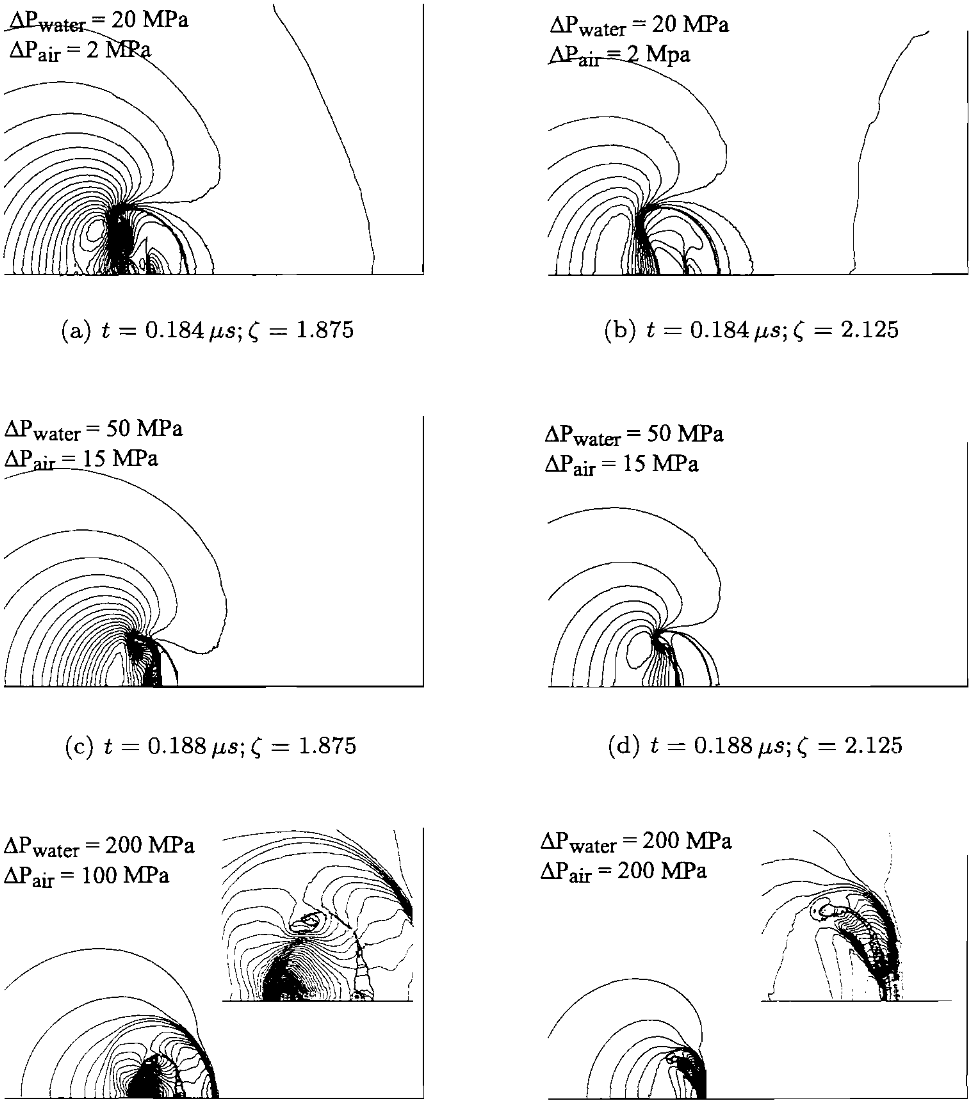

(a) $t = 0.184\,\mu s; \zeta = 1.875$

(b) $t = 0.184\,\mu s; \zeta = 2.125$

(c) $t = 0.188\,\mu s; \zeta = 1.875$

(d) $t = 0.188\,\mu s; \zeta = 2.125$

(e) $t = 0.192\,\mu s; \zeta = 1.875$

(f) $t = 0.192\,\mu s; \zeta = 2.125$

Figure 8.18: *Stand-off parameter* study, ζ. Pressure contours of a bubble with initial radius $R_0 = 40\,\mu m$ collapsed by a lithotripter shock wave with strength of $P^+ = 60\,MPa$. Left column $\zeta = 1.875$; Right column $\zeta = 2.125$. The insert frame is a magnification of the flow and bubble interface.

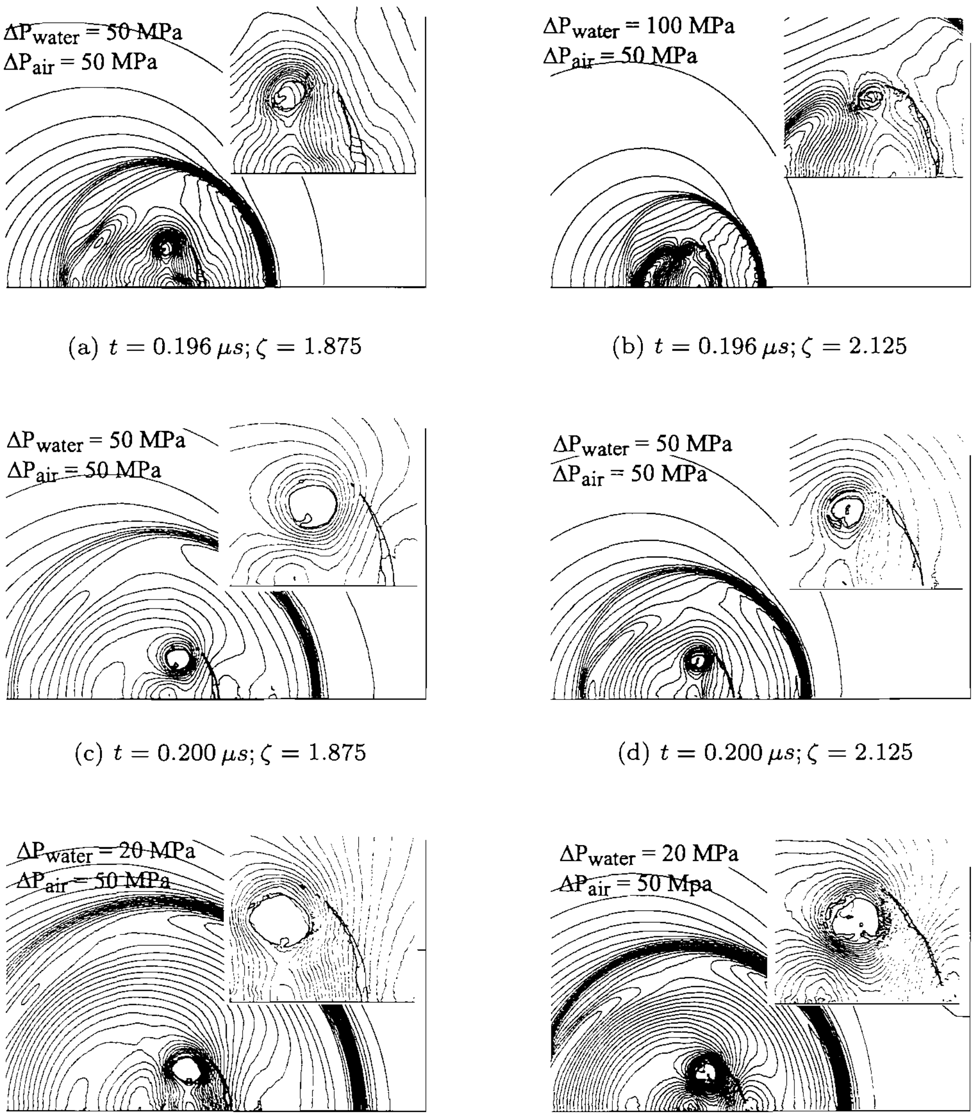

(a) $t = 0.196\,\mu s; \zeta = 1.875$

(b) $t = 0.196\,\mu s; \zeta = 2.125$

(c) $t = 0.200\,\mu s; \zeta = 1.875$

(d) $t = 0.200\,\mu s; \zeta = 2.125$

(e) $t = 0.204\,\mu s; \zeta = 1.875$

(f) $t = 0.204\,\mu s; \zeta = 2.125$

Figure 8.19: *Stand-off parameter* study, ζ. Pressure contours of a bubble with initial radius $R_0 = 40\,\mu m$ collapsed by a lithotripter shock wave with strength of $P^+ = 60\,MPa$. Left column $\zeta = 1.875$; Right column $\zeta = 2.125$. The insert frame is a magnification of the flow and bubble interface.

surface occurs at $t \simeq 0.168\,\mu s$ for $\zeta = 1.0625$ and 1.125 (Fig. 8.8(e) and (f)), $t \simeq 0.172\,\mu s$ for $\zeta = 1.375$ (Fig. 8.13(a)), $t \simeq 0.176\,\mu s$ for $\zeta = 1.625$ (Fig. 8.13(d)), $t \simeq 0.184\,\mu s$ for $\zeta = 1.875$ (Fig. 8.18(a)) and $t \simeq 0.188\,\mu s$ for $\zeta = 2.125$ (Fig. 8.18(d)).

Towards the end of the collapse phase, the bubble undergoes a rapid deformation with the formation of a high-speed liquid jet that penetrates through the bubble. This is a consequence of the acceleration of the water on the upstream side towards the rigid boundary that causes the upstream surface to involute and forms a jet as shown in Fig. 8.9(e) and (f), Fig. 8.13(e) and (f) and Fig. 8.18(a) and (c). In turn, it generates additional compression waves in the air near the upstream bubble wall resulting in a secondary air shock being transmitted into the bubble. The shape of the jet is more distinct, i.e. sharper, in Case 1 and Case 2 compared to the other four cases where the 'shoulder' of the jet is more pronounced. Furthermore, owing to the circulation flow near the upstream bubble wall, the liquid jet is concave and consequently the first impact of the jet head on the downstream wall does not occur on the centre line of the bubble as depicted in the 'free-field' problem. Since the velocity of the jet on the axis is larger in Cases 1 and 2 than in Cases 3 to 6 (Fig. 8.5), the concavity of the nose of the jet near the axis subsides resulting in a much sharper jet tip in the two former cases. The smaller jet tip width in Cases 1 and 2 is also due to the elongation of the collapsing bubble. The slight elongation of the wall is due to the interaction with the reflected incident shock which induces the contraction of the top bubble surface.

The concavity of the jet head is highly prominent for $\zeta = 1.375$ and $\zeta = 1.625$. The jet head is relatively wide and much flatter especially in Cases 5 and 6, and, because the development time for the circulating flow near the upstream surface is larger as the bubble gets further away from the rigid boundary, the deviation of the jet head from the axial increases with increasing ζ. As the jet accelerates towards the rigid boundary, the pressure inside the bubble increases rapidly. The liquid jet hits the downstream wall between $t = 0.184\,\mu s$ and $t = 0.184\,\mu s$ for Cases 1 to 4 and between $t = 0.188\,\mu s$ and $t = 0.192\,\mu s$ for Cases 5 and 6. The time to minimum bubble volume on the other hand is smaller with decreasing ζ (Fig. 8.6).

On impact, the jet produces an intense blast wave in the surrounding water. The maximum pressure loading recorded by the transducer on the boundary varies from nearly $7000\,MPa$ for $\zeta = 1.0625$ to a mere $500\,MPa$ for Case 6 where $\zeta = 2.125$ (Fig. 8.7). For Cases 1 and 2, at $t = 0.192\,\mu s$, the jet has penetrated through the bubble isolating a toroidal bubble in $3D$ of trapped air and highly compressed gas (Fig. 8.10(e) and (f)). In Cases 3 to 6, because of the highly concave jet, the impact of the jet on the downstream wall splits the air bubble into two, isolating two rings of highly compressed air, separated by tiny circular gas or bubble fragments. These bubble fragments originate from the air layer trapped between the jet tip and the downstream interface prior to impact. In addition, the high pressure within the bubble will cause these fragments and lobes of air to expand.

In Cases 1 and 2, where the collapse occurs very close to the rigid boundary, the flow of the jet following jet impact is redirected radially along the boundary. The penetration of the jet induces a circulation in the air inside the bubble. This leads to the formation of a ring vortex that brings the bubble even closer to the rigid boundary. In Cases 3 to 6, the formation of the vortex flow is mainly due to the interaction between the high-momentum liquid jet and the downstream low-momentum water. The strong spherical blast wave propagating to the right will impact on the rigid boundary and will be reflected back into the surrounding fluid. Part of this wave will interact with the expanding bubble. The damage potential arising from the collapse of the bubble such as in Cases 3 to 6 is small as the jet flow and the strong blast wave are dampened by the water separating the bubble and the solid boundary.

8.2.3 Far-field Calculations

Kirchhoff Results

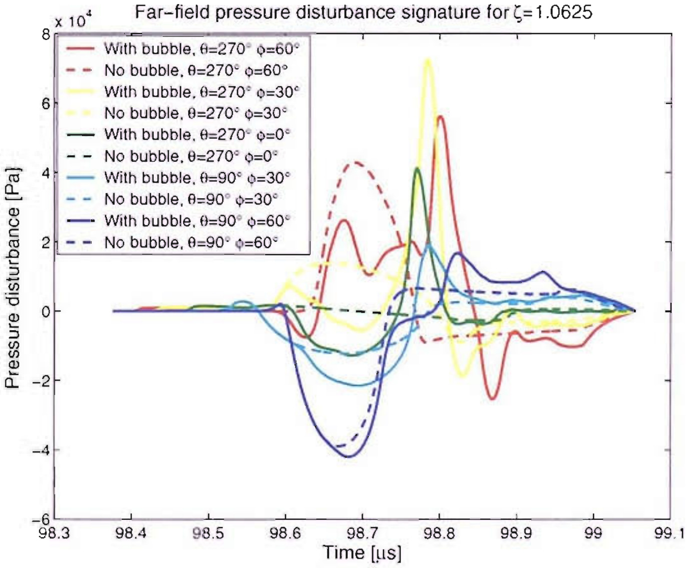

Figure 8.20: The far-field pressure signature predicted using the Kirchhoff method at an observer positioned 150 mm from the initial bubble centre, with $\zeta = 1.0625$. The results for various θ and ϕ are plotted for comparison.

Fig. 8.20 and Fig. 8.21 shows the pressure-time history calculated in the far-field for

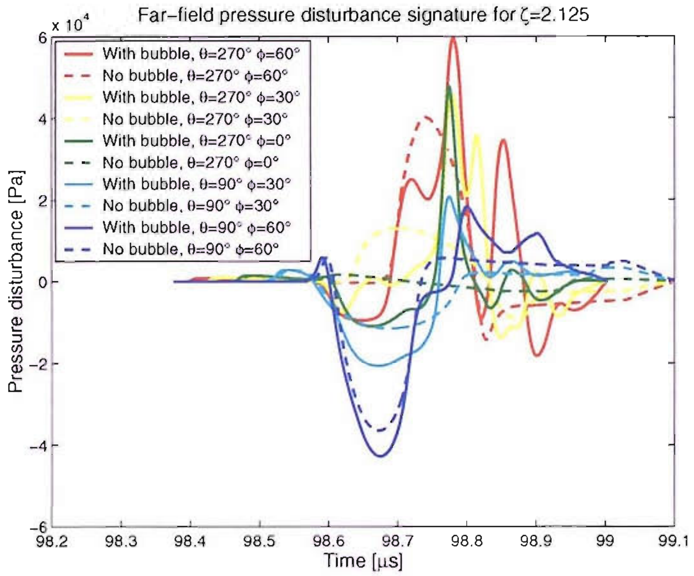

Figure 8.21: The far-field pressure signature predicted using the Kirchhoff method at an observer positioned 150 mm from the initial bubble centre, with $\zeta = 2.125$. The results for various θ and ϕ are plotted for comparison.

$\zeta = 1.0625$ and $\zeta = 2.125$ respectively. Results for various θ and ϕ are plotted for comparison in order to determine the variation in the far-field pressure profile at different observer positions and the dependency on the directionality of the lithotripter shock wave. The same set of integration surface and CFD input data were used for all calculations. Similarly to the free-field problem, calculations for bubble-free problems were also carried out (plotted as dashed lines).

Unlike the free-field problem, the effect of the propagating shock wave is more significant as the rigid boundary reflects the incident lithotripter shock wave. Therefore, the propagating incident shock wave are captured twice in the Kirchhoff and FWH surface integral. Nevertheless, the blast wave could still be captured as a sharp peak. The timing of the arrival of the blast wave peak relative to the contamination from the lithotripter shock wave does not overlap. The far-field pressure waveforms for bubble-free problems (plotted as dotted line) clearly show that the blast wave can be unambiguously separated from the lithotripter signature. For example, the large trough for $\zeta = 1.0625$ (solid blue line) between 98.6 μs to 98.75 μs can be attributed to the incident shock wave. The large negative pressure for the free-field case (dashed blue line) confirms this. The maximum pressure amplitude predicted for $\zeta = 1.0625$ is approx 70 kPa and this value decreases by approximately 10 kPa when $\zeta = 2.125$. The reduction in the maximum pressure amplitude is because of the increase in the initial bubble centre distance from the rigid boundary.

For $\zeta = 1.0625$ (Fig. 8.4), the reflection of the blast wave is not very clear. The second pressure peak is not as obvious as when $\zeta = 2.125$. This is because the delay between the primary and reflected shocks may be too small to resolve. For $\zeta = 2.125$, owing to the distance of the bubble from the rigid boundary, the blast wave has time to develop into a full spherical pressure wave and is reflected clearly on the rigid boundary.

FWH Results

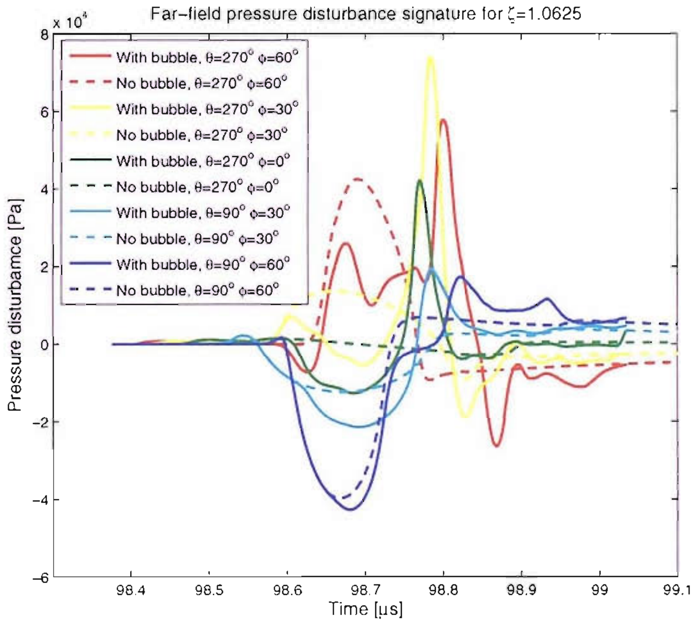

Figure 8.22: The far-field pressure signature predicted using the FWH method at an observer positioned $150\,mm$ from the initial bubble centre, with $\zeta = 1.0625$. The results for various θ and ϕ are plotted for comparison.

As in the Kirchhoff problem discussed above, the integration surface is located $150\,mm$ from the initial bubble centre. The calculation is performed on 90 control points placed along the half circumference of the axisymmetric control surface. The results of the predicted far-field noise using the FWH method for control surface radii of $0.2\,mm$ is shown in Fig. 8.22. The results for $R_{cs} = 0.2\,mm$ is in agreement with that of the Kirchhoff results (Fig. 8.20). The results for $R_{cs} = 0.2\,mm$ are identical and the peak pressures of using the FWH method match really well with that plotted in Fig. 8.20. The variation of the pressure waveforms for different observer position also agrees well. The results show that there is no difference in the two methods ability to distinguish

Case	Initial Radius, R_0 (μm)	Shock Strength, P^+ (MPa)	Distance, d (μm)	Stand-off distance, ζ
7	40	60	30.0	0.75
8	40	60	35.0	0.875
9	40	60	38.0	0.95

Table 8.3: Various cases for '*stand-off distance* study of pre-attached bubbles

the lithotripter signature from the blast wave signature. The problem has high degree of nonlinearity owing to the incident shock wave, its reflection on the rigid boundary and the high pressure amplitude of the blast wave. As some degree of nonlinearities are taken into account by the surface integrals in the FWH formulation, the FWH method gives a more consistent and acceptable results regardless of the control surface position. In addition, the cost of calculations is the same for both methods.

8.3 The interaction of lithotripter shock wave with an attached bubble

In this section, numerical simulations are carried out in order to study the interaction of a pre-attached bubble on a rigid boundary with a lithotripter shock wave pulse. The initial layout and specifications of the computational domain is similar to the problem near a solid boundary discussed in previous section, but with the distance of the initial bubble centre d smaller than the initial radius of the bubble, R_0, i.e. $\zeta < 1$. The initial properties for both air and water are at ISA sea-level conditions. A planar lithotripter shock wave, with $P^+ = 60\,MPa$ and $P^- = -10\,MPa$, propagates through the water from left to right.

A pressure recording point is positioned at the solid boundary on the axis of symmetry and therefore lies within the air bubble. The parameters of the current problems are given in Table 8.3. Time is measured from the moment of shock impact in each case.

8.3.1 Results and discussion

The upstream bubble wall time history is given in Fig. 8.23. Initially, the velocity of the upstream wall increases gradually. It then accelerate as it approaches the final stage of collapse. The end the curves represents the point at which jet impact on the solid boundary occurs. The velocity variation for $\zeta = 0.875$ and $\zeta = 0.95$ are almost identical, while for $\zeta = 0.75$ the upstream wall velocity deviates from that of the former at around

$0.1\,\mu s$. Consequently, the collapse rate for Case 7 is higher than Case 8 and 9 as depicted in the bubble volume time history curves in Fig. 8.24. The relationship of the impact wall pressure and the dimensionless stand-off distance is shown in Fig. 8.25. It is clear that the maximum pressure loading on the wall decreases with increasing ζ. The initial pressure rise at the bottom of the curves originated from the impact of the secondary air shock on the rigid boundary. The impact wall pressure, when $\zeta = 1.0625$ is nearly $7000\,MPa$ (Fig. 8.7). For $\zeta < 1$, where the bubble collapses with some parts touching the wall, the impact pressure decreases to a minimum ($\simeq 4000\,MPa$ for $\zeta = 0.95$). However, if ζ is reduced even further, the maximum impact wall pressure begins to increase again. This trend was observed experimentally by Shima [80].

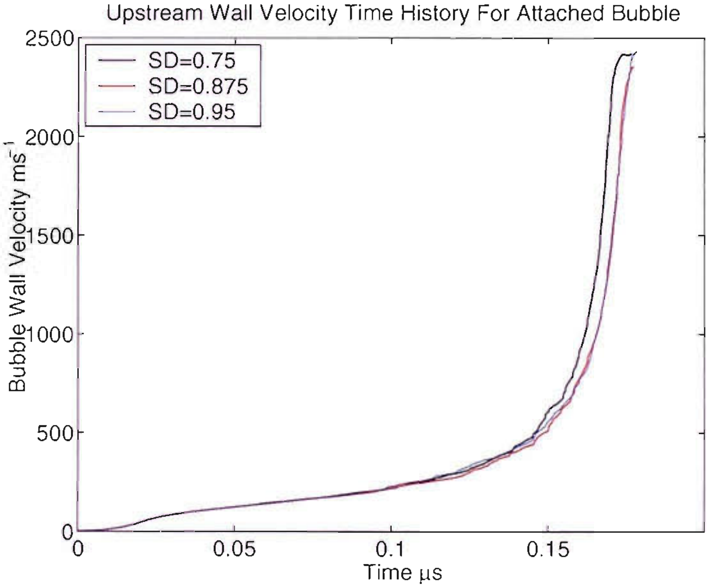

Figure 8.23: Upstream and downstream wall velocity time history for a pre-attached bubbles. Comparison for different stand-off distance, ζ, as given in Table 8.3.

The next few figures presented here are preliminary results. A more detailed analysis is required in order to determine the right contact angle between the attached bubble surface on the rigid boundary as a consequent of surface tension. In the following study, the effect of surface tension is neglected and the contact angle is assumed to be at right angle to the rigid boundary. For any given solid/liquid interaction, there exists a range of contact angles which may be found. The value of the contact angle is dependent on the surface tension and the boundary surface roughness.

The evolution of the pre-attached bubble with different stand-off distance ($\zeta < 1$) is depicted in Fig. 8.26 - Fig. 8.29. Pressure contours are plotted in air and water from which the reflection, transmission and refraction of the shock waves near the bubble are investigated to provide a clear view of the bubble response. The heavy line in the figures represents the bubble interface.

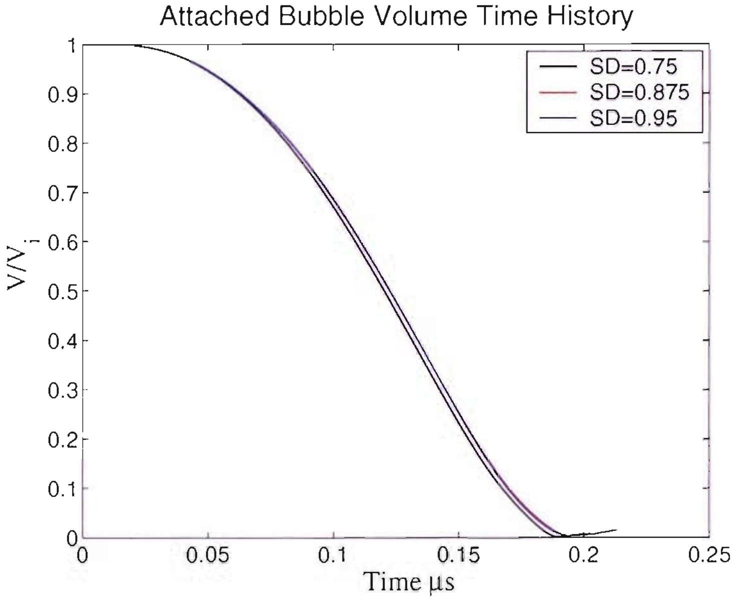

Figure 8.24: Pre-attached bubbles volume time history. Comparison for different stand-off distance, ζ, as given in Table 8.3.

The sequence starts $0.02\,\mu s$ after shock impact. The impact of the lithotripter shock on the bubble wall transmit a weak shock into the bubble and a strong expansion wave into the surrounding water. The earlier stages of the bubble collapse is similar to the case where $\zeta > 1$. At this early stage, the deformation of the bubble wall and dynamics of the flow around the bubble are identical for the three different stand-off distances for $\zeta < 1$ as well as the six cases where $\zeta > 1$ discussed earlier.

The sequence shown in Fig. 8.27 shows that the pressure gradient in the water near the upstream side of the bubble increases as time progresses. The first apparent difference between the three cases is the 'wetted area'[1] of the attached bubble increases with decreasing ζ. This is true from $t = 0$ and is an artefact of the initial geometry of the bubble.

At about $t = 0.168\,\mu s$, the upstream bubble wall starts to involute to form a liquid jet running to the right along the symmetric axis (Fig. 8.28(b),(f) and (j)). Like the previous cases, secondary compression waves are induced inside the bubble due to the high deformation of the upstream wall by the jet and the large pressure gradient(Fig. 8.28(d),(h) and (l)). This secondary shock will impact directly onto the solid boundary and the

---

[1] The circular area of the bubble attached to the rigid boundary.

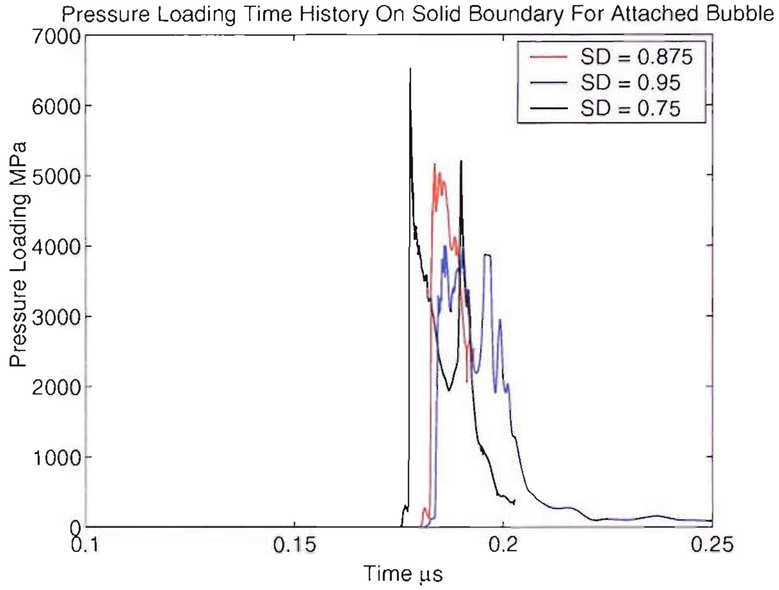

Figure 8.25: Pressure loading time history recorded on the solid boundary for different stand-off distance for pre-attached bubbles as given in Table 8.3.

time at which the impact occurs varies with stand-off distance, i.e. at $t = 0.176\,\mu s$ for $\zeta = 0.75$; at $t = 0.180\,\mu s$ for $\zeta = 0.875$ and at $t = 0.184\,\mu s$ for $\zeta = 0.95$. This is fundamentally different from the previous cases. In cases where $\zeta > 1$, the shock reflects from an air-water interface, where as here the shock impacts directly on the boundary which could be a kidney stone, and thus could be a potential damage mechanism.

The collapse time of these bubble are very short, less than $0.18\,\mu s$ for $\zeta = 0.75$. Therefore, it is immediately apparent that the collapse process of the gas bubble by the lithotripter shock wave is very violent. The acceleration of the liquid jet will continue until it eventually impacts directly onto the solid boundary. The time to impact increases with increasing ζ. A close up of the liquid jet impact on the boundary is given in Fig. 8.30. It is clear from the Fig. 8.30 that the jet diameter decreases with decreasing ζ. The liquid jet impact emits a very strong asymmetric blast wave into the surrounding water which subsequently interacts with the isolated toroidal bubble, causing it to collapse even further as shown in Fig. 8.29((g), (h), (k) and (l)). Prior to jet impact the secondary air shock forms an oblique reflection at the top bubble wall (Fig. 8.30(a) and (b)). At the final stages of collapse, the radial velocity at the base of the gas bubble attains a high value. Due to the presence of the boundary, the jet flow is redirected radially outward and consequently forms a radially spreading sheet of water (radial jet) which propagates along the rigid boundary. The formation of this radial jet was not expected, thus no measurement was made on its velocity. However, it is believed that the jet achieved a high velocity upon impact on the top wall, as a strong 'hemispherical' ring blast wave is emitted into the water due to the liquid-liquid impact. It is postulated that this could be a potential additional damage mechanism for shock wave lithotripsy. This secondary jet is also much narrower than the primary jet (Fig. 8.30(d), (e) and (f)).

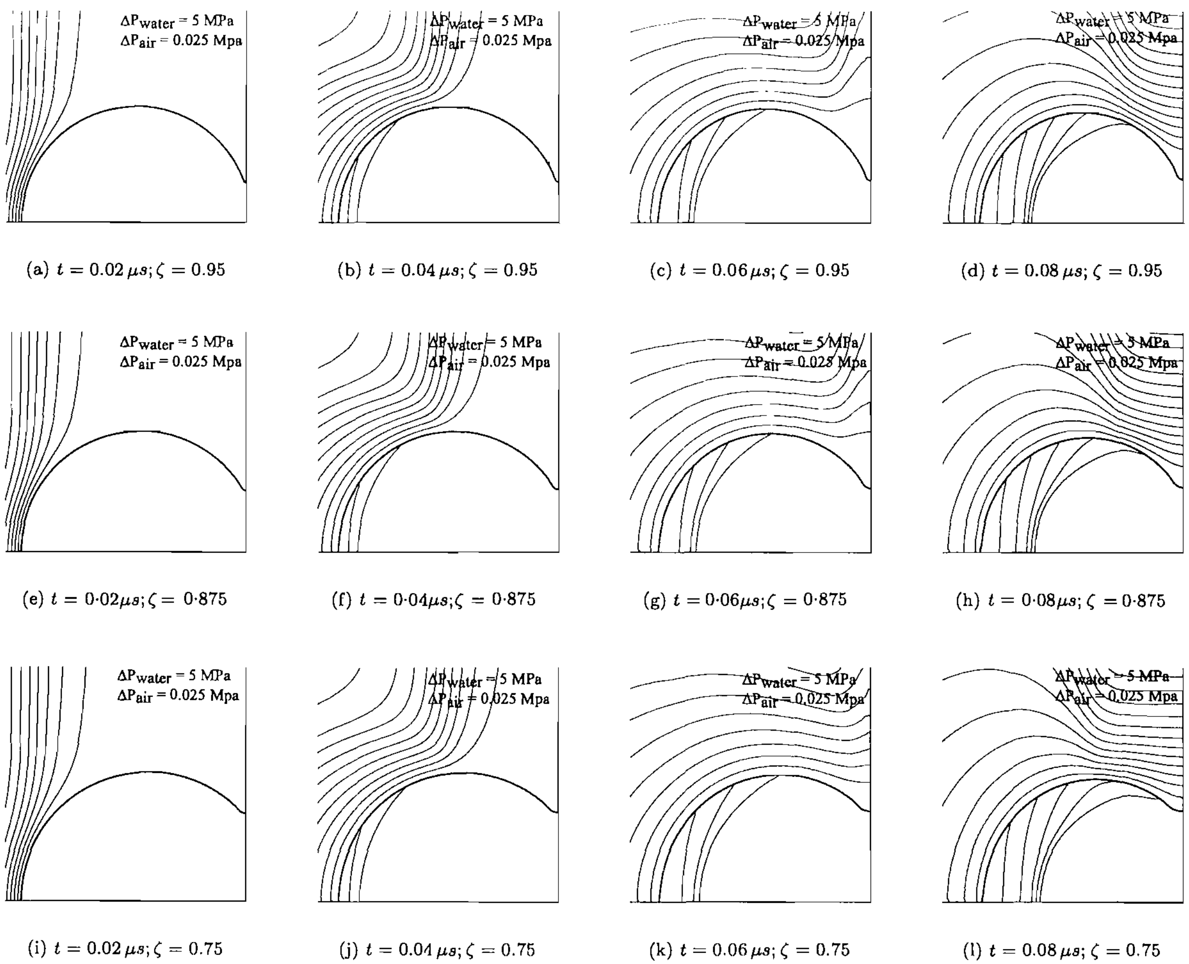

(a) $t = 0.02\,\mu s; \zeta = 0.95$ (b) $t = 0.04\,\mu s; \zeta = 0.95$ (c) $t = 0.06\,\mu s; \zeta = 0.95$ (d) $t = 0.08\,\mu s; \zeta = 0.95$

(e) $t = 0{\cdot}02\mu s; \zeta = 0{\cdot}875$ (f) $t = 0{\cdot}04\mu s; \zeta = 0{\cdot}875$ (g) $t = 0{\cdot}06\mu s; \zeta = 0{\cdot}875$ (h) $t = 0{\cdot}08\mu s; \zeta = 0{\cdot}875$

(i) $t = 0.02\,\mu s; \zeta = 0.75$ (j) $t = 0.04\,\mu s; \zeta = 0.75$ (k) $t = 0.06\,\mu s; \zeta = 0.75$ (l) $t = 0.08\,\mu s; \zeta = 0.75$

Figure 8.26: Pressure contours of an attached bubble with initial radius $R_0 = 40\,\mu m$ collapsed by a lithotripter shock wave with strength of $P^+ = 60\,MPa$. Comparison for different *stand-off distance*, ζ. Top row: $\zeta = 0.95$; Middle row: $\zeta = 0.875$; Bottom row: $\zeta = 0.75$.

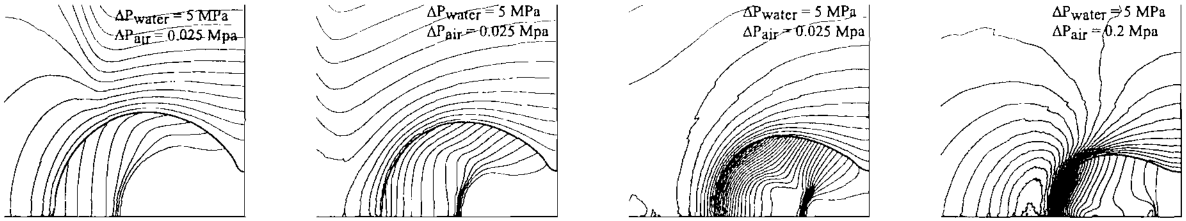

(a) $t = 0.10\,\mu s; \zeta = 0.95$ (b) $t = 0.12\,\mu s; \zeta = 0.95$ (c) $t = 0.14\,\mu s; \zeta = 0.95$ (d) $t = 0.16\,\mu s; \zeta = 0.95$

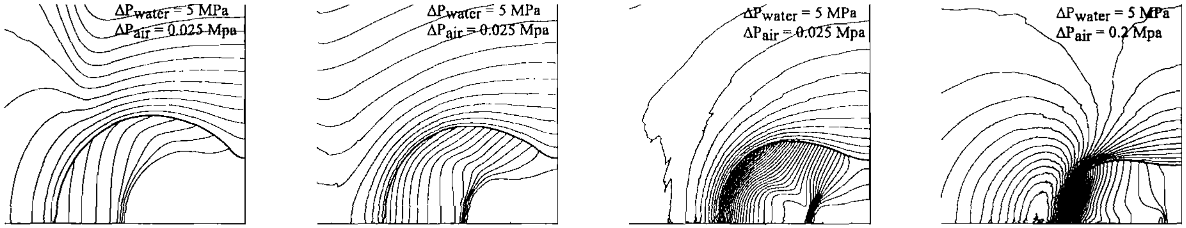

(e) $t = 0.10\,\mu s; \zeta = 0.875$ (f) $t = 0.12\,\mu s; \zeta = 0.875$ (g) $t = 0.14\,\mu s; \zeta = 0.875$ (h) $t = 0.16\,\mu s; \zeta = 0.875$

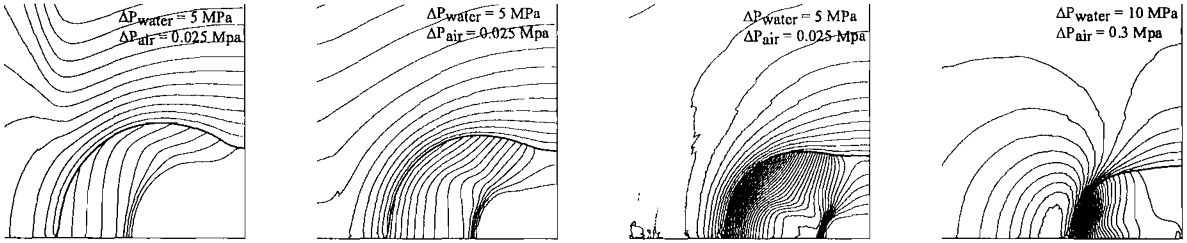

(i) $t = 0.10\,\mu s; \zeta = 0.75$ (j) $t = 0.12\,\mu s; \zeta = 0.75$ (k) $t = 0.14\,\mu s; \zeta = 0.75$ (l) $t = 0.16\,\mu s; \zeta = 0.75$

Figure 8.27: Pressure contours of a bubble with initial radius $R_0 = 40\,\mu m$ collapsed by a lithotripter shock wave with strength of $P^+ = 60\,MPa$. Comparison for different *stand-off distance*, ζ. Top row: $\zeta = 0.95$; Middle row: $\zeta = 0.875$; Bottom row: $\zeta = 0.75$.

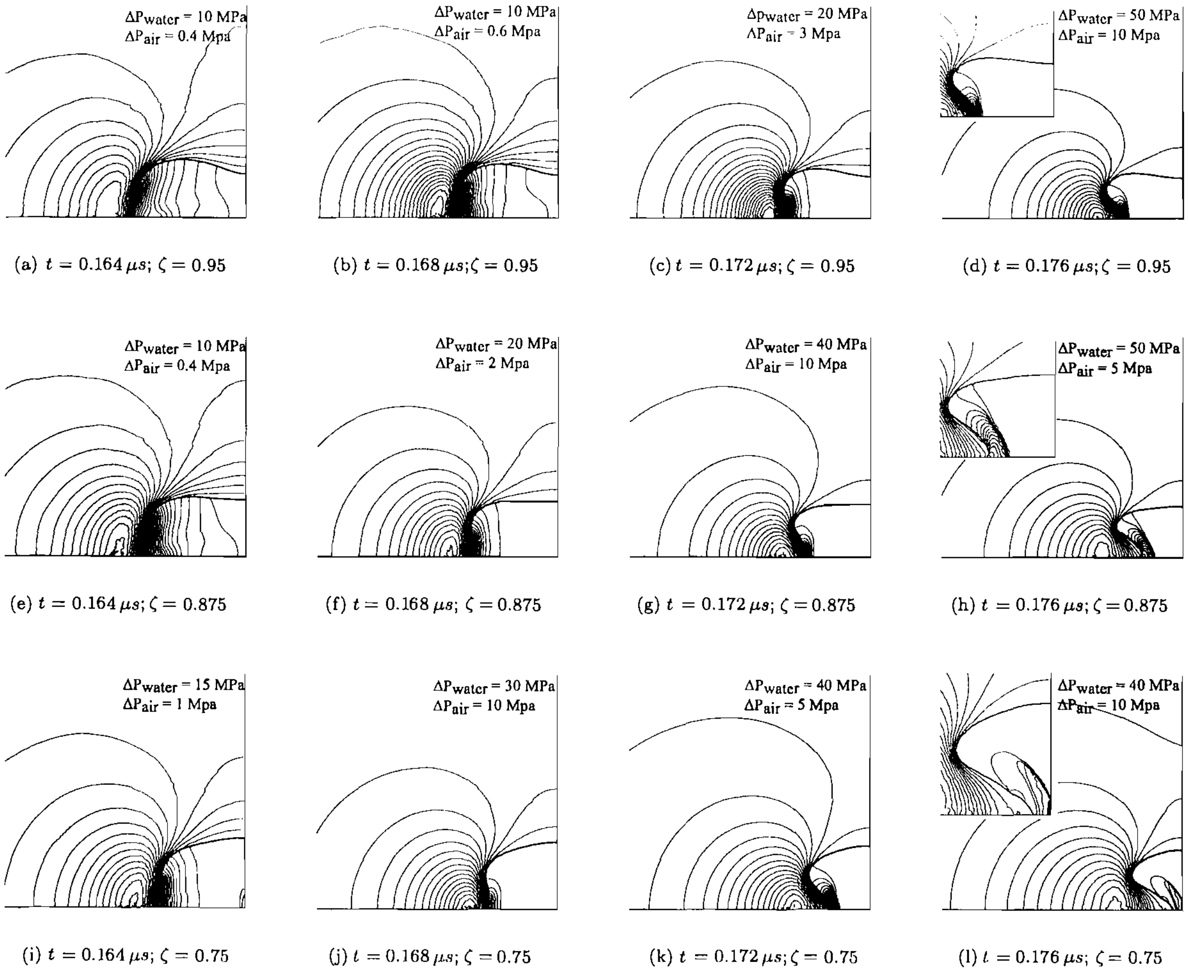

(a) $t = 0.164\,\mu s;\ \zeta = 0.95$ (b) $t = 0.168\,\mu s; \zeta = 0.95$ (c) $t = 0.172\,\mu s; \zeta = 0.95$ (d) $t = 0.176\,\mu s; \zeta = 0.95$

(e) $t = 0.164\,\mu s; \zeta = 0.875$ (f) $t = 0.168\,\mu s;\ \zeta = 0.875$ (g) $t = 0.172\,\mu s;\ \zeta = 0.875$ (h) $t = 0.176\,\mu s; \zeta = 0.875$

(i) $t = 0.164\,\mu s;\ \zeta = 0.75$ (j) $t = 0.168\,\mu s;\ \zeta = 0.75$ (k) $t = 0.172\,\mu s; \zeta = 0.75$ (l) $t = 0.176\,\mu s;\ \zeta = 0.75$

Figure 8.28: Pressure contours of a bubble with initial radius $R_0 = 40\,\mu m$ collapsed by a lithotripter shock wave with strength of $P^+ = 60\,MPa$. Comparison for different *stand-off distance*, ζ. Top row: $\zeta = 0.95$; Middle row: $\zeta = 0.875$; Bottom row: $\zeta = 0.75$.

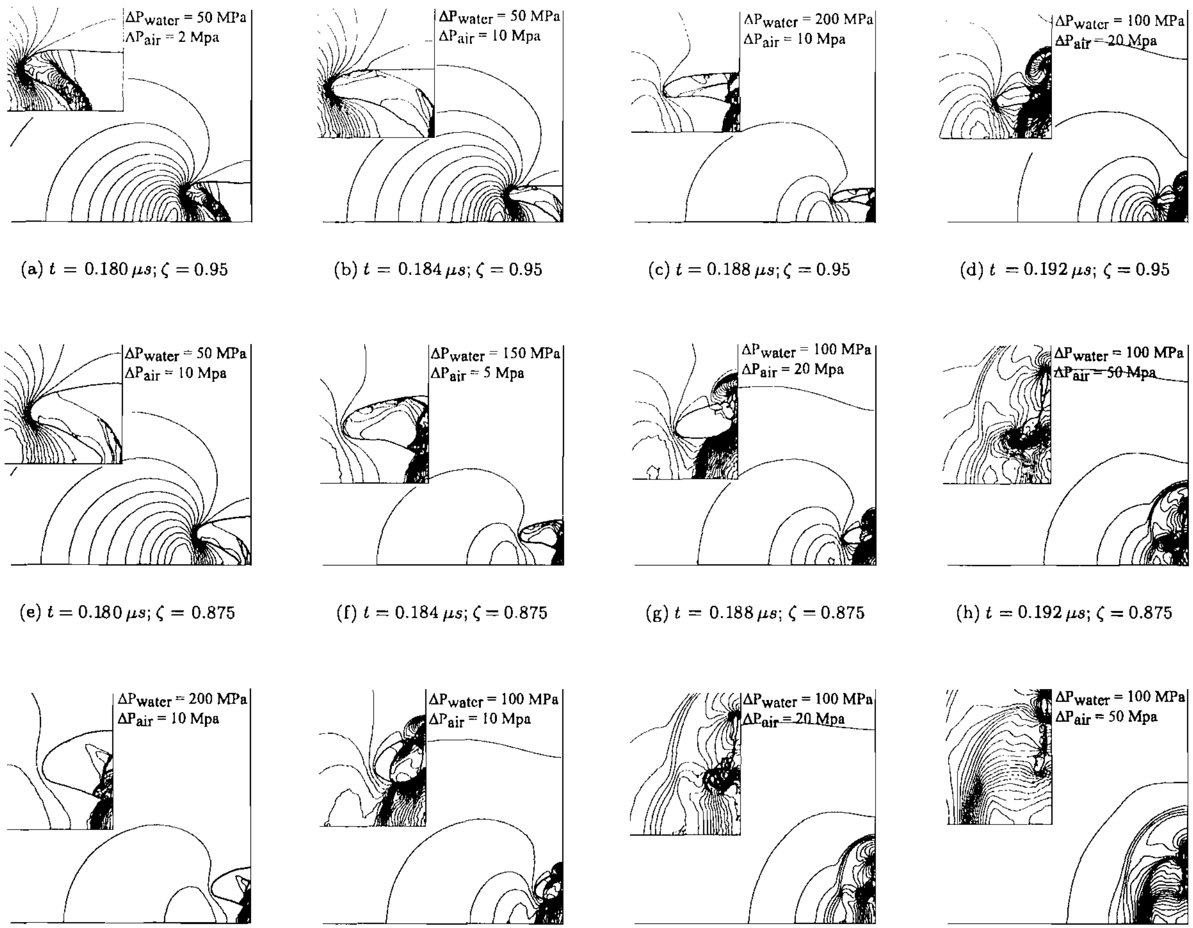

(a) $t = 0.180\,\mu s$; $\zeta = 0.95$ (b) $t = 0.184\,\mu s$; $\zeta = 0.95$ (c) $t = 0.188\,\mu s$; $\zeta = 0.95$ (d) $t = 0.192\,\mu s$; $\zeta = 0.95$

(e) $t = 0.180\,\mu s$; $\zeta = 0.875$ (f) $t = 0.184\,\mu s$; $\zeta = 0.875$ (g) $t = 0.188\,\mu s$; $\zeta = 0.875$ (h) $t = 0.192\,\mu s$; $\zeta = 0.875$

(i) $t = 0.180\,\mu s$; $\zeta = 0.75$ (j) $t = 0.184\,\mu s$; $\zeta = 0.75$ (k) $t = 0.188\,\mu s$; $\zeta = 0.75$ (l) $t = 0.192\,\mu s$; $\zeta = 0.75$

Figure 8.29: Pressure contours of a bubble with initial radius $R_0 = 40\,\mu m$ collapsed by a lithotripter shock wave with strength of $P^+ = 60\,MPa$. Comparison for different *stand-off distance*, ζ. Top row: $\zeta = 0.95$; Middle row: $\zeta = 0.875$; Bottom row: $\zeta = 0.75$.

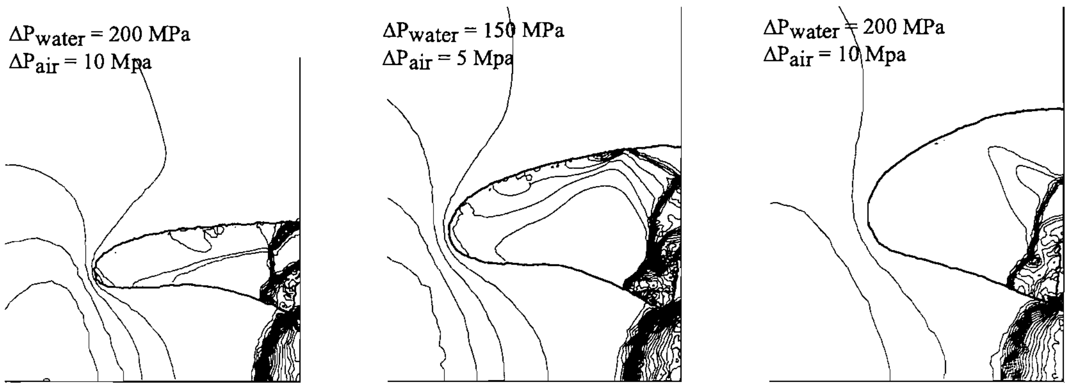

(a) $t = 0.188\,\mu s; \zeta = 0.95$ (b) $t = 0.184\,\mu s; \zeta = 0.875$ (c) $t = 0.180\,\mu s; \zeta = 0.75$

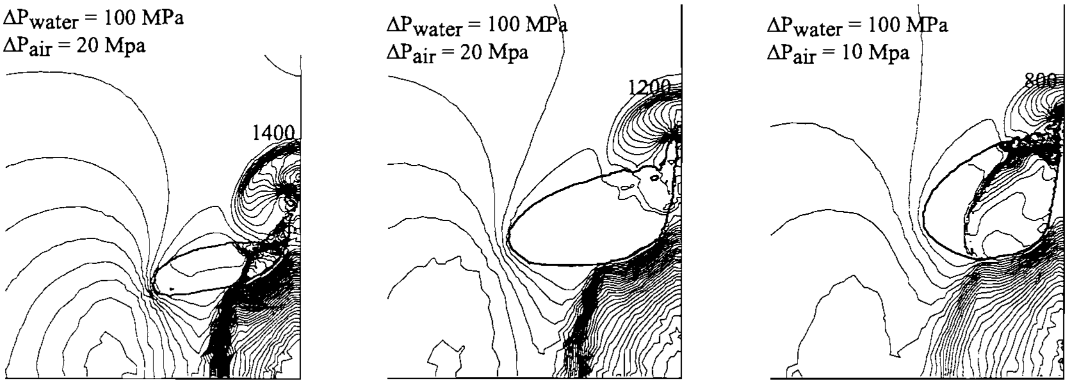

(d) $t = 0.192\,\mu s; \zeta = 0.95$ (e) $t = 0.188\,\mu s; \zeta = 0.875$ (f) $t = 0.184\,\mu s; \zeta = 0.75$

Figure 8.30: Close-up of secondary liquid jet and resulting blast wave due to jet impact on the top bubble wall. Initial radius is $40\,\mu m$ and shock wave strength of $P^+ = 60\,MPa$. Comparison for different *stand-off distance*, ζ. Left column: $\zeta = 0.95$; Middle column: $\zeta = 0.875$; Right column: $\zeta = 0.75$.

8.4 Conclusions

The numerical simulations of asymmetric cavitation bubble collapse, induced by a lithotripter shock wave, using the Free-Lagrange method have been successfully carried out. Various problems have been investigated for different stand-off distance. The results show the general features of asymmetric bubble collapse. These include,

- the formation of a high-speed liquid jet that penetrates the interior of the bubble. The direction of the jet is normal to the incident shock and towards the rigid boundary when the collapse occurs near the proximity of a solid wall. It would be interesting to see the jet direction if the shock and the solid boundary are not aligned, but this would require a full $3D$ simulation, which is outside the scope of the present work.

- the emission of a blast wave as a result of a liquid-liquid impact when the high-speed liquid jet impacts on the downstream bubble surface.
- the elongation of the bubble for small values of ζ.
- the generation of a secondary air shock for bubble collapse near solid boundary.
- the formation of a radially spreading sheet of water in the pre-attached problems. The jet is induced by the radial flow of the primary jet on the rigid boundary. The impact of this jet on the top bubble wall generates a relatively strong blast wave into the surrounding fluid.
- The air shock propagates through the bubble with increasing strength, and for cases where $\zeta < 1.375$, the shock converges near the downstream bubble wall and influences the direction of the fluid flow within the bubble. For cases where $\zeta \geq 1.375$, the air shock will impact on the downstream bubble surface and is reflected back into the bubble.
- The incident shock is reflected by the boundary and the impact on the downstream and top bubble wall causes lateral compression of the bubble.
- The plots for upstream and downstream bubble wall velocity variation with time show that there exists a transition value for ζ at which the contribution of the solid boundary on the bubble behaviour is significant. The study showed that for $P^+ \simeq 60\,MPa$ and $R_0 = 40\,\mu m$, this transition point lies between $1.125 < \zeta < 1.375$.
- The jet has a concave tip such that the leading annular front of the jet will actually impact on the downstream wall earlier than the jet centreline.
- In addition, the rate of collapse of a bubble near a solid boundary increases with decreasing ζ.
- The maximum pressure registered on the rigid boundary decreases with increasing ζ due to the characteristics of a spherical shock where the strength decreases rapidly with increasing radial distance from the centre of the shock source.

- For problems involving pre-attached bubbles, where $\zeta < 1$, the maximum impact pressure on the wall falls to a minimum, but increases back again as ζ is decreased even further.
- Numerical simulations on the interaction of a pre-attached bubble with a lithotripter shock also showed the formation of a radially spreading liquid jet.

Chapter 9

Multi-bubble Simulations

In practical cases, where cavitation or two-phase flow occurs, cavitation bubbles seldom exist as a single bubble, and as a result they interact with each other. This is especially so in cases where clouds of bubbles exist. The degree of influence of a bubble on its neighbours is dependent on their separation distance. In this chapter, simulations of the response of an array of air bubble to a lithotripter shock wave using the *Vucalm* Free-Lagrange method are presented.

The objectives of the current simulations are:

1. to model the interaction of a lithotripter shock wave with two stable spherical bubble, and to observe:
    - the reflection, transmission and refraction of the shock waves
    - the collapse of the spherical bubbles in free-field
    - the formation of the high-speed liquid jet and its velocity-time history
    - the effect of the bubble separation distance and degree of influence of neighbouring bubbles
    - bubble wall position time history for both air bubbles
2. to predict the far-field pressure wave signature emitted from a cloud of bubbles

9.1 Lithotripter shock wave-bubble array interaction in Free-field

The problem studied in the present work comprises two spherical air bubbles immersed in water (Fig. 9.1). The water is represented by the Tait Equation of State (EOS) and is initially at ISA sea level conditions, i.e. the pressure, temperature and density are

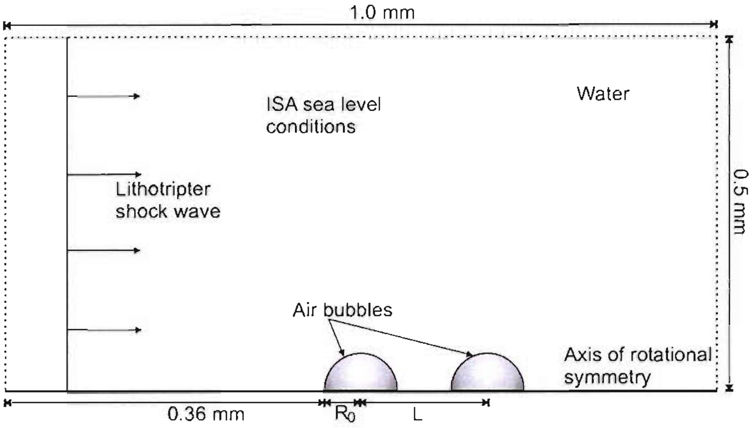

Figure 9.1: The geometry of the problem (Not to scale).

101.325 kPa, 288.15 K and 1000 kgm^{-3} respectively. The bubbles are assumed to contain air, which is represented by the ideal gas EOS. Thus the ratio of specific heat, γ, is 1.4. The initial temperature, density and pressure for the air are 288.15 K, 1.2246 kgm^{-3} and 101.325 kPa respectively. A planar lithotripter pulse, similar to the one used in Chapter 7, with $P^+ = 90\,MPa$ and $P^- = -10\,MPa$, propagates through the water from left to right. The lower domain boundary represents the axis of symmetry. All elapsed times are measured from the first shock/bubble impact. The lithotripter pulse is introduced by imposing a time-dependent pressure boundary condition on the left boundary. The top and right boundaries are non-reflecting at all times.

The separation distance between the initial centre of the bubble is given by L. Simulations for four different L were studied and are discussed in this chapter, i.e. $L = 0.085\,mm$, $L = 0.09\,mm$, $L = 0.1\,mm$ and $L = 0.2\,mm$. The initial air bubble radius, R_0 is $0.04\,mm$.

9.1.1 Results and discussion

The results for the lithotripter shock wave-bubble array interaction problem in free-field are given in Fig. 9.2-9.5. The shock waves moves from left to right. The bubbles are separated by 0.09 mm. The symbols $\triangle P_w$ is increments between contours in the water, while $\triangle P_{a1}$ and $\triangle P_{a2}$ indicate the increments between contours in the air in bubble 1 and bubble 2 respectively.

At $t = 0.111\,\mu s$, the incident shock has traversed the two bubbles (Fig. 9.2(a)). The interaction between the shock and expansion waves originating at the bubble surface results in weakening and curvature of the shock. The dynamics of the collapse of bubble 1 is nearly identical to the problem for a single air bubble in free-field. Bubble 1 is collapsed by the shock wave and a strong air shock propagates in bubble 1, while a weak

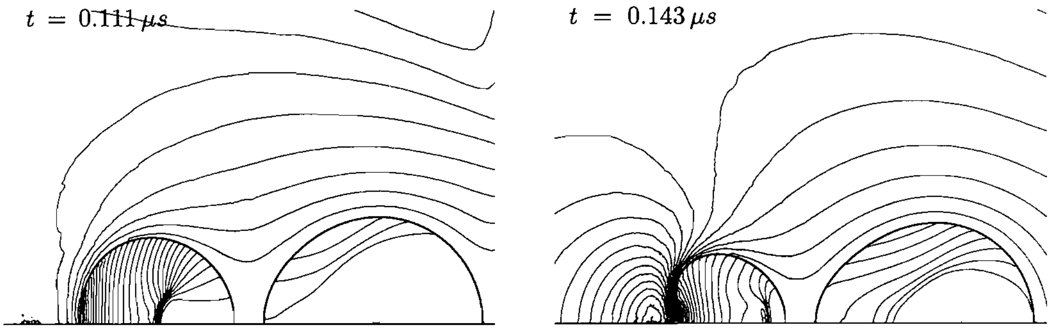

(a) $\Delta P_{a1} = 0.2\,Pa$, $\Delta P_{a2} = 0.2\,Pa$
$\Delta P_w = 50\,Pa$

(b) $\Delta P_{a1} = 1\,Pa$, $\Delta P_{a2} = 0.1\,Pa$
$\Delta P_w = 50\,Pa$

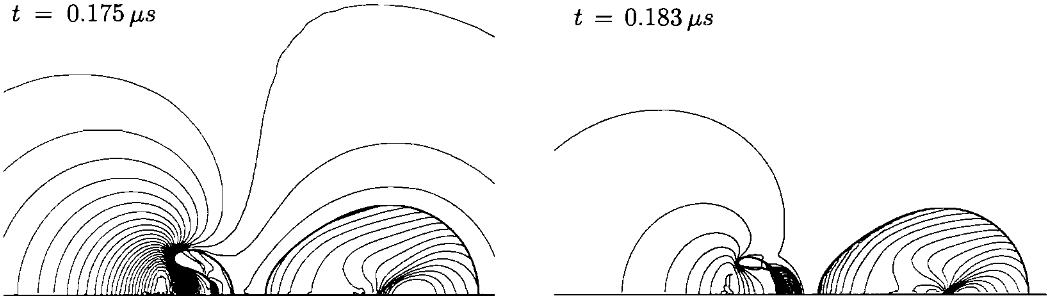

(c) $\Delta P_{a1} = 20\,Pa$, $\Delta P_{a2} = 0.1\,Pa$
$\Delta P_w = 100\,Pa$

(d) $\Delta P_{a1} = 500\,Pa$, $\Delta P_{a2} = 2\,Pa$
$\Delta P_w = 500\,Pa$

Figure 9.2: Pressure contours for an array of air bubbles impacted by a lithotripter shock. Separation distance, L is $0.09\,mm$. Figure shows the collapse of the bubbles and the formation of a liquid jet in bubble 1 (left).

pressure wave is transmitted in the air of bubble 2. During the time that bubble 1 is collapsing, bubble 2 has been shielded from the initial incident shock wave and has only experienced a slight lateral compression (see Fig. 9.2(c) onwards). The liquid jet begins to form in bubble 1 Fig. 9.2(b), developing in amplitude by Fig. 9.2(c). The jet travels across the bubble and reaches the downstream wall at approximately $t = 0.182\,\mu s$ (Fig. 9.2(d)). At this time, bubble 2 shows no sign of liquid jet formation.

At $t = 0.191\,\mu s$ (Fig. 9.3(a)), the air cavity of bubble 1 is drawn into the vortex core while the blast wave continues to propagate outwards radially from the bubble. The blast wave arising from the liquid-liquid jet impact of bubble 1 impacts on the upstream wall of bubble 2, causing it to collapse to produce a jet (Fig. 9.3(c)-(d)). On impact, the strength of the blast wave is calculated to be approximately $0.5\,GPa$. A strong air shock is also transmitted in bubble 2. The strength of the blast wave decreases as it propagates into the surrounding water. It is clear that the collapse of bubble 2 is greatly amplified by the blast wave originating from the collapse of bubble 1. Following jet impact, the

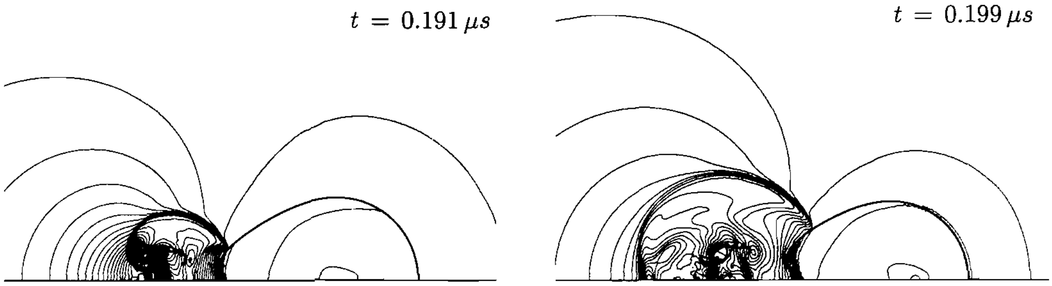

(a) $\Delta P_{a1} = 500\,Pa$, $\Delta P_{a2} = 4\,Pa$
$\Delta P_w = 200\,Pa$

(b) $\Delta P_{a1} = 500\,Pa$, $\Delta P_{a2} = 5\,Pa$
$\Delta P_w = 200\,Pa$

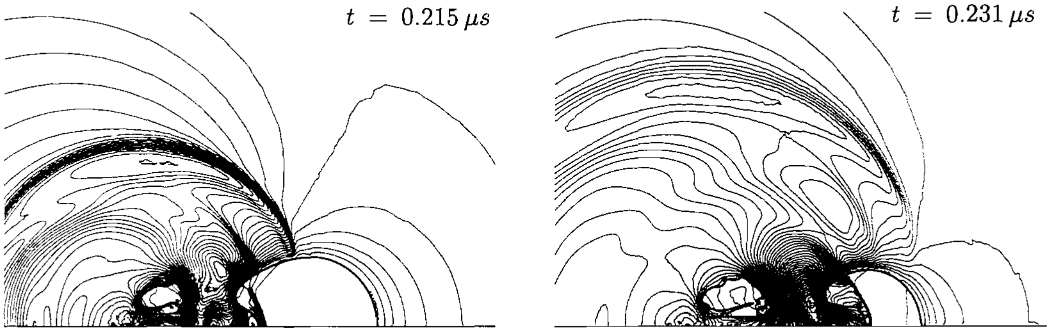

(c) $\Delta P_{a1} = 20\,Pa$, $\Delta P_{a2} = 10\,Pa$
$\Delta P_w = 50\,Pa$

(d) $\Delta P_{a1} = 10\,Pa$, $\Delta P_{a2} = 10\,Pa$
$\Delta P_w = 50\,Pa$

Figure 9.3: The blast wave generated by bubble 1 impacts on bubble 2, leading to the formation of a liquid jet ($L = 0.09\,mm$).

high pressure in bubble 1 causes it to expand.

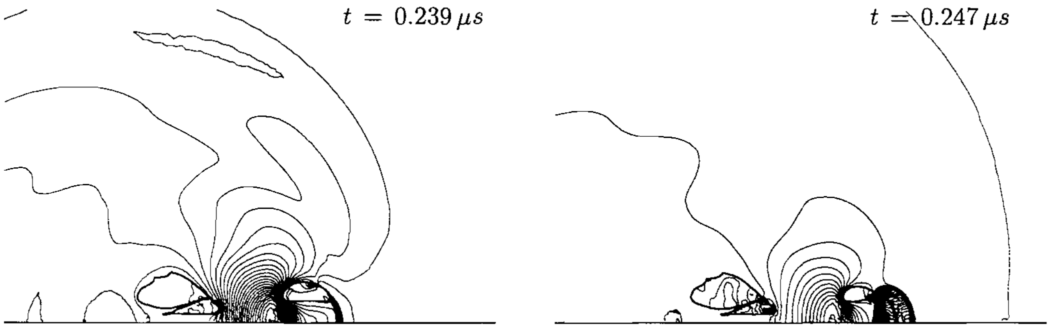

(a) $\Delta P_{a1} = 500\,Pa$, $\Delta P_{a2} = 100\,Pa$
$\Delta P_w = 200\,Pa$

(b) $\Delta P_{a1} = 500\,Pa$, $\Delta P_{a2} = 500\,Pa$
$\Delta P_w = 200\,Pa$

Figure 9.4: The liquid jet pierces through bubble 2 and impacts on the downstream wall. Separation distance, L, is $0.09\,mm$.

By $t = 0.239\,\mu s$ (Fig. 9.4(a)), bubble 1 has expanded to a volume greater than the collapsing bubble 2. The pressure gradient near the upstream of bubble 2 continues to increase with time. A high speed liquid jet is formed and impacts on the downstream wall of bubble 2 at $0.239\,\mu s$. As a result of the lateral compression experienced by bubble 2 earlier in the collapse process, the liquid jet that is formed is narrower than that of bubble 1. On impact, the jet produces an intense blast wave in the surrounding water (Fig. 9.4(b)). This blast wave will interact with the expanded bubble 1, and cause the latter to undergo a secondary collapse. At $t = 0.248\,\mu s$, the jet has penetrated through the bubble isolating a lobe of trapped air and highly compressed gas that resembles a tear-drop (Fig. 9.5(b)).

It is believed that if a third bubble is positioned downstream of bubble 2, a chain reaction would occur and the third bubble would collapsed in a similar manner by the collapse and rebound of the second bubble. This situations for bubble collapse and jet formation are likely to take place during typical cavitation conditions, since pressure waves from the collapse and rebound of some bubbles will pass over neighbouring bubbles. Therefore, it is necessary to carry out a study to investigate how the collapse of neighbouring bubbles are affected by their mutual interactions. It is shown here, that for $L = 0.09\,mm$, bubble 2 is shielded from the incident lithotripter shock wave. However, the blast wave originating from the collapse of bubble 1 interacts with bubble 2. This is analogous to an incident shock wave passing over bubble 2, causing a jet in the direction of the shock. The study here is limited to axisymmetric geometries and the bubbles are positioned in a line normal to the incident shock wave. Dear & Field [30] carried out experimental work to study the behaviour of triangular arrays of $2D$ cavities, where the cavities are staggered in a three, two and one array. It was observed that a chain reaction of collapse occurs. Unlike the results shown here, the second cavity is only partly in the shadow of the first cavity and therefore the incident shock wave impacts on the second bubble asymmetrically. As a result, the liquid jet formed by cavity two is not so well formed and is not normal to the incident shock wave.

Three other cases for different separation distance, L, were studied, and the results are depicted in Fig. 9.6. The bubble wall time history for bubble 1 is plotted in black. The continuous lines depicts the upstream wall of the bubble whilst the dashed lines refers to the downstream bubble wall. The point where the two line meet is where the liquid-liquid jet impact occurs that produces an intense blast wave in the surrounding water. For bubble 1, this point of impact is labeled 'X'. The wall position of bubble 2 for the four cases are plotted in colour. The plotted curves make it easier to observe the effect of separation distance on the bubble wall motion, for bubble 2 in particular.

As the incident shock wave hits the upstream wall of bubble 1 (black lines), the upstream wall collapse gradually and then accelerates towards the downstream wall, forming a high-speed liquid jet. However, throughout the duration of the collapse, the downstream

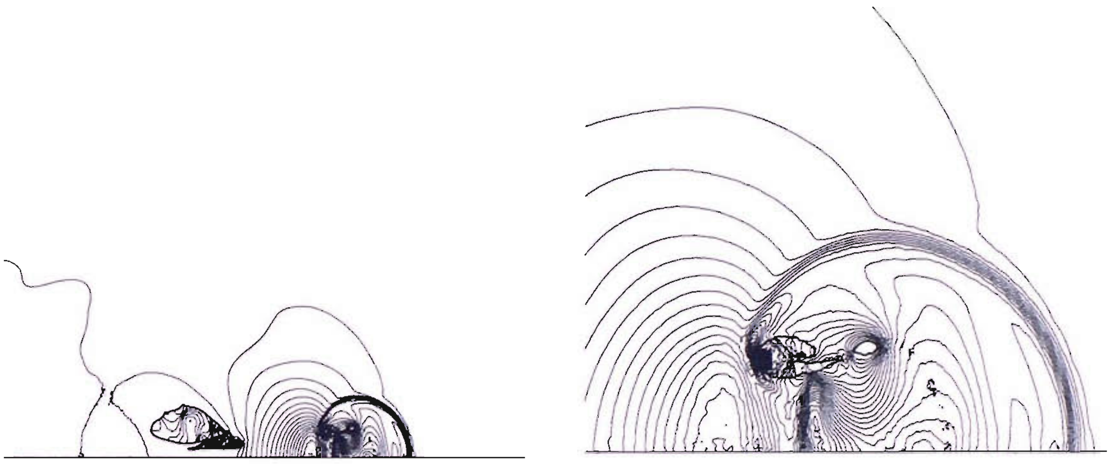
(a)
(b)

Figure 9.5: Near spherical blast wave emitted from the liquid-liquid impact as the jet impacts on the downstream wall of bubble 2. The time is $0.248\,\mu s$, $\Delta P_{a1} = 500\,Pa$, $\Delta P_{a2} = 5\,Pa$; $\Delta P_w = 200\,Pa$ and $L = 0.09\,mm$. Fig. *(b)* is a magnification of bubble 2 in (a).

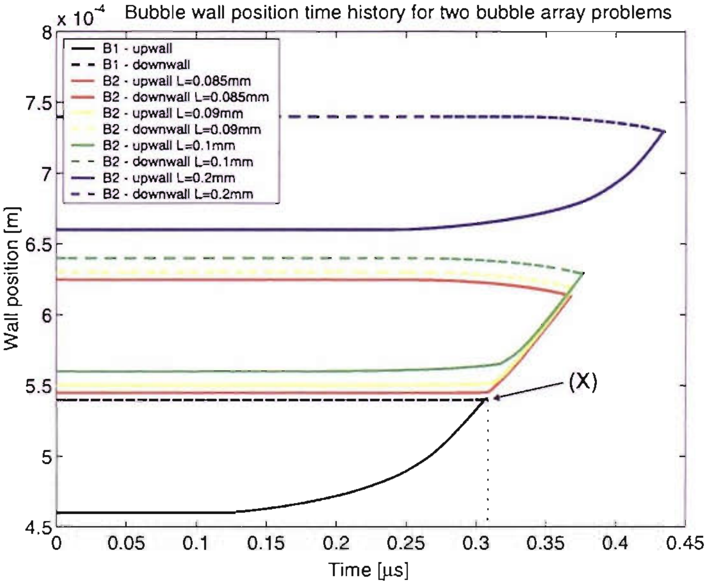

Figure 9.6: Bubble wall position time history for bubble 1 and 2.

wall appears to remain almost stationary. However, if the collapse of the bubble 1 was to be examined closely, it was found that the collapse of the downstream wall does take place (Fig. 9.7). For $L = 0.085\,mm$, the upstream wall of bubble 2 is shielded by bubble 1. The collapse of the former only occurs following the liquid jet impact of bubble 1. It is apparent that the collapse is initiated by the blast wave that is generated by the liquid-

liquid impact at point X on the curve. Similar trend can be observed for $L = 0.09\,mm$ (yellow lines) and $L = 0.1\,mm$ (green lines). The influence of the incident lithotripter shock wave on the upstream wall of bubble 2 gradually increase at large value of L. For $L = 0.2\,mm$, the collapse of the upstream wall motion increases gradually and accelerates towards the end of the collapse phase where a liquid jet is formed. The motion of the wall is similar to that of bubble 1.

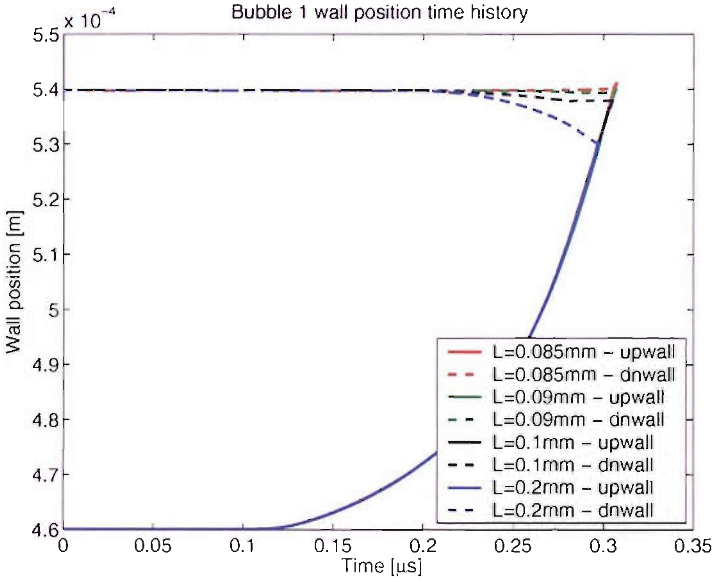

Figure 9.7: Bubble 1 wall position time history for various L.

From Fig. 9.7, it is clear that the bubble wall time history of bubble 1 are different for all four cases towards the end of the collapse phase. The upstream wall collapse at the same rate while the degree of collapse of the downstream wall varies with separation distance L. It is apparent that bubble 2 shields the downstream wall of bubble 1 from the incident shock wave. For $L = 0.085\,mm$ where the bubbles are very close to one another, the inward collapse motion of the downstream wall is minute in comparison to the case when $L = 0.2\,mm$ (dashed blue line). As a consequent of this motion of the downstream wall, the time to jet impact decreases with increasing L.

It is believed that there is a critical value of L above which bubble 2 behaves like an isolated bubble in free-field with no mutual interactions with bubble 1. This is depicted by plotting a dimensionless parameter A_L against the normalised separation distance L/R_0. This is given in Fig. 9.8. The parameter A_L is given by the following equation,

$$A_L = (L/U_s)/(t_{j2} - t_{j1})) \qquad (9.1)$$

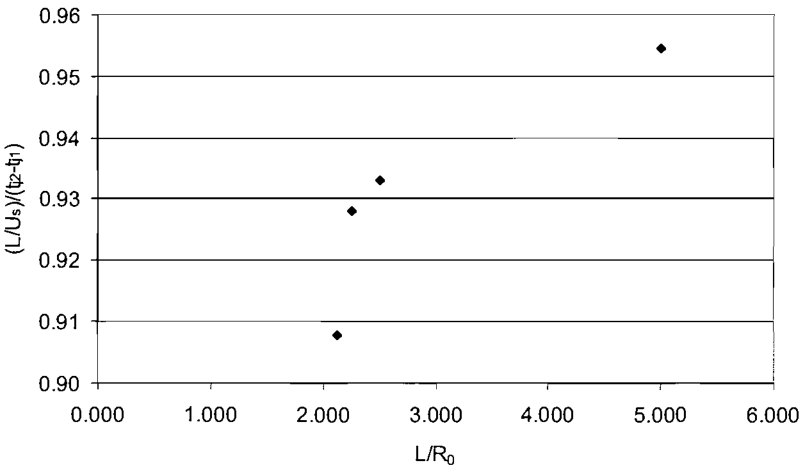

Figure 9.8: Bubble array interaction study. Normalised parameter A_L against separation distance L.

where L is the bubble initial separation distance, U_s is the incident shock wave velocity, and t_{j2} and t_{j1} are the time to jet impact for bubble 2 and bubble 1 respectively. It is clear from Fig. 9.8 that A_L reaches an asymptotic value for large value of L. If the separation distance is greater than $0.2\,mm$, it can be assumed that the two bubbles are sufficiently far apart that they do not affect the dynamics of one another. This information will be used in the next section, where the far-field pressure wave signature from a cloud of cavitation bubbles are carried out. If $L/R_0 \simeq 5$, the bubbles can be neglected from the calculation.

9.1.2 Far-field Pressure Signature From Cavitation Cloud

In this section, the Kirchhoff solution for a single bubble in free-field is extended to a multi-bubble problem. A Gaussian normal distribution is used to randomly distribute the bubbles in water, with high bubble density concentrated around the focal point of the converging incident lithotripter shock wave (Fig. 9.9 and Fig. 9.10).The focal size is commonly used to describe the spatial pressure distribution of the acoustic field of a lithotripter. In water, the region of the focal point coincides with the position of high temporal peak negative pressure. In this study, the focal region of the lithotripter shock wave is approximated to be of a cigar-shaped volume, $60\,mm$ long and $10\,mm$ in diameter [27, 23][1]

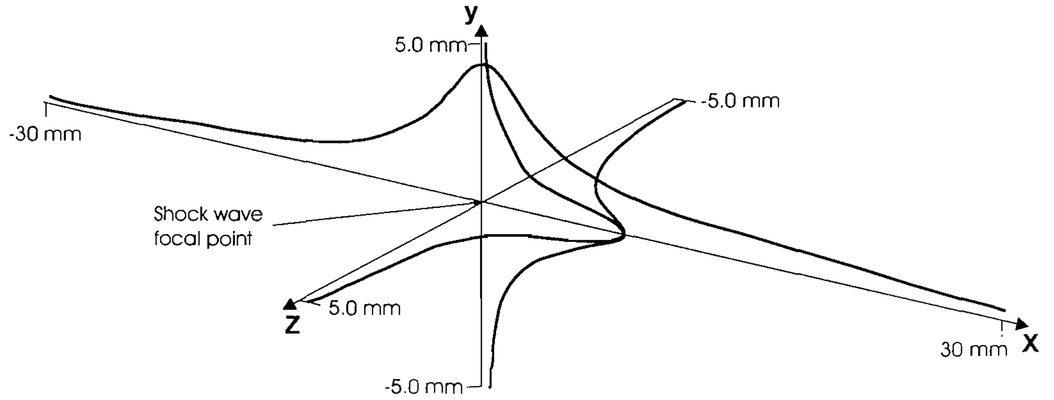

Figure 9.9: Cigar-shaped lithotripter shock wave focal point. A normal distribution of the bubbles relative to the focal point.

Although it is described here that air bubbles are distributed randomly, it is actually the Kirchhoff control surface for an an isolated air bubble that is distributed based on a normal distribution about the focal point of the shock wave (Fig. 9.11). Hence, each control surface represents a single bubble in free-field, each emanating an identical far-field pressure signature to that shown in Fig. 7.15 in Chapter 7. In the study here, 1000 bubbles are randomly generated and the observer is positioned 500 mm from the bubble cloud centre, where $\theta = 270^o$ and $\phi = 45^o$.

A number of assumptions have been made for the prediction of the far-field bubble cloud pressure signature. They are as follows:

1. Highest density of bubbles is near the focal point of the lithotripter shock wave and that the distribution is approximated as a Gaussian distribution.
2. There is no shielding effect between bubbles, as discussed in previous section.
3. The collapse of the bubbles is caused by the incident lithotripter shock wave and not the blast wave emanated from liquid jet impact of neighbouring bubbles.
4. The pressure peak positive amplitude seen by each bubbles is identical at $P^+ = 90\,MPa$, i.e. the strength of the shock wave remains constant as it traverses through the cloud of bubbles.

---

[1] These values are used as the limits when distributing the bubbles using the normal distribution. The bubble cloud size generated is therefore $< 60\,mm$ in the X-direction and $< 10\,mm$ in the Y and Z-direction.

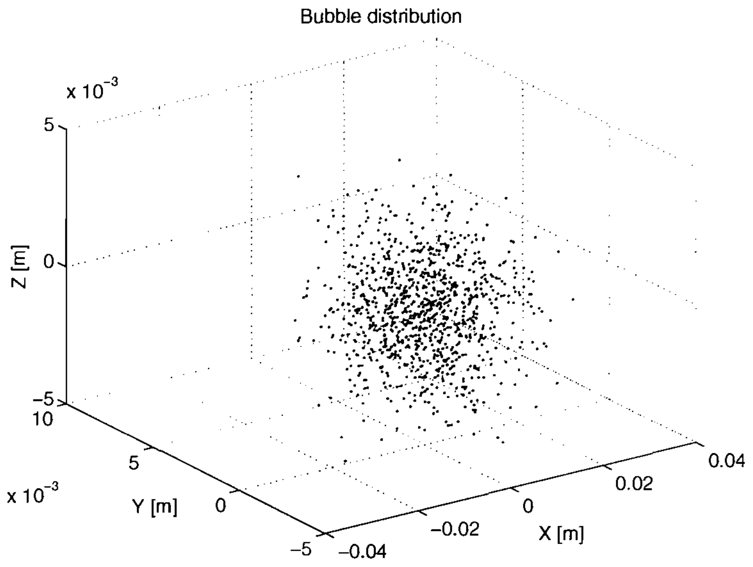

Figure 9.10: Three-dimensional plot showing the bubble (Kirchhoff control surface) distribution.

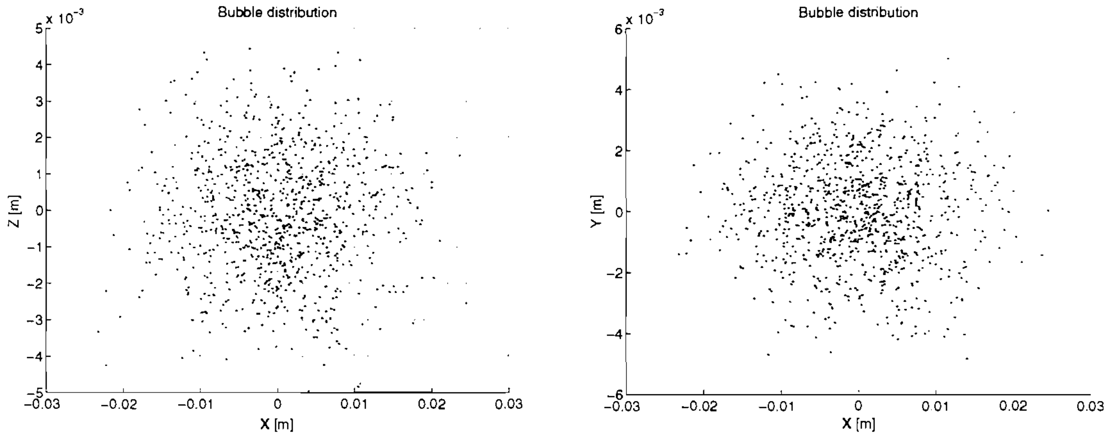

(a) $X - Z\,plane$

(b) $X - Y\,plane$

Figure 9.11: Random bubble distribution in X-Y and X-Z plane.

5. The cloud of bubbles is initiated from cavitation nuclei by a preceding lithotripter shock wave. The bubbles then undergo a series of expansion and collapse phase before reaching a stable equilibrium size of $40\,\mu m$. The far-field acoustic wave of the bubble cloud predicted here is for the interaction of these stable bubbles with the subsequent incident lithotripter shock wave.

6. The pressure signature of the bubble cloud at the observer point is given by a linear summation of the pressure signatures of the individual bubbles.

7. Any scattering and attenuation by soft tissues or fluid are neglected.
8. The collapse time of the bubbles is staggered to simulate the finite time taken for the shock to sweep through the cloud.

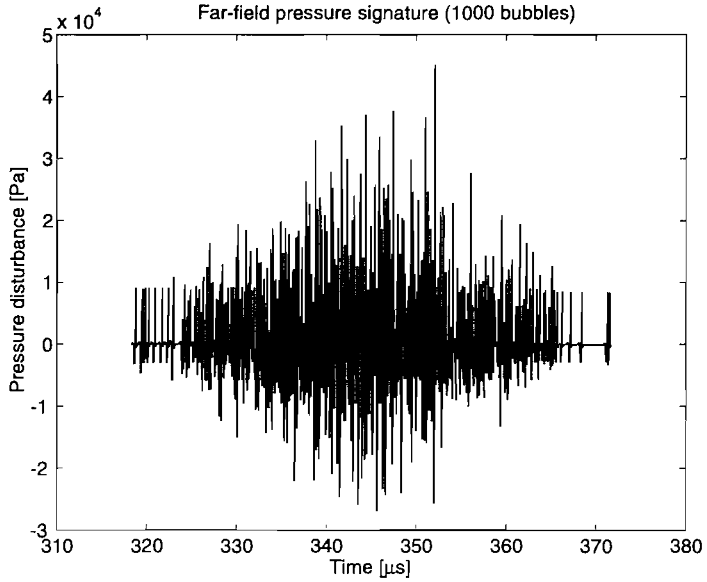

Figure 9.12: Predicted pressure signature emanated from a bubble cloud which consists of 1000 bubbles.

The far-field pressure signature shown in Fig. 9.12 is calculated by taking a linear summation of the pressure signatures of individual bubble. Thus, the high pressure region of the far-field signal (between 335 μs - 355 μs) corresponds to the region of high bubble density. Pressure waveforms originating from a single bubble can also be clearly seen in Fig. 9.12 around $t = 320\,\mu s$ and $t = 370\,\mu s$. It is also apparent that the duration of the signal is highly dependent on the position of the observer, the distribution of the air bubbles and the size of the bubble cloud. If the results shown in Fig. 9.12 are comparable to the results calculated from the Gilmore model, then one could argue that there are only minor discrepancies between the results from the spherical collapse and the asymmetric collapse. It is postulated that the distribution of the bubbles and size of the bubble cloud in experimental study can be approximated using the method described above.

Chapter 10

Conclusion and Future Work

This chapter summarises the work conducted in this research, including all important findings related to the validation of the Free-Lagrange method and its application in shock-bubble interaction studies. In addition, suggestions for possible future work are presented.

10.1 Conclusions

The newly developed axisymmetric version of the Free-Lagrange code *Vucalm* has been used to simulate the interaction between a shock wave and a spherical air bubble. This methodology has been chosen as it allows the material interfaces to be sharply resolved at all times. Since material interfaces are always stationary relative to the mesh, no additional interface tracking or modeling algorithm is required in multi-material problems. The method also helps to reduce numerical diffusion at the material interface as well as ensuring exact conservation of mass. In addition, Lagrangian methods allow the time history of individual parcels of fluid to be tracked, including, for reacting flows, their chemical history. The use of the Free-Lagrange method for simulations involving multi-phase flows is attractive because it avoids mesh tangling issues experienced by conventional fixed-connectivity schemes such as conventional Lagrangian schemes.

Validation of the axisymmetric version of the Free-Lagrange, *Vucalm* code has been carried out in order to show the ability of the code to solve flow problems in axisymmetric form. The validation was performed by carrying out two numerical simulations involving multi-phase flows. The two problems are

- shock-induced collapse of a spherical air bubble by a planar step shock (Ding and Graceswki [35])
- the interaction of a shock with a water column (Igra and Takayama [52])

In the comparison with the present work and Ding and Graceswki's, the numerical simulation agrees with the previously published numerical data in that the jet speed is independent of the initial gas cavity size, but depends on the applied shock strength. The results also show good agreement in the pressure contours, Mach contours and velocity vector. The shock-cavity interactions is shown to be physically complex. The interaction of a planar shock wave with a water column was presented in the second part of Chapter 6. Isopycnics and interferogram images at two different stages of the flow were obtained from reference [52] and were compared with that using the *vucalm* code. The results obtained agreed well with the numerical and experimental findings of Igra and Takayama. Both results show the Mach stems and triple point as well as secondary triple point at later stages of the flow. The interferogram at $t = 43\,\mu s$ not only revealed a high pressure region downstream of the water column but also a vortex flow. The fringe number and spacing in air agreed quite well with the experimental interferogram images.

The numerical simulations of asymmetric cavitation bubble collapse induced by a lithotripter shock wave in free-field as well as for nine different stand-off distance have been successfully carried out. The results show the general features of asymmetric bubble collapse. This include:

- The formation of high-speed liquid jet that penetrates the interior of the bubble.
- The emission of a blast wave as a result of a liquid-liquid impact when the high-speed liquid jet impacts on the downstream bubble surface.
- The elongation of the bubble for small value of ζ.
- The generation of a secondary air shock for bubble collapse near a solid boundary
- The induced radially spreading sheet of water along the solid boundary in the pre-attached bubble problems.
- The formation of a concave liquid jet head which is thought to be caused by the interaction of the collapsing bubble with the reflected incident shock wave.
- In the bubble array study, it was found that mutual interaction between neighbouring bubbles is minimal when the separation distance, L, is over $5R_0$.
- For $5R_0$, shielding of the incident lithotripter shock wave on one bubble (bubble 2) occurs. Furthermore, if the separation distance is small enough, the blast wave generated from the collapse of one bubble can enhanced the collapse of neighbouring bubbles.

The work presented here includes the development and implementation of two aeroacoustic codes for the study of shock-bubble interaction to predict the acoustic signature in the far-field. The two acoustic formulations implemented are the Kirchhoff's method and Ffowcs-Williams-Hawkings method. When coupled to the Free-Lagrange code, each method can be used to obtain the far-field pressure signatures of cavitation events. Both numerical codes have been validated against analytical results in predicting the far-field pressure signature emitted from an oscillating solid sphere.

The Kirchhoff's and FWH integral formulations allow the radiating sound to be evaluated based on quantities on an arbitrary near-field control surface. The idea is to solve the non-linear problems in the near-field, using *Vucalm*, and a surface integral of the solution over the control surface then gives enough information for the analytical calculation in the far-field. It was clearly shown that two methods work well. To summarise:

- The FWH requires the storage of (ρ, p' and ρu_i) for each control point, while ($p, \partial p/\partial n$ and $\partial p/\partial t$) are required by Kirchhoff.
- The Kirchhoff method is simpler, and easier to implement. However, the method puts more stringent requirements on the CFD method to reach to the linear acoustic field.
- The porous FWH method allows for nonlinearities on the control surface, whereas the Kirchhoff method assumes a solution of the linear wave equation on the surface S.
- The predicted far-field waveform clearly captures the radiated expansion wave and the sharp peak of the blast wave, generated from the liquid jet impact.
- The variation of the pressure waveform for different observer position using the two methods agree well for $R_{cs} = 5R_0$.
- The results of the predicted far-field pressure signature of a bubble cloud show that the density of the signal is highly dependent on the bubble distribution.

10.2 Future Work

The axisymmetric Free-Lagrange code, which has been used and developed here offers a lot of potential for future exploitation. This includes physical and computational aspects. Possible future works include:

10.2.1 Physical aspects

- Simulations of shock-induced collapse of an air bubble with different initial radius and shock strength.
- Simulations near an elastic/plastic boundary or a material with strength such as copper, steel or materials that can be used to represent kidney stones.
- Simulations with different surface geometry, e.g. notch shapes and sizes, for a range of stand-off distances.

10.2.2 Computational issues

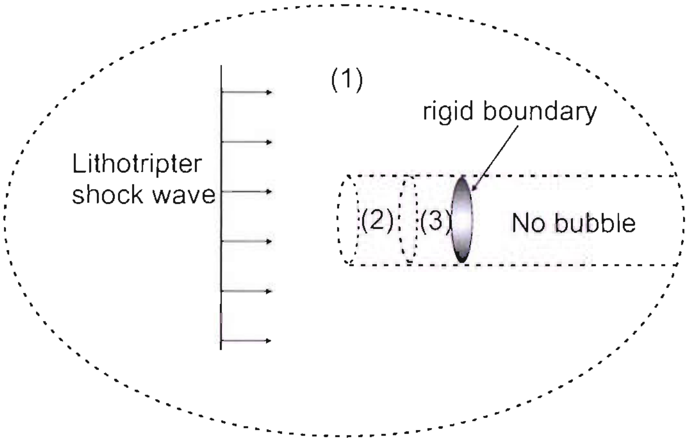

Figure 10.1: Bubble cloud problem diagram. Region 1: Free-field; Region 2: $\zeta = 2.125$; and Region 3: $\zeta = 1.0625$.

- Incorporate the long expansion and subsequent collapses into the CFD simulations. As discussed in Chapter 2, the interaction of the shock wave with the bubble will cause it to collapse, and after which, the negative tail of the driving waveform initiates a long expansion phase of the bubble. Following the long expansion phase, the overgrown bubble will undergo a violent inertial collapse. Subsequent cycles of rebound and collapse will occur until the bubble reaches an equilibrium state with the surrounding water. In the current work, numerical simulations are stopped following primary collapse of the bubble by the lithotripter shock wave. Current simulations show that the time to collapse is about $0.18\mu s$ and, according to the Gilmore-Akulichev model, the interaction of the tensile part of the lithotripter shock with the collapsed bubble will induce an expansion phase for over $200\mu s$. Modeling this long expansion phase is therefore time consuming and very expensive. One way of modeling the expansion phase is to incorporate the Gilmore model. The idea is to used the Free-Lagrange code to numerically simulate the primary collapse of the bubble, then incorporate the Gilmore model to calculate the long expansion phase and obtained important parameters which will then be incorporated back into *Vucalm* to simulate the secondary collapse of the over-expanded bubble. The geometry of the bubble need to be simplified to a sphere for the period when the Gilmore model is used. The third stage of the work is quite similar to an underwater explosion or laser-induced cavitation problem, but the simulation starts from the stage at which the bubble has already reached its maximum size and is at the point of collapsing.

- The bubble cloud far-field pressure signature presented in Chapter 9 was generated from near-field data from the free-field simulation of a single bubble. It would be interesting to study the predicted far-field waveform generated from the near-field signatures from different cases, e.g. the near rigid boundary problem with different stand-off distances. See Fig. 10.1. The ellipsoidal dotted line represents the focal region of the lithotripter shock wave. Three regions are identified, a free-field region (Region 1) and two regions near a rigid boundary, e.g. Region 3: $\zeta = 1.0625$ and Region 2: $\zeta = 2.125$. 1000 bubbles are generated randomly and three different solutions will be used to model this problem. The rigid boundary represents a kidney stone, and downstream of this boundary, the fluid is shielded from the lithotripter shock wave, and therefore no bubble exists. This model will look at the affects of the rigid boundary on the predicted far-field waveform.

- The far-field pressure signature predicted from the collapse of a bubble cloud can be regenerated by using a delta function of $0.2\,\mu s$ duration as the density frequency distribution is highly dependent on the bubble density and distribution. As *Vucalm* solution is expensive, the use of a delta function is attractive as it is reproducible for any cases. For example, the pressure signature emanated from a bubble cloud studied in Chapter 9 can be taken as a linear summation of a delta function that would replace the solution obtain using the *Vucalm* and aeroacoustic codes. The frequency from the predicted far-field pressure signature is approximately $0.5\,\mu s$ duration, which gives a frequency in the order of MHz. This agrees with experimental findings which suggest that the frequency content from the collapse of micro-bubbles is of the same order. With this information, the work could usefully be extended to compare with experimental results.

Appendix A

Conservation Laws for Continuous Media

A set of conservation equations arising from first principles describes the fluid behaviour. There exist three fundamental principles of conservation. These are

- Conservation of Mass
- Conservation of Momentum
- Conservation of Energy

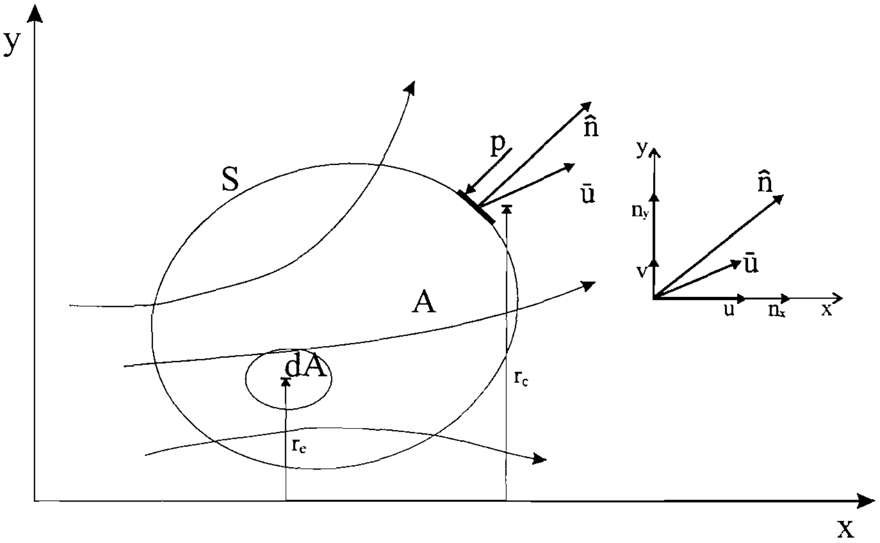

Figure A.1: An arbitrary fixed area A bounded by surface boundary S in $x - y$ plane

Consider the detailed Eulerian finite volume model shown in Fig. A.1 and apply to this model physical principles. Let A be an imaginary face area, enclosed by a surface boundary S that is fixed in the $x-y$ plane. Within the control volume and on the bounding surface, an elemental surface area dA with its centroid ordinate r_ϵ, and elemental surface boundary dS can be constructed respectively. On the elemental line dS with an ordinate of its middle point r_c, pressure p is acting inwards into the area A, while a unit vector, normal to the surface $\hat{n}$, and a velocity vector $\bar{u}$ are pointing outwards. Note that the overbar symbol denotes a vector. In a Cartesian coordinate system, these two vectors can be divided into x and y components as illustrated in Fig. A.1.

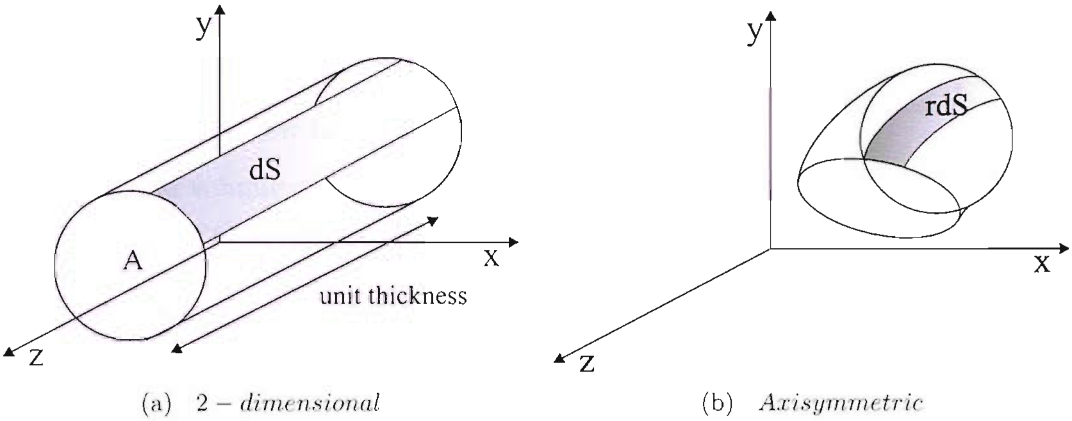

(a) $2-$*dimensional* (b) *Axisymmetric*

Figure A.2: Schematic diagram of (a) 2D and (b) axisymmetric

For a $2D$ problem (Fig. A.2(a)), the area A and line S represent the volume and 'circumferential' area respectively. The flow is planar and is defined as per unit thickness - in $2D$ *Vucalm* code, thickness is taken as $1m$.

On the other hand, in the axisymmetric case, the face area A enclosed by line S is rotated about an axis of symmetry, chosen here to be the x-axis, to give a ring-like control volume as depicted in Fig. A.2(b). The y-axis is equivalent to the r-axis. As a consequence, both the volume and surface area enclosing the control volume are functions of radial distance r, measured from the axis of symmetry. Following Pappus theorem [98], the volume is the product of the face area A and the circumference θr_ϵ, and θ is the angle of rotation. Thus, the control volume and the wrapping surface area are

$$\text{Volume} = \theta \int_A r_\epsilon \, dA \qquad \text{Surface Area} = \theta \int_S r_\epsilon \, dS \tag{A.1}$$

In the derivation of the axisymmetric governing equations, the angle of rotation, θ is taken as $1 radian$. It is important that the surface boundary S enclosing face area A does not intersect with the axis of symmetry to give an unphysical negative volume that violates the axisymmetric geometry. It should be noted that, because the control volume is fixed in the frame in the Eulerian reference frame, both the surface area and control volume are not time dependent parameters. In the next section, the three physical principles are considered to formulate the governing equation.

A.1 Conservation of Mass - Continuity Equation

Let the first physical principle be - Mass is conserved. For a finite control volume fixed in space, the following statement can be constructed:

$$\begin{pmatrix} \text{Rate of change of Mass of} \\ \text{Fluid Occupying Volume} \\ \text{Enclosed by Surface} \end{pmatrix} = \begin{pmatrix} \text{Mass Flux of Fluid} \\ \text{Through Control Surface} \end{pmatrix}$$

For an elemental volume of $r_e dA$, the mass of this element would then be $\rho r dA$. Hence, the mass of fluid in the elemental volume is $\rho r_e dA$. Therefore, the total mass m contained within the control volume V is given by the integral

$$m = \int_A \rho r_e \, dA \tag{A.2}$$

where ρ is the density. The rate of change of mass m is therefore

$$\dot{m} = \frac{\partial m}{\partial t} = \frac{\partial}{\partial t} \int_A \rho r_e \, dS \tag{A.3}$$

and this is the left-hand side of statement A.1. Now, consider the volume flux across the control surface element $r_c dS$ which is

$$-\hat{n} \cdot \bar{u} r_c \, dS \tag{A.4}$$

Hence, the mass flux through the elemental surface area is given by:

$$\delta m_f = -\hat{n} \cdot \rho \bar{u} r_c \, dS \tag{A.5}$$

Since $\hat{n}$ is by convention positive when pointing outwards from the control volume, the mass flow is negative or out of the control volume when $\hat{n} \cdot \bar{u}$ is positive. It follows that the net mass flux can be written as

$$\delta m_f = -\oint_S \hat{n} \cdot \rho \bar{u} r_c \, dS \tag{A.6}$$

Therefore, by conservation,

$$\frac{\partial}{\partial t} \int_A \rho r_e \, dA + \oint_S \hat{n} \cdot \rho \bar{u} r_c \, dS = 0 \tag{A.7}$$

which is the first governing equation and is known as the mass conservation or continuity equation. As in this case, a swirl free axisymmetric flow is considered, the gradient in the circumferential direction is equal to zero,

$$\frac{\partial}{\partial\theta} = 0 \tag{A.8}$$

In addition, there is no circumferential velocity ($v_\theta = 0$) and hence no net mass flux in the circumferential direction of the control volume.

A.2 Conservation of Momentum

By definition, momentum is conserved. Thus we have,

$$\begin{pmatrix}\text{Rate of change of}\\\text{Momentum of Fluid}\\\text{Enclosed by Surface}\end{pmatrix} = \begin{pmatrix}\text{Net Momentum Flux}\\\text{of Fluid Through}\\\text{Control Surface}\end{pmatrix} + \begin{pmatrix}\text{Body Force}\\\text{Acting On}\\\text{Control Volume}\end{pmatrix}$$

This is base on Newton's 2^{nd} Law which states that *the time rate of change of the momentum in the control volume is equal to the force acting on the control volume.*

The forces that act on fluid elements can be categorised into two - *body forces* and *surface forces*. *Body forces* are forces which act from a distance (external effects) on the mass of material contained within the control volume. Examples include magnetic, gravitational and electric forces. *Surface forces* on the other hand, are due to the pressure distribution over the control surface as well as viscous forces due to normal and shear stresses within the material. The viscous forces can be ignored when considering momentum conservation in an inviscid media. As in the current work, normal and shear stresses due to viscosity are excluded. The inclusion of body forces will only be considered for specific problem.

Hence, the elemental volume $r_e dA$ has mass,

$$\rho r_e dA \tag{A.9}$$

Hence, the momentum of fluid element is simply the product of the elemental mass (Eqn. A.9) and the local velocity $\bar{u}$. The total momentum over the whole control volume is therefore,

$$\int_A \rho\bar{u}r_e dA \tag{A.10}$$

and the rate of change of momentum is

$$\frac{\partial}{\partial t}\int_A \rho\bar{u}r_e dA \tag{A.11}$$

The mass flux across the control surface is defined earlier in Eqn. A.6. Its product with the velocity $\bar{u}$ gives the momentum flux. Thus the net momentum flux over the whole control surface S is the sum of all the elemental momentum flux as follows,

$$-\oint_S \hat{n}\cdot\rho\bar{u}\bar{u}r_c dS \tag{A.12}$$

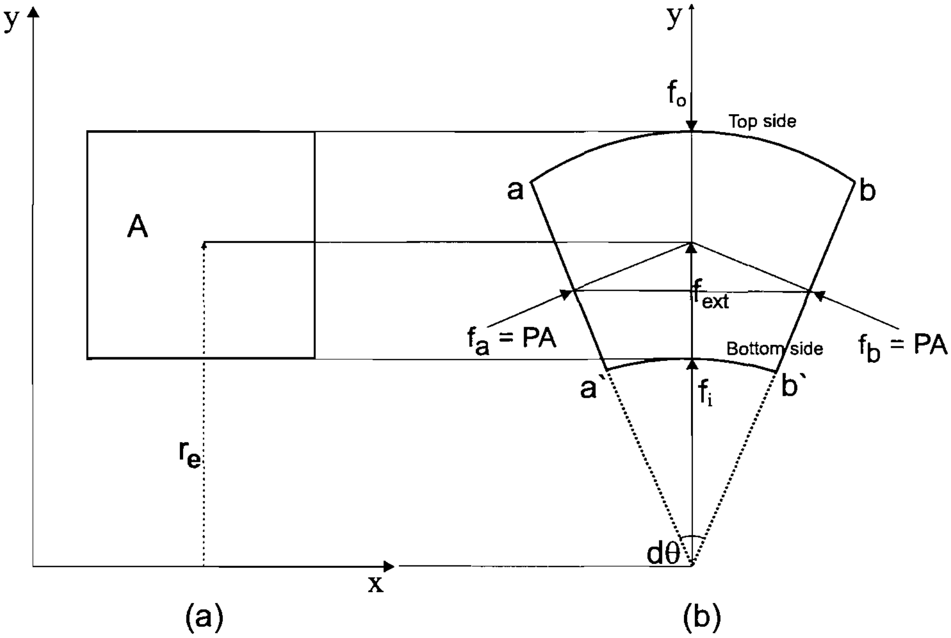

Figure A.3: Finite volume of angular extent $d\theta$

The force that acts on the control surface is categorised into a normal force that is the total contribution of pressure force and normal stress of materials, and a shear stress of materials. Now let us consider the forces acting on the surface r_cS and let $\bar{\tau}$ be the *total stress tensor*. In the Cartesian coordinate system where one axis is set as the axis of symmetry, the components of this stress are given in the x, y and θ directions. First, let F_t be the total surface force acting on the boundary surface r_cS, then

$$F_t = \oint_S \hat{n}\bar{\tau}r_c dS \tag{A.13}$$

where the stress tensor $\bar{\tau}$ is defined in a matrix form as

$$\acute{\tau} = \begin{bmatrix} \sigma_x & \tau_{xy} & \tau_{xz} \\ \tau_{yx} & \sigma_y & \tau_{yz} \\ \tau_{zx} & \tau_{zy} & \sigma_z \end{bmatrix} = \begin{bmatrix} -p & 0 & 0 \\ 0 & -p & 0 \\ 0 & 0 & -p \end{bmatrix} = -Ip \tag{A.14}$$

The entries τ_{ij} are all zeros as only the pressure distribution is considered. The negative sign is because the pressure is acting inwards. I is the unit tensor.

Thus the total surface force $\bar{F}_t$ acting on the control volume fixed in space can be written as

$$\bar{F}_t = -\oint_S \hat{n} I p r_c dS \tag{A.15}$$

The extra forces arising from the axisymmetric geometry of the problem are classified into a source term in the governing equations. Now consider Figure A.3 below which show an arbitrary area A, presented here as a rectangle for simplicity, is rotated with respect to the x-axis to give a finite control volume of angular extent $d\theta$.

Due to geometry, the surface area on the outer part of the control volume, $a - b$, is larger than the inner part, $\acute{a} - \acute{b}$. As a consequent, by assuming a uniform pressure in the surrounding fluid, the force f_{out} is larger than the force f_{in}. These forces act in opposite direction to each other and are in equilibrium due to an extra force f_{ext} from contribution of pressure P acting normal to either side of the control volume (labeled a and b on Figure A.3). Note that the sides $a\acute{a}$ and $b\acute{b}$ have the same area, i.e. $A_{a\acute{a}} = A_{b\acute{b}} = A$. As the area are the same, $f_a = f_b$. It should be noted that, this pressure P, should not be confused with the p pressure acting on the boundary (wrapping) surface of the control volume. Although, in the case of a uniform pressure field $p = P$, f_a and f_b do not cancel each other out as they are not parallel, but accelerate the control volume in the positive radial direction.

The radial component of f_a and f_b gives the extra resultant force, f_{ext}. Since $f_a = f_b = PA$, the radial component of the force acting on sides a and b is given by

$$f_{ext} = 2PA\sin\left(\frac{1}{2}d\theta\right) \tag{A.16}$$

For small angle approximation, Equation A.16 reduces to

$$f_{ext} = PAd\theta \tag{A.17}$$

For the entire control volume of 1 radian rotation, the total extra force in the radial direction is given by,

$$F_{ext} = \int_0^1 PA\, d\theta = PA \tag{A.18}$$

or in vector notation

$$\bar{F}_{ext} = \int_A \frac{\bar{e}_y P}{r_e} r_e dA = \int_A \bar{g} r_e dA \tag{A.19}$$

where

$$g = \frac{\bar{e}_y P}{r_e} \tag{A.20}$$

and $\bar{e}_y$ is the unit radial vector.

This shows that the extra force that exists due to the geometry of the axisymmetric flow acts only in the radial direction, i.e. y-component of momentum.

Therefore, combining all the expressions (A.10, A.12, A.15, A.19) gives,

$$\frac{\partial}{\partial t} \int_A \rho \bar{u} r_e dA = -\oint_S \hat{n} \cdot \rho \bar{u} \bar{u} r_c dS - \oint_S \hat{n} \cdot I p r_c dS + \int_A \bar{g} r_e dA \tag{A.21}$$

or

$$\frac{\partial}{\partial t} \int_A \rho \bar{u} r_e dA + \oint_S \hat{n} \cdot (\rho \bar{u} \bar{u} + I p) r_c dS = \int_A \bar{g} r_e dA \tag{A.22}$$

A.3 Conservation of Energy

In order to formulate a complete system of conservation laws, the conservation of energy must be considered. This law is deduced from the *First Law of Thermodynamics* and is defined as follows:

$$\begin{pmatrix} \text{Rate of change} \\ \text{of Energy of} \\ \text{Fluid in} \\ \text{Control Volume} \end{pmatrix} = \begin{pmatrix} \text{Net Energy Flux} \\ \text{of Fluid into Control} \\ \text{Volume across} \\ \text{Control Surface} \end{pmatrix} + \begin{pmatrix} \text{Work done on} \\ \text{the Control} \\ \text{Volume at the} \\ \text{Control Surface} \end{pmatrix}$$

The energy contain within an elemental volume $r_e dA$ is,

$$E \rho r_e dA \tag{A.23}$$

where,

$$E = e + \frac{\bar{u} \cdot \bar{u}}{2} \tag{A.24}$$

is the total specific energy (per unit mass), which comprises of ϵ is the specific internal energy and kinetic energy. Therefore, the total energy in the entire control volume is

$$\int_A E\rho r_e dA \tag{A.25}$$

Hence, the rate of change of total energy is given by

$$\frac{\partial}{\partial t}\int_A E\rho r_e dA \tag{A.26}$$

The mass flow across the surface element $r_c dS$ is

$$-\hat{n}\cdot\rho\bar{u}r_c dS \tag{A.27}$$

Hence, the energy flux is the product of energy E and mass flux $-\hat{n}\cdot\rho\bar{u}r_c dS$ across the surface element. It follows that

$$-\hat{n}\cdot\rho\bar{u}Er_c dS \tag{A.28}$$

and over the entire control surface, the total energy flow is given by

$$-\oint_S \hat{n}\cdot\rho\bar{u}Er_c dS \tag{A.29}$$

Now, the rate of work done due to the pressure force acting on the surface element rdS is given by the principle *rate of work done = force × velocity*. Given the force due to the pressure distribution on the surface element is $-\hat{n}\cdot pr_c dS$, the rate of work done in vector form is $-\hat{n}\cdot p\bar{u}r_c dS$. Integrating over the entire control surface yields the total rate of work done,

$$-\oint_S \hat{n}\cdot p\bar{u}r_c dS \tag{A.30}$$

Hence, the energy equation can be expressed as

$$\frac{\partial}{\partial t}\int_A E\rho r_e dA + \oint_S \hat{n}\cdot(\rho\bar{u}E + \bar{u}p)r_c dS = 0 \tag{A.31}$$

which is the third and final conservation equation. The external force f_{ext}, described earlier in Section A.2, does not do any work since the circumferential velocity is equal to zero. Therefore, there is no energy term in $\bar{G}$. The three conservation equations, Equation A.7, Equation A.22 and Equation A.31 may be conveniently expressed in a compact form as follows:

$$\frac{\partial}{\partial t}\int_A \bar{U} r_e dA + \oint_S \hat{n} \cdot \bar{F} r_c dS = \int_A \bar{G} r_e dA \tag{A.32}$$

where

$$\bar{U} = \begin{bmatrix} \rho \\ \rho \bar{u} \\ \rho E \end{bmatrix} \quad \bar{F} = \begin{bmatrix} \rho \bar{u} & & \\ \rho \bar{u}\bar{u} & + & Ip \\ \rho \bar{u}\bar{E} & + & \bar{u}p \end{bmatrix} \quad \bar{G} = \begin{bmatrix} 0 \\ \frac{\bar{e}_y P}{r_e} \\ 0 \end{bmatrix} \tag{A.33}$$

The vectors $\bar{U}$ and $\bar{F}$ are the conserved variable vector and flux vector respectively. The vectors $\bar{G}$ and $\bar{H}$ are the source vectors resulting from the consideration of axisymmetric geometry. These governing equations (Eqn. A.32 and A.33) are the unsteady, compressible Euler equations in axisymmetric form.

A.4 Conservation of Volume

Transformation from Eulerian to Lagrangian reference frame causes the convective terms in the flux vector to vanish. As a consequence the continuity equation becomes

$$\frac{\partial}{\partial t}\int_A \rho r_e dA = 0 \tag{A.34}$$

which is a redundant expression since it states that the mass within the control volume is invariant with time. Therefore, another physical principle - volume is conserved - is required to provide a close set of governing equations. The principle states that

$$\begin{pmatrix} \text{Rate of change} \\ \text{of Volume} \\ \text{in Control Volume} \end{pmatrix} = \begin{pmatrix} \text{Volume Changed} \\ \text{due to Movement} \\ \text{of Boundary} \end{pmatrix}$$

Considering a volume element $r_e dA$ and integrating, the volume enclosed by control surface $r_c dS$ is given by,

$$V = \int_{A(t)} r_e dA \tag{A.35}$$

Thus the rate of change of volume is

$$\dot{V} = \frac{\partial}{\partial t}\int_{A(t)} r_e dA \tag{A.36}$$

The volume change due to the movement of the elemental surfaces is given by

$$\hat{n} \cdot \bar{u} r_c dS \tag{A.37}$$

Integrating for the entire control surface gives,

$$\oint_S \hat{n} \cdot \bar{u} r_c dS \tag{A.38}$$

Equating the rate of change of volume and the total volume change, we have,

$$\frac{\partial}{\partial t} \int_{A(t)} r_e dA + \oint_{S(t)} \hat{n} \cdot \bar{u} r_c dS = 0 \tag{A.39}$$

Therefore, the Euler equations in the Lagrangian reference frame can be written in a compact form as:

$$\frac{\partial}{\partial t} \int_{A(t)} \bar{U} r_e dA + \oint_{S(t)} \hat{n} \cdot \bar{F} r_c DS = \int_{A(t)} \bar{G} r_e dA \tag{A.40}$$

Therefore, the vector of conserved variables becomes,

$$\overline{U} = \begin{bmatrix} 1 \\ \rho \bar{u} \\ \rho E \end{bmatrix} \tag{A.41}$$

and the flux vector becomes,

$$\overline{F} = \begin{bmatrix} -\bar{u} \\ Ip \\ \bar{u}p \end{bmatrix} \tag{A.42}$$

Hence, the integral form of the conservation laws for an inviscid, unsteady, compressible Euler equations in the Lagrangian reference frame are obtained.

Bibliography

[1] R. E. Apfel, *Sonic effervescence: A tutorial on acoustic cavitation*, J. Acoust. Soc. Am. **101** (1987), no. 3, 1227–1237.

[2] D. G. Assimos, W. H. Boyse, L. H. Harrison, D. L. McCollough, and R. L. Kroovand, *The role of open stone surgery since extracorporeal shock wave lithotripsy*, J. Urol. **142** (1989), 263–267.

[3] G. J. Ball, *A Free-Lagrange method for unsteady compressible flow: simulation of a confined cylindrical blast wave*, J. Shock Waves **5** (1996), 311–325.

[4] G. J. Ball and R. A. East, *Shock and blast attenuation by aqueous foam barriers: influences of barrier geometry*, J. Shock Waves **9** (1999), 37–47.

[5] G. J. Ball, A. L. Gordon, J. C. Hunter, P. H. Richards, and G. T. Thompson, *Application of holographic interferogram for mapping of gas density in a transonic flow*, Pro. **8** (1985), 37–47.

[6] G. J. Ball, B. P. Howell, T. G. Leighton, and M. J. Schofield, *Shock-induced collapse of a cylindrical air cavity in water*, J. Shock Waves **10** (2000), 265–276.

[7] T. B. Benjamin and A. T. Ellis, *The collapse of cavitation bubbles and the pressure thereby produced against solid boundaries*, Philos. Trans. R. Soc. London, Ser. A **260** (1966), 221–240.

[8] W. H. Besant, *Hydrostatics and hydrodynamics*, Oxford University Press, London: CUP, 1859.

[9] J. P. Best, *The formation of toroidal bubbles upon the collapse of transient cavities*, J. Fluid Mech. **251** (1993), 79–107.

[10] J. R. Blake and D. C. Gibson, *Growth and collapse of a vapour cavity near a free-surface*, J. Fluid Mechanics **111** (1981), 123–140.

[11] J. R. Blake and D. C. Gibson., *Cavitation bubbles near boundaries*, Am. Rev. Fluid Mech. **19** (1987), 99–123.

[12] J. R. Blake, G. S. Keen, R. P. Tong, and M. Wilson, *Acoustic cavitation: The fluid dynamics of non-sperical bubbles*, Phil. Trans. R. Soc. Lond. **357** (1999), 251–267.

[13] J. R. Blake, B. B. Taib, and G. Doherty, *Transient cavities near boundaries: Part 1. Rigid boundary*, J. Fluid Mechanics **170** (1986), 479–497.

[14] N. K. Bourne and J. E. Field, *Bubble collapse and the initiation of explosion*, Proc. Roy. Soc. Lond. **A435** (1991), 423–435.

[15] N. K. Bourne and J. E. Field., *Shock-induced collapse of single cavities in liquids*, Journal of Fluid Mechanics **244** (1992), 225–240.

[16] N. K. Bourne and J. E. Field, *Shock-induced collapse and luminescence by cavities*, Phil. Trans. R. Soc. Lond. A **357** (1999), 295–311.

[17] K. S. Brentner and F. Farassat, *Analytical comparison of the acoustic analogy and kirchhoff formulation for moving surfaces*, AIAA **36** (1998), no. 8, 1379–1386.

[18] E. A. Brujan, K. nahen, P. Schmidt, and A. Vogel, *Dynamics of laser-induced cavitation bubbles near elastic boundaries: influence of the elastic modulus*, J. Fluid Mechanics **433** (2001), 283–314.

[19] G. L. Chahine, G. S. Frederick, C. J. Lambrecht, G. S. Harris, and H. U. Mair, *Spark-generated bubbles as laboratory-scale models of underwater explosions and their use for validation of simulation tools*, SAVIAC Proceedings 66^{th} Shock and Vibrations Symposium **2** (1995), 265–276.

[20] C. Chaussy, J. Schuller, E. Schmiedt, H. Brandl, D. Jocham, and B. Liedl, *Extracorporeal shock-wave lithotripsy (eswl) for treatment of urolithiasis*, Urology **23** (1984), 59–66.

[21] C. J. Chuong, P. Zhong, and G. M. Preminger, *A comparison of stone damage caused by different modes of shock wave generation*, J. Urol. **148** (1992), 200–205.

[22] C. C. Church, *A theoretical study of cavitation generated by an extracorporeal shock wave lithotripter*, J. Acoust. Soc. Am **86** (1989), no. 1, 215–227.

[23] R. O. Cleveland, D. A. Lifshitz, B. A. Connors, A. P. Evan, L. R. Willis, and L. A. Crum, *In vivo pressure measurements of lithotripsy shock waves in pigs*, Ultrasound Med. Biol. **24** (1998), no. 2, 293–306.

[24] A. J. Coleman, M. J. Choi, J. E. Saunders, and T. G. Leighton, *Acoustic emission and sonoluminescence due to cavitation at the beam focus of an electrohydraulic shock wave lithotripter*, Ultrasound Med. Biol. **18** (1992), no. 3, 267–281.

[25] A. J. Coleman and J. E. Saunders, *A survey of the acoustic output of commercial extracorporeal shock wave lithotripters*, Ultrasound Med. Biol. **15** (1989), 213–227.

[26] A. J. Coleman, J. E. Saunders, L. A. Crum, and M. Dyson, *Acoustic cavitation generated by an extracorporeal shock-wave lithotripter*, Ultrasound Med. Biol. **13** (1987), 69–76.

[27] A. J. Coleman, M. Whitlock, T. G. Leighton, and J. E. Saunders, *The spatial distribution of cavitation induced acoustic emission, sonoluminescence and cell lysis in the field of a shock wave lithotripter*, Phys. Med. Biol. **38** (1993), 1545–1560.

[28] L. A. Crum, *Cavitation microjets as a contributory mechanism for renal calculi disintegration in eswl*, Journal of Urology **140** (1988), 1587–1590.

[29] K. B. Cunningham, A. J. Coleman, T. G. Leighton, and P. R. White, *Characterising in vivo acoustic cavitation during lithotripsy with time-frequency methods*, Acoustics Bulletin **26** (2001), no. 5, 10–16.

[30] J. P. Dear and J. E. Field, *A study of the collapse of arrays of cavities*, J. Fluid Mech. **190** (1988), 409–425.

[31] J. P. Dear, J. E. Field, and A. J. Walton, *Gas compression and jet formation in cavities collapse by shock wave*, Nature **332** (1988), 505–508.

[32] M. Delius, *Medical applications and bioeffects of extracorporeal shock waves*, Shock Waves **4** (1994), 55–72.

[33] M. Delius, G. Enders, G. Heine, J. Stark, K. Remberger, and W. Brendel, *Biological effects of shock waves: lung hemorrhage by shock waves in dogs-pressure dependence*, Ultrasound Med. Biol. **13** (1987), 61–67.

[34] P. di Francescantonio, *A new boundary integral formulation for the prediction of sound radiation*, Journal of Sound and Vibration **202** (1997), no. 4, 491–509.

[35] Z. Ding and S. M. Graceswki, *The behaviour of a gas cavity impacted by a weak or strong shock wave*, J. Fluid Mech. **309** (1996), 183–209.

[36] J. H. Duncan and S. Zhang, *On the interaction of a collapsing cavity and a compliant wall*, J. Fluid Mech. **226** (1991), 401–423.

[37] B. Einfeldt, *On Godunov-type method for gas dynamics*, Siam J. Numer. Analysis **25** (1988), no. 2, 294–318.

[38] A. P. Evan, L. R. Willis, B. Connors, G. Reed, J. A. McAteer, and J. E. Lingeman, *Shock wave lithotripsy-induced renal injury*, Am. J. Kidney Dis. **17** (1991), 445–450.

[39] F. Farassat and M. K. Myers, *Extension of kirchhoff's formula to radiation from moving surfaces*, J. Sound Vibration **123** (1988), no. 3, 451–461.

[40] F. Farassat and G. P. Succi, *The prediction of helicopter discrete frequency noise*, Vertica **7** (1983), no. 4, 309–320.

[41] M. J. Gaston, J. A. Reizes, and G. M. Evans, *Numerical modelling of multiple three dimensional gas bubbles rising in a quiescent liquid using a volume of fluid method*, The 2^{nd} International Conference of Computational Fluid Dynamics, 2002.

[42] F. R. Gilmore, *The growth or collapse of a spherical bubble in a viscous compressible liquid*, California Institute Technology, Pasadena, CA, Rep. **26** (1952), no. 4, 1–40.

[43] S. K. Godunov, *A difference scheme for numerical computation of discontinuous solutions of equations of fluid dynamics*, Mat. Sb **47** (1959), 271–290.

[44] M. F. Hamilton and D. T. Blackstock, *Nonlinear acoustics, theory and applications*, Academic Press, New York, US, 1998.

[45] F. G. Hammitt, *Cavitation and Multiphase Flow Phenomena*, McGraw-Hill, US, 1980.

[46] A. Harten, P. D. Lax, and B. van Leer, *On upstream differencing and Godunov-type schemes for hyperbolic conservartion law*, Siam Review **25** (1983), no. 1, 35–61.

[47] D. Howard and B. Sturtevant, *In vitro study of the mechanical effects of shock-wave lithotripsy*, Ultrasound Med. Bio. **23** (1997), 1107–1122.

[48] B. P. Howell, *An investigation of Lagrangian-Riemann Methods Incorporating Material Strength*, Ph.D. thesis, University of Southampton, Aeronautics and Astronautics, 2000.

[49] B. P. Howell and G. J. Ball, *Damping of mesh-induced errors in Free-Lagrange simulations of richtmyer-meshkov instability*, J. Shock Waves **10** (2000), no. 4, 253–264.

[50] L. Howle, D. G. Schaeffer, M. Sheare, and P. Zhong, *Lithotripsy: The treatment of kidney stones with shock waves*, SIAM Review **40** (1998), no. 2, 356–371.

[51] D. Igra and K. Takayama, *Investigations of aerodynamic breakup of a cylindrical water droplet*, Reports of the Institute f Fluid Science, Tohoku University **11** (1999), 123–134.

[52] D. Igra and K. Takayama., *Simulation of shock wave interaction with a water column*, Shock Waves **11** (2001), 219–228.

[53] J. D. Anderson Jr, *Computational fluid dynamics, the basics with applications*, McGraw-Hill, USA, 1995.

[54] L. E. Kinsler, A. R. Frey, A. B. Coppens, and J. V. Sanders, *Fundamentals of acoustics*, John Wiley, NY, 1982.

[55] C. L. Kling and F. G. Hammitt, *A photographic study of spark-induced cavitation bubble collapse*, J. Basic Eng. Trans. ASME D **94** (1972), 825–833.

[56] T. Kodama and K. Takayama, *Dynamic behaviour of bubbles during extraxcorporeal shock-wave lithotripsy*, Ultrasound Med. Bio. **24** (1998), 723–738.

[57] T. Kodama, K. Takayama, and N. Nagayasu, *The dynamics of two air bubbles loaded by an underwater shock wave*, J. Appl. Phys. **80** (1996), no. 10, 5587–5592.

[58] B. Koren, E. H. van Brummelen, P. W. Hemker, M. R. Lewis, and B. van Leer, *Fixes for solutions errors near interfaces in two-fluid flow computations*, The 2^{nd} International Conference of Computational Fluid Dynamics, 2002.

[59] M. Kornfeld and L. Suvorov, *On the destructive action of cavitation*, J. Appl. Physics **15** (1944), 495–506.

[60] M. Kuwahara, N. Ioritani, K. Kambe, S. Orikasa, and K. Takayama, *Anti-miss-shot control device for selective stone disintegration in extracorporeal shock wave lithotripsy*, Shock Waves **1** (1991), 145–148.

[61] W. Lauterborn and H. Bolle, *Experimental investigation of cavitation-bubble collapse in neighbourhood of a solid boundary*, J. Fluid Mechanics **72** (1975), 391–399.

[62] T. G. Leighton, *The acoustic bubble*, The Academic Press, London, 1994.

[63] M. Loyez, *Free-lagrange simulations of flame/vortex interactions, including detailed finite rate chemical kinetics and heat release*, Ph.D. thesis, University of Southampton, Aeronautics and Astronautics, 1997.

[64] H. Luo, J. D. NBaum, and R Löhner, *On the computation of multi-material flows using ale formulation*, The 2^{nd} International Conference of Computational Fluid Dynamics, 2002.

[65] P. A. Lush, K. Takayama, T. Tomita, and T. Obara, *Cavitation and induced shock wave-bubble interaction as a cause of human tissue damage in extracorporeal shock wave lithotripsy*, Cavitation, Proceedings of the Institution of Mechanical Engineers, 1992, pp. 55–64.

[66] A. S. Lyrintzis, *Review: The use of kirchhoff's method in computational aeroacoustics*, Transactions of the ASME: J. Fluids Engineering **116** (1994), 665–676.

[67] A. S. Lyrintzis and A. R. George, *Use of the kirchhoff method in acoustics*, AIAA Journal **27** (1989), no. 10, 1451–1453.

[68] A. S. Lyrintzis and Y. Xue, *Study of the noise mechanisms of transonic blade-vortex interactions*, AIAA Journal **29** (1991), no. 10, 1562–1572.

[69] C. F. Naude and A. T. Ellis, *On the mechanism of cavitation damage by nonhemispherical cavities collapsing in contact with a solid boundary*, J. Basic Engr. Trans. ASME, Series D **83** (1961), 648.

[70] M. Orkisz, M. Bourlin, G. Gimenez, and T. A. Flam, *Real-time target tracking applied to improve fragmentation of renal stones in extra-corporeal lithotripsy*, Machine Vision and Applications **11** (1999), 138–144.

[71] A. Philipp, M. Delius, C. Scheffczyk, V. Vogel, and W. Lauterborn, *Interaction of lithotripter-generated shock waves with air bubbles*, J. Acoust. Soc. Am. **93** (1993), no. 5, 2496–2509.

[72] A. Philipp and W. Lauterborn, *Cavitation erosion by single laser-produced bubbles*, J. Fluid Mechanics **361** (1998), 75–116.

[73] M. S. Plesset and R. B. Chapman, *Collapse of an initially spherical vapour cavity in the neighbourhood of a solid boundary*, J. Fluid Mechanics **47** (1971), 283–290.

[74] M. S. Plesset and A. Prosperetti, *Bubble dynamics and cavitation*, Ann. Rev. Fluid Mech. **9** (1977), 145–185.

[75] Lord Rayleigh, *On the pressure developed in a liquid during the collapse of a spherical cavity*, Philos. Mag. **34** (1917), 94–98.

[76] W. Saas, M. Brunlich, H.P. Dreyer, E. Matura, W. Folberth, H. Priesmeyer, and J. Seifert, *The mechanisms of stone disintegration by shock waves*, Ultrasound Med. Biol. **17** (1991), no. 3, 239–243.

[77] K. Sato, Y. Tomita, and A. Shima, *Numerical analysis of a gas bubble near a rigid boundary in an oscillatory pressure field*, J. Acoust. Soc. Am. **95** (May 1994), no. 5(1), 2416–2424.

[78] S. J. Shaw, W. P. Schiffers, T. P. Gentry, and D. C. Emmony, *A study of the interaction of a laser-generated cavity with a nearby solid boundary*, J. Phys. D: Appl.Phys **32** (1999), 1612–1617.

[79] A. Shima, *Studies of bubble dynamics*, J. Shock Waves **7** (1997), 33–42.

[80] A. Shima, K. Takayama, Y. Tomita, and N. Ohsawa, *Mechanism of impact pressure generation from spark-generated bubble collapse near a wall*, AIAA Journal **21** (1983), 55–59.

[81] A. Shima, Y. Tomita, D. C. Gibson, and J. R. Blake, *The growth and collapse of cavitation bubbles near composite surfaces*, J. Fluid Mech. **203** (1989), 199–214.

[82] N. D. Shutler and R. B. Mesler, *A photographic study of the dynamics and damage capabilities of bubbles collapsing near solid boundaries*, Trans. ASME, J. Basic Eng. D **87** (1965), 511–517.

[83] R. W. Smith, *Ausm(ale): A Geometrically Conservative Arbitrary Lagrangian-Eulerian Flux Slitting Scheme*, J. Comp. Physics **150** (1999), 268–286.

[84] D. H. Sokolov, M. R. Bailey, and L. A. Crum, *Dual-pulse lithotripter accelerates stone fragmentation and reduces cell lysis in vitro*, Ultrasoud Med. Biol. **29/7** (2003), 1045–1052.

[85] P. Testud-Giovanneschi, A. P. Alloncle, and D. Dufresne, *Collective effects of cavitation: Experimental study of bubble-bubble and bubble-shock wave interactions*, J. Appl. Phys. **67** (1990), no. 8, 3560–3564.

[86] Y. Tomita, T. Obara, K. Takayama, and M. Kuwahara, *Cavitation phenomena in extracorporeal microexplosion lithotripsy*, Shock Waves **3** (1994), 149–157.

[87] Y. Tomita and A. Shima, *Mechanisms of impulsive pressure generation and damage pit formation by bubble collapse*, J. Fluid Mech. **169** (1986), 535–564.

[88] Y. Tomita and A. Shima., *High speed photographic observations of laser-induced cavitation bubbles in water*, Acustica **71** (1990), 161–171.

[89] Y. Tomita, A. Shima, and K. Takahashi, *The collapse of a gas bubble attached to a solid wall by a shock wave and the induced impact pressure*, Trans. ASME I: J. Fluids Eng. **105** (1983), 341–349.

[90] Y. Tomita, M. Tsubota, K. Nagane, and N. An-naka, *Behaviour of laser-induced cavitation bubbles in liquid nitrogen*, J. Applied Physics **88** (2000), no. 10, 5993-6001.

[91] R. P. Tong, W. P. Schiffers, S. J. Shaw, J. R. Blake, and D. C. Emmony, *The role of 'splashing' in the collapse of a laser-generated cavity near a rigid boundary*, J. Fluid Mechanics **380** (1999), 339–361.

[92] E. F. Toro, M. Spruce, and W Speares, *Restoration of the contact surface in the HLL-Riemann solver*, J. Shock Waves **4** (1994), 25–34.

[93] J. Y. Trépanier, M. Reggio, M. Paraschivoiu, and R. Camarero, *Unsteady Euler solutions for arbitrarily moving bodies and boundaries*, AIAA **31** (1993), no. 10, 1869 1876.

[94] C. K. Turangan, *Free-lagrange simulations of cavitation bubble collapse*, Ph.D. thesis, University of Southampton, Aeronautics and Astronautics, 2002.

[95] C. K. Turangan and G. J. Ball, *Ale and free-lagrange simulations of shock-bubble interaction*, The 23^{rd} International Symposium on Shock Wave, 2001.

[96] B. van Leer, *Towards the ultimate conservative difference scheme. v. a second order sequel to Godunov's method*, J. Comp. Physics **32** (1979), 101–136.

[97] A. Vogel, W Lauterborn, and R. Timm, *Optical and acoustic investigations of dynamics of laser-produced cavitation bubbles near solid boundary*, J. Fluid Mechanics **206** (1989), 299–338.

[98] K. Weltner, J. Grosjean, P. Schuster, and W. J. Weber, *Mathematics for engineering students*, Stanley Thornes, UK, 1986.

[99] L. R. Willis, A. P. Evan, and J. E. Lingeman, *The impact of high-dose lithotripsy on renal function*, Contemporary Urology **11** (1999), 45–50.

[100] X. Xi and P. Zhong, *Improvement of stone fragmentation during shock-wave lithotripsy using a combined eh/peaa shock-wave generator-in vitro experiments*, Ultrasound Med. Biol. **26** (2000), no. 3, 457–467.

[101] F. Xiao and T. Yabe, *A method to trace sharp interface of two fluids in calculations involving shocks*, Shock Waves **4** (1995), 101–108.

[102] A. Yasuda and H. Takahira, *Numerical analysis of temperature fields inside non-spherical bubbles in the final stage of collapse*, The 4^{th} International Symposium on Cavitation, 2001.

[103] R. K. Zeman, W. J. Davros, J. A. Goldberg, B. S. Garra, W. S. Hayes, E. L. Cattau, S. C. Horii, C. J. Cooper, and P. M. Silverman, *Cavitation effects during lithotripsy.part ii. clinical observations*, Radiology **177** (1990), 163–166.

[104] S. Zhang, J. H. Duncan, and G. L. Chahine, *The final stage of the collapse of a cavitation bubble near rigid wall*, J. Fluid Mechanics **257** (1993), 147–181.

[105] Y. L. Zhang, K. S. Yeo, B. C. Khoo, and W. K. Chong, *Three-dimensional computation of bubbles near a free surafce*, J. Comp. Physics **146** (1998), 105–123.

[106] Y. L. Zhang, K. S. Yeo, B. C. Khoo, and C. Wang, *3d jet impact and toroidal bubbles*, J. Comp. Physics **166** (2001), 336–360.

[107] P. Zhong, I. Cioanta, F. H. Cocks, and G. M. Preminger, *Inertial cavitation and associated acoustic emission produced during electrohydraulic shock wave lithotripsy*, J. Acoust. Soc. Am. **101** (1997), no. 5(1), 2940–2950.

[108] P. Zhong, F. H. Cocks, I. Cioanta, and G. M. Preminger, *Controlled. forced collapse of cavitation bubbles for improved stone fragmentation during shock wave lithotripsy*, J. Urol. **158** (1997), 2323–2328.

[109] P. Zhong, H. Lin, X. Xi, S. Zhu, and E. S. Bhogte, *Shock wave-inertial microbubble interaction: Methodology, physical characterisation, and bioeffect study*, J. Acoust. Soc. Am. **105** (March 1999), no. 3, 1997–2009.

[110] S. Zhu, F. H. Cocks, G. M. Preminger, and P. Zhong, *The role of stress waves and cavitation in stone comminution in shock wave lithotripsy*, Ultrasound Med. Biol. **28** (2002), no. 5, 661–671.